Organic Semiconductors for Photocatalytic Carbon Dioxide Reduction

Zhiwei Fu

June 2021

Thesis submitted in accordance with the requirements of the University of Liverpool for the degree of Doctor of Philosophy

Abstract

Photocatalytic carbon dioxide (CO_2) reduction into chemical fuels using efficient and economically viable photocatalysts is a promising method to utilize solar energy and help mitigate the greenhouse effect. Carbon monoxide (CO) is of significant interest because CO is used in many large-scale industrial processes. Organic semiconductors have diverse chemical functionalities and pore structures, allowing controllable tuning of their physicochemical properties such as band gaps and surface areas. In this thesis, linear polymers and covalent organic frameworks (COFs) were explored for photocatalytic CO_2 reduction to understand the relationships between material properties and photocatalytic activity.

A range of linear conjugated polymers with different structures of backbone was synthesized and measured by using high-throughput methods. Optical properties, electronic properties, and dispersibility were investigated for their effects on differences in performance. A dibenzo[*b*,*d*]thiophene sulfone co-polymer with phenylene (P7) had the highest rate of CO production, but also of H_2 co-evolution. The co-evolution of hydrogen is facilitated by residual palladium from polymer synthesis. By varying the amount of palladium in P7, syngas could be obtained with varying ratios of H_2 to CO.

To overcome the long-term instability of the reversible bond-formation chemistry used in making most COFs and reduce the influence of residual metals on product selectivity, a new olefin COF was synthesized via Knoevenagel condensation. The obtained Bpy-sp^2c-COF with bipyridine sites inside could incorporate with rhenium complexes to afford a heterogeneous photocatalyst with an improved catalytic performance over its homogeneous Re counterpart. The COF is porous and can be further dye-sensitized to enhance the activity. The addition of platinum resulted in the production of syngas, *i.e.*, the co-formation of H_2 and CO, the chemical composition of which could be adjusted by varying the ratio of COF to platinum. An amorphous analogue of the COF showed significantly lower CO production rates, suggesting that crystallinity of the COF is vital to its photocatalytic performance in CO_2 reduction.

A series of fluorinated COFs and their isostructural COFs were rationally designed and synthesized, exhibiting excellent CO_2 reduction with cobalt (II) bipyridine complexes as cocatalyst under visible light irradiation. Fluorinated COFs showed excellent stability and a CO_2-to-CO performance comparable with the homogeneous ruthenium bipyridine complex system under similar conditions.

Acknowledgements

First and foremost, I would like to express my sincerest gratitude to my supervisor, Prof Andrew I. Cooper, for giving me the opportunity to do research work in this top-class laboratory. His guidance, advice, encouragement, and support over the years have allowed me to have an enjoyable PhD experience. Thanks also to the China Scholarship Council for providing the PhD studentship for this research.

There are many people of whom I would like to thank. Without them, the completion of this thesis would not have been possible. I would like to extend my sincere thanks to Dr Linjiang Chen, who has been a huge support throughout my PhD. His suggestions have benefited me a lot in both scientific research and daily life. Many thanks go to Dr Reiner Sebastian Sprick for co-supervising my PhD research and for his help and guidance.

I would also like to thank all those I have collaborated with on this work, especially Dr Samantha Y. Chong, Dr Gaia Neri, Dr Charlotte Smith, Prof Alexander J. Cowan, Dr Matthew Bilton and Dr Adrian M. Gardner at the University of Liverpool and Dr Martijn A. Zwijnenburg at UCL. Thanks must also go to Cooper group members past and present for their help, including Dr Marc Little, Dr Michael Briggs, Dr Yue Wu, Dr Xiaoyan Wang, Dr Yang Bai, Dr Xiaobo Li, Dr Guohong Ning, Dr Anastasia Vogel, Dr Ming Liu, Dr Christian Mier, Dr Duncan Woods, Dr Catherine M. Aitchison, Dr Weiwei Zhang, Dr Xiaofeng Wu. Special thanks to Rob Clowes for training and fixing all the instruments.

Thanks must go to Zhongfu Pang, Lunjie Liu, Xue Wang, Yu Che, Aiting Kai, Peng Cui, Yongjie Xu, Hui Gao, Ai He, etc. for their assistance and company throughout this challenging process.

Finally, I am indebted to my family members for their continuous support, encouragement, and love. Last but not least, I want to thank my wife, Yuankun Liu. We share our ups and downs with each other. I cannot wait to see what our future holds.

List of Publications

1. **Z. Fu**, X. Y. Wang, A. M. Gardner, X. Wang, S. Y. Chong, G. Neri, A. J. Cowan, L. Liu, X. Li, A. Vogel, R. Clowes, M. Bilton, L. Chen, R. S. Sprick, A. I. Cooper, A stable covalent organic framework for photocatalytic carbon dioxide reduction, *Chem. Sci.* 2020, **11**, 543–550.

2. **Z. Fu**, A. Vogel, M. A. Zwijnenburg, A. I. Cooper, R. S. Sprick. Photocatalytic syngas production using conjugated organic polymers, *J. Mater. Chem. A*, 2021, **9**, 4291-4296.

3. X. Wang, **Z. Fu**, L. Zheng, C. Zhao, X. Wang, S. Y. Chong, F. McBride, R. Raval, M. Bilton, L. Liu, X. Wu, L. Chen, R. S. Sprick, A. I. Cooper, Covalent Organic Framework Nanosheets Embedding Single Cobalt Sites for Photocatalytic Reduction of Carbon Dioxide, *Chem. Mater*. 2020, **32**, 9107-9114.

4. **Z. Fu**, X. Wang, L. Liu, K. Wang, R. Clowes, X.Y. Wang, L. Chen, A. I. Cooper, Highly selective photocatalytic CO_2 reduction from fluorinated covalent organic frameworks with molecular Co co-catalysts. ***In preparation***.

Table of Contents

List of Abbreviations

2D	Two-dimensional
3D	Three-dimensional
AM1.5G	Air mass 1.5 global filter
APS	Artificial photosynthetic system
AQY	Apparent quantum yield
BA	Barbituric acid
BCN	Boron carbon nitride
BDBA	1,4-benzenediboronic acid
BET	Brunauer Emmett Teller
BIH	1,3-Dimethyl-2-phenyl-2,3-dihydro-1H-benzo[d]-imidazole
Bpy	2,2’-bipyridine
BT	2,1,3-benzothiadiazole-,4,7-bis (boronic acid pinacol ester)
CB	Conduction band
CdS	Cadmium sulfide
CLPs	Conjugated linear polymers
CMPs	Conjugated microporous polymers
COFs	Covalent organic frameworks
CPs	Conjugated polymers
CRC	CO_2 reduction co-catalysts
CTFs	Covalent triazine frameworks
CV	Cyclic voltammetry
DFT	Density functional theory
EA	Electron affinity of photocatalyst’s ground state
EA*	Electron affinity of photocatalyst’s excited state
EDX	Energy-dispersive X-ray spectroscopy
EQE	External quantum efficiency
ERDN	3-ethylrho-danine
FBP	4,4′-diamino-2,2′-difluorobiphenyl
FeTCPP	Tetra(4-carboxyphenyl) porphyrin iron(III) chloride

FSA	3,9-diamino-benzo[1,2-*b*:4,5-*b*']bis[1]benzothiophene-5,5,11,11-tetraoxide
FTIR	Fourier transform infrared spectroscopy
FTO	Fluoride-tin oxide
g-C_3N_4	Graphitic carbon nitrides
HCCP	Hexachlorocyclo-triphosphazene
HCPs	Hyper-crosslinked polymers
HER	Hydrogen evolution reaction
HHTP	2,3,6,7,10,11-hexahydroxytriphenylene
HOMO	Highest occupied molecular orbital
ICP-OES	Inductively coupled plasma optical emission spectrometry
IP	Ionisation potential of photocatalyst's ground state
IP*	Ionisation potential of photocatalyst's excited state
LDH	Layered double hydroxide
LOMO	Lowest unoccupied molecular orbital
LSPR	Localized surface plasmon resonance
MeCN	Acetonitrile
MOF	Metal organic frameworks
NHE	Normal hydrogen electrode
NL-DFT	Nonlocal density functional theory
NOP-COP	N, O, P-containing covalent organic polymers
PDAN	Phenylenediacetonitrile
PIA	Photoinduced absorption
PXRD	Powder X-ray diffraction
RHE	Reversible hydrogen electrode
SA	3,7-diaminodibenzo[*b,d*]thiophene sulfone
SA_{BET}	Brunauer–Emmett–Teller surface area
SEM	Scanning electron microscope
S_NAr	Nucleophilic aromatic substitution
STEM	Scanning transmission electron microscopy
TA	Transient absorption

TBPT-Br	2,4,6-tris(4-bromophenyl)-1,3,5-triazine
TCSPC	Time-correlated single photon counting
TEM	Transmission electron microscope
TEOA	Triethanolamine
TFG	1,3,5-triformylphloroglucinol
TFPC	2,3,5,6-tetrafluoro-4-pyridinecarbonitrile
TFPN	Tetrafluorophthalonitrile
TFPPy	1,3,6,8-tetrakis(4-formylphenyl)pyrene
TGA	Thermogravimetric analysis
TiO_2-FG	TiO_2-functionalized graphene
TON	Turnover number
VB	Valence band
WOC	Water oxidation co-catalysts
XPS	X-ray photoelectron spectroscopy

Chapter 1

Introduction

1.1 Utilization of solar energy

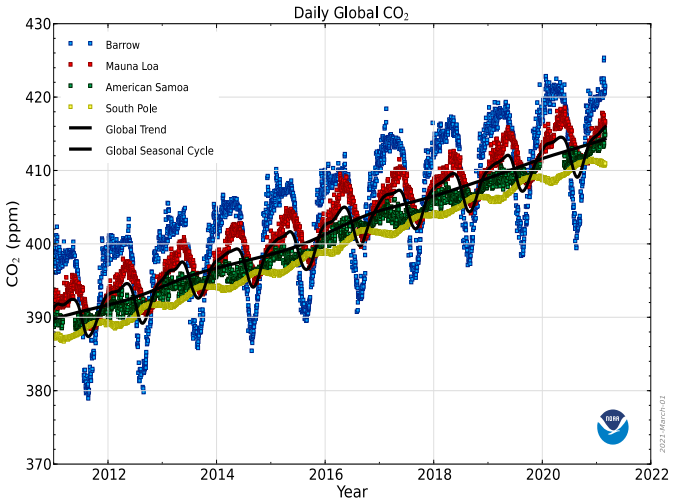

Figure 1.1 Daily averaged CO_2 from four Global Monitoring Laboratory Baseline observatories. Barrow, Alaska (in blue), Mauna Loa, Hawaii (in red), American Samoa (in green), and South Pole, Antarctica (in yellow). Figure reprinted from National Oceanic & Atmospheric Administration.[1]

With the progress of human civilization, carbon dioxide is produced in all aspects of daily life, such as thermal power generation and automobile exhaust. The consumption of fossil energy and its resulting greenhouse effect have endangered human life and the environment.[2] According to research, from 1959 to 2012, approximately 350 billion tonnes of carbon have been emitted by humans to the atmosphere.[3] From the daily data monitored by Global Monitoring Laboratory from four observatories around the world (Figure 1.1), the global CO_2 concentration indicates a significant increasing trend in the past decade.

Solar energy is the energy produced by the continuous nuclear fusion reaction process inside the sun. Although the energy radiated by the sun into the earth's atmosphere is only 1 in 2.2 billionths of its total radiant energy,[4] it is still a huge amount of energy that human can be used for industrial production and daily living. In order to eliminate the harm caused by greenhouse gases, it is a potential approach for a bright future to mimic natural photosynthesis. Developing an artificial photosynthetic system (APS) can convert the abundant solar energy into commercial products.[5] Theoretically, photosynthesis contains water oxidation reactions in Photosystem II and CO_2 reduction in Photosystem I.[6] Unfortunately, at present, it is challenging to establish an APS by using just a single catalytic system. To achieve this goal, scientists

divided the subject into two parts. One is water oxidation to O_2 and proton reduction to H_2.[7,8] The other is photocatalytic CO_2 reduction to fuels such as CO, methane or methanol.[9–12]

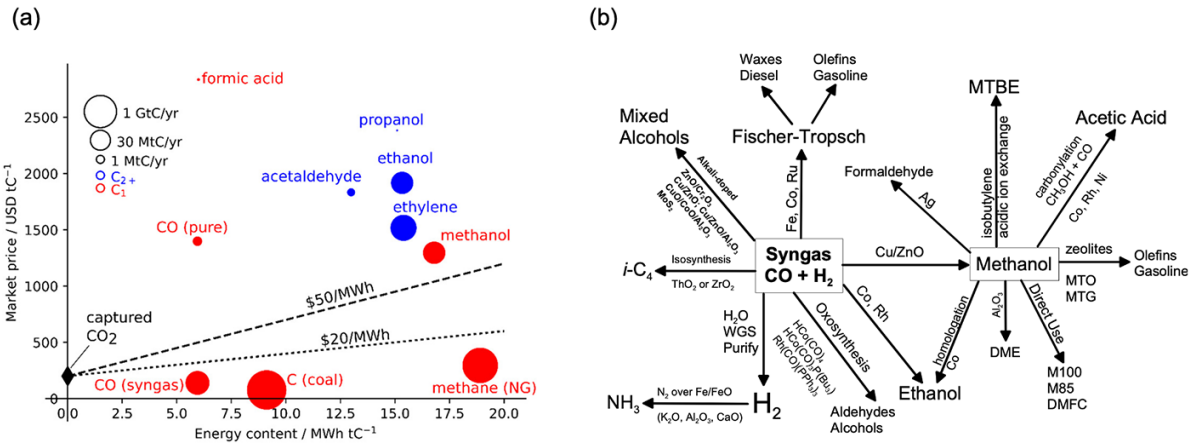

Figure 1.2 (a) Energy contents and market prices of CO_2 reduction products;[13] (b) Syngas conversion processes.[14] Figures were reproduced from references.[13,14]

Given a price of CO_2 captured from power plants and electricity prices for electrochemical CO_2 reduction, the dashed and dotted lines in Figure 1.2a are the minimum cost of production. Among all the CO_2 reduction products (Figure 1.2a), small scale specialty chemicals like formic acid and propanol are desirable due to their high market prices.[13] Ethylene and ethanol as C2 fuels are applied mainly in the industrial areas of plastics and ethylene glycol production. This thesis focuses on CO and syngas (CO and H_2 mixtures with a certain ratio) because generating pure CO or syngas is very promising considering their market price and scale. Different ratios of syngas can be used for various industrial processes (Figure 1.2b). For instance, methanation needs the CO and H_2 mixture with a ratio of 3:1 H_2 / CO, and the generation of aldehydes via hydroformylation of alkene needs a ratio of 1:1 H_2 / CO as well as the methanol synthesis. The following equation describes the methanation and Fischer−Tropsch reaction:

$$CO + 3H_2 \rightarrow CH_4 + H_2O \qquad \text{Methanation}$$

$$nCO + (2n + 1)H_2 \rightarrow C_nH_{2n+2} + nH_2O \qquad \text{Fischer−Tropsch}$$

1.1.1 Basic principles of photocatalytic CO_2 reduction

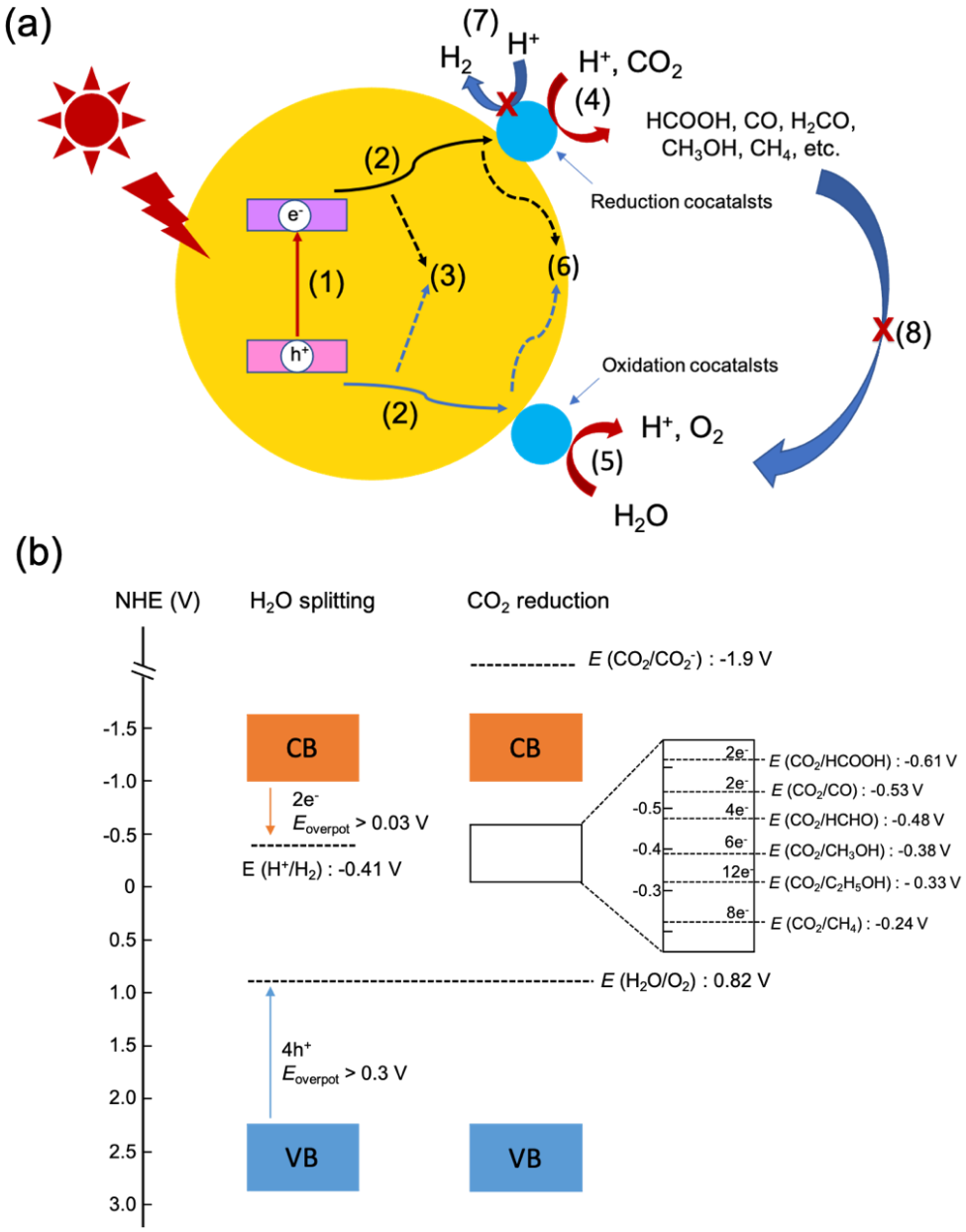

Figure 1.3 (a) Scheme of processes for photocatalytic CO_2 reduction;[15] (b) Schematic representation of conduction band (orange), valence band (blue) and relative redox potentials of the products involved in water splitting and CO_2 reduction at pH 7. Figure was reproduced from the reference.[16]

Photocatalytic CO_2 reduction over a semiconductor is believed as one of the best ways to use solar energy and overcome environmental problems. Many factors can influence the overall efficiency of photocatalytic CO_2 reduction, such as photocatalytic processes and CO_2 reduction kinetics. There are several processes for photocatalytic CO_2 reduction including excitation,

transport, separation, reduction and oxidation. As shown in Figure 1.3a, the photocatalytic processes of CO_2 reduction on the surface of a semiconductor can be divided into eight steps. The steps are (1) excitation of photo-generated electron-hole pairs; (2) charge separation and charge migration to the surface; (3) the bulk charge recombination; (4) reduction of CO_2 with certain cocatalyst; (5) oxidation of H_2O with cocatalyst or oxidation of sacrificial electron donors; (6) surface charge recombination; (7) H_2 evolution as the competitive step and (8) oxidation of reduction products.

In the first step, electron-hole pairs in the bulk of semiconductor materials are generated by absorbing photons with an energy equal to or greater than the band gap (E_g) separating the valence band (VB) from the conduction band (CB) of a material. Electrons from the VB are excited to the CB, leaving an equal number of holes in the VB. The second step is spatial separation and migration of photogenerated electrons and holes. Simultaneously, bulk charge recombination (3) is a competing process and a main deactivation step of the overall catalysis. The fourth and fifth steps are the surface redox reactions. The CB bottom level must be more negative than the redox potential of CO_2 reduction (Figure 1.3b), and the VB edge should be more positive than the redox potential of water oxidation (0.817 V vs SHE in pH 7.0 aqueous solution). Besides, a certain amount of excess energy (overpotential, $E_{overpot}$) is necessary to drive reactions at high rates. As too large a band gap will limit the solar spectrum utilization, a narrow band gap is ideal (E_g > 3.0 eV or λ > 415 nm). Surface photogenerated electrons and holes can separately drive different half reactions: electrons for reducing CO_2 in the CO_2 reduction co-catalysts (CRC) or the surface-active sites to simple C1 or C2 fuels such as CO, CH_4, HCOOH, CH_3OH, C_2H_5OH or other hydrocarbons (4), and holes for oxidizing water in the water oxidation co-catalysts (WOC) or the surface-active sites to molecular O_2 (5). When there are not enough active sites or a lack of co-catalysts, the surface electrons and holes may recombine (6), analogous to step 3 in bulk. Finally, steps 7 and 8 are unfavourable H_2 evolution and oxidation of reduction products by water oxidation co-catalysts. Steps 3, 6, 7 and 8 should be avoided due to the loss of photogenerated electrons and holes to side reactions and generation of unfavourable products.

Table 1.1 Reduction potentials of CO_2

Reaction	E^0 (V) *vs.* NHE at pH 7
Reduction potentials of CO_2	
$2H^+ + e^- \rightarrow H_2$	-0.41
$CO_2 + e^- \rightarrow CO_2^{\bullet-}$	-1.9
$CO_2 + 2H^+ + e^- \rightarrow HCO_2H$	-0.61
$CO_2 + 2H^+ + 2e^- \rightarrow CO + H_2O$	-0.53
$CO_2 + 4H^+ + 4e^- \rightarrow C + 2H_2O$	-0.2
$CO_2 + 4H^+ + 4e^- \rightarrow HCHO + 2H_2O$	-0.48
$CO_2 + 6H^+ + 6e^- \rightarrow CH_3OH + H_2O$	-0.38
$CO_2 + 8H^+ + 8e^- \rightarrow CH_4 + 2H_2O$	-0.24
$2CO_2 + 8H_2O + 12e^- \rightarrow C_2H_4 + 12OH^-$	-0.34
$2CO_2 + 9H_2O + 12e^- \rightarrow C_2H_5OH + 12OH^-$	-0.33
$3CO_2 + 13H_2O + 18e^- \rightarrow C_3H_7OH + 18OH^-$	-0.32

In 1978, Halmannn first observed that CO_2 was reduced to CH_3OH and CO on a p-type GaP electrode under light illumination.[17] However, the reduction of CO_2 proves to be highly challenging as it needs a higher reduction potential of 1.9 eV *vs*. normal hydrogen electrode (NHE) for CO_2 reduction towards the $CO_2^{\bullet-}$ radical.[15] To overcome such high one-electron reduction potentials, multi-electron reduction pathways coupled with the proton-transfer reaction towards desirable alternative products such as methane and methanol are more favourable.[6] Table 1.1 shows an overview of different potentials in multi-electronic processes (at pH 7 in aqueous solution *vs*. NHE).[15]

1.1.2 Mechanism of photocatalytic CO_2 reduction

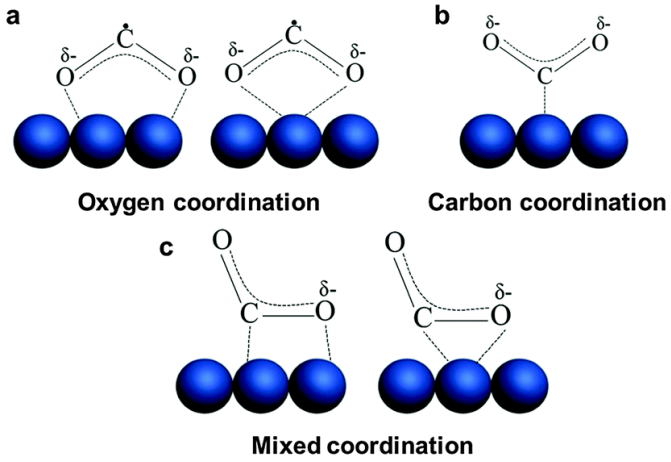

Figure 1.4 Possible surface structures of adsorbed partially charged species $CO_2^{\delta-}$ on catalysts. Figure was reproduced from the reference.[18]

For photocatalytic CO_2 reduction, the initial step is forming partially charged $CO_2^{\delta\cdot-}$ species on a catalyst. There are three kinds of adsorption modes on the surface of catalysts. Different binding modes lead to different products.[18] If the $CO_2^{\cdot-}$ species binds to the surface of catalysts through the oxygen atoms as shown in Figure 1.4a, formic acid may be the final product after combining one hydrogen atom for forming a formate anion and then a proton for producing the final product. If the $CO_2^{\cdot-}$ species binds through the carbon atom (Figure 1.4b and c), a carboxyl radical is formed, and then it disintegrates into adsorbed carbon monoxide. The adsorbed CO can be further hydrogenated to generate other products.

1.1.2.1 Mechanisms of cobalt and rhenium complexes for CO_2 reduction

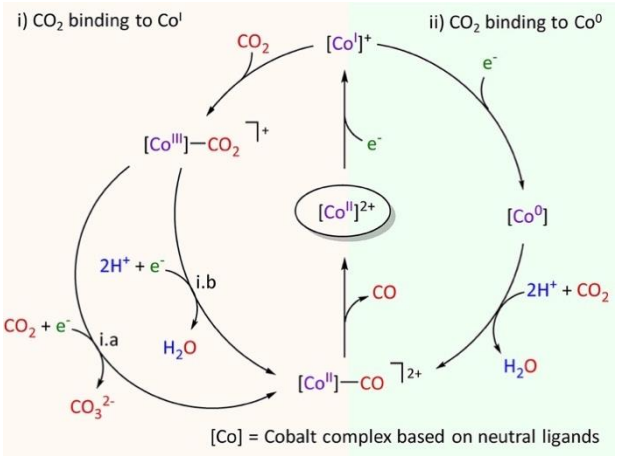

Figure 1.5 Possible mechanisms of photocatalytic CO_2 reduction by cobalt complexes bearing neutral ligands. Figure was reproduced from the reference.[19]

Many systems applied metal complexes, such as cobalt or rhenium bipyridine complexes, as cocatalysts for CO_2 reduction.[20–23] In 1982, Lehn and Ziessel first reported cobalt bipyridine complexes ($[Co(bpy)_3]^{2+}$) as the electron-transfer mediator for photocatalytic CO_2 reduction with ruthenium complexes as the photosensitizer.[24] Since then, many studies have been conducted on photocatalytic CO_2 reduction using $[Co(bpy)_3]^{2+}$ as the cocatalyst and other semiconductors as the photosensitizer.[20,25–28] The proposed mechanisms for CO_2 to CO conversion by Co complexes based on nitrogen donor ligands are shown in Figure 1.5. There are different hypotheses for Co^{II} complexes containing highly basic ligand frameworks and less basic ligands. Initially, one-electron reduction leads to formation of Co^{I} complexes, which are nucleophilic for coordinating CO_2. In the first system, CO_2 coordinates with Co^{I} species through electrophilic attack and $Co^{III}CO_2$ species are formed, which react with a second molecule of the substrate to give free CO_3^{2+} (route i.a) or react with protons (route i.b). Finally, CO is released from the Co^{II}-CO intermediate. In the second system containing less basic ligands, a Co^{0} intermediate is generated and then reacts with CO_2 and protons to produce a Co^{II}-CO intermediate. In 2018, Lin et al. reported a system with CdS as a photocatalyst and $[Co(bpy)_3]Cl_2$ as an electron mediator for CO_2 reduction.[26] The possible mechanism was proposed as route i.b in the binary phase system.

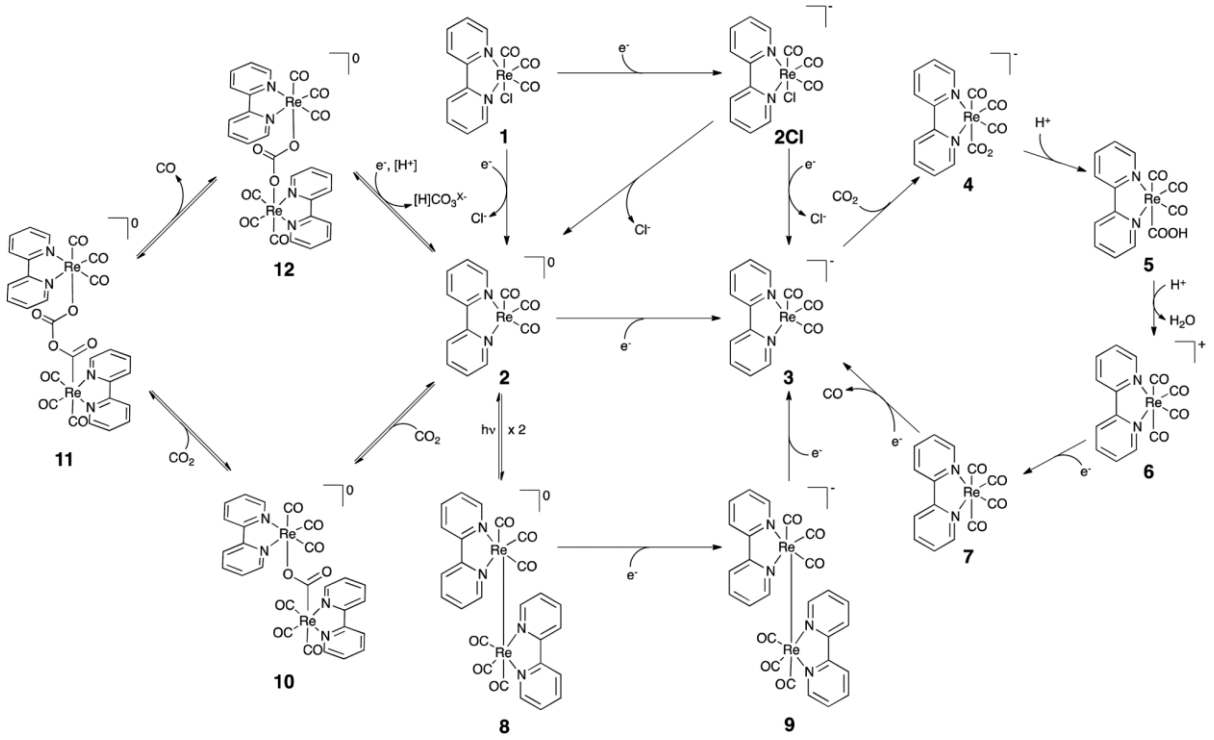

Figure 1.6 Overview of the proposed CO_2 reduction cycles using Re(bpy)$(CO)_3$Cl (1) as the catalyst. Figure was reproduced from the reference.[29]

Rhenium (I) bipyridine complexes are the most efficient catalysts for CO_2 reduction with high yield and selectivity. Lehn et al. first reported a system with rhenium (I) complexes in 1983.[30] In photocatalytic processes, the triplet metal-to-ligand charge transfer (^{3}MLCT) state of the rhenium complex is generated and then the excited state is quenched by the sacrificial donors. The one-electron reduced species **2Cl** eliminates the chloride ion and then forms the doubly reduced species **3**, which is the catalytically active species. CO_2 is bound at the empty coordination site to produce the carboxylic intermediate **4**. After one proton addition, the hydroxycarbonyl species **5** is formed, which reacts with the second proton to yield the cationic tetracarbonyl intermediate **6**. Finally, one molecule of carbon monoxide is released, and the species **3** is reformed. In the absence of protons, another mechanism was proposed by Sullivan et al. in 1985 for producing CO and carbonate.[31] This process suggests that after reacting one CO_2 molecule with two species **2**, the intermediate species **10** is formed, which reacts with another one CO_2 molecule to yield intermediate species **11**. Following releasing CO and losing the CO_3^{2-} upon protonation, the species **2** is reformed.

1.1.3 Differences between photocatalytic HER and CO_2 reduction

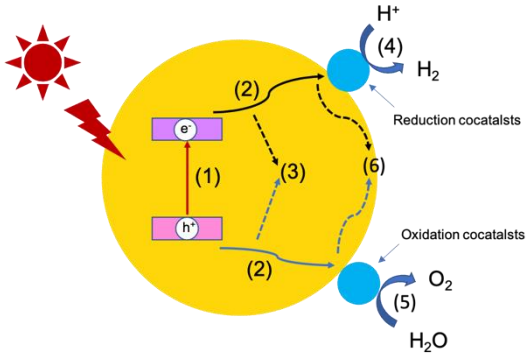

Figure 1.7 Scheme of photocatalytic hydrogen evolution reaction.

Hydrogen evolution from water is another way of utilizing solar energy to generate clean energy. At the same time, hydrogen evolution competes with CO_2 reduction. Compared with that of photocatalytic CO_2 reduction, the mechanism of H_2 evolution is relatively simple (Figure 1.7). All the basic steps for the hydrogen evolution reaction (HER) are similar to CO_2 reduction. HER happens in the reduction cocatalyst without any other competitive reaction. Scientists worked on water splitting earlier than photocatalytic CO_2 reduction. In 1972, Honda and Fujishima were the first to discover photocatalytic water splitting on TiO_2 electrodes.[32]

Table 1.2 Differences between HER and CO_2 reduction.[33]

Photocatalytic HER	**Photocatalytic CO_2 reduction**	**How to achieve photocatalytic CO_2 reduction**
Water as the source of H_2	Low CO_2 solubility in water	Apply organic solvent or gas phase reaction
Single product	Many possible products	Presence of co-catalysts
Simple mechanism	Mechanism involving several e^- and H^+ transfers	Presence of acid sites
H_2 diffusing out of the liquid phase	Products in contact with the photocatalyst with decomposition	Continuous flow
Thermodynamically uphill	Thermodynamically much less favourable than H_2 production	e- with appropriate reduction potential

The differences between CO_2 reduction and H_2 evolution are shown in Table 1.2.[33] Normally,

for HER, the reaction is conducted in water which is the source of the single product H_2. On the contrary, due to the low solubility of CO_2 in water, it is preferable to perform CO_2 reduction in the organic solvent or gas phase to improve the interaction between CO_2 and photocatalysts. Besides, as shown in Table 1.1, many products such as CO, formic acid, CH_4, as well as hydrogen production as a competitive reaction can be generated. Some features are necessary for an efficient CO_2 reduction system. For instance, applying an alternative co-catalyst instead of metallic platinum which favours the competing H_2 evolution reaction. Thermodynamically, in Table 1.2, achieving photocatalytic CO_2 reduction needs more electrons and more negative reduction potential than H_2 evolution. Besides, it is much more complicated for CO_2 reduction in mechanism than H_2 evolution. Because of these, in the process of exploring inorganic or organic photocatalysis, hydrogen production is relatively easy to be achieved.

1.1.4 The half-reaction of CO_2 reduction in the presence of sacrificial donors

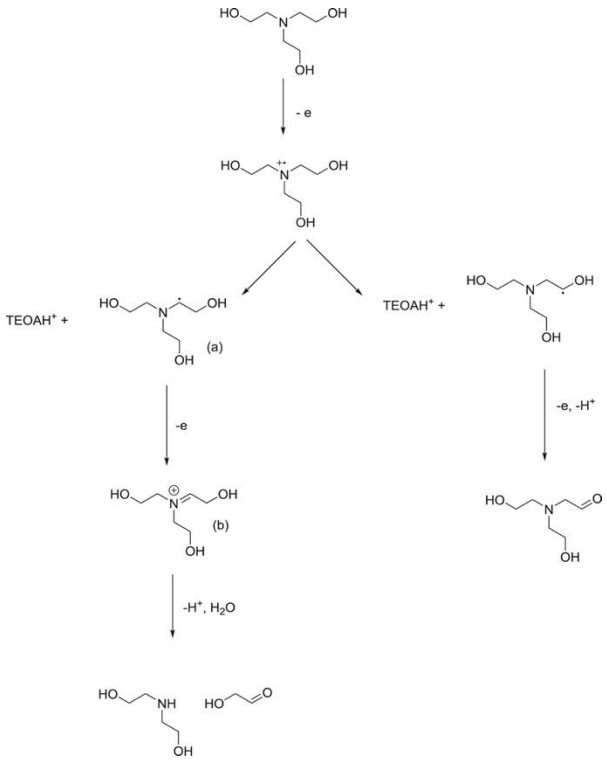

Figure 1.8 The degradation pathway of TEOA. Figure was reprinted from reference.[34]

Achieving overall CO_2 reduction is very difficult due to the sluggish kinetics of the four-electron reaction of water oxidation. Besides, the charge carriers can recombine quickly in the bulk or on the surface of most photocatalysts, which restricts their reactivity. Sacrificial

electron donor reagents such as triethylamine (TEA) and triethanolamine (TEOA), which have low oxidation potentials and high relative permittivities, are used in most studies to scavenge the photogenerated holes and suppress the recombination of charge carriers. TEOA will be used in this thesis to focus on the half reaction of CO_2 reduction. The degradation pathway of TEOA is shown in Figure 1.8. When under irradiation, photocatalysts are promoted to their excited state, and TEOA scavenges holes from it, extending the lifetime of photo-generated electrons and facilitating the reduction reaction. In recent years, applying other sustainable oxidation reactions instead of using sacrificial electron donor reagents with proton reduction reaction is of great interest. For instance, the oxidation of plastic waste can promote not only photocatalytic H_2 production but also solve environmental pollution problems.[35]

1.1.5 Performance evaluation of photocatalytic CO_2 reduction

Five technical parameters are generally used to quantify the efficiency of photocatalytic CO_2 reduction, including generation rate, selectivity, long-term stability, turnover number (TON) and apparent quantum yield (AQY) or external quantum efficiency (EQE).

The generation rate is the amount of CO_2 reduction products that occur per gram photocatalyst over a certain time. The unit for generation rate is mol h^{-1} g^{-1}, μmol h^{-1} g^{-1} or ppm h^{-1} g^{-1}. Selectivity is defined as the molar ratio of the CO_2 reduction products to that of hydrogen. Long-term stability is an important parameter in the performance of a photocatalytic system. TON is the number of moles of reduction products arising from a mole of catalyst over a certain time. Since experimental conditions such as the quantity of photocatalyst, light source, light intensity and light area vary, the efficiency of a photocatalysts can be compared by their AQY or EQE. The formula of AQE or EQE is shown as below:

$$\text{AQY or EQE (\%)} = \frac{\text{number of reacted electrons}}{\text{number of incident photons}} \times 100\%$$

1.1.6 Properties of CO_2 reduction photocatalysts

Table 1.3 The desired properties of an excellent photocatalyst and its effects on CO_2 reduction and ways to achieve these properties.[33]

Properties	Effects	How to accomplish the properties
High surface area	High adsorption	Small particle size or porous structure
Single site structure	Homogeneity	Crystalline material
Light absorption	Higher efficiency	Engineering band gap
Efficient charge separation	Low recombination	Preferential migration along a certain direction
Long lifetime of charge separation	Possibility of chemical reaction	Presence of co-catalysts
High mobility of charge carriers	More efficient charge separation	High crystallinity
Selectivity towards a single product	Efficient chemical process	Adequate co-catalysts

To design an effective photocatalyst for CO_2 reduction, some features of semiconductors need to be considered (Table 1.3).[33] For the purpose of using solar energy over the visible light range, an optimal band gap is desirable. However, most inorganic semiconductors have large band gaps and only can absorb photons of light in the ultraviolet domain. For instance, TiO_2 has a band gap of 3.2 eV and it can only achieve photocatalysis under UV light ($\lambda < 400$ nm). Organic semiconductors with different band gaps, by contrast, can be designed and synthesized via various monomers. To enhance the interaction between CO_2 and photocatalysts, materials with porosity and high surface area are essential. Crystallinity has also been proven as a crucial factor for CO_2 reduction or HER.[36–38] Most important, to generate certain products, suitable cocatalysts are needed for CO_2 reduction, which could provide the active site and extend the lifetime of photo-generated charges. For CO_2 reduction, high selectivity for certain products is also desirable.

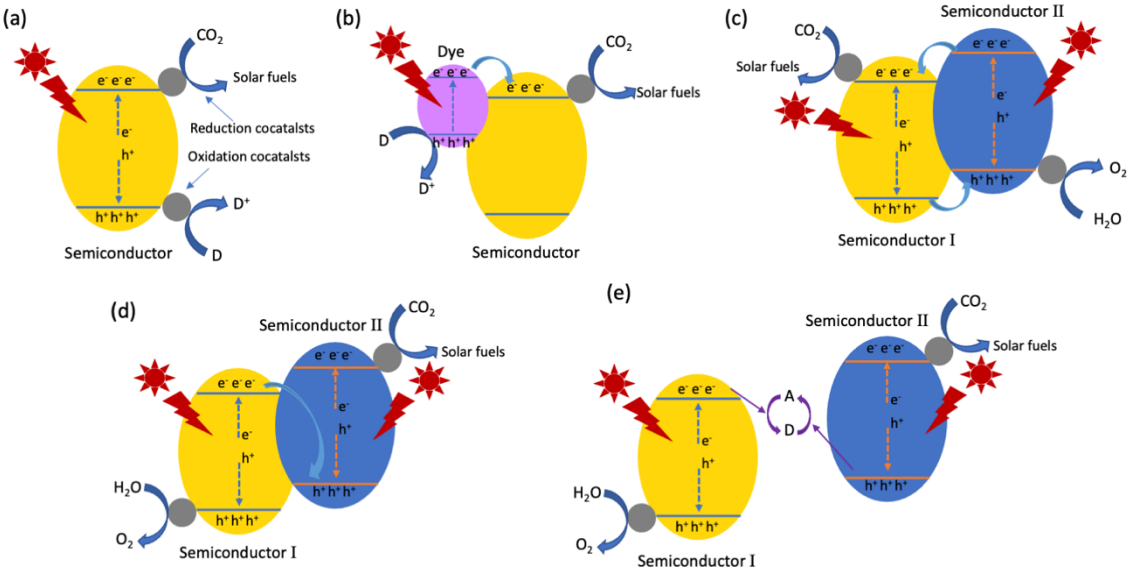

Figure 1.9 Scheme of charge separation mechanisms for photocatalytic CO_2 reduction.[39]

Based on the differences in light absorption and charge separation mechanisms, photocatalytic CO_2 reduction systems can be divided into four types.[39] As shown in Figure 1.9a, most reported systems in literature are one-step excitation systems. These systems can generate electrons and holes in the bulk of semiconductors and achieve CO_2 reduction with suitable reduction cocatalysts and oxidation cocatalysts. The second type (Figure 1.9b) is the photosensitized system which contains dyes, semiconductors and reduction cocatalysts. The dye can generate electrons and holes by absorbing light and then transmit them from the lowest unoccupied molecular orbital (LUMO) of dye to the CB of the semiconductor. Then the electrons transfer to the cocatalyst for converting CO_2 into fuels. The third and fourth types are the systems combining two semiconductors to form heterojunctions or Z-scheme systems. In a heterojunction system (Figure 1.9c), photogenerated electrons transfer from semiconductor II to semiconductor I with more positive CB or LUMO. The photogenerated holes move from semiconductor I to semiconductor II with more negative VB or highest occupied molecular orbital (HOMO). Figure 1.9d shows the direct Z-scheme system. The photogenerated electrons inject from CB or LUMO of semiconductor I to VB or HOMO of semiconductor II. Another Z-scheme system is two semiconductors combined with reversible redox shuttles (electron donor/acceptor pairs) or conductive medium (Figure 1.9e).

1.2 Inorganic semiconductors

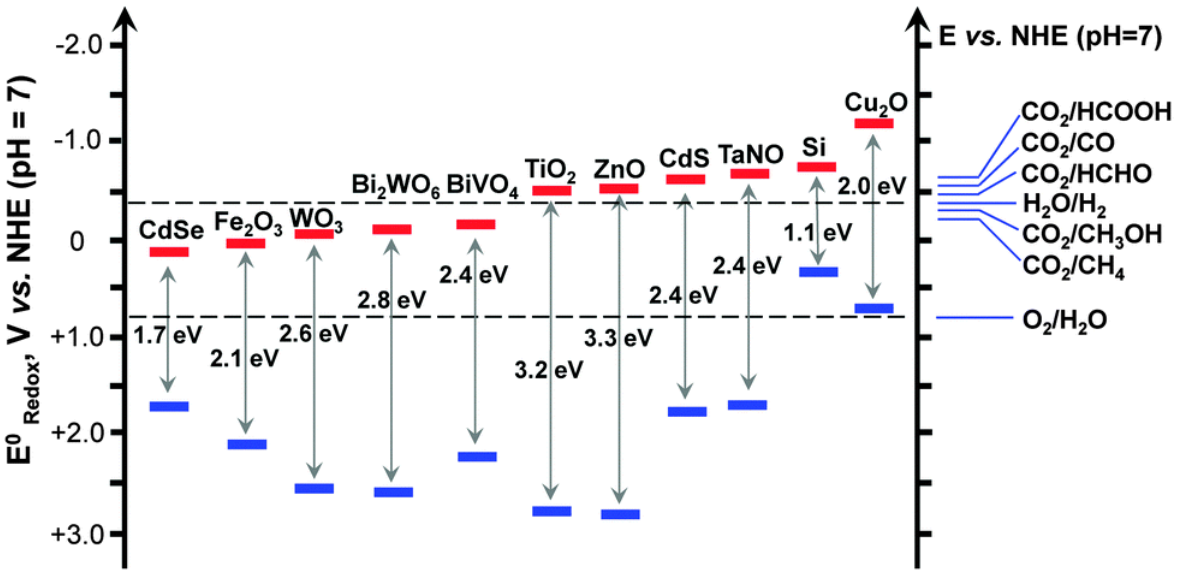

Figure 1.10 Band positions of some inorganic semiconductors and the redox potentials of CO_2 reduction at pH 7. Figure was reproduced from the reference.[40]

Since 1978, many inorganic semiconductors were investigated for photocatalytic CO_2 reduction such as metal oxide (TiO_2, CuO, ZnO, WO_3, $ZnGeO_4$, $NaNbO_3$), metal sulfides (CdS, ZnS), metal nitrides and phosphides (GaN, GaP), layered double hydroxide (LDH, such as Zn-Al LDH) and metal-organic frameworks (MOFs, such as MOF-253 with $Ru(bpy)(CO)_3Br$).[15]

TiO_2 is one of the best-investigated inorganic semiconductors due to its high photoactivity, low price and low toxicity.[41] However, TiO_2 (Figure 1.10) has a band gap of 3.2 eV and it can only absorb photons of light in the ultraviolet domain ($\lambda < 400$ nm).[15] This domain is less than 5% of the entire solar spectrum. Impurity doping[42], metal deposition[43], alkali modification[44], heterojunction construction[45] and carbon-based material loading[46] are the common approaches for improving the photocatalytic performance of TiO_2. For instance, in 2014, Farcia and coworkers modified commercial TiO_2 (P25) by using Au-Cu alloy nanoparticles as cocatalyst.[47] The rate of CH_4 was more than 2000 μmol g^{-1} h^{-1}. The high rate was attributed to the surface plasmon band of Au. However, the constant activity was achieved under sun simulated light only.

Many inorganic photocatalysts either have unsuitably aligned conduction/valence band

positions or relatively large band gaps (Figure 1.10), limiting their visible light absorption. Moreover, the long-term stability of most inorganic photocatalysts is not ideal. Furthermore, most systems still need additional noble metal complexes (*e.g.*, bipyridine Ru complexes) as a photosensitizer. Hence, exploring photocatalysts that can be utilized in visible light without noble metal photosensitizers with excellent CO_2 reduction performance and long-term stability is very attractive.

1.3 Organic semiconductors

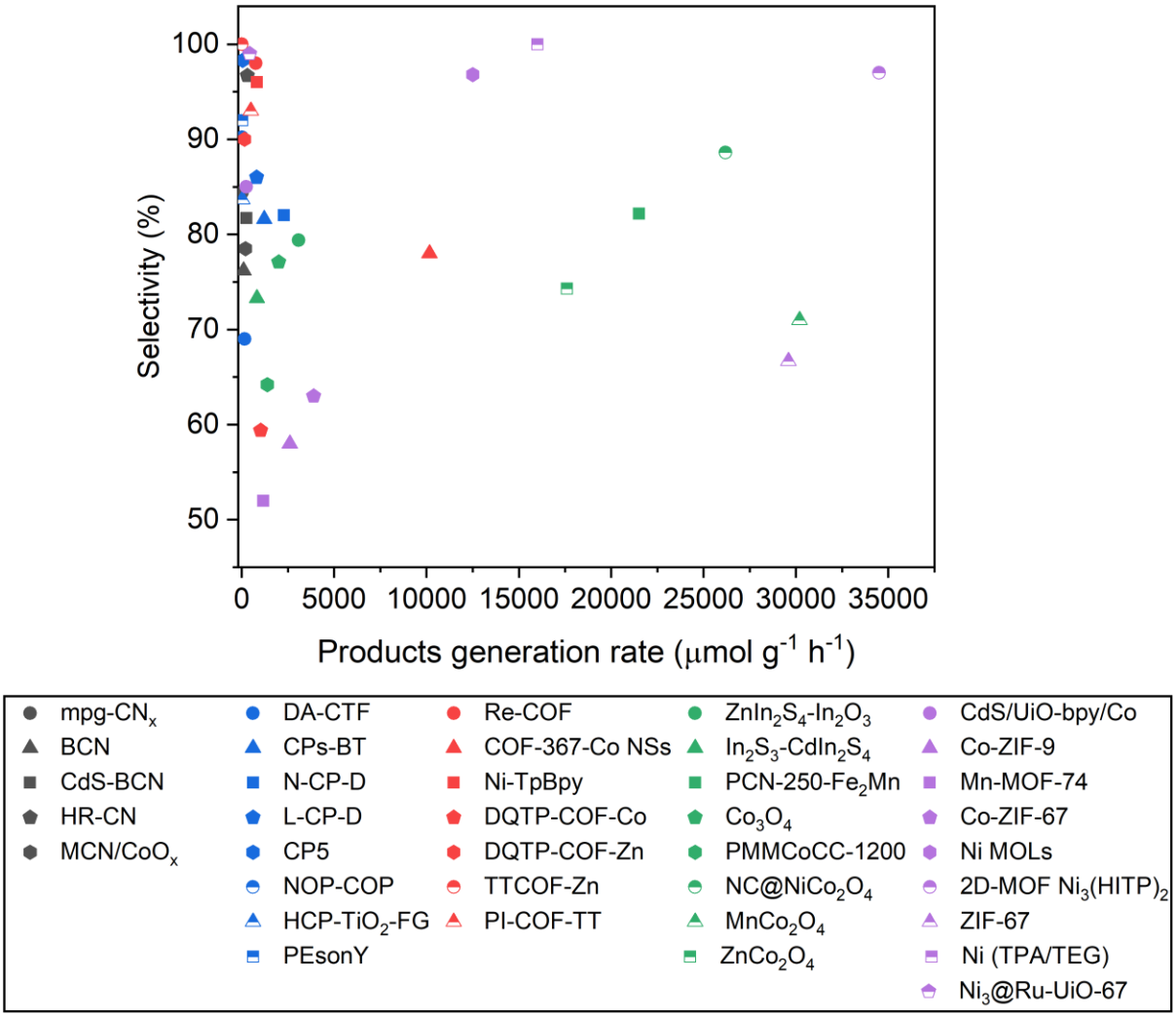

Figure 1.11 Comparison of CO_2 reduction performances for representative g-C_3N_4 (black),[20,48–51] CMPs (blue)[22,28,52–56] and COFs (red),[57–62] inorganic photocatalysts (green),[21,27,63–67] and MOFs (purple)[68–75].

The band gap in organic semiconductors can be tuned readily through the incorporation of a diverse range of monomers.[76–78]In recent years, porous organic materials such as carbon nitrides,[20,79,80] conjugated microporous polymers (CMPs),[54,81] covalent triazine-based frameworks (CTFs)[28] and hyper-crosslinked polymers (HCPs)[55] have been studied for photocatalytic CO_2 reduction. Figure 1.11 shows the product generation rates and selectivities of some representative materials including inorganic and organic photocatalysts. From the results in Figure 1.11, the product generation rates of organic photocatalysts are typically lower than inorganic systems. This is due to organic photocatalysts being new materials for CO_2 reduction. Some organic materials have

disordered structures resulting in lower charge carrier mobilities.[82] However, the tunability and diverse formation reaction of organic photocatalysts can solve these limitations.

1.3.1 Graphitic carbon nitrides

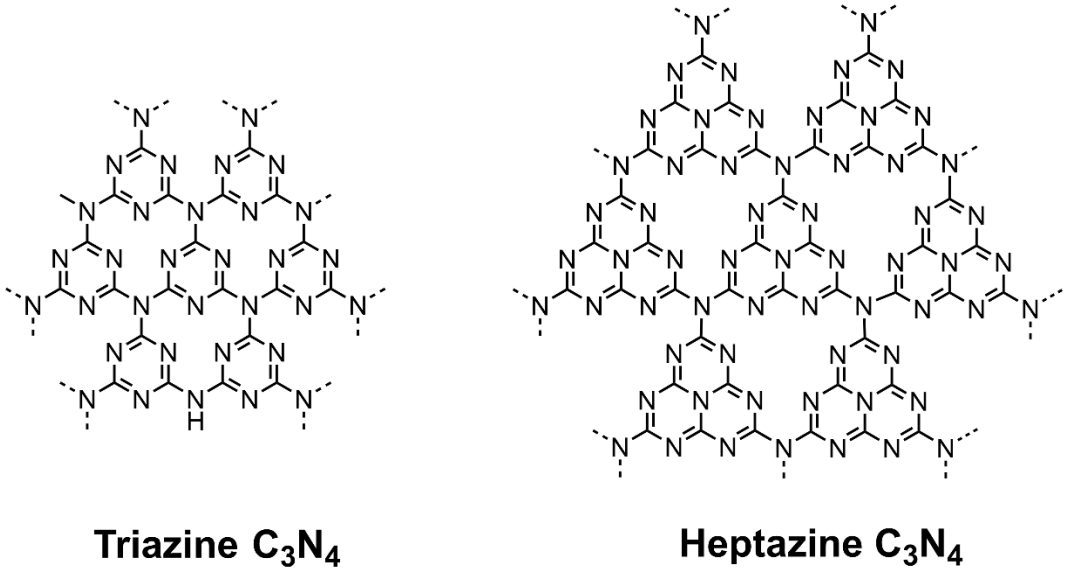

Figure 1.12 Idealised chemical structures of g-C_3N_4 with triazine (a) and heptazine as units.

Graphitic carbon nitride (g-C_3N_4) is a class of polymeric materials with a two-dimensional lamellar structure based on triazine rings and tri-s-triazine (heptazine) rings as its basic unit (Figure 1.12). g-C_3N_4 can be prepared by polymerization of cyanamide, dicyandiamide or melamine. Since 2009, g-C_3N_4 reported by X. Wang et al. as a polymeric photocatalyst for H_2 evolution sparked the surge of interest in organic photocatalysts around the world because it is sufficiently efficient, stable, inexpensive and has a band gap of approximately 2.7 eV which results in absorption of visible light.[79]

1.3.1.1 g-C_3N_4 for photocatalytic CO_2 reduction

Integrating molecular catalysts as active sites on g-C_3N_4 is promising because such a hybrid system combines the excellent selectivity of the molecular cocatalyst and the durability of g-C_3N_4.[10,25] Co (II) bipyridine complexes as cocatalysts were investigated for photocatalytic CO_2 reduction to CO in this strategy. Boron carbon nitride (BCN) with cadmium sulfide (CdS) nanoparticles or g-C_3N_4 with $Co(bpy)_3Cl_2$ as a reductive catalyst could achieve CO production

under visible light irradiation.[20,50] A similar strategy was also reported and used for iron quaterpyridine and cobalt quaterpyridine complexes.[83,84] However, the hybrid systems also suffer from the worse long-term stabilities of molecular complex cocatalysts.

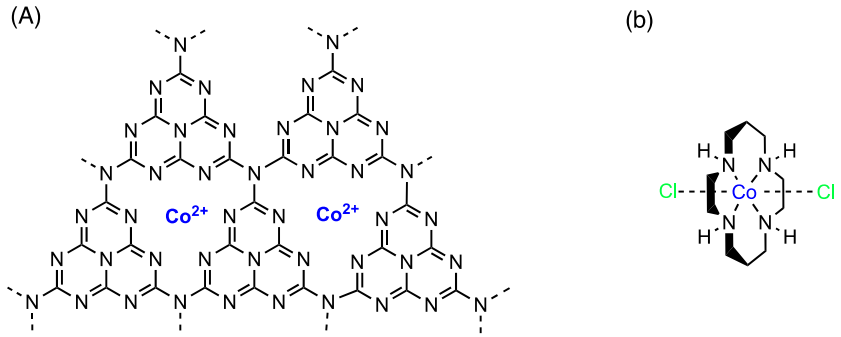

Figure 1.13 (a) Stucture of g-C_3N_4 loaded with single cobalt sites; (b) Stucture of molecular catalyst [Co(cyclam)Cl_2]Cl (cyclam = 1,4,8,11-tetraazacyclotetradecane).

The molecular catalyst [Co(cyclam)Cl_2]Cl (cyclam = 1,4,8,11-tetraazacyclotetradecane) is a well-known cocatalyst for CO_2 reduction (Figure 1.13b). The g-C_3N_4 based on heptazine units has a similar coordination to that of cyclam for single atoms. In 2018, Huang et al. worked on single Co^{2+} sites on g-C_3N_4 through Co-N coordination for CO_2 reduction without additional ligands (Figure 1.13a).[85] This work makes use of the structural characteristics of heptazine units in carbon nitride. However, this method has its limitations and is not suitable for g-C_3N_4 with triazine rings unit.

Until now, plenty of strategies were applied for better photocatalytic CO_2 reduction performance such as defect engineering[86], surface functioning[87], cocatalyst loading[88] and Z-scheme system constructing[89]. The inadequate band gap tunability, in contrast, still limits g-C_3N_4 as an excellent photocatalyst to adapt to a wider range of redox potentials. Besides, the synthesis of g-C_3N_4 is limited by low yield, high temperature and a small number of precursors. Other shortcomings such as small surface area, fast recombination of charge, poor crystallinity and many surface defects also restrict the application of g-C_3N_4.[90] Hence, the research into new materials with a tunable band gap, large surface area and high stability is still worthy of further investigation.

1.3.2 Conjugated microporous polymers

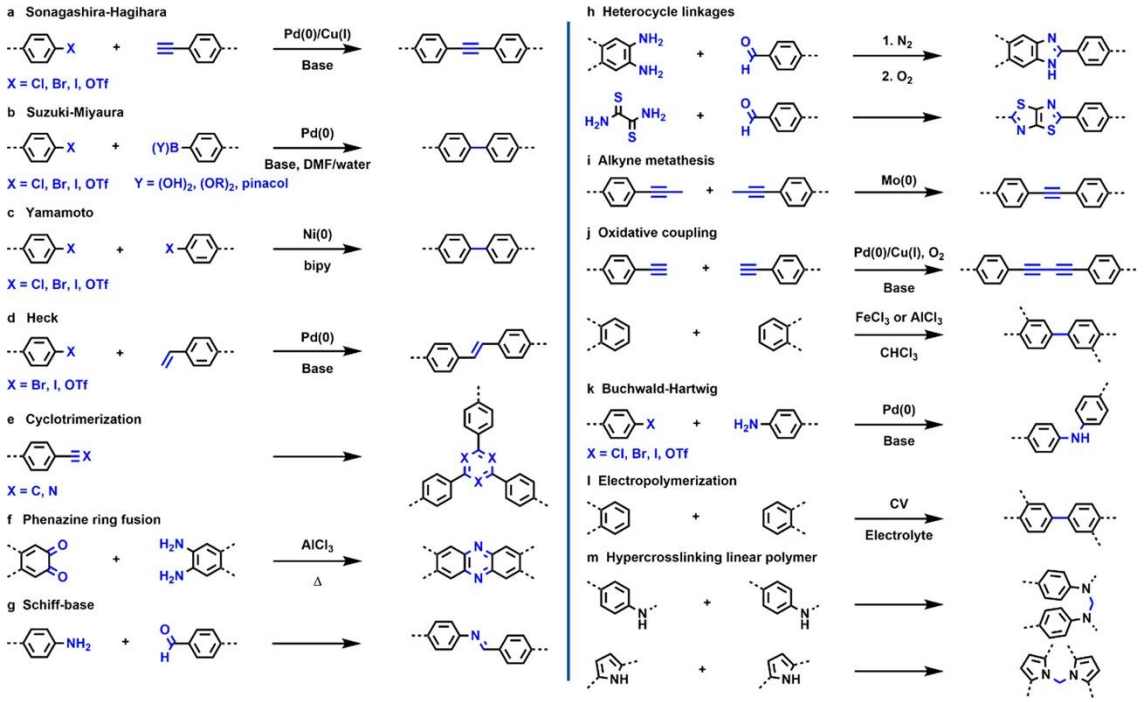

Figure 1.14 Various reactions for synthesizing CMPs. Figure was reproduced from reference.[91]

Conjugated microporous polymers (CMPs) have received much attention as a new type of photocatalyst due to their low cost, high chemical stability, and molecularly tunable optoelectronic properties.[92] CMPs have strong covalent, π-conjugated network, high porosity and versatile gas adsorption and were first reported in 2007.[93] CMPs are easily accessible via different cross-coupling reactions in mild experimental conditions as shown in Figure 1.14. According to the application requirements, CMPs can be designed through abundant commercial monomers and various synthetic chemistry. Hence, the band gaps of CMPs can be adjusted by the combination of different electron donors and acceptors.[94]

As heterogeneous photocatalysts, CMPs were firstly investigated for photocatalytic activity in 2015 for water splitting.[76] This study proved over a broad range tunable optical gap by the combination of various monomers. The optimal combination enables the resultant polymers to be effective for photocatalytic hydrogen evolution with diethylamine as sacrificial agent and Pt as cocatalyst under visible light. Subsequently, by incorporating extended planarized units into the backbones, linear polymers (P1-P7) were demonstrated as good photocatalysts for HER.[95] After that, porosity,[96] hydrophilicity,[97] heteroatoms[98] and residual Pd[99] have been

proven as factors for photocatalytic H_2 evolution.

Moreover, the use of high-throughput workflows in material discovery can accelerate the identification of the best photocatalysts. In 2019, 39 structurally diverse CMPs were reported by C. Meier et al. and tested for H_2 evolution using a high-throughput workflow.[100] Y. Bai et al. enlarged the library of co-polymers and found that P64 achieved an HER rate of 6 mmol g^{-1} h^{-1}, outstanding among 170 synthesized photocatalysts.[101]

1.3.2.1 CMPs for photocatalytic CO_2 reduction

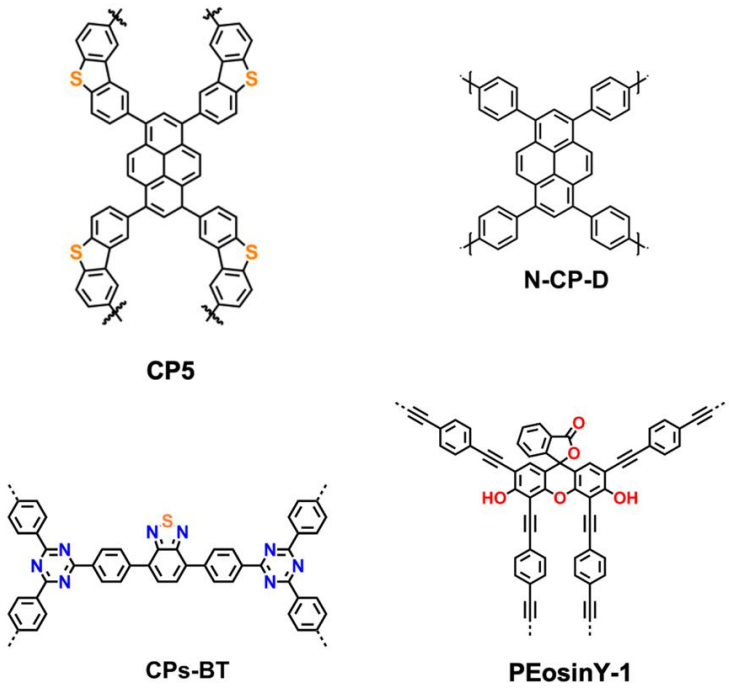

Figure 1.15 Chemical structures of CP5, CPs-BT, N-CP-D and PEsoinY-1.

The success of photocatalytic hydrogen production by CMPs stimulated the development of their application for carbon dioxide reduction. Incorporating extended planarized units into the backbones is also used for designing and synthesizing CMPs for CO_2 reduction. In 2017, Chen et al. reported a series of pyrene-based conjugated polymers containing different planarized units such as carbazole, dibenzo[*b*,*d*]furan and dibenzo[*b*,*d*]thiophene, resulting in band gaps between 2.17 eV and 2.86 eV. The ionic liquid was used to capture CO_2 and H_2O from the air, and the CP5 containing dibenzo[*b*,*d*]thiophene units (Figure 1.15) converted CO_2 to CO under visible light with a rate of 47.37 μmol g^{-1} and a selectivity of 98.3%.[53] This work demonstrated

that rationally designed CMPs could well achieve photocatalytic CO_2 reduction. However, the CO generation rate was very low compared with those of inorganic materials and g-C_3N_4. Besides, the low surface area of CP5, residual nickel and the limited CO_2 adsorption ability of ionic liquid restricted the performance.

The integration of an electron mediator, which exhibits high quantum efficiencies, with semiconductor photocatalysts is a promising method to build efficient and stable artificial photosynthetic systems. Compared with pristine semiconductors, hybrid systems can remarkably enhance photocatalytic activity due to the acceleration of charge transfer and separation.[81] For instance, CMPs containing benzothiadiazole units (CPs-BT in Figure 1.15) and CMPs without alkynyl groups (N-CP-D in Figure 1.15) can convert CO_2 into CO under visible light with cobalt bipyridine complexes as the cocatalyst.[22,28] N-CP-D reported in 2020 had the best CO generation rate (2274 μmol g^{-1} h^{-1}) among CMPs so far with a CO selectivity of 82% and an AQY of 3.39%.[22] The strong interaction between CMPs and $[Co(bpy)_3]^{2+}$ made it easy for photogenerated electrons to be transferred from the semiconductor to the cocatalyst. However, these CMPs were tested under 0.8 atm of pure CO_2 gas instead of 1 atm and N-CP-D had 0.66 wt% palladium residue inside, which could be a cocatalyst for H_2 evolution and influence CO selectivity.

To overcome the limited interaction between dissolved CO_2 in the solvent with photocatalysts, conducting CO_2 reduction in the gas phase is involved. Eosin Y-functionalized CMPs (PEosinY-1 in Figure 1.15) was designed to introduce dye into the backbone to increase the visible light absorption ability.[56] PEosinY-1 (Figure 1.15) could do gas-phase CO_2 reduction with gaseous H_2O as a sacrificial agent and produced CO at a rate of 33 μmol g^{-1} h^{-1} and a selectivity of 92% over H_2 under visible light ($\lambda > 420$ nm) irradiation. Photocatalysts could achieve high CO selectivity in gas phase condition. However, water oxidation is hard to be achieved by most CMPs due to insufficient driving force.[16] The reported product generation rates in the gas phase are very low compared with those in the liquid phase with sacrificial donors. At present, most systems still use a liquid phase system to do half CO_2 reduction reaction with high products generation rates.

In conclusion, the photocatalytic reduction of CO_2 in an aqueous solution towards valuable products is a great challenge in the area of green chemistry. Further research on CMPs for the photocatalytic reduction of CO_2 into organic products is highly significant. Hence, exploring and designing novel CMPs with excellent photocatalytic performance for CO_2 reduction in aqueous solution will be a promising research area. Through the reported modification methods and design in the structure of CMPs, photocatalytic CO_2 reduction in aqueous solutions will be systematically investigated and provide renewable energy for human beings. Besides, some factors such as residual metal and lack of crystallinity will affect the photocatalytic CO_2 reduction activities in generation rate and selectivity towards certain products. The Pd residue has been proven to be a cocatalyst for HER and plays a significant role in photocatalytic hydrogen production, which is a competing reaction and influences the selectivity of CO_2 reduction.[102,103] It will be interesting to develop other crystalline organic semiconductors without any metal residues or to rational use of the metal residual to convert solar energy and CO_2 reduction.

1.3.3 Covalent organic frameworks

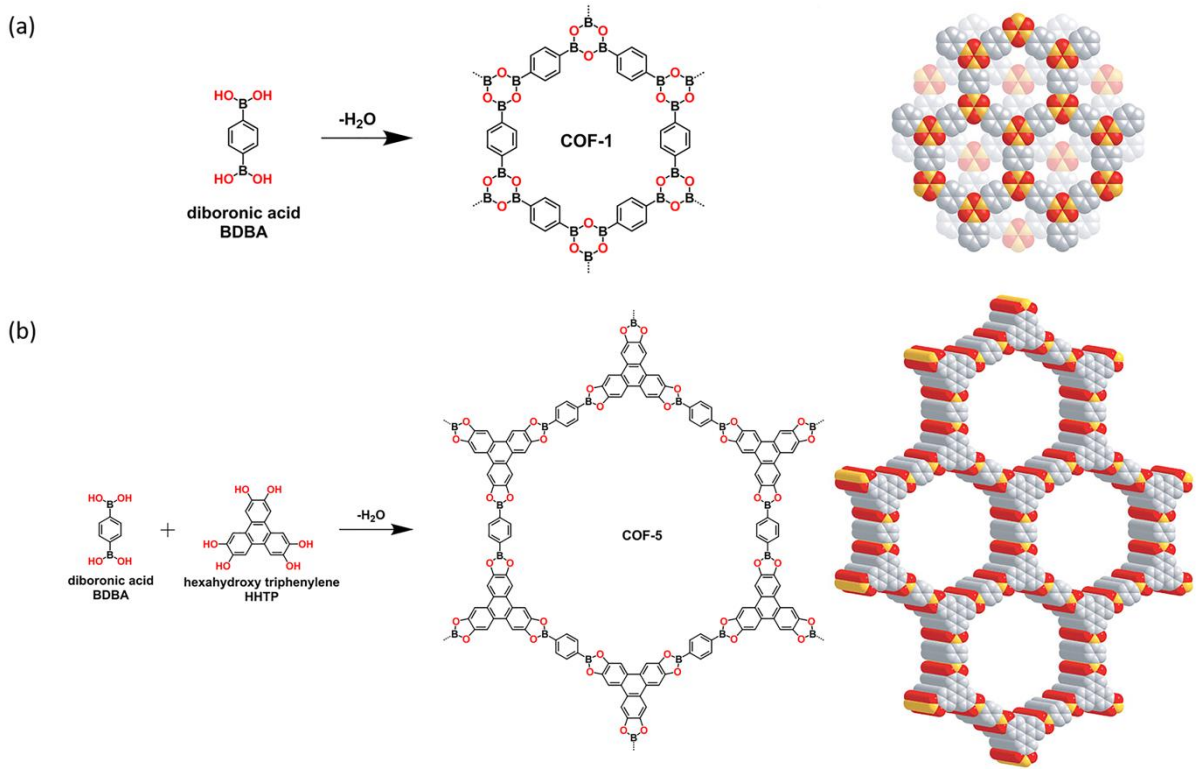

Figure 1.16 Synthesis of COF-1 and COF-6. Figure was reproduced from the reference.[104]

Covalent organic frameworks (COFs) are a class of porous materials with extended crystalline structures. Two two-dimensional (2D) COFs (COF-1 and COF-5 in Figure 1.16) were firstly reported by Omar M. Yaghi and coworkers in 2005.[104] Since, many literatures were reported for forming new types of linkage (Figure 1.17), such as triazine linked COFs in 2008,[105] imine linked COFs in 2009,[106] hydrazone linked COFs in 2011,[107] β-ketoenamine linked COFs in 2012,[108] and polyimide linked COFs in 2014.[109] Post-synthetic methods like linkage exchange or conversion are also explored to obtain functional COFs. For instance, imine-linked COFs can be oxidized to form amide linked COFs[110] or reduced to generate amine linked COFs.[111] Three dimensional (3D) topological structures were achieved as a new interesting domain. By combining various knots and linkers, 2D or 3D COFs with diverse topologies could be generated. It is promising for COFs serving as candidates for photocatalysts like g-C_3N_4. On the one hand, the combination of various knots and linkers enables COFs with designable HOMO-LUMO levels and band gaps. On the other hand, the discovery of new chemistry (Figure 1.17) makes the obtained COFs stable in water and other harsh experimental conditions.

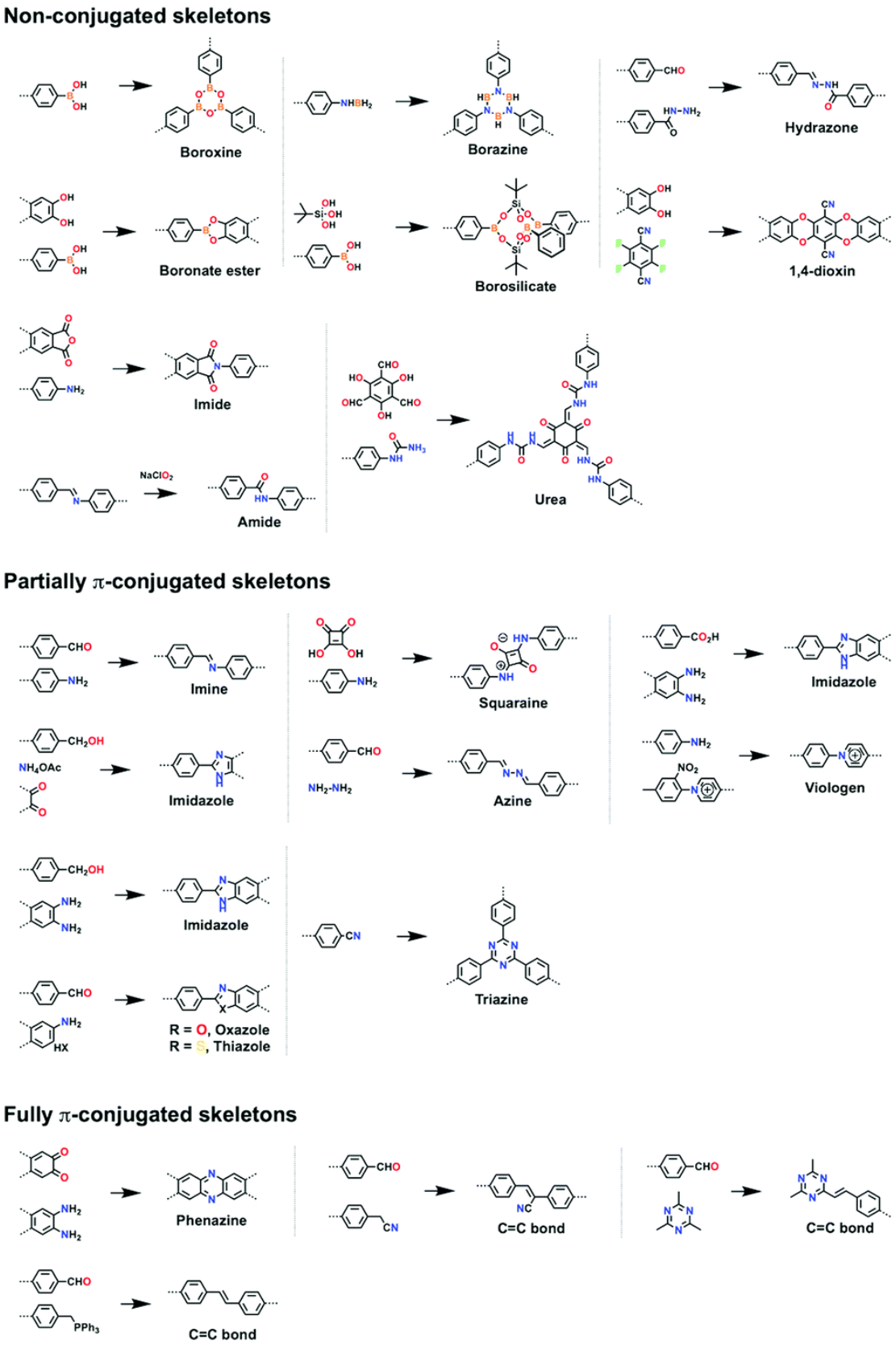

Figure 1.17 Reported synthetic reactions for differential linkages. Figure was reproduced from the reference.[112]

1.3.3.1 Olefin COFs

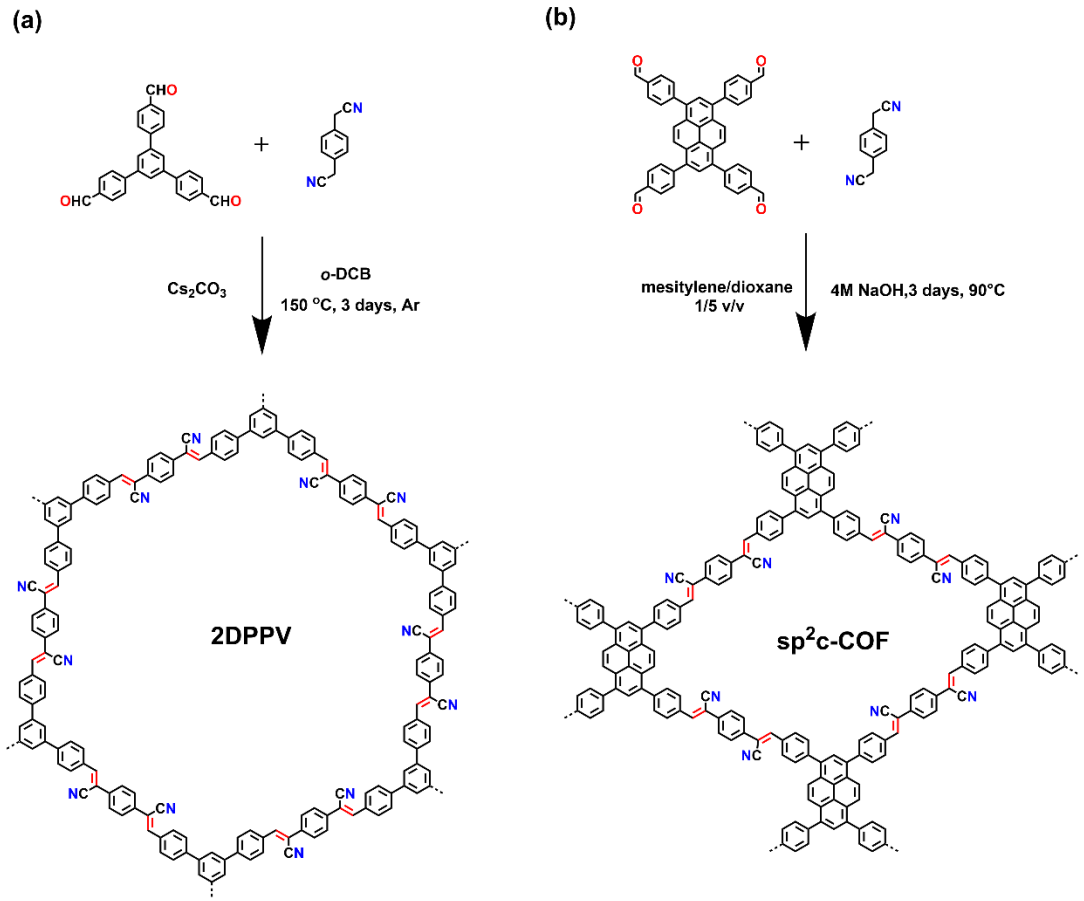

Figure 1.18 Synthesis of 2DPPV and sp^2c-COF via Knoevenagel condensation reaction.

Before 2016, dynamic error correction from the full reversibility of the bond formation is necessary for yielding crystalline COFs. In such a case, the relationship between the feasibility of forming crystalline structures and the chemical stability of the resultant COFs is inverse. In 2016, X. Zhuang et al. developed an olefin-linked 2D conjugated COFs (Figure 1.18a) by using an irreversible Knoevenagel condensation reaction of 1,3,5-tris(4-formylphenyl)benzene and *p*-phenylenediacetonitrile with Cs_2CO_3 as a base.[113] A fully conjugated pyrene-based sp^2c-COFs (Figure 1.18b) was also designed and constructed by D. Jiang and coworkers via Knoevenagel condensation reaction of tetrakis(4-formylphenyl)pyrene and *p*-phenylenediacetonitrile with NaOH (4 M) as a base.[114] The obtained sp^2c-COFs involving substituted acrylonitrile [-CH=C(CN)-] show π conjugation along both the x and y directions. After that, several unsubstituted olefin-linked COFs (Figure 1.19) were successfully synthesized via Knoevenagel or Aldol condensation between 2,4,6-trimethyl-1,3,5-triazine and

aldehyde monomers.[115,116] These olefin COFs, which have good light absorbance ability and stability, have shown excellent photocatalytic performance. In 2019, Jiang et al. showed that the sp^2c-COF_{ERDN} exhibited an HER rate of 2120 μmol g^{-1} h^{-1} under visible light.[117] The 3-ethylrho-danine (ERDN) electron deficient unit as an end-capping group was introduced to the sp^2c-COF lattice, leading to a push-and-pull effect to the skeleton. The sp^2c-COF_{ERDN} showed excellent stability and could retain their crystalline structures after photocatalysis or exposure to air for one year.

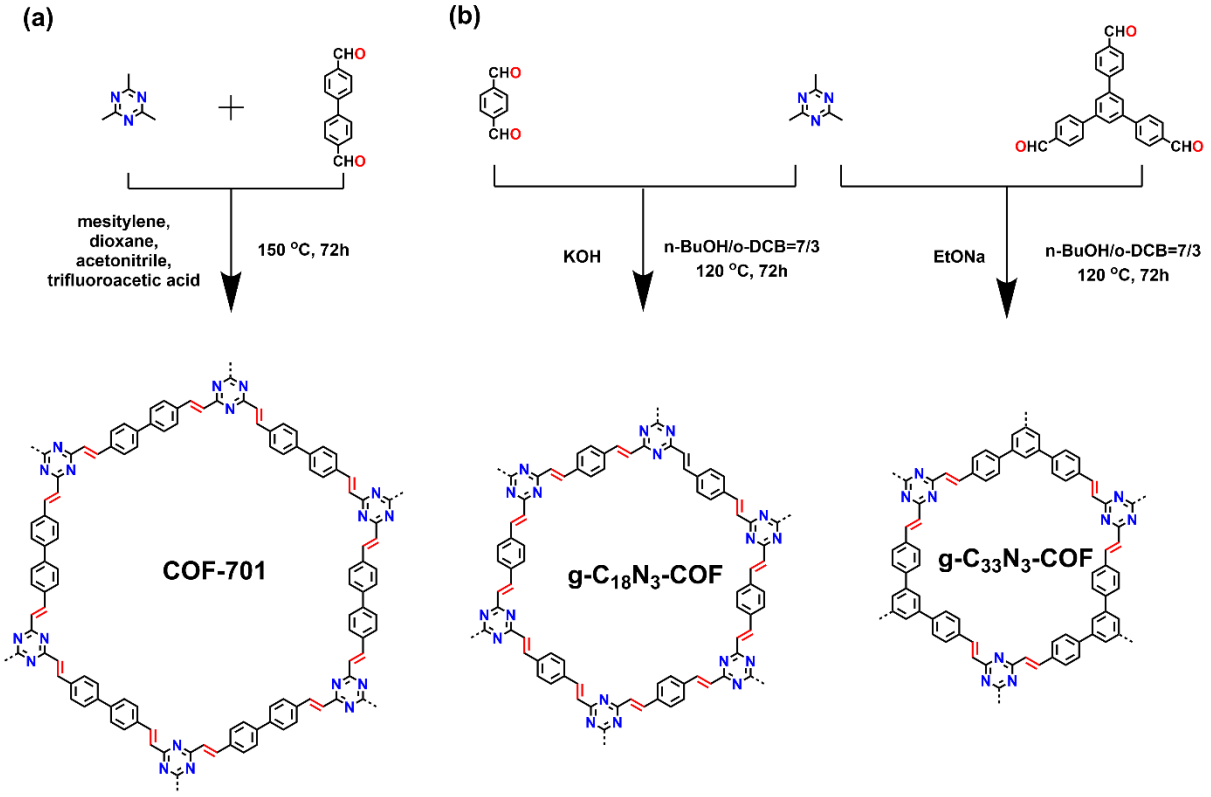

Figure 1.19 (a) Synthesis of olefin COF (COF-701) via Aldol condensation reaction; (b) Synthesis of g-$C_{18}N_3$-COF and g-$C_{33}N_3$-COF via Knoevenagel condensation reaction.

1.3.3.2 COFs for photocatalytic CO_2 reduction

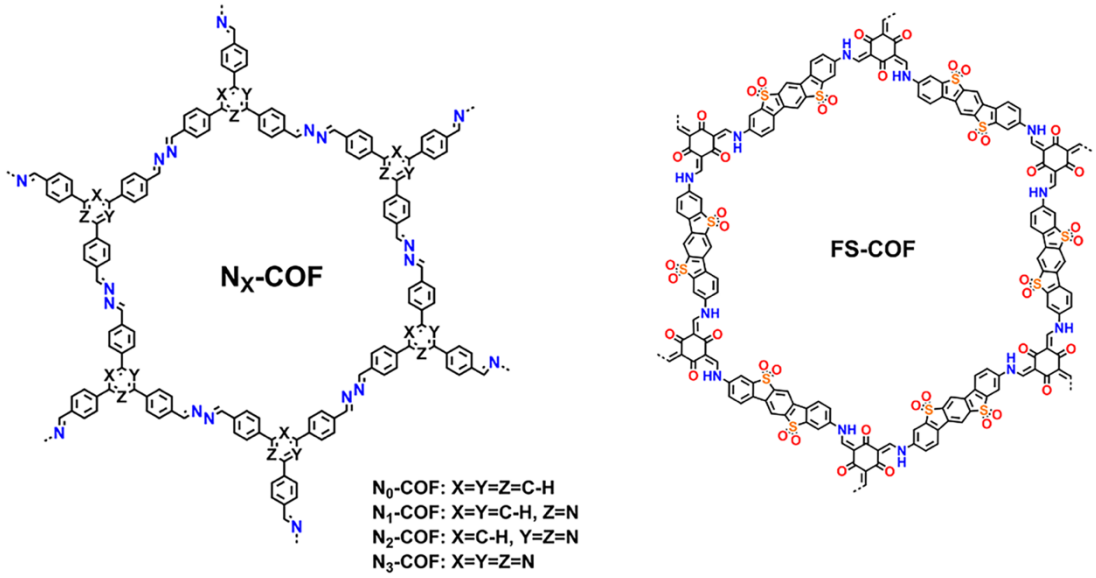

Figure 1.20 Schematic representation of the structures of N_x-COF and FS-COF.

COFs have the potential as photocatalysts due to their crystallinity, porosity, and extended conjugation with molecular tunability. The first photocatalytic application of COFs was reported by Lotsch and coworkers in 2014.[118] This work picks a new way for COFs as photocatalysts. Subsequently, Lotsch et al. reported a series of azine-COFs named N_x-COF (x = 0-3) for HER by adjusting the number of nitrogen atoms in the central aryl ring.[119] Linear polymers P7 and P10, containing dibenzo[*b*,*d*]thiophene sulfone in backbones, have been reported as excellent photocatalysts for water splitting.[95,97] Inspired by P7 and P10, a sulfone-containing COFs, FS-COFs (Figure 1.20), exhibited an HER rate of 10.1 mmol g^{-1} h^{-1}, which was the highest photocatalytic activity for HER for COFs.[36] Besides, the porous FS-COFs could be further sensitized by different dyes. All of these reported results demonstrated the molecular-level design space of tunable catalytic properties of COFs as photocatalysts. It also makes us believe that COFs can be excellent candidate semiconductors for photocatalytic CO_2 reduction.

With the successful development of COFs for HER, photocatalytic carbon dioxide reduction by using COFs is also studied step by step. N_3-COF has been proven as an excellent photocatalyst for HER. In 2018, N_3-COF (Figure 1.22) was first applied as photocatalysts for

CO_2 reduction. N_3-COF can do gas-phase CO_2 reduction with H_2O as the electron donor under visible irradiation (800 nm ≥ λ ≥ 420 nm), producing methanol at rates of 13.7 μmol g^{-1} in 24 hours.[120] This work demonstrated that COFs could be promising photocatalysts for CO_2 reduction. However, the final product yield is very low by using COFs for CO_2 reduction in gas phase conditions, which is the same issue as CMPs and g-C_3N_4.

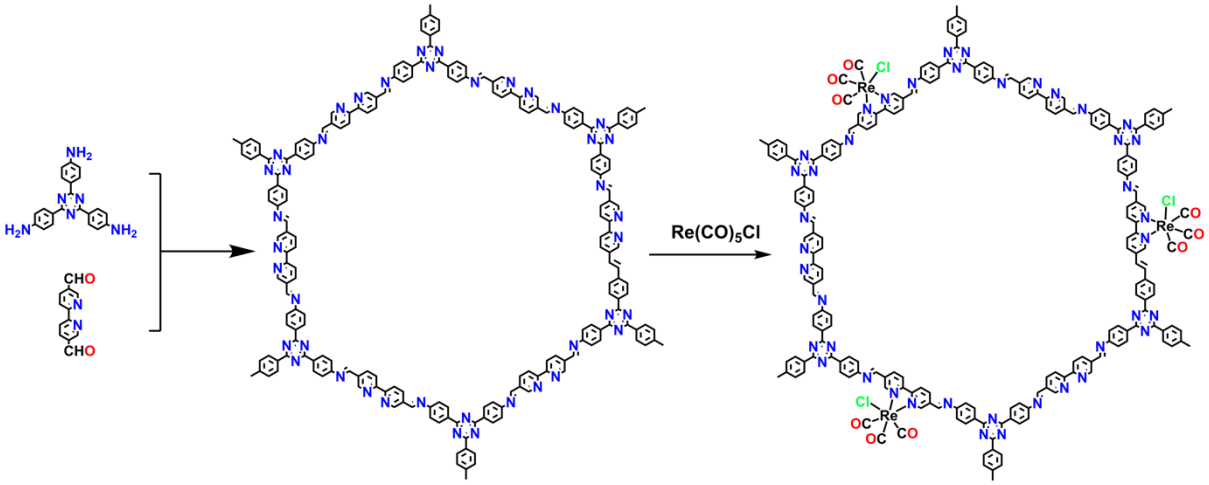

Figure 1.21 Synthesis of 2D triazine COF and Re-COF.

Previous studies have shown that rhenium (I) bipyridine complexes *fac*-[Re^{I}(bpy)$(CO)_3$Cl] can act as a promising photocatalyst for generating CO with a high rate and selectivity.[30] Unfortunately, homogeneous photocatalysts are suffered from recovery and reuse. COFs incorporated with active molecular sites as heterogeneous catalysts can combine the good photocatalytic properties of molecular catalysts and the durability of COFs. A 2D triazine-based imine COF containing bipyridine as linker and coordination sites was rational designed and synthesized via Schiff-base condensation of 2,2-bipyridyl-5,5-dialdehydeby and tris(4-aminophenyl)triazine (Figure 1.21). The resultant 2D-COF was then anchored with rhenium complexes ($Re(CO)_5Cl$) to form Re-COF.[57] Under visible light irradiation, Re-COF could produce 750 μmol g^{-1} h^{-1} of CO with 98% selectivity in acetonitrile and TEOA mixture (15/1). It was proven that electrons transfer from the COF to the Re moiety. However, the 2D structure of Re-COF formed by imine bonds is partially π-conjugated, which still influences the charge separation and is not stable in base experimental conditions. The CO generation rate decreased after 10 hours of irradiation, which might be due to the loss of crystallinity in the presence of TEOA.

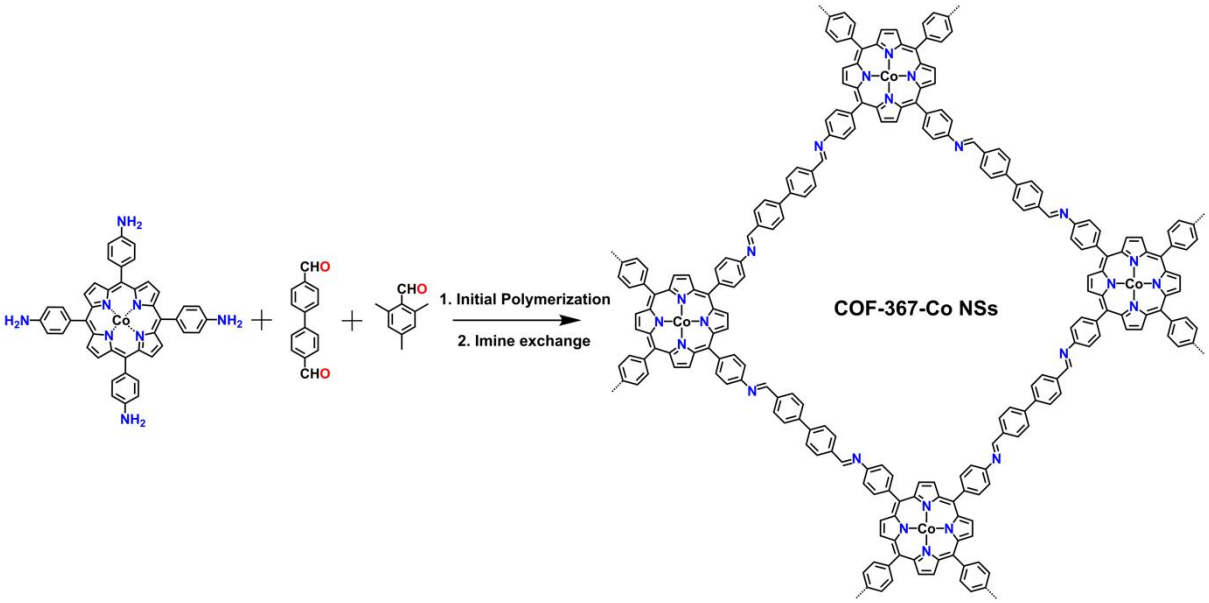

Figure 1.22 Synthetic method of COF-367-Co nanosheets.

2D COFs have been demonstrated as porous scaffolds for molecular metal catalysts. Moreover, COFs could be exfoliated to increase the surface area and expose more catalytic metal sites to enhance their activity. Jiang and coworkers applied the bottom-up method to yield < 2 nm ultrathin imine-based porphyrin COF (COF-367-Co, Figure 1.22). COF-367-Co nanosheets could act as the photocatalyst for CO_2 reduction and produced CO at a rate of 10162 μmol g^{-1} h^{-1} with 78% selectivity of CO under visible light in aqueous media with additional $[Ru(bpy)_3]Cl_2$ as the photosensitizer.[58] The formed nanosheets can expose more cobalt active sites, which increase the interaction between CO_2 and reaction sites for CO_2 reduction. By comparison, the obtained bulk COF-367-Co exhibited a low CO generation rate of 124 μmol g^{-1} h^{-1} with 13% selectivity of CO under the same conditions. This is the highest reported CO generation rate from CO_2 reduction by COFs. However, the COF-367-Co has no activity without additional dye, and the stability of COF nanosheets is another issue for this imine type COF. Moreover, the selectivity is 78% which is lower than those of other COFs and CMPs. Also, the bottom-up approach via imine-exchange synthesis strategy can only be used for COFs synthesized by reversible reactions.

In conclusion, compared with CMPs, COFs with well-defined crystalline structures are promising for CO_2 reduction due to the controllable properties. Without any metal residue

inside, COFs can achieve high selectivity for certain products. However, the long-term stabilities of reported COFs are one problem. All the reported COFs for CO_2 reduction are imine or β-ketoenamine linked COFs, which are partially π-conjugated and not stable in base experimental conditions. These reported COFs only achieved CO_2 reduction for less than 10 hours. Also, some COFs need additional dye for sensitization due to their limited light-harvesting and/or the subsequent energy transfer abilities. It is very attractive to build fully π-conjugated or stable COFs for CO_2 reduction with high product generation rate, high selectivity for the final product and long-term stability. Applying irreversible chemistry to build olefin COFs or rationally modifying COFs is a new way for synthesizing photocatalysts for CO_2 reduction.

Table 1.4 Summary of the representative photocatalysts for photocatalytic CO_2 reduction in Figure 1.11.

Photocatalyst	Photosensitizer	Product evolution rate ($\mu mol \cdot g^{-1} \cdot h^{-1}$)	TOF	Selectivity (%)	Reaction solvent	Reference
mpg-CN_x	-	17.9 (CO)	-	84.4	MeCN/TEOA	48
BCN	-	94 (CO)	-	-	MeCN/H_2O/TEOA	50
CdS/BCN	-	250 (CO)	-	81.1%	MeCN/H_2O/TEOA	50
HR-CN	-	297 (CO)	-	96.7%	MeCN/TEOA	51
MCN/CoO_x	-	204 (CO)	-	78.5%	MeCN/H_2O/TEOA	20
DA-CTF	-	155 (CO)	-	69%	MeCN/H_2O/TEOA	52
CPs-BT	-	1213 (CO)	-	81.6%	MeCN/H_2O/TEOA	28
N-CP-D	-	2247 (CO)	-	82%	MeCN/H_2O/TEOA	22
L-CP-D	-	806 (CO)	-	86%	MeCN/H_2O/TEOA	22
CP5	-	47.37 (CO)	-	98.3	Ionic liquid/TEOA	53
NOP-COP	-	22.5 (CH_4)	-	90.2	MeCN/H_2O/TEOA	54
HCP-TiO_2-FG	-	27.63 (CH_4)	-	83.7%	CO_2/H_2O vapor	55
PEson-Y	-	33 (CO)	-	92%	CO_2/H_2O vapor	56
Re-COF	-	750 (CO)	-	98%	MeCN/TEOA	57
Re-TpBpy COF	-	275 (CO)	-	-	MeCN/H_2O/TEOA	121
TTCOF-Zn	-	2.06 (CO)	-	100%	H_2O	61
COF-318-TiO_2	-	69.67 (CO)	-	-	CO_2/H_2O vapor	122
PI-COF-TT	-	483 (CO)	-	93%	MeCN/TEOA	62
Ni-TpBpy-COF	$[Ru(bpy)_3]Cl_2$	966 (CO)	-	96%	MeCN/H_2O/TEOA	59
COF-367-CoNSs	$[Ru(bpy)_3]Cl_2$	10162 (CO)	-	78%	Aqueous $KHCO_3$ solution/AA	58
DQTP COF-Co	$[Ru(bpy)_3]Cl_2$	1020 (CO)	-	69.4%	MeCN/TEOA	60
DQTP COF-Zn	$[Ru(bpy)_3]Cl_2$	152.5 (HCOOH)	-	90%	MeCN/TEOA	60
Co-ZIF-9	$[Ru(bpy)_3]Cl_2$	2600 (CO)	89.6	58%	MeCN/H_2O/TEOA	69
Mn-MOF-74	$[Ru(bpy)_3]Cl_2$	1170 (CO)	5.5	52%	MeCN/H_2O/TEOA	69
Co-ZIF-67	$[Ru(bpy)_3]Cl_2$	3890 (CO)	-	63%	MeCN/H_2O/TEOA	70
Ni MOLs	$[Ru(bpy)_3]Cl_2$	12500 (CO)	-	96.8%	MeCN/H_2O/TEOA	71
2D-MOF $Ni_3(HITP)_2$	$[Ru(bpy)_3]Cl_2$	34500 (CO)	83.16	97%	MeCN/H_2O/TEOA	72
ZIF-67	$[Ru(bpy)_3]Cl_2$	29600 (CO)	112	66.7%	MeCN/H_2O/TEOA	73
Ni(TPA/TEG)	$[Ru(bpy)_3]Cl_2$	16000 (CO)	11.5	100%	MeCN/H_2O/TEOA	74
Ni3@Ru-UiO-67	-	426.05 (CO)	581	99%	DMF/H_2O/TEOA/ BIH	75
$ZnIn_2S_4$-In_2O_3	-	3075 (CO)		79.4%	MeCN/H_2O/TEOA	21
In_2S_3-$CdIn_2S_4$	-	825 (CO)		73.3%	MeCN/H_2O/TEOA	27
PCN-250-Fe_2Mn	$[Ru(bpy)_3]Cl_2$	21510 (CO)	-	82.17%	MeCN/H_2O/TIPA	63
Co_3O_4	$[Ru(bpy)_3]Cl_2$	2003 (CO)	1.45	77.1%	MeCN/H_2O/TEOA	64
PMMCoCC-1200	$[Ru(bpy)_3]Cl_2$	1380 (CO)	-	64.21%	MeCN/TEOA	65
NC@$NiCo_2O_4$	$[Ru(bpy)_3]Cl_2$	26200 (CO)	-	88.6%	MeCN/H_2O	66
$MnCo_2O_4$	$[Ru(bpy)_3]Cl_2$	30200 (CO)	9.3	71%	MeCN/H_2O/TEOA	123
$ZnCo_2O_4$	$[Ru(bpy)_3]Cl_2$	17600 (CO)	10.8	74.3%	MeCN/H_2O/TEOA	67

1.4 Aims and objectives

The core aim of this thesis is to achieve the conversion of carbon dioxide into value-added products, CO or syngas, by using organic semiconductors in the presence of sacrificial agents. The use of conjugated polymers as photocatalysts is of growing interest due to their earth-abundance (mainly composed of C, H, O, N and S) and wide molecular-level design space giving remarkable structural and functional diversity.

The main objectives of this thesis were:

- To establish a workflow for high throughput screening linear polymers to find promising photocatalysts for syngas generation.
- To synthesize sp^2c covalent organic frameworks (COFs) for producing CO with high activity.
- To study fluorinated COFs as a stable imine-COF-based photocatalyst with non-noble metal complexes as cocatalysts for generating CO with high yield and selectivity.

In **Chapter 2**, we tested linear polymers for syngas generation with the help of a high throughput system. Linear polymers and commercial semiconductors were first measured because they have been proved as good photocatalysts for HER and can be largely used for CO_2 reduction screenings to get a basic understanding. The optical properties, electronic properties, dispersibility, and residual metal amounts of linear polymers were studied for the activity and selectivity for CO_2 reduction.

In **Chapter 3**, we focused on fully conjugated olefin COFs for producing CO with high selectivity. Chemical robustness, photosensitization and crystallinity were investigated for designing highly active COFs photocatalysts for CO_2 reduction. COFs were chosen because they can combine porosity with crystallinity and have shown strong potentials as solar fuels photocatalysts. The properties of COFs are easily tuned through the modular incorporation of different building blocks. Meanwhile, most COFs have no residual metals inside, which can reduce the effect of residual palladium on CO selectivity and obtain highly active photocatalysts. One challenge here is the reversible bond-formation chemistry used in making

most COFs, which leads to varying degrees of long-term instability under photocatalytic conditions. Instability is perhaps the central challenge for such materials, even more than catalytic rate and selectivity. Olefin COFs can keep their crystallinity in base and acid experimental conditions. The chemical robustness of the olefin COF stems from its fully π-conjugated backbone, which is also beneficial for efficient light-harvesting and charge transport, and hence photocatalytic activity.

In **Chapter 4**, we measured the fluorinated COFs as stable imine-COF-based photocatalysts combined with non-noble-metal-based molecular complexes as the cocatalyst to achieve both a high CO_2 reduction efficiency and a high CO selectivity. The introduction of fluorine atoms in the COFs' backbone is a strategy to improve the interaction between COF layers and the affinity of the materials to CO_2 molecules. We explored their structure−property−activity relationships by screening CO_2 reduction photoactivity for isostructural COFs under the same conditions. CO_2 affinity, pore size, and light absorption of photosensitizer significantly influenced photocatalytic CO_2 reduction activity.

1.5 Reference

1 AOAN, Global Monitoring Laboratory - Carbon Cycle Greenhouse Gases, https://www.esrl.noaa.gov/gmd/ccgg/trends/, (accessed 18 October 2020).

2 K. Li, B. Peng and T. Peng, *ACS Catal.*, 2016, **6**, 7485–7527.

3 A. P. Ballantyne, C. B. Alden, J. B. Miller, P. P. Trans and J. W. C. White, *Nature*, 2012, **488**, 70–73.

4 The Sun Facts | Information, History, Size, Formation & Definition, https://nineplanets.org/the-sun/, (accessed 2 May 2021).

5 J. Wu, Y. Huang, W. Ye and Y. Li, *Adv. Sci.*, 2017, **4**, 1700194.

6 J. L. White, M. F. Baruch, J. E. Pander, Y. Hu, I. C. Fortmeyer, J. E. Park, T. Zhang, K. Liao, J. Gu, Y. Yan, T. W. Shaw, E. Abelev and A. B. Bocarsly, *Chem. Rev.*, 2015, **115**, 12888–12935.

7 C. Wang, Z. Xie, K. E. Dekrafft and W. Lin, *J. Am. Chem. Soc.*, 2011, **133**, 13445–13454.

8 Q. Wang, T. Hisatomi, Q. Jia, H. Tokudome, M. Zhong, C. Wang, Z. Pan, T. Takata, M. Nakabayashi, N. Shibata, Y. Li, I. D. Sharp, A. Kudo, T. Yamada and K. Domen, *Nat. Mater.*, 2016, **15**, 611–615.

9 D. Voiry, H. S. Shin, K. P. Loh and M. Chhowalla, *Nat. Rev. Chem.*, 2018, **2**, 0105.

10 H. Abdullah, M. M. R. Khan, H. R. Ong and Z. Yaakob, *J. CO_2 Util.*, 2017, **22**, 15–32.

11 R. Kuriki, K. Sekizawa, O. Ishitani and K. Maeda, *Angew. Chem. Int. Ed.*, 2015, **54**, 2406–2409.

12 L. Zhou, H. Zhang, H. Sun, S. Liu, M. O. Tade, S. Wang and W. Jin, *Catal. Sci. Technol.*, 2016, **6**, 7002–7023.

13 S. Nitopi, E. Bertheussen, S. B. Scott, X. Liu, A. K. Engstfeld, S. Horch, B. Seger, I. E. L. Stephens, K. Chan, C. Hahn, J. K. Nørskov, T. F. Jaramillo and I. Chorkendorff, *Chem. Rev.*, 2019, **119**, 7610–7672.

14 P. L. Spath and D. C. Dayton, *Natl. Renew. Energy Lab.*, 2003, 1–160.

15 X. Li, J. Wen, J. Low, Y. Fang and J. Yu, *Sci. China Mater.*, 2014, **57**, 70–100.

16 T. Banerjee, F. Podjaski, J. Kröger, B. P. Biswal and B. V. Lotsch, *Nat. Rev. Mater.*, 2021, **6**, 168–190.

17 M. Halmann, *Nature*, 1978, 275, 115–116.

18 X. Chang, T. Wang and J. Gong, *Energy Environ. Sci.*, 2016, **9**, 2177–2196.

19 S. Fernández, F. Franco, C. Casadevall, V. Martin-Diaconescu, J. M. Luis and J. Lloret-Fillol, *J. Am. Chem. Soc.*, 2020, **142**, 120–133.

20 J. Lin, Z. Pan and X. Wang, *ACS Sustain. Chem. Eng.*, 2014, **2**, 353–358.

21 S. Wang, B. Y. Guan and X. W. D. Lou, *J. Am. Chem. Soc.*, 2018, **140**, 5037–5040.

22 S. Wang, X. Hai, X. Ding, S. Jin, Y. Xiang, P. Wang, B. Jiang, F. Ichihara, M. Oshikiri, X. Meng, Y. Li,

W. Matsuda, J. Ma, S. Seki, X. Wang, H. Huang, Y. Wada, H. Chen and J. Ye, *Nat. Commun.*, 2020, **11**, 1149.

23 C. D. Windle, E. Pastor, A. Reynal, A. C. Whitwood, Y. Vaynzof, J. R. Durrant, R. N. Perutz and E. Reisner, *Chem. - A Eur. J.*, 2015, **21**, 3746–3754.

24 J.-M. Lehn and R. Ziessel, *Proc. Natl. Acad. Sci.*, 1982, **79**, 701–704.

25 J. Lin, X. Sun, B. Qin and T. Yu, *RSC Adv.*, 2018, **8**, 20543–20548.

26 J. Lin, R. Liao and J. Xu, *RSC Adv.*, 2018, **8**, 3798–3802.

27 S. Wang, B. Y. Guan, Y. Lu and X. W. Lou, *J. Am. Chem. Soc.*, 2017, **139**, 17305–17308.

28 C. Yang, W. Huang, L. C. da Silva, K. A. I. Zhang and X. Wang, *Chem. - A Eur. J.*, 2018, **24**, 17454–17458.

29 P. Lang, R. Giereth, S. Tschierlei and M. Schwalbe, *Chem. Commun.*, 2019, **55**, 600–603.

30 J. Hawecker, J.-M. Lehn and R. Ziessel, *Chem. Commun.*, 1983, 536–538.

31 B. P. Sullivan, C. M. Bolinger, D. Conrad, W. J. Vining and T. J. Meyer, *J. Chem. Soc. Chem. Commun.*, 1985, 1414–1416.

32 A. Fujishima and K. Honda, *Nature*, 1972, **238**, 37–38.

33 Ş. Neaţu, J. A. Maciá-Agulló and H. Garcia, *Int. J. Mol. Sci.*, 2014, **15**, 5246–5262.

34 Y. Pellegrin and F. Odobel, *Comptes Rendus Chim.*, 2017, **20**, 283–295.

35 T. Uekert, M. F. Kuehnel, D. W. Wakerley and E. Reisner, *Energy Environ. Sci*, 2018, **11**, 2853.

36 X. Wang, L. Chen, S. Y. Chong, M. A. Little, Y. Wu, W. H. Zhu, R. Clowes, Y. Yan, M. A. Zwijnenburg, R. S. Sprick and A. I. Cooper, *Nat. Chem.*, 2018, **10**, 1180–1189.

37 Y. Wang, A. Vogel, M. Sachs, R. S. Sprick, L. Wilbraham, S. J. A. Moniz, R. Godin, M. A. Zwijnenburg, J. R. Durrant, A. I. Cooper and J. Tang, *Nat. Energy*, 2019, **4**, 746–760.

38 C. S. Diercks, Y. Liu, K. E. Cordova and O. M. Yaghi, *Nat. Mater.*, 2018, **17**, 301–307.

39 K. Li, B. Peng and T. Peng, *ACS Catal.*, 2016, **6**, 7485–7527.

40 S. Xie, Q. Zhang, G. Liu and Y. Wang, *Chem. Commun.*, 2016, **52**, 35–59.

41 S. N. Habisreutinger, L. Schmidt-Mende and J. K. Stolarczyk, *Angew. Chem. Int. Ed.*, 2013, **52**, 7372–7408.

42 ţefan Neatu, J. A. Maciá-Agullò, P. Concepciòn and H. Garcia, *J. Am. Chem. Soc.*, 2014, **136**, 15969–15976.

43 X. Feng, J. D. Sloppy, T. J. LaTempa, M. Paulose, S. Komarneni, N. Bao and C. A. Grimes, *J. Mater.*

Chem., 2011, **21**, 13429.

44 X. Meng, S. Ouyang, T. Kako, P. Li, Q. Yu, T. Wang and J. Ye, *Chem. Commun.*, 2014, **50**, 11517–11519.

45 A. Sarkar, E. Gracia-Espino, T. Wågberg, A. Shchukarev, M. Mohl, A. R. Rautio, O. Pitkänen, T. Sharifi, K. Kordas and J. P. Mikkola, *Nano Res.*, 2016, **9**, 1956–1968.

46 C. Lin, Y. Song, L. Cao and S. Chen, *Nanoscale*, 2013, **5**, 4986.

47 Ş. Neaţu, J. A. Maciá-Agulló, P. Concepción and H. Garcia, *J. Am. Chem. Soc.*, 2014, **136**, 15969–15976.

48 S. Roy and E. Reisner, *Angew. Chem. Int. Ed.*, 2019, **58**, 12180–12184.

49 C. Huang, C. Chen, M. Zhang, L. Lin, X. Ye, S. Lin, M. Antonietti and X. Wang, *Nat. Commun.*, 2015, **6**, 7698.

50 M. Zhou, S. Wang, P. Yang, C. Huang and X. Wang, *ACS Catal.*, 2018, **8**, 4928–4936.

51 Y. Zheng, L. Lin, X. Ye, F. Guo and X. Wang, *Angew. Chem. Int. Ed.*, 2014, **53**, 11926–11930.

52 H. Zhong, Z. Hong, C. Yang, L. Li, Y. Xu, X. Wang and R. Wang, *ChemSusChem*, 2019, **12**, 4493–4499.

53 Y. Chen, G. Ji, S. Guo, B. Yu, Y. Zhao, Y. Wu, H. Zhang, Z. Liu, B. Han and Z. Liu, *Green Chem.*, 2017, **19**, 5777–5781.

54 S. Guo, H. Zhang, Y. Chen, Z. Liu, B. Yu, Y. Zhao, Z. Yang, B. Han and Z. Liu, *ACS Catal.*, 2018, **8**, 4576–4581.

55 S. Wang, M. Xu, T. Peng, C. Zhang, T. Li, I. Hussain, J. Wang and B. Tan, *Nat. Commun.*, 2019, **10**, 676.

56 X. Yu, Z. Yang, B. Qiu, S. Guo, P. Yang, B. Yu, H. Zhang, Y. Zhao, X. Yang, B. Han and Z. Liu, *Angew. Chem. Int. Ed.*, 2019, **58**, 632–636.

57 S. Yang, W. Hu, X. Zhang, P. He, B. Pattengale, C. Liu, M. Cendejas, I. Hermans, X. Zhang, J. Zhang and J. Huang, *J. Am. Chem. Soc.*, 2018, **140**, 14614–14618.

58 W. Liu, X. Li, C. Wang, H. Pan, W. Liu, K. Wang, Q. Zeng, R. Wang and J. Jiang, *J. Am. Chem. Soc.*, 2019, **141**, 17431–17440.

59 W. Zhong, R. Sa, L. Li, Y. He, L. Li, J. Bi, Z. Zhuang, Y. Yu and Z. Zou, *J. Am. Chem. Soc.*, 2019, **141**, 7615–7621.

60 M. Lu, Q. Li, J. Liu, F. M. Zhang, L. Zhang, J. L. Wang, Z. H. Kang and Y. Q. Lan, *Appl. Catal. B Environ.*, 2019, **254**, 624–633.

61 M. Lu, J. Liu, Q. Li, M. Zhang, M. Liu, J. L. Wang, D. Q. Yuan and Y. Q. Lan, *Angew. Chem. Int. Ed.*, 2019, **58**, 12392–12397.

62 X. Chen, Q. Dang, R. Sa, L. Li, L. Li, J. Bi, Z. Zhang, J. Long, Y. Yu and Z. Zou, *Chem. Sci.*, 2020, **11**,

6915–6922.

63 H. Dong, X. Zhang, Y. Lu, Y. Yang, Y. P. Zhang, H. L. Tang, F. M. Zhang, Z. Di Yang, X. Sun and Y. Feng, *Appl. Catal. B Environ.*, 2020, **276**, 119173.

64 C. Gao, Q. Meng, K. Zhao, H. Yin, D. Wang, J. Guo, S. Zhao, L. Chang, M. He, Q. Li, H. Zhao, X. Huang, Y. Gao and Z. Tang, *Adv. Mater.*, 2016, **28**, 6485–6490.

65 K. Zhao, S. Zhao, C. Gao, J. Qi, H. Yin, D. Wei, M. F. Mideksa, X. Wang, Y. Gao, Z. Tang and R. Yu, *Small*, 2018, **14**, 1800762.

66 S. Wang, B. Y. Guan and X. W. Lou, *Energy Environ. Sci.*, 2018, **11**, 306–310.

67 S. Wang, Z. Ding and X. Wang, *Chem. Commun.*, 2015, **51**, 1517–1519.

68 C. Chen, T. Wu, H. Wu, H. Liu, Q. Qian, Z. Liu, G. Yang and B. Han, *Chem. Sci.*, 2018, **9**, 8890–8894.

69 S. Wang, W. Yao, J. Lin, Z. Ding and X. Wang, *Angew. Chem. Int. Ed.*, 2014, **53**, 1034–1038.

70 M. Wang, J. Liu, C. Guo, X. Gao, C. Gong, Y. Wang, B. Liu, X. Li, G. G. Gurzadyan and L. Sun, *J. Mater. Chem. A*, 2018, **6**, 4768–4775.

71 B. Han, X. Ou, Z. Deng, Y. Song, C. Tian, H. Deng, Y. J. Xu and Z. Lin, *Angew. Chem. Int. Ed.*, 2018, **57**, 16811–16815.

72 W. Zhu, C. Zhang, Q. Li, L. Xiong, R. Chen, X. Wan, Z. Wang, W. Chen, Z. Deng and Y. Peng, *Appl. Catal. B Environ.*, 2018, **238**, 339–345.

73 J. Qin, S. Wang and X. Wang, *Appl. Catal. B Environ.*, 2017, **209**, 476–482.

74 K. Niu, Y. Xu, H. Wang, R. Ye, H. L. Xin, F. Lin, C. Tian, Y. Lum, K. C. Bustillo, M. M. Doeff, M. T. M. Koper, J. Ager, R. Xu and H. Zheng, *Sci. Adv.*, 2017, **3**, e1700921.

75 Z. H. Yan, B. Ma, S. R. Li, J. Liu, R. Chen, M. H. Du, S. Jin, G. L. Zhuang, L. S. Long, X. J. Kong and L. S. Zheng, *Sci. Bull.*, 2019, **64**, 976–985.

76 R. S. Sprick, J. X. Jiang, B. Bonillo, S. Ren, T. Ratvijitvech, P. Guiglion, M. A. Zwijnenburg, D. J. Adams and A. I. Cooper, *J. Am. Chem. Soc.*, 2015, **137**, 3265–3270.

77 M. Sachs, R. S. Sprick, D. Pearce, S. A. J. Hillman, A. Monti, A. A. Y. Guilbert, N. J. Brownbill, S. Dimitrov, X. Shi, F. Blanc, M. A. Zwijnenburg, J. Nelson, J. R. Durrant and A. I. Cooper, *Nat. Commun.*, 2018, **9**, 4968.

78 R. S. Sprick, L. Wilbraham, Y. Bai, P. Guiglion, A. Monti, R. Clowes, A. I. Cooper and M. A. Zwijnenburg, *Chem. Mater.*, 2018, **30**, 5733–5742.

79 X. Wang, K. Maeda, A. Thomas, K. Takanabe, G. Xin, J. M. Carlsson, K. Domen and M. Antonietti, *Nat.*

Mater., 2009, **8**, 76–80.

80 J. Qin, S. Wang, H. Ren, Y. Hou and X. Wang, *Appl. Catal. B Environ.*, 2015, **179**, 1–8.

81 H. P. Liang, A. Acharjya, D. A. Anito, S. Vogl, T. X. Wang, A. Thomas and B. H. Han, *ACS Catal.*, 2019, **10**, 3959–3968.

82 S. Shoaee, M. Stolterfoht and D. Neher, *Adv. Energy Mater.*, 2018, **8**, 1703355.

83 C. Cometto, R. Kuriki, L. Chen, K. Maeda, T. C. Lau, O. Ishitani and M. Robert, *J. Am. Chem. Soc.*, 2018, **140**, 7437–7440.

84 B. Ma, G. Chen, C. Fave, L. Chen, R. Kuriki, K. Maeda, O. Ishitani, T. C. Lau, J. Bonin and M. Robert, *J. Am. Chem. Soc.*, 2020, **142**, 6188–6195.

85 P. Huang, J. Huang, S. A. Pantovich, A. D. Carl, T. G. Fenton, C. A. Caputo, R. L. Grimm, A. I. Frenkel and G. Li, *J. Am. Chem. Soc.*, 2018, **140**, 16042–16047.

86 K. Wang, Q. Li, B. Liu, B. Cheng, W. Ho and J. Yu, *Appl. Catal. B Environ.*, 2015, **176–177**, 44–52.

87 Z. Sun, J. M. T. A. Fischer, Q. Li, J. Hu, Q. Tang, H. Wang, Z. Wu, M. Hankel, D. J. Searles and L. Wang, *Appl. Catal. B Environ.*, 2017, **216**, 146–155.

88 G. Zhao, H. Pang, G. Liu, P. Li, H. Liu, H. Zhang, L. Shi and J. Ye, *Appl. Catal. B Environ.*, 2017, **200**, 141–149.

89 J. C. Wang, H. C. Yao, Z. Y. Fan, L. Zhang, J. S. Wang, S. Q. Zang and Z. J. Li, *ACS Appl. Mater. Interfaces*, 2016, **8**, 3765–3775.

90 Y. Zheng, L. Lin, B. Wang and X. Wang, *Angew. Chem. Int. Ed.*, 2015, **54**, 12868–12884.

91 J. S. M. Lee and A. I. Cooper, *Chem. Rev.*, 2020, **120**, 2171–2214.

92 C. Dai and B. Liu, *Energy Environ. Sci.*, 2020, **13**, 24–52.

93 J. X. Jiang, F. Su, A. Trewin, C. D. Wood, N. L. Campbell, H. Niu, C. Dickinson, A. Y. Ganin, M. J. Rosseinsky, Y. Z. Khimyak and A. I. Cooper, *Angew. Chem. Int. Ed.*, 2007, **46**, 8574–8578.

94 J. Lu and J. Zhang, *Photochemistry*, 2018, **45**, 191–220.

95 R. S. Sprick, B. Bonillo, R. Clowes, P. Guiglion, N. J. Brownbill, B. J. Slater, F. Blanc, M. A. Zwijnenburg, D. J. Adams and A. I. Cooper, *Angew. Chem. Int. Ed.*, 2016, **55**, 1792–1796.

96 R. S. Sprick, Y. Bai, A. A. Y. Guilbert, M. Zbiri, C. M. Aitchison, L. Wilbraham, Y. Yan, D. J. Woods, M. A. Zwijnenburg and A. I. Cooper, *Chem. Mater.*, 2019, **31**, 305–313.

97 M. Sachs, R. S. Sprick, D. Pearce, S. A. J. Hillman, A. Monti, A. A. Y. Guilbert, N. J. Brownbill, S. Dimitrov, X. Shi, F. Blanc, M. A. Zwijnenburg, J. Nelson, J. R. Durrant and A. I. Cooper, *Nat. Commun.*,

2018, **9**, 4968.

98 Y. Bai, D. J. Woods, L. Wilbraham, C. M. Aitchison, M. A. Zwijnenburg, R. S. Sprick and A. I. Cooper, *J. Mater. Chem. A*, 2020, **8**, 8700–8705.

99 M. Sachs, H. Cha, J. Kosco, C. M. Aitchison, L. Francàs, S. Corby, C. L. Chiang, A. A. Wilson, R. Godin, A. Fahey-Williams, A. I. Cooper, R. S. Sprick, I. McCulloch and J. R. Durrant, *J. Am. Chem. Soc.*, 2020, **142**, 14574–14587.

100 C. B. Meier, R. Clowes, E. Berardo, K. E. Jelfs, M. A. Zwijnenburg, R. S. Sprick and A. I. Cooper, *Chem. Mater.*, 2019, **31**, 8830–8838.

101 Y. Bai, L. Wilbraham, B. J. Slater, M. A. Zwijnenburg, R. S. Sprick and A. I. Cooper, *J. Am. Chem. Soc.*, 2019, **141**, 9063–9071.

102 J. Kosco, M. Sachs, R. Godin, M. Kirkus, L. Francas, M. Bidwell, M. Qureshi, D. Anjum, J. R. Durrant and I. McCulloch, *Adv. Energy Mater.*, 2018, **8**, 1802181.

103 R. S. Sprick, Y. Bai, A. A. Y. Guilbert, M. Zbiri, C. M. Aitchison, L. Wilbraham, Y. Yan, D. J. Woods, M. A. Zwijnenburg and A. I. Cooper, *Chem. Mater.*, 2019, **31**, 305–313.

104 A. P. Côté, A. I. Benin, N. W. Ockwig, M. O'Keeffe, A. J. Matzger and O. M. Yaghi, *Science*, 2005, **310**, 1166–1170.

105 P. Kuhn, M. Antonietti and A. Thomas, *Angew. Chem. Int. Ed.*, 2008, **47**, 3450–3453.

106 F. J. Uribe-Romo, J. R. Hunt, H. Furukawa, C. Klöck, M. O'Keeffe and O. M. Yaghi, *J. Am. Chem. Soc.*, 2009, **131**, 4570–4571.

107 F. J. Uribe-Romo, C. J. Doonan, H. Furukawa, K. Oisaki and O. M. Yaghi, *J. Am. Chem. Soc.*, 2011, **133**, 11478–11481.

108 S. Kandambeth, A. Mallick, B. Lukose, M. V. Mane, T. Heine and R. Banerjee, *J. Am. Chem. Soc.*, 2012, **134**, 19524–19527.

109 Q. Fang, Z. Zhuang, S. Gu, R. B. Kaspar, J. Zheng, J. Wang, S. Qiu and Y. Yan, *Nat. Commun.*, 2014, **5**, 4503.

110 P. J. Waller, S. J. Lyle, T. M. Osborn Popp, C. S. Diercks, J. A. Reimer and O. M. Yaghi, *J. Am. Chem. Soc.*, 2016, **138**, 15519–15522.

111 H. Liu, J. Chu, Z. Yin, X. Cai, L. Zhuang and H. Deng, *Chem*, 2018, **4**, 1696–1709.

112 R. Liu, K. T. Tan, Y. Gong, Y. Chen, Z. Li, S. Xie, T. He, Z. Lu, H. Yang and D. Jiang, *Chem. Soc. Rev.*, 2021, 50, 120–242.

113 X. Zhuang, W. Zhao, F. Zhang, Y. Cao, F. Liu, S. Bi and X. Feng, *Polym. Chem.*, 2016, **7**, 4176–4181.

114 E. Jin, M. Asada, Q. Xu, S. Dalapati, M. A. Addicoat, M. A. Brady, H. Xu, T. Nakamura, T. Heine, Q. Chen and D. Jiang, *Science*, 2017, **357**, 673–676.

115 S. Wei, F. Zhang, W. Zhang, P. Qiang, K. Yu, X. Fu, D. Wu, S. Bi and F. Zhang, *J. Am. Chem. Soc.*, 2019, **141**, 14272–14279.

116 H. Lyu, C. S. Diercks, C. Zhu and O. M. Yaghi, *J. Am. Chem. Soc.*, 2019, **141**, 6848–6852.

117 E. Jin, Z. Lan, Q. Jiang, K. Geng, G. Li, X. Wang and D. Jiang, *Chem*, 2019, **5**, 1632–1647.

118 L. Stegbauer, K. Schwinghammer and B. V. Lotsch, *Chem. Sci.*, 2014, **5**, 2789–2793.

119 V. S. Vyas, F. Haase, L. Stegbauer, G. Savasci, F. Podjaski, C. Ochsenfeld and B. V. Lotsch, *Nat. Commun.*, 2015, **6**, 1–9.

120 Y. Fu, X. Zhu, L. Huang, X. Zhang, F. Zhang and W. Zhu, *Appl. Catal. B Environ.*, 2018, **239**, 46–51.

121 S. Y. Li, S. Meng, X. Zou, M. El-Roz, I. Telegeev, O. Thili, T. X. Liu and G. Zhu, *Microporous Mesoporous Mater.*, 2019, **285**, 195–201.

122 M. Zhang, M. Lu, Z. Lang, J. Liu, M. Liu, J. Chang, L. Li, L. Shang, M. Wang, S. Li and Y. Lan, *Angew. Chem. Int. Ed.*, 2020, **59**, 6500–6506.

123 S. Wang, Y. Hou and X. Wang, *ACS Appl. Mater. Interfaces*, 2015, **7**, 4327–4335.

Chapter 2

Photocatalytic syngas production using conjugated organic polymers

2.1 Author contributions

All the polymers used in this chapter were synthesized by the thesis author except P1K, P10Y, P29, P30, P31 and P74 polymers, which were prepared by Dr Reiner Sebastian Sprick. SEM images were carried out by Lunjie Liu. Dr Catherine Aitchison captured TEM images. $^{13}CO_2$ labelling experiments were performed by Dr G. Neri and Prof. A. Cowan in the Stephenson Institute for Renewable Energy (SIRE). Calculations were performed by I. Heath-Apostolopoulos and Prof Martijn Zwijnenburg. Rob Clowes is thanked for his assistance with high-throughput measurements.

Portions of this chapter have been published in:

Z. Fu, A. Vogel, M. A. Zwijnenburg, A. I. Cooper, R. S. Sprick. Photocatalytic syngas production using conjugated organic polymers, *J. Mater. Chem. A*, 2021, **9**, 4291-4296.

2.2 Introduction

Organic materials such as conjugated microporous polymers (CMPs)[1,2], covalent triazine-based frameworks (CTFs)[3,4], covalent organic frameworks (COFs)[5–8] and unbranched conjugated polymers[9] are regarded as candidates for CO_2 reduction. When using photocatalysts for syngas generation and application for further industrial processing, different syngas compositions containing either CO-rich or H_2-rich mixtures are required.[10–13] Because controlling the H_2/CO generation in certain ratios is very difficult, much research is focused on obtaining photocatalysts with high selectivity for CO over H_2. It is worthwhile to generate syngas of different ratios by certain organic photocatalysts.

In this chapter, initially, to establish a workflow for high throughput screening materials for CO_2 reduction and accelerate our understanding of material design, conjugated polymers such as P1 or P7 and commercial photocatalysts such as g-C_3N_4 or TiO_2 were used to meet the need for a large amount of material required for screenings. First, we measured different experimental conditions for commercial materials and conjugated polymers for CO_2 reduction and chose the liquid phase for further investigation. Second, variations of metal doped polymers were tested as cocatalysts to improve the rates and selectivity of CO production. Third, cobalt chloride ($CoCl_2$) and 2,2'-bipyridine (bpy) as a cheap, easy-prepared and efficient molecular cocatalysts for high throughput screening were introduced into experiment condition. Results showed that CO generation rate could be enhanced by the system with molecular cocatalyst. Hence, we chose system containing cobalt complexes for further screening. Next, the influence of residual palladium was tested. We tried to remove the palladium and reduce its influence. Then, we screened a series of linear polymers with different chemical structures in the backbone, such as sulfone units, carbazole units, benzothiadiazole units or linear polymers containing different nitrogen atoms which could change the properties of polymers, for CO_2 reduction by using molecular cocatalysts to find the principles of design for promising CO_2 reduction photocatalysts to generate different ratios of CO and H_2. P7 was found that has the best CO generation rate and CO selectivity. However, Pd residual was also demonstrated could be cocatalysts for hydrogen evolution which influences the selectivity of CO. Finally, P7 with different amounts of Pd residue was synthesized for controllable syngas generation.

2.3 Experimental section

2.3.1 General methods

All reagents were obtained from Sigma-Aldrich, TCI, ABCR, Fisher Scientific or Fluorochem and used as received. Cobalt (II) chloride hexahydrate (BioReagent), 2,2'-bipyridyl (bpy, Reagent Plus, ≥99%) and triethanolamine (≥99.0%) were purchased from Sigma-Aldrich. Acetonitrile (HPLC gradient grade), *N*,*N*-dimethylformamide (GC Headspace Grade) were obtained from Fisher Scientific. Water for the CO_2 reduction experiments was purified using an ELGA LabWater system with a Purelab Option S filtration and ion exchange column (ρ = 15 MΩ cm^{-1}) without pH level adjustment. Reactions were carried out under nitrogen atmosphere using standard Schlenk techniques. Photocatalysts P1K,[14] P1S,[14] P4,[14] P7,[14] P10,[15] P29,[16] P30,[16] and P31[16] were prepared according to literature procedures.

2.3.2 Synthesis of P1K (Kumada-type polycondensation)

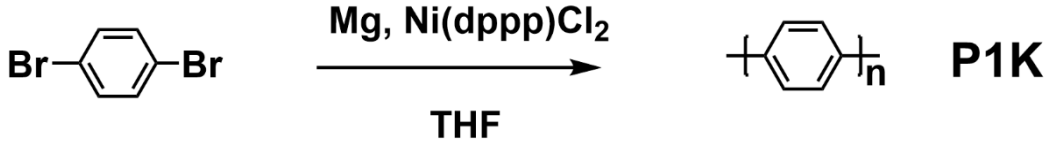

Figure 2.1 Synthesis of P1K via Kumada-type polycondensation.[14]

1,4-Dibromobenzene (2.95 g, 12.61 mmol), magnesium (0.305g, 12.55 mmol) and THF (20 mL, anhydrous) were first heated to reflux for 45 min. Then, [1,3-Bis(diphenylphosphino)propane]dichloro-nickel(II) (50 mg, 0.1 mmol) were added and the reaction was kept at reflux for 22 hours. After cooling, the crude polymer was poured into acetone. Next, the mixture was filtered and washed with hydrochloric acid (1 M), water, methanol and THF. Next, the material was purified by Soxhlet extraction with methanol and THF for three days. After drying under reduced pressure, the product was obtained as a light green powder.

2.3.3 Synthesis of P1S (Suzuki-Miyaura-type polycondensation)

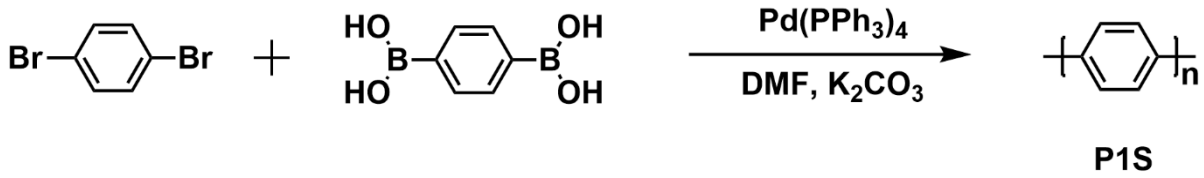

Figure 2.2 Synthesis of P1S via Suzuki-Miyaura-type polycondensation.[14]

1,4-Dibromobenzene (1.18 g, 5.0 mmol), 1,4-benzene diboronic acid (0.829 g, 5.0 mmol), [$Pd(PPh_3)_4$] (38 mg, 0.7 mol%), *N*,*N*-dimethylformamide (75 mL) and aqueous K_2CO_3 (2.0 M, 15 mL) were added into a flask and degassed by bubbling with N_2 for 30 min. Then the mixture was heated to reflux for three days. After cooling, the crude polymer was poured into water. Next, the mixture was filtered and washed with water, THF and methanol. Next, the material was purified by Soxhlet extraction with chloroform for three days. After that, the product was obtained as a grey powder.

2.3.4 Synthesis of P4

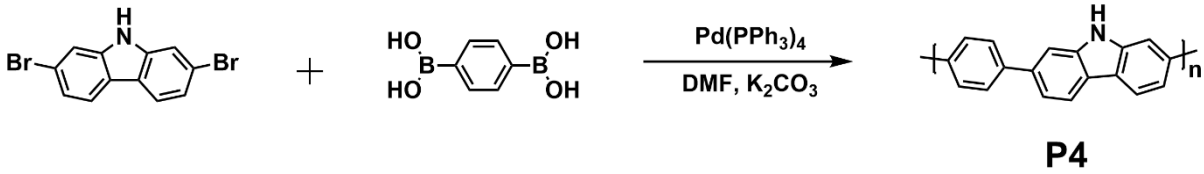

Figure 2.3 Synthesis of P4 via Suzuki-Miyaura-type polycondensation.[14]

2,7-Dibromo-9*H*-carbazole (0.325 g, 1.0 mmol), 1,4-benzene diboronic acid (0.165 g, 1.0 mmol), [$Pd(PPh_3)_4$] (15 mg, 1.3 mol%), *N*,*N*-dimethylformamide (15 mL) and aqueous K_2CO_3 (2.0 M, 3 mL) were added into a flask and degassed by bubbling with N_2 for 30 min. Then the mixture was heated to reflux for three days. After cooling, the crude polymer was poured into water. Next, the mixture was filtered and washed with water, THF and methanol. Next, the material was purified by Soxhlet extraction with chloroform for three days. After that, the product was obtained as a green-grey powder.

2.3.5 Synthesis of P7

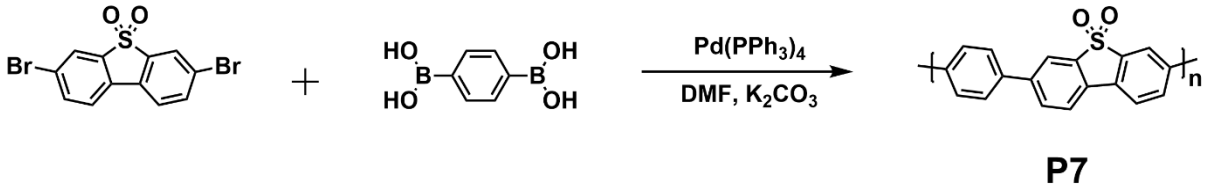

Figure 2.4 Synthesis of P7 via Suzuki-Miyaura-type polycondensation.[14]

3,7-dibromodibenzo[*b*,*d*]thiophene 5,5-dioxide (0.748 g, 2.0 mmol), 1,4-benzene diboronic acid (0.331 g, 2.0 mmol), [$Pd(PPh_3)_4$] (20 mg, 0.9 mol%), *N*,*N*-dimethylformamide (40 mL) and aqueous K_2CO_3 (2.0 M, 8 mL) were added into a flask and degassed by bubbling with N_2 for 30 min. Then the mixture was heated to reflux for three days. After cooling, the crude polymer was poured into water. Next, the mixture was filtered and washed with water, THF and methanol. Next, the material was purified by Soxhlet extraction with chloroform for three days. After that, the product was obtained as a green powder.

2.3.6 Synthesis of P10S (Suzuki-Miyaura-type polycondensation)

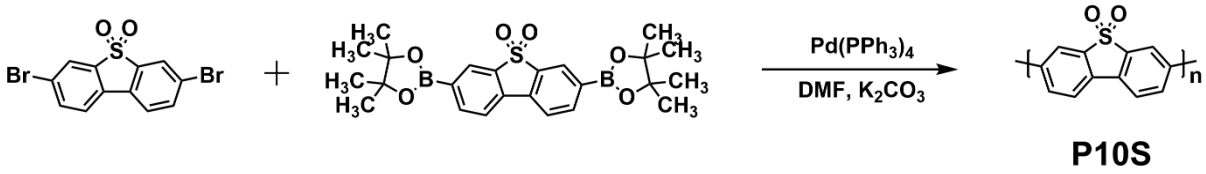

Figure 2.5 Synthesis of P10S via Suzuki-Miyaura-type polycondensation.[15]

3,7-dibromodibenzo[*b*,*d*]thiophene-5,5-dioxide (281 mg, 0.75 mmol), 3,7-bis(4,4,5,5-tetramethyl-1,3,2-dioxaborolan-2-yl)dibenzo[*b*,*d*]thio-phene-5,5-dioxide (351 mg, 0.75 mmol), *N*,*N*-dimethylformamide (20 mL), an aqueous solution of K_2CO_3 (4 mL, 2.0M), and [$Pd(PPh_3)_4$] (15 mg) were added into a flask and degassed by bubbling with N_2 for 30 min. Then the mixture was heated to reflux for three days. After cooling, the crude polymer was poured into water. Next, the mixture was filtered and washed with water, THF and methanol. Next, the material was purified by Soxhlet extraction with chloroform for three days. After that, the product was obtained as a yellow-green powder.

2.3.7 Synthesis of P10Y (Yamamoto coupling)

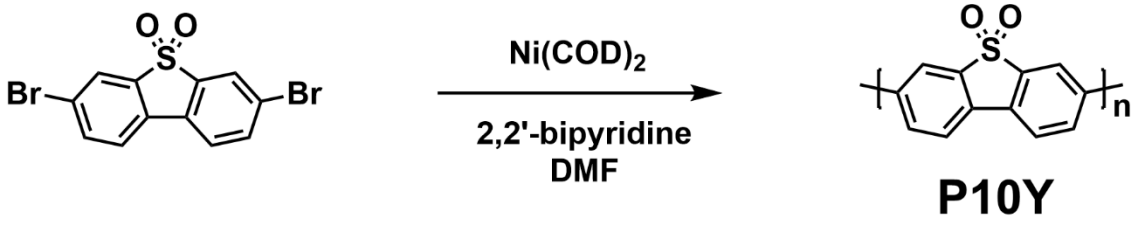

Figure 2.6 Synthesis of P10Y via Yamamoto coupling polycondensation.[15]

3,7-dibromodibenzo[*b*,*d*]thiophene 5,5-dioxide (374 mg, 1.00 mmol), 2,2'-bipyridine (344 mg, 2.20 mmol) were charged in a flame-dried Schlenk flask and transferred into a glove-box. The bis(cyclooctadiene)nickel(0) (660 mg, 2.40 mmol) was added in the glove-box. Outside the glove-box, 1,5-cyclooctadiene (338 mg, 2.20 mmol) and *N*,*N*-dimethylformamide (anhydrous, 20 mL) were added, and the resulting suspension was heated to 80 °C under nitrogen for three days. After cooling to room temperature, hydrochloric acid was added (conc., 20 mL), and the polymer was filtered off. The polymer was washed with water until neutral, and then methanol and tetrahydrofuran. Next, the material was purified by Soxhlet extraction with chloroform for three days. The product was obtained as a yellow powder.

2.3.8 Synthesis of P29

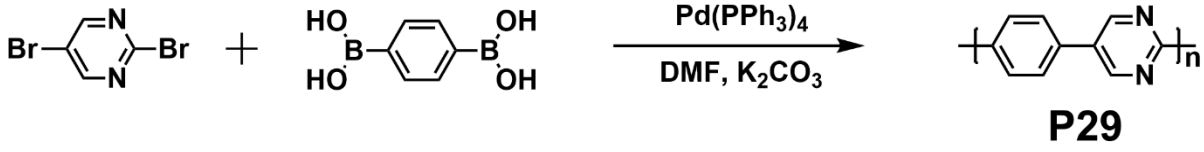

Figure 2.7 Synthesis of P29 via Suzuki-Miyaura-type polycondensation.[16]

2,5-Dibromopyrrimidine (476 mg, 2.0 mmol), benzene-1,4-diboronic acid (332 mg, 2.0 mmol), an aqueous solution of K_2CO_3 (8 mL, 2.0 M), *N*,*N*-dimethylformamide (40 mL), and [$Pd(PPh_3)_4$] (40 mg) were added into a flask and degassed by bubbling with N_2 for 30 min. Then the mixture was heated to reflux for three days. After cooling, the crude polymer was poured into water. Next, the mixture was filtered and washed with water, THF and methanol. Next, the material was purified by Soxhlet extraction with chloroform for three days. The product was obtained as a dark gray powder.

2.3.9 Synthesis of P30

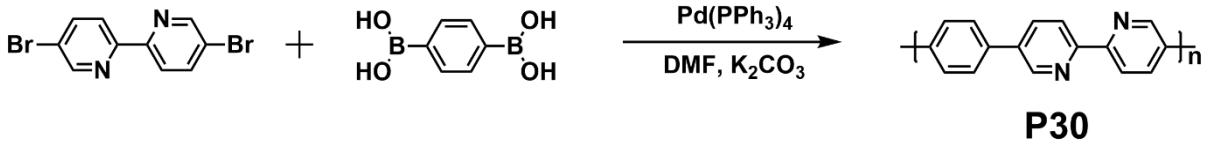

P30

Figure 2.8 Synthesis of P30 via Suzuki-Miyaura-type polycondensation.[16]

5,5′-Dibromo-2,2′-bipyridine (1.26 g, 4.0 mmol), benzene-1,4-diboronic acid (0.663 g, 4.0 mmol), an aqueous solution of K_2CO_3 (12 mL, 2.0 M), *N*,*N*-dimethylformamide (80 mL), and [$Pd(PPh_3)_4$] (60 mg) were added into a flask and degassed by bubbling with N_2 for 30 min. Then the mixture was heated to reflux for three days. After cooling, the crude polymer was poured into water. Next, the mixture was filtered and washed with water, THF and methanol. Next, the material was purified by Soxhlet extraction with chloroform for three days. The product was obtained as a green powder.

2.3.10 Synthesis of P31

P31

Figure 2.9 Synthesis of P31 via Suzuki-Miyaura-type polycondensation.[16]

2-Bromopyridine-5-boronic acid pinacol ester (1.13 g, 4.0 mmol), an aqueous solution of K_2CO_3 (8 mL, 2.0 M), *N*,*N*-dimethylformamide (40 mL), and [$Pd(PPh_3)_4$] (20 mg) were added into a flask and degassed by bubbling with N_2 for 30 min. Then the mixture was heated to reflux for three days. After cooling, the crude polymer was poured into water. Next, the mixture was filtered and washed with water, THF and methanol. Next, the material was purified by Soxhlet extraction with chloroform for three days. The product was obtained as a dark green powder.

2.3.11 Synthesis of P74

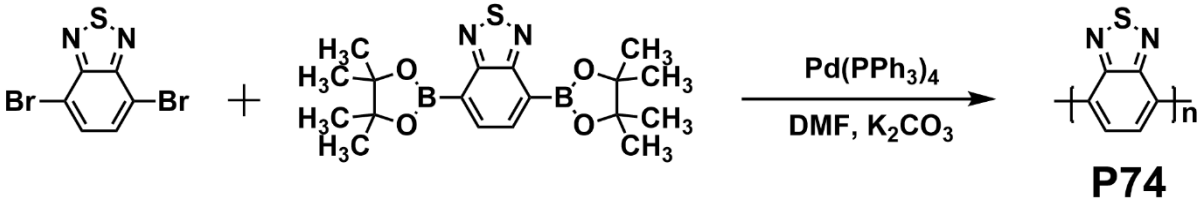

Figure 2.10 Synthesis of P74 via Suzuki-Miyaura-type polycondensation.

4,7-Dibromo-2,1,3-benzothiadiazole (412 mg, 1.4 mmol), 2,1,3-benzothiadiazole-4,7-bis(boronic acid pinacol ester) (543 mg, 1.4 mL), *N*,*N*-dimethylformamide (40 mL) and K_2CO_3 (aqueous, 2 M, 8 mL) were combined and degassed with nitrogen for 30 minutes. Then [$Pd(PPh_3)_4$] (40 mg) was added and the mixture was heated to 150 °C for two days. After cooling to room temperature, the reaction mixture was poured into water. The solids were filtered off and washed with methanol. The polymer was purified using Soxhlet extraction with chloroform to give P74 as a dark powder (387 mg, quant.). Anal. calcd for $(C_6H_2N_2S)_n$: C, 53.72; H, 1.50; N, 20.88%; found C, 49.13; H, 0.95; N, 18.26%

2.3.12 High-throughput CO_2 reduction experiments

Photocatalysts (5 mg), $CoCl_2$ (0.5-10 μmol) and 2,2'-bipyridine (1.0-20 mg) were added into sample vials (V = 12.5 mL) and purged with carbon dioxide in a Sweigher Chemspeed Technologies robotic platform for 3 hours. A liquid handling system transferred water/solvent/hole-scavenger mixture (water/acetonitrile/triethanolamine, 3:1:1, 5 mL) from stock jars inside the system into the sample vials. A capper/crimper tool was then used to seal the vials under the CO_2 atmosphere automatically. All sample vials were ultrasonicated in an ultrasonic bath for 5 minutes before illumination using a solar simulator (AM1.5G, Class AAA, IEC/JIS/ASTM, 1440 W xenon, 12 × 12 in., MODEL:94123A) for the time specified while constantly being redispersed with a rocker/roller device. Samples of gaseous products were analysed using a Shimadzu 2014 HS-GC gas chromatograph equipped with a ShinCarbon ST micropacked column (Restek 80-100 mesh, 2 m length, 0.53 mm inner diameter) and a thermal conductivity detector. All samples were duplicated to ensure reproducibility within a run.

2.3.13 CO_2 reduction experiments

A quartz flask was charged with polymer powder (5 mg), 2,2'-bipyridine (10 mg), cobalt (II) chloride (5 μmol), a mixture of acetonitrile, water and triethanolamine (3:1:1 vol., 25 mL), and sealed with a septum. The resulting suspension was ultrasonicated for 20 minutes and then purged with CO_2 for 30 minutes. The mixture was illuminated by an Oriel Instruments LSH-7320 Solar Simulator (IEC ABA certified) with 1 Sun output. Laser adjustment of the instrument was used to adjust the distance of the reaction flask to the light source. Samples of gaseous products were taken with a gas-tight syringe and run on a Shimadzu GC-2014 gas chromatograph equipped with a ShinCarbon ST micropacked column (Restek 80-100 mesh, 2 m length, 0.53 mm inner diameter) and a thermal conductivity detector. Gases dissolved in the reaction mixture, and the pressure increase generated by the evolved gases were neglected in the calculations.

2.3.14 Determination of external quantum efficiency for CO production

The external quantum efficiencies of CO production were determined using monochromatic LED light (λ = 395, 405, 420, 490 and 515 nm). The reactions were conducted on the same photochemical experimental setup under the optimized reaction conditions. For the experiments, P7-0.1% (1 mg) 2,2'-bipyridine (2 mg) and cobalt (II) chloride (1 μmol) were suspended in acetonitrile, water and triethanolamine (3:1:1 vol. mixture, 5 mL). The illuminated area was 8 cm^2 and the light intensity was measured by a ThorLabs PM100D Power and Energy Meter Console with a ThorLabs S120VC photodiode power sensor. The EQE was calculated using the following equation:

$$EQE\% = 2 \times [(n\ CO) \times N_A \times h \times c)] \times 100\% / (I \times S \times t \times \lambda)$$

Where, N_A is Avogadro constant (6.022×10^{23} mol^{-1}), h is the Planck constant (6.626×10^{-34} J s), c is the speed of light (3×10^8 m s^{-1}), S is the irradiation area (cm^2), I is the intensity of irradiation light (W cm^{-2}), t is the photoreaction time (s), λ is the wavelength of the monochromatic light (m).

2.3.15 Isotopic labelling experiments

$^{13}CO_2$ Labelling experiments were carried on a Bruker Vertex 70V Fourier-transform infrared spectrometer with an argon-purged custom-made gas IR cell. A vial containing the photocatalyst, 2,2'-bipyridine and cobalt (II) chloride in a mixture of acetonitrile/water/triethanolamine (3:1:1) was purged with $^{13}CO_2$ (Sigma-Aldrich, 99 atom % ^{13}C, <3 atom % ^{18}O) for 3 minutes. Then the resulting suspension was illuminated for 1 hour using an Oriel Instruments LSH-7320 Solar Simulator (IEC ABA certified) with 1 Sun output. A sample of the gas headspace (1000 µL) was injected into the gas IR cell, and the IR spectrum was measured (32 scans with a resolution of 0.5 cm^{-1}). The background was measured using Ar purged cell and subtracted from the measurement.

2.4 Methodology for CO_2 reduction by high throughput screening

2.4.1 Test of different experimental conditions

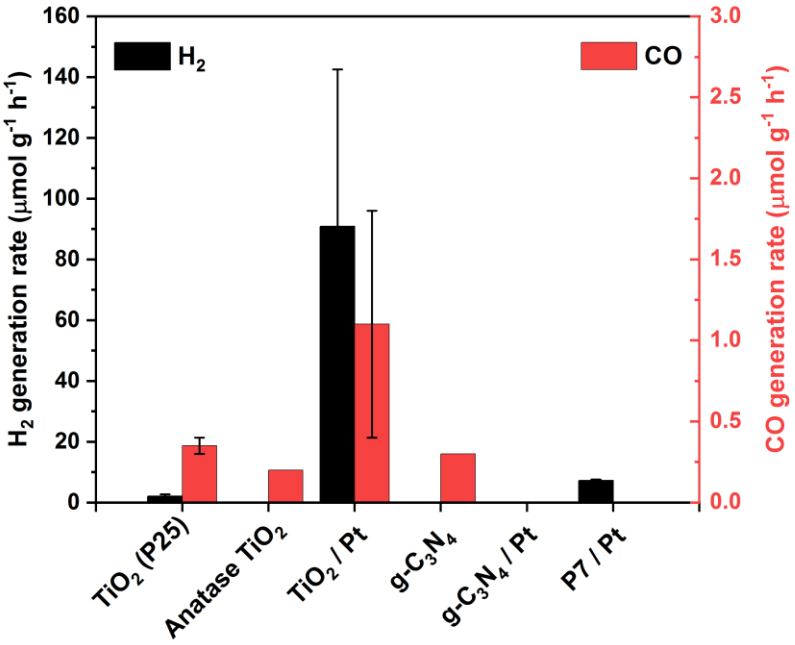

Figure 2.11 Evolution rates of H_2 (left y-axis) and CO (right y-axis) from pure water using different catalysts. Reaction conditions: photocatalyst (5 mg), solution (5.0 mL H_2O). Reaction time: 5 h.

Figure 2.11-2.14 showed the results of commercial photocatalysts and polymers for CO_2 reduction under different experimental conditions with the help of a high throughput system. Every sample was measured twice to minimize the error.

In the pure water experimental condition (Figure 2.11), the production of H_2, CO or CH_4 were very low. Among them, 5% Pt loaded TiO_2 had a relatively good performance. Graphene carbon nitride or g-C_3N_4 with Pt as co-catalyst did not show the presence of gaseous products above the detection limit. The H_2 evolution rate of Pt loaded P7 only achieved 7 μmol g^{-1} h^{-1}. In aqueous systems without additional electrons donors inside, the lifetimes of photo-generated electrons are too short due to the surface or bulk charge recombination of photo-generated electrons. Besides, the solubility of CO_2 in water is quite low. And CO_2 reduction is a more complex and challenging process to realize than hydrogen generation from water. Hence, CO was not detected.

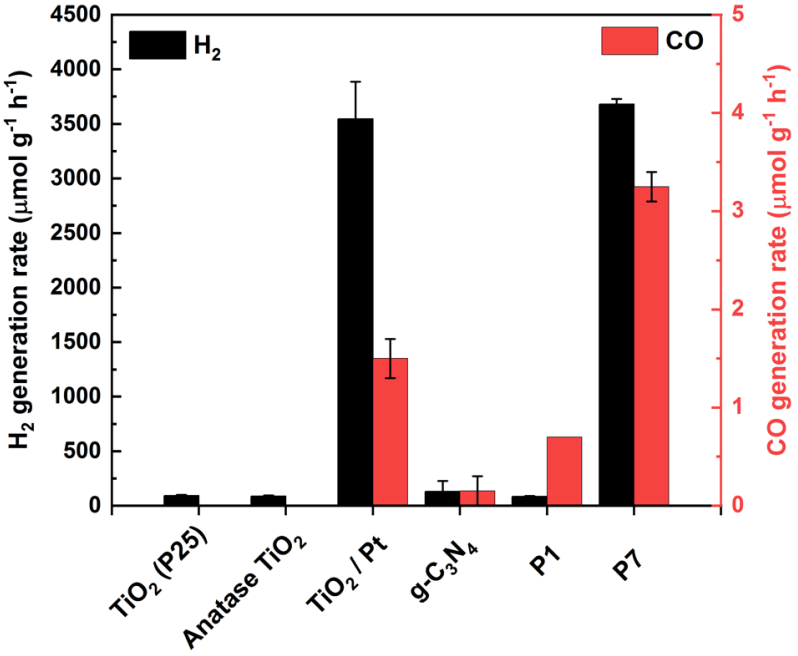

Figure 2.12 Evolution rates of H_2 (left y-axis) and CO (right y-axis) from water with TEOA scavenger. Reaction conditions: photocatalyst (5 mg), solution: 5.0 mL of 4/1 (v/v) H_2O/TEOA. Reaction time: 5 h.

After using TEOA as scavengers in water (Figure 2.12), the rates of H_2 and CO generation increased hugely. The rate of H_2 generation for TiO_2 improved from 2 μmol g^{-1} h^{-1} to 100 μmol g^{-1} h^{-1}. Among the tested photocatalysts, the H_2 evolution rates of TiO_2/Pt and P7 achieved over 3000 μmol g^{-1} h^{-1}. However, the CO_2 conversion results were still not ideal. P25 or anatase TiO_2 could not generate any detectable CO. P1, P7 or g-C_3N_4 produced 0.3, 0.7 and 3.3 μmol g^{-1} h^{-1} of CO, respectively. Interestingly, TiO_2/Pt could produce CO and CH_4 with rates of 1.7 and 2.1 μmol g^{-1} h^{-1} simultaneously. However, the CO generation rate and selectivity were low.

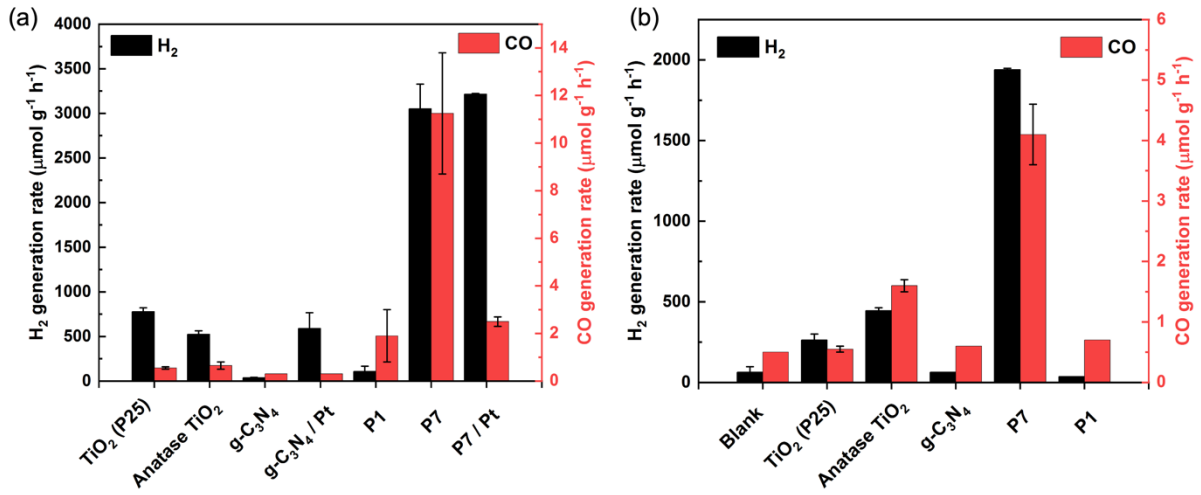

Figure 2.13 (a) Evolution rates of H_2 (left y-axis) and CO (right y-axis) from acetonitrile/water solution with

TEOA scavenger; (b) Results of different photocatalysts in tetrahydrofuran/water mixed solution with TEOA as scavengers. Reaction conditions: photocatalyst (5 mg), 5.0 mL of 3:1:1 (v/v/v) MeCN/H_2O/TEOA or 5.0 mL of 3:1:1 (v/v/v) THF/H_2O/TEOA. Reaction time: 5 h.

Considering the limited solubility of CO_2 in water, organic solvents were tried to increase the amount of dissolved CO_2. Moreover, an appropriate amount of H_2O was added into the reduction system as the resource of protons. Results in Figure 2.13 indicate applying organic solvents (acetonitrile and tetrahydrofuran) could enhance the CO_2 reduction performance. For P7 in acetonitrile, the CO evolution rate was over 13 μmol g^{-1} h^{-1} which was three times than that in THF and water. Even though H_2 evolution rates in MeCN/H_2O system were higher than those in the THF/H_2O system, we chose the MeCN/H_2O system to gain excellent CO evolution rates.

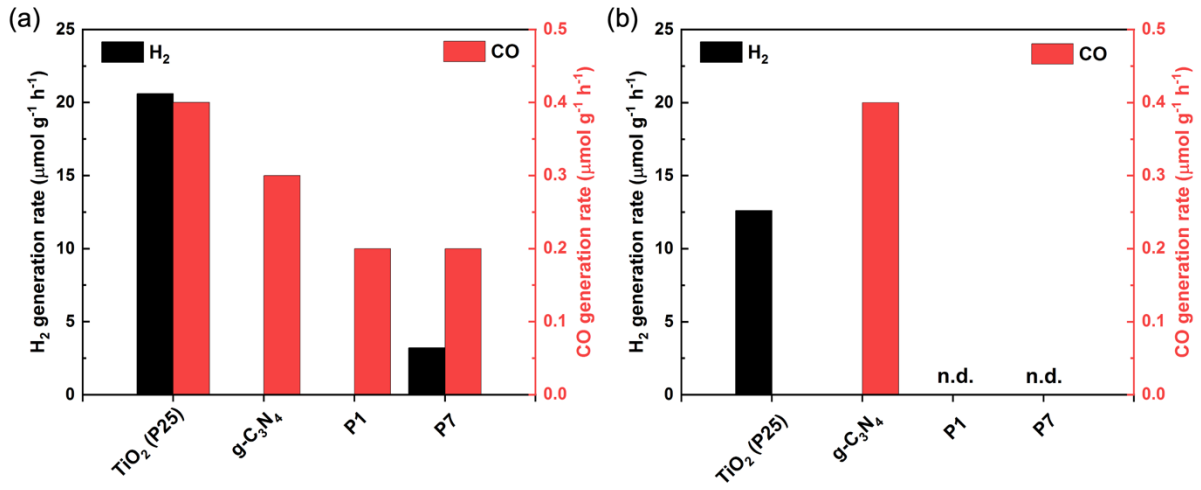

Figure 2.14 Evolution rates of H_2 (left y-axis) and CO (right y-axis) from CO_2 and 0.05 mL water (a) or 0.1 mL water (b). Reaction conditions: photocatalyst (5 mg), 0.05 mL or 0.1 mL H_2O, heat at 90 ℃. Reaction time: 5 h. n.d.: not detectable.

Gas-phase photoreaction was also measured by adding different amounts of water into vials (Figure 2.14). To do CO_2 reduction in the gas-phase, 0.05 mL or 0.1 mL H_2O were added into vials and then heated to 90 ℃ to generate water vapour. With 0.05 mL H_2O, P7 produced 3.23 μmol g^{-1} h^{-1} of H_2 and 0.22 μmol g^{-1} h^{-1} of CO and P1 produced 0.22 μmol g^{-1} h^{-1} of CO but no detected H_2. However, with 0.1 mL H_2O, both P1 and P7 could not produce detectable H_2 or CO. This means that the volume of H_2O has a significant influence on CO_2 reduction. Too

much H_2O would change the reaction system into an aqueous system. TiO_2 showed a similar tendency. TiO_2 produced 20.59 μmol g^{-1} h^{-1} of H_2 and 0.35 μmol g^{-1} h^{-1} of CO with 0.05 mL H_2O but generated 12.64 μmol g^{-1} h^{-1} of H_2 only with 0.1 mL H_2O.

In conclusion, gas-phase photoreactions give better results of selectivity for polymers. However, in such a system, strict requirements are needed for materials because the photocatalysts need to achieve CO_2 reduction reaction and water oxidation reaction simultaneously. To study the CO_2 reduction step by step, we selected liquid-phase with sacrificial electrons donors for investigation first.

2.4.2 Variations of metal doping as cocatalyst

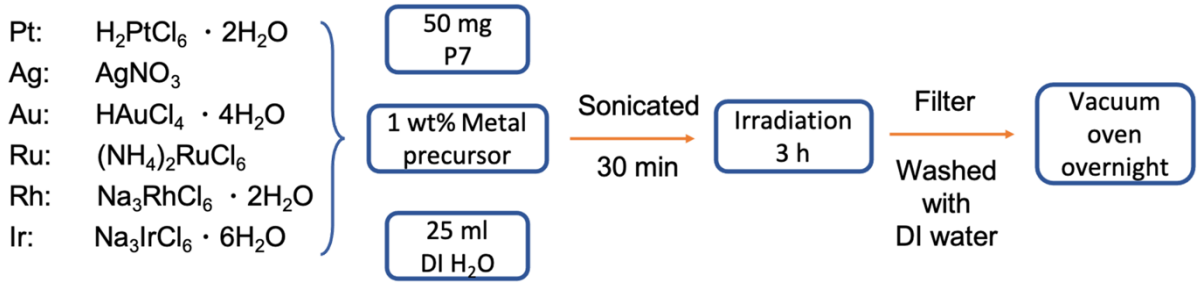

Figure 2.15 Schematic illustration of the synthesis of different metal-nanoparticle-loaded P7

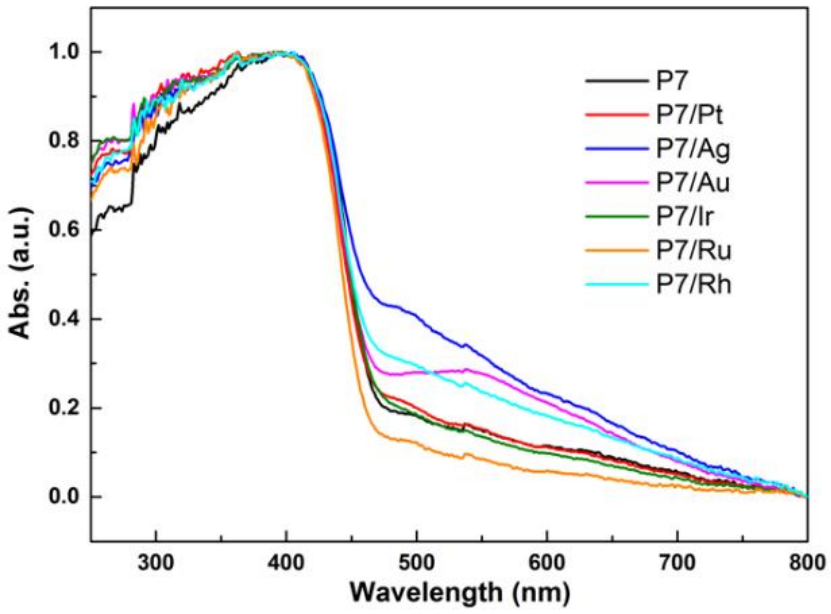

Figure 2.16 UV-vis spectra of P7 as synthesized and loaded with different metal nanoparticles.

As discussed above, the performance of P7 and P7/Pt is not ideal due to the low CO generation

rate and CO selectivity. Finding the right co-catalysts could improve the rate and selectivity of product evolution. In this section, by doping different metals in P7, we tested the influence of variations of metal nanoparticles. Figure 2.15 shows a flow chart of doping different metal nanoparticles in P7 by adjusting the methods in the literature.[17] UV-Visible spectroscopy (UV-Vis) measures the extinction (scatter + absorption) of light passing through a sample. Nanoparticles have unique optical properties that are sensitive to the size, shape, concentration, agglomeration state, and refractive index near the nanoparticle surface, which makes UV-Vis a valuable tool for identifying, characterizing, and studying nanomaterials. UV-vis spectra (Figure 2.16) suggested 5-10 nm red-shifts when loading Ag, Au, Rh, Pt and Ir, but 12 nm blue shifts for Ru which meant the band gap changes. P7 with Ag, Au, Rh, Pt and Ir had a lower band gap than pure P7, but P7/Ru had a bigger band gap. Besides, gold nanoparticles exhibit a distinct feature commonly referred to as localized surface plasmon resonance (LSPR). The collective oscillation of electrons in the conduction band of gold nanoparticles in resonance with a specific wavelength of incident light. LSPPR of Au/P7 results in a strong absorbance band in the 500-600 nm.[18]

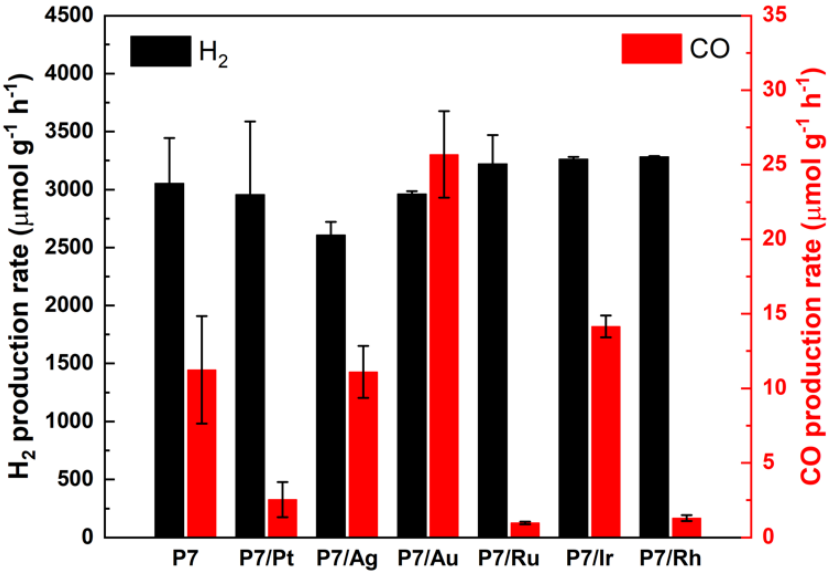

Figure 2.17 Gas evolution rates of H_2 (left y-axis) and CO (right y-axis) of P7 as synthesized and loaded with various metal nanoparticles. Reaction conditions: photocatalyst (5 mg), 5.0 mL of 3:1:1 (v/v/v) MeCN/H_2O/TEOA. Reaction time: 5 h.

From the results shown in Figure 2.17, all the samples had almost the same H_2 generation rates (about 3000 μmol g^{-1} h^{-1}). P7/Au achieved more than 27 μmol g^{-1} h^{-1} and 0.9 % selectivity for

CO evolution rate which suggested gold nanoparticles were the best co-catalyst compared with other metal nanoparticles. However, both the rate and selectivity were relatively low. The different metal-nanoparticle-loaded P7 needs to be prepared in advance and the yield is limited which cannot meet the need for high-throughput experiments. Moreover, noble metal-based cocatalysts are not suitable for future industrial-scale applications for CO_2 reduction due to their scarcity and high price.[19] It is still needed to find other efficient and selective co-catalysts such as molecular co-catalyst with different conjugated polymers for high throughput screening CO_2 reduction experiments.

2.4.3 Molecular co-catalyst

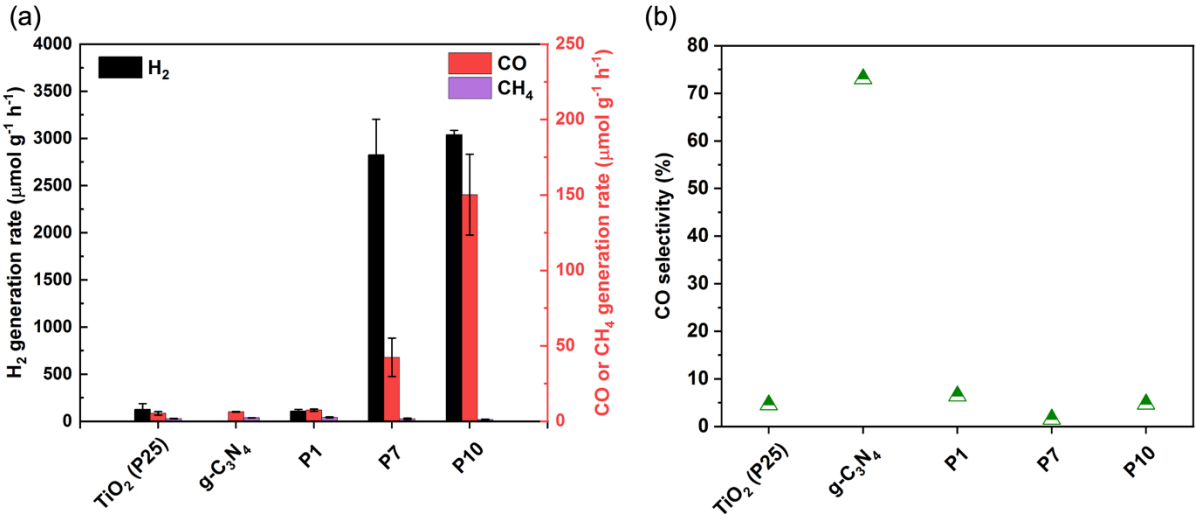

Figure 2.18 (a) Gas evolution rates of H_2 (left y-axis) and CO or CH_4 (right y-axis) of different photocatalysts with $Co(bpy)_3^{2+}$; (b) CO selectivity of different photocatalysts with $Co(bpy)_3^{2+}$. Reaction conditions: photocatalyst (5 mg), bpy (2 mg), $CoCl_2$ (0.001 μmol), 5.0 mL of 3:1:1 (v/v/v) MeCN/H_2O/TEOA. Reaction time: 5 h.

In 2013, Xinchen Wang and his colleagues introduced $[Co(bpy)_n]^{2+}$ acting as a solution-based molecular co-catalyst, the g-C_3N_4 hybrid system achieved good CO_2 conversion performance.[20] Besides, in 2016, Walsh et al. investigated g-C_3N_4 with $[Co(bpy)_n]^{2+}$ as a cocatalyst for photocatalytic CO_2 reduction.[21] Many other semiconductors such as CdS, conjugated polymers or $ZnIn_2S_4$–In_2O_3 were reported for CO_2 reduction by using $[Co(bpy)_3]^{2+}$ as a cocatalyst.[3,22,23] These works provided an easy and efficient strategy to enhance CO_2 reduction ability.

Initially, 0.001 μmol cobalt (II) chloride ($CoCl_2$) and 2 mg bpy were added into the

photoreduction experimental system. Following this strategy, various photocatalysts including several excellent hydrogen evolution photocatalysts were tested (Figure 2.18). It is noted that both the CO production and selectivity of g-C_3N_4, TiO_2, P1 and P7 increased significantly when $CoCl_2$ and bpy were added. 100 μmol g^{-1} h^{-1} CO was produced by P10 which was almost two times than that of P7. For selectivity of CO, g-C_3N_4 reached more than 70% while P7 and P10 could afford 2% and 5%. In the absence of $[Co(bpy)_3]^{2+}$, the CO_2 reduction performance was not satisfactory. All the results revealed that $[Co(bpy)_3]^{2+}$ could be an effective and efficient CO_2 reduction co-catalyst for polymer photocatalysts. Moreover, the system containing cobalt complexes can be easy prepared for high throughput screening. Hence, we use $[Co(bpy)_3]^{2+}$ as a cocatalyst for further high throughput experiments.

2.4.4 Extraction of palladium in P7

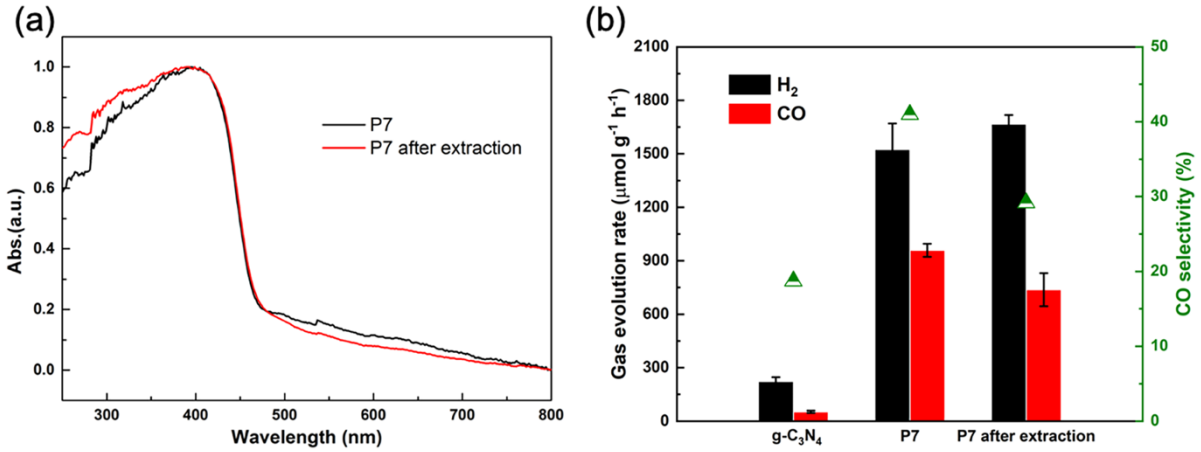

Figure 2.19 (a) UV-vis spectra of P7 and P7 after extraction; (b) CO selectivity and yield of H_2 and CO of g-C_3N_4, P7 and P7 after extraction. Reaction conditions: photocatalyst (5 mg), bpy (2 mg), $CoCl_2$ (1 μmol), 5.0 mL of 3:1:1 (v/v/v) MeCN/H_2O/TEOA. Reaction time: 5 h.

The results from P7 with different noble metal doping indicated the influence of different metal cocatalysts for CO generation. Besides, it is known that palladium residue in the final polymer cannot be avoided when carrying out Pd(0)-catalyzed Suzuki-Miyaura polycondensation. Pd also acts as a co-catalyst for photocatalytic CO_2 conversion. The effect of noble metal co-catalysts was examined and it was found that the rate of CH_4 formation from TiO_2 increased in the sequence of Ag < Rh < Au < Pd < Pt, corresponding well to the increase in the efficiency

of electron-hole separation.[24] However, the reduction of H_2O to H_2 was accelerated more than the reduction of CO_2 with Pd as a cocatalyst for TiO_2, leading to a lower selectivity for CO_2 reduction.[24] In this case, it is necessary to investigate the effect of residual Pd in polymers. To do this, 100 mg P7 was put in 50 mL sodium diethyldithiocarbamate solution (0.05M), and the suspension was stirred at 65 ℃ overnight. After that, P7 was washed with DI water and methanol several times. Finally, the obtained P7 was dried in a vacuum at 80 ℃ overnight. A slight difference was noticed in the UV-vis spectra (Figure 2.19a). The CO_2 reduction performance of P7, P7 after extraction and g-C_3N_4 were tested under the optimized experimental conditions. P7 before and after the extraction showed no significant changes in their photocatalytic performance (Figure 2.19b). More than 1400 μmol g^{-1} h^{-1} of H_2 and 650 μmol g^{-1} h^{-1} of CO were generated in both P7 before and after the extraction. Considering the yield of CO and selectivity for CO over H_2, P7 achieved better results than commercial g-C_3N_4 (200 μmol g^{-1} h^{-1} of H_2, 47 μmol g^{-1} h^{-1} of CO, 18% CO selectivity). However, the performance of P7 was not good due to the low selectivity of CO, demonstrating the Pd residuals were hard to be removed.

2.5 High-throughput screening of conjugated polymers

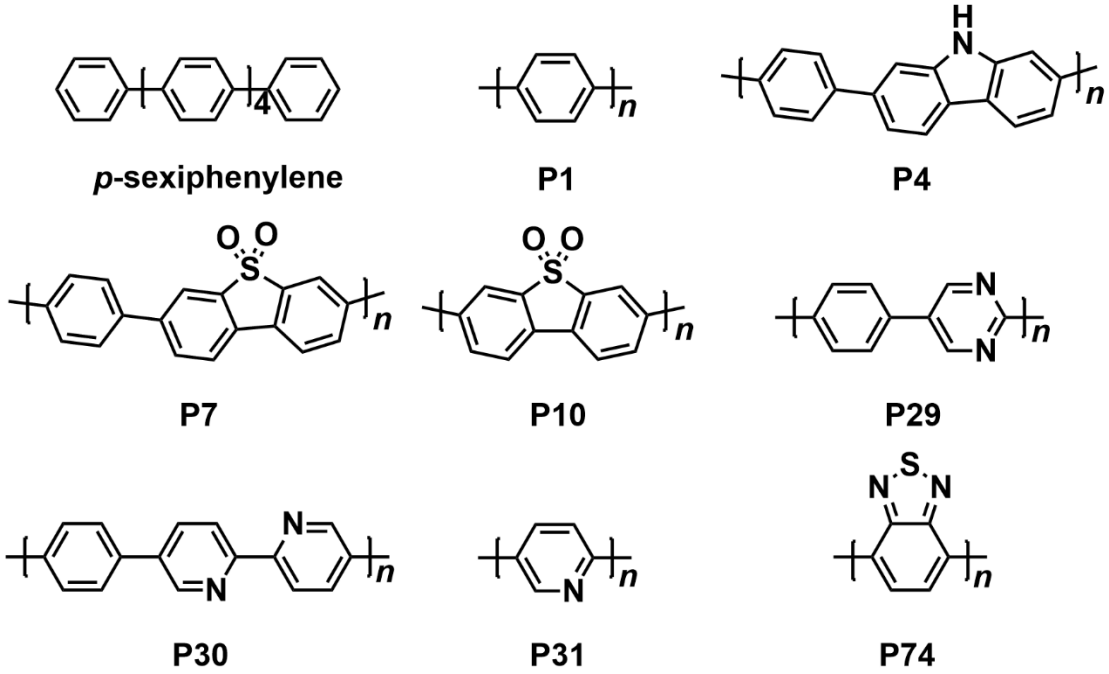

Figure 2.20 Structures of the photocatalysts.

The aim of this section is to explore whether a single photocatalyst could generate both H_2 and CO and the H_2:CO ratio could be controlled. To do this, a series of conjugated polymers was synthesized via Suzuki-Miyaura polycondensation using Pd(0), which leads to the presence of residual palladium particles within the material (Figure 2.20). The residual palladium has been demonstrated to act as a co-catalyst for hydrogen production from water in previous literature.[25–27] Here, a range of photocatalysts was investigated: *p*-sexiphenylene,[28] poly(*p*-phenylene) (P1),[14] a carbazole-phenylene co-polymer (P4),[14] a dibenzo[*b*,*d*]thiophene sulfone co-polymer (P7),[14,15] the homopolymer of dibenzo[*b*,*d*]thiophene sulfone (P10),[15] a pyrimidine-phenylene co-polymer (P29),[16] a bipyridine-phenylene co-polymer (P30),[16] poly(pyridine) (P31),[16] and poly(benzothiadiazole) (P74).

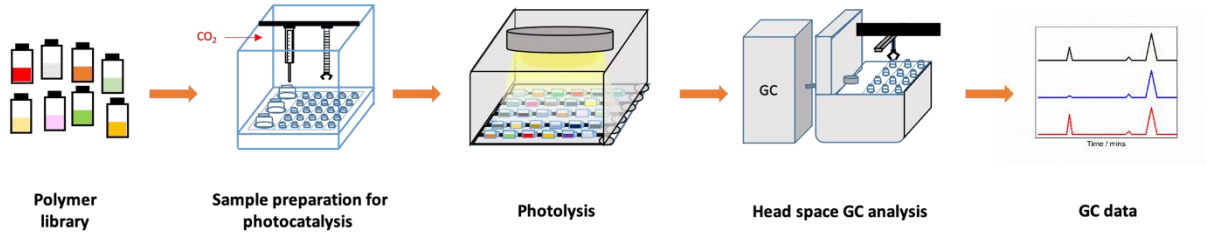

Figure 2.21 Workflow for high-throughput property screening of conjugated polymers.[29]

The high-throughput workflow used here for screening HER photocatalysts has been reported (Figure 2.21).[29,30]. All the polymers were measured as photocatalysts for CO_2 reduction under solar irradiation with such a workflow. To do high-throughput screening of photocatalytic CO_2 reduction, vials (V = 12.5 mL) were firstly charged with photocatalysts (5 mg), $CoCl_2$ (1 μmol), which acts as the co-catalyst, and 2,2'-bipyridine (bpy, 2 mg), which is required to form catalytically active Co centres.[9,20–22,31]

After transferring vials into a liquid handling robot, the system was closed and purged for three hours with CO_2. The liquid handler then added water (1 mL), acetonitrile (MeCN, 3 mL), acting as an inert co-solvent, and triethanolamine (TEOA, 1 mL), which acts as the hole scavenger, before capping the vials. After capping, the samples were sonicated to disperse the photocatalysts and transferred to a solar simulator (AM1.5G, 1600 W xenon light source, air mass 1.5G filter, 350−1000 nm). The samples were irradiated with constant agitation for a specific time. The gaseous products were measured using an automated gas chromatograph.

2.6 CO_2 reduction results of linear polymers by high-throughput screening

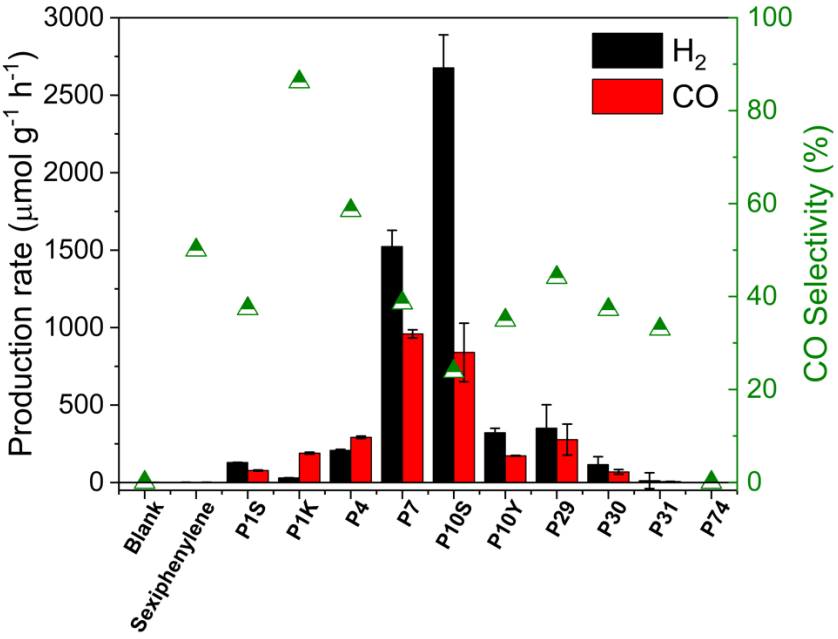

Figure 2.22 Evolution rates and selectivity of gaseous products produced by all photocatalysts in a high-throughput screening. Conditions: polymers (5 mg), $CoCl_2$ (1 μmol), 2,2'-bipyridine (2 mg), solvent (4 mL, MeCN/H_2O=3:1), TEOA (1 mL), solar simulator (5 hours), CO_2 atmosphere.

Table 2.1 Evolution rates of gaseous products for high-throughput screening polymer photocatalysts.

Photocatalyst	H_2 Evolution rate (μmol g^{-1} h^{-1})[a]	CO Evolution rate (μmol g^{-1} h^{-1})[a]	CO selectivity (%)[b]
Blank	-[c]	0.8 ± 0.6	-[c]
***p*-Sexiphenylene**	1.0 ± 0.9	1.0 ± 0.6	50.0
P1S	129.8 ± 0.6	77.7 ± 3.5	37.4
P1K	30.3 ± 0.8	189.7 ± 6.3	86.2
P4	207.4 ± 6.7	291.9 ± 8.0	58.5
P7	1523.7 ± 104.0	959.1 ± 26.3	38.6
P10S	2575.6 ± 64.2	156.5 ± 6.4	5.7
P10Y	321.6 ± 28.0	172.4 ± 2.2	34.9
P29	351.0 ± 150.9	276.9 ± 100.4	44.1
P30	115.9 ± 51.0	68.8 ± 15.0	37.2
P31	12.3 ± 0.4	6.1 ± 1.7	33.0
P74	-[c]	0.3 ± 0.1	-[c]

[a] Average of two runs. Conditions: polymers (5 mg), $CoCl_2$ (1 μmol), 2,2'-biyridine (2 mg) solvent (4 mL, MeCN / H_2O=3:1), TEOA (1 mL), solar simulator (5 h), GC-TCD Headspace; [b] Selectivity = $\frac{n_{CO}}{(n_{CO}+n_{H_2})} \times 100\%$; [c] Not detected.

Under the experimental conditions, it was found that *p*-sexiphenylene, P31 and P74 showed little or no activity for either CO or H_2 generation (Figure 2.22 and Table 2.1). Photocatalysts P1, P4, P29, and P30 all generated CO with rates between 68.8 μmol g^{-1} h^{-1} for P30 and 291.9 μmol g^{-1} h^{-1} for P4 and selectivities between 37% for P30 and 59% for P4 due to large amounts of H_2 were produced by P1, P4, P29, and P30. Significantly, both P7 and P10 indicated much higher CO production with a rate of 959.1 μmol g^{-1} h^{-1} and 839.7 μmol g^{-1} h^{-1}. However, the high CO generation rates of P7 and P10 are accompanied by a high H_2 evolution rate of 1523.7 μmol g^{-1} h^{-1} for P7 and an even

higher H_2 evolution rate of 2676.3 μmol g^{-1} h^{-1} for P10, which is in line with the observation that P10 is a better hydrogen evolution photocatalyst than P7.[15]

It seems that the high hydrogen evolution rates do not originate from oxidative dehydrogenation of TEOA as a side reaction.[20] This may be explained by the presence of residual palladium, which acts as an efficient co-catalyst for proton reduction[26,27] competing with cobalt sites for electrons. Moreover, the kinetics of CO_2 reduction is sluggish, resulting in poor CO production selectivity compared with other materials. No other products, such as methane, methanol, acetaldehyde or formate, were detected by gas chromatography and ion chromatography. To further demonstrate the role of palladium in the proton reduction reaction, poly(*p*-phenylene) (P1K) that contains residual nickel (a poorer hydrogen evolution co-catalyst) was made via nickel-catalyzed Kumada polycondensation. Results showed that P1K has a higher CO evolution rate compared to P1 made via Suzuki−Miyaura polycondensation (189.7 *vs* 77.7 μmol g^{-1} h^{-1}), and a higher selectivity for CO production (86% *vs* 37%). Similarly, P10 synthesized *via* Yamamoto coupling (P10Y) has a higher selectivity for CO over H_2 compared to the Suzuki-Miyaura polycondensation product (35% vs 24%).

These observations indicate that residual palladium plays a negative role on CO/H_2 selectivity. In line with this, literature reports of photocatalysts with good selectivities are generally synthesized by using metal-free experimental conditions thus leading to photocatalysts that have no residual metal present that facilitate hydrogen production.[7] However, several systems with photocatalysts that were made using Pd-catalysed cross-coupling reactions have been proven by other researchers to generate CO with good selectivity over H_2 despite their Pd-content.[3]

2.7 Analysis of linear polymers for CO_2 reduction

From the previous work on HER photocatalysts, it is known that the performance of photocatalysts will be affected by the polymers' optical properties (optical gap, the onset of light absorption), electronic properties, and the dispersibility of the catalyst in the reaction medium.[32] These factors might also drive the difference of CO/H_2 selectivity. It is noted that one or more of these properties result in oligomers and polymers with low activity.

2.7.1 Redox potentials and band gaps

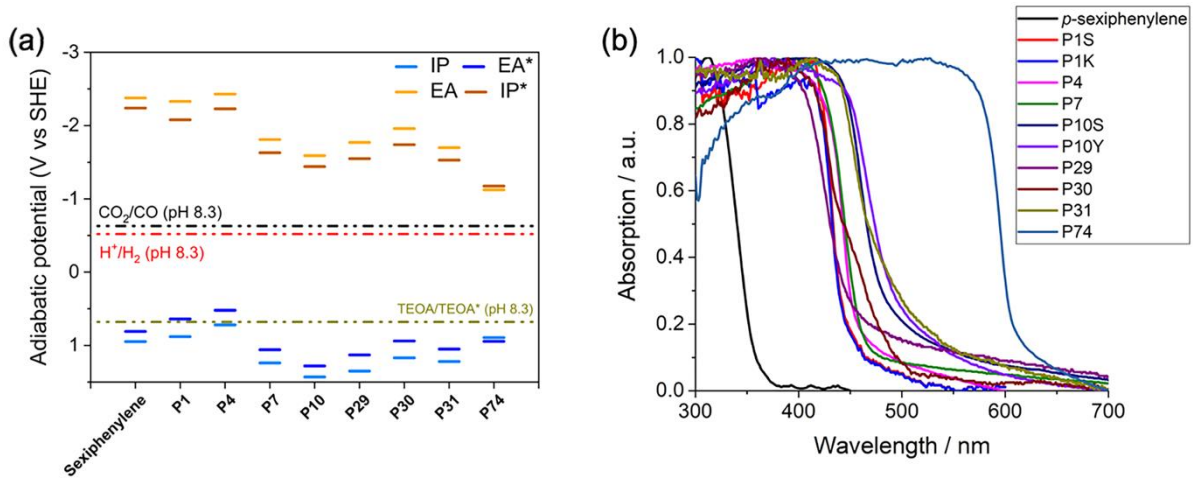

Figure 2.23 (a) Predicted redox potentials of the polymer photocatalysts taken from the literature (P1-P31)[14–16,33] or calculated in this study (P74) and solution potentials (CO_2 and proton reduction, TEOA oxidation) at pH 8.3 (the pH of the reaction mixture saturated with CO_2); (b) UV-Vis Spectra of all photocatalysts in this study measured in the solid-state.

Table 2.2 IP, EA, IP* and EA* values of polymer P74.

	IP / V	**EA / V**	**IP* / V**	**EA* / V**
P74[a]	0.89	-1.12	-1.17	0.94

[a] Calculated for an oligomer of 12 monomer units long with B3LYP/DZP/COSMO (ε_r 80.1).

Table 2.3 Predicted redox solution potentials for the oxidation of TEOA at pH 0 and pH 8.3 relative to the Standard Hydrogen Electrode.

	E / V	
	pH 0	pH 8.3
DEOA (aq) + ET (aq) + 2 H^+ (aq) + 2 e^- -> TEOA (aq) + 2 H_2O (l)	0.03	-0.46
$TEOA^{\cdot}$ (aq) + H^+ (aq) + e^- -> TEOA (aq)	1.20	0.71
$TEOA^+$ (aq) + e^- -> TEOA (aq)	0.67	0.67

DEOA diethanolamine, ET 1,1,2-ethanetriol, $TEOA^{\cdot}$ triethanolamine radical ($N(CH_2CH_2OH)_2(CH{\cdot}CH_2OH)$).

Calculations were performed to predict redox potentials of the polymers. The driving forces for CO_2 reduction and oxidation of TEOA were estimated by comparing the potentials for CO_2 reduction and oxidation of TEOA with the electron affinities (EA) and the ionisation potentials (IP) of the polymers. Among the polymers, *p*-Sexiphenylene, P1 and P4 have the least positive IP values, which controls the driving force for the oxidation of TEOA. Thus, they have the smallest driving force for the one-hole oxidation of TEOA (Figure 2.23a). P74 is a new reported polymers and the redox potential was calculated in Table 2.2. However, P74 has the least negative EA value (electron affinity; that is, the LUMO) of -1.12 V and hence the smallest driving force for proton or CO_2 reduction. P10 which has a similar structure with P7 has particularly poor CO selectivity. The reason is that the EA of P10 is less negative than for P7[15] (Figure 2.23a). Therefore, P10 has a reduced thermodynamic driving force for reduction potential relative to P7. It is known that CO_2 reduction is thermodynamically slightly less favoured than the reduction of protons. Potentials of oxidation of TEOA (Table 2.3) were calculated under the assumption that oxidation takes place on or near the nitrogen atom rather than one of the OH groups, and that the 2-electron overall oxidation products of TEOA are diethanolamine and 1,1,2-ethanetriol, *i.e.* that the glycolaldehyde formed instantaneously hydrolyses to 1,1,2-ethanetriol. The experimentally measured pH of the reaction mixture saturated with CO_2 is 8.3. In such conditions, $E(CO_2,H^+/CO)$ and $E(H^+/H_2)$ vs. the standard hydrogen electrode are -0.63 V[34] and -0.52 V, respectively. Hence, we believed that the reduction in driving force has a more significant impact on CO_2 reduction.

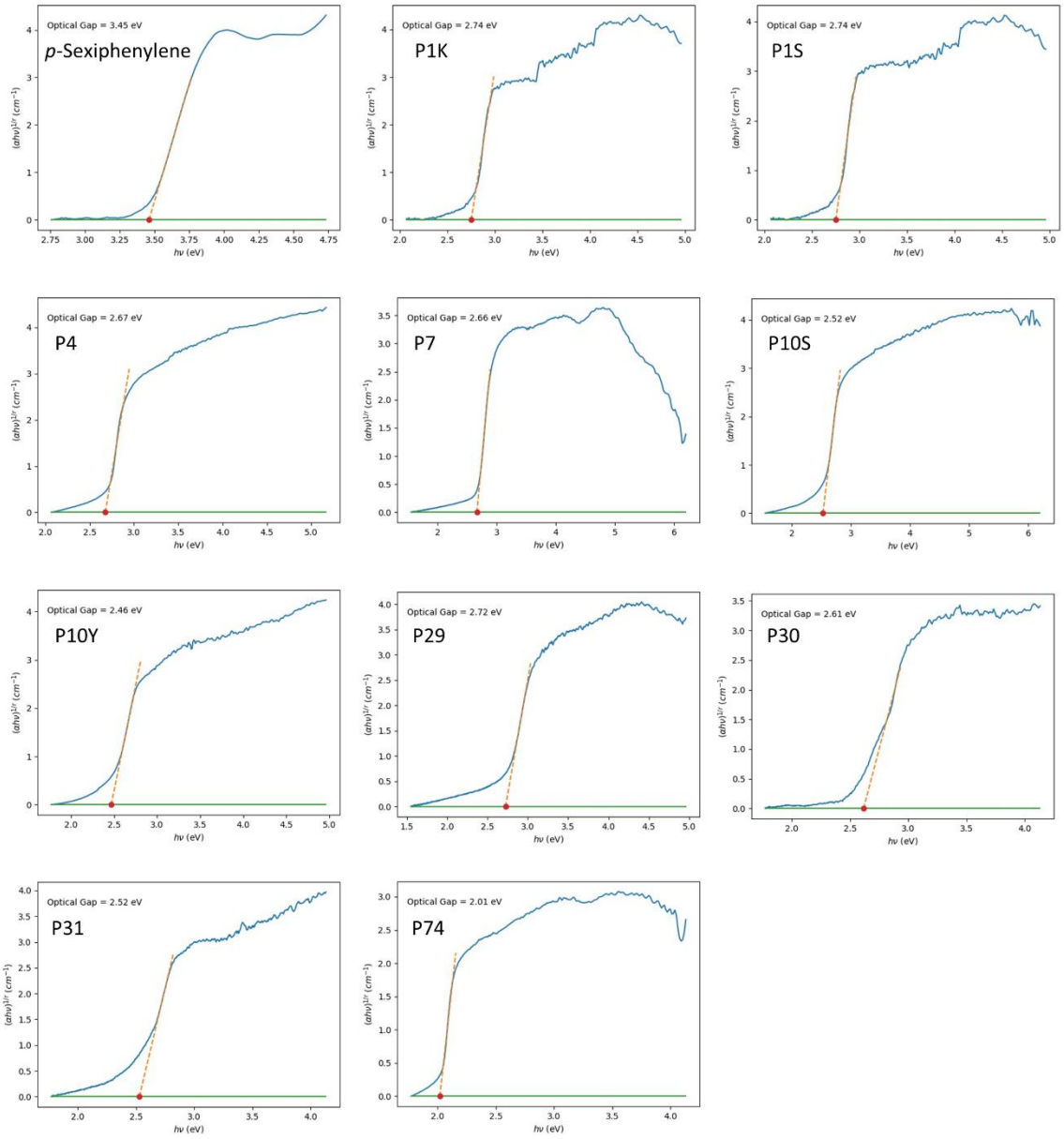

Figure 2.24 Tauc plots for all photocatalysts in this section.

Table 2.4 Optical properties of photocatalysts.

Photocatalysts	Sexiphenylene	P1K	P1S	P4	P7	P10S	P10Y	P29	P30	P31	P74
Optical gap / eV	3.45	2.74	2.74	2.67	2.66	2.52	2.46	2.72	2.61	2.52	2.01

Light absorption ability is believed to be one factor that influences CO_2 reduction performance. Band gaps (E_g) of organic semiconductors materials are the difference between the highest occupied molecular orbital (HOMO) and the lowest unoccupied

molecular orbital (LUMO) energy levels in the polymers. As we discussed in **Chapter 1**, electron-hole pairs in the bulk of semiconductor materials are generated by absorbing photons with an energy equal to or greater than the band gap.

The Tauc method (Figure 2.24) can be used as an easy and straightforward method to accurately estimate band gap energies from UV-vis spectra. The equation of Tauc plot is shown below:

$$(\alpha h\nu)^{1/n} = A\left(h\nu - E_g\right)$$

Where α is the absorption coefficient of the material, h is the Planck constant, ν is the photon's frequency, E_g is the band gap energy, and A is a constant. The n factor is equal to 1/2 or 2 for the direct and indirect transition band gaps, respectively.[35]

From the UV spectra (Figure 2.23b) and band gap (Table 2.4), *p*-Sexiphenylene and P1 have the most blue-shifted optical gaps, limiting visible light absorption ability. Other linear polymers have suitable optical gaps for the absorption of visible light; however, some of them still have limited CO_2 reduction performance. The influences of EA and IP values for driving CO_2 reduction have been discussed above. The materials should have suitable bandgap for visible light absorption and enough driving force for CO_2 reduction and oxidation of TEOA.

2.7.2 Dispersibility

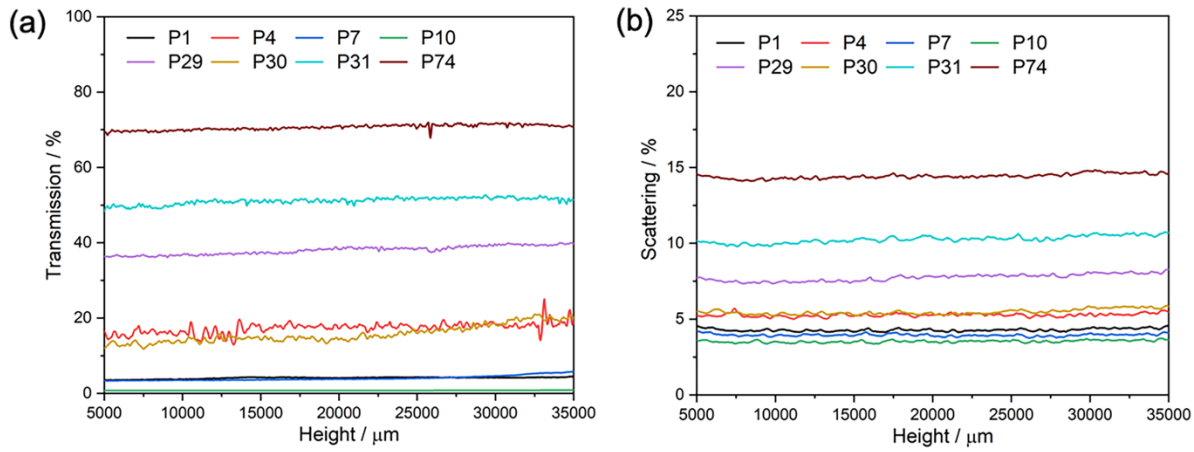

Figure 2.25 (a) Transmission experiments of photocatalysts suspended in MeCN/H_2O/TEOA mixture (3/1/1). The transmission of suspensions was measured at 180° relative to the light source; (b) Backscattering experiments of photocatalysts suspended in MeCN/H_2O/TEOA mixture (3/1/1). The backscattering of the suspensions was measured at 45° relative to the light source.

Here, we supposed that the dispersibilities of polymers as another factor that impacts CO_2 reduction performance. Transmission and backscattering experiments were involved for further investigation. Transmission and backscattering experiments in Figure 2.25a and 2.25b are measurements of how well a polymer disperses in the reaction medium for CO_2 reduction. The transmittance and backscattering of the suspensions were measured with a laser for scanning the height of the measurement reactor at 180° and 45° relative to the light source. Before the measurements, samples were dispersed in 20 mL MeCN/H_2O/TEOA mixture and sonicated for 15 minutes. Then, the transmission and backscattering of the suspensions were measured in cylindrical glass cells from 5000 to 35,000 μm every 40 μm. The suspensions appear to be stable for the duration of the measurement as the transmission and backscattering values are similar for the entire height of the measurement reactor, with low transmission values in both cases showing that a material disperses well in a MeCN/H_2O/TEOA mixture. From the results (Figure 2.25), P29, P31 and especially P74 disperse very poorly in the reaction mixture. The poor dispersibility of these polymers may result from their wettability and physical density,[36] which will influence interaction between polymers

and cocatalysts and their activity for CO_2 product generation. P7 and P10, which disperse well in the reaction mixture and have the most positive IP values and the largest driving force for TEOA oxidation, are the most active materials. Also, especially for P10, these two polymers absorb a significant part of the visible spectrum. Considering its CO generation rate and selectivity, P7 was chosen as a good photocatalyst for CO_2 reduction for the remaining experiments.

2.7.3 Time-correlated single photon counting (TCSPC) measurements

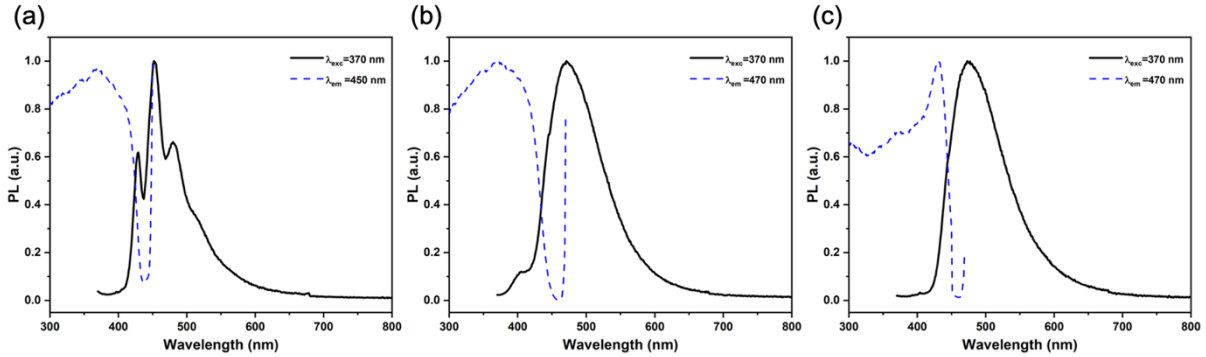

Figure 2.26 (a) Fluorescence emission and excitation spectra of P1 in acetonitrile, water and triethanolamine (3/1/1) solution; (b) Fluorescence emission and excitation spectra of P7 in acetonitrile; (c) Fluorescence emission and excitation spectra of P7 in acetonitrile, water and triethanolamine (3/1/1) solution.

The lifetime of excited states is believed to be crucial in letting charges to be separated before recombination. To investigate the kinetics of the excited states of P1 and P7, time-correlated single photon counting (TCSPC) was involved. The optoelectronic properties of P1 and P7 were first measured by photoluminescence (PL) spectroscopy in Figure 2.26 with an excitation wavelength of 370 nm. λ_{max} at 453 nm was observed for P1 in acetonitrile, water and triethanolamine (3/1/1) solvent. λ_{max} at 475 nm was detected for P7 in pure acetonitrile or acetonitrile/water/triethanolamine (3/1/1) solvent mixture. The lifetimes of the excited states of P1 and P7 were studied by TCSPC experiments upon excitation at λ_{exc} = 370 nm with a laser and observed at λ_{em} = 453 and 475 nm.

Table 2.5 Fluorescence life-time measurements.

Materials	λ_{em} / nm	τ_1 / ns	B_1 / %	τ_2 / ns	B_2 / %	τ_3 / ns	B_3 / %	χ^2	τ_{AVG}
P7[a]	475	0.23	31.95	0.91	43.57	2.67	24.48	1.05	1.13
P7[b]	475	0.22	32.06	0.90	43.33	2.57	24.61	1.09	1.05
P7[c]	475	0.14	35.72	0.66	40.89	2.05	23.39	1.10	0.80
P7[d]	475	0.24	30.70	0.89	46.57	2.93	22.73	1.04	1.15
P1[c]	453	0.20	64.04	0.64	27.85	2.35	8.11	1.18	0.50
P1[d]	453	0.16	71.17	0.54	22.05	2.10	6.78	1.28	0.37

[a] Acetonitrile purged with N_2; [b] Acetonitrile purged with CO_2; [c] Acetonitrile water and triethanolamine (3/1/1) purged with N_2; [d] Acetonitrile water and triethanolamine (3/1/1) purged with CO_2; [d] Fluorescence lifetimes obtained upon excitation at λ_{exc} = 370 nm with a laser and observed at λ_{em} = 453, 475 nm.

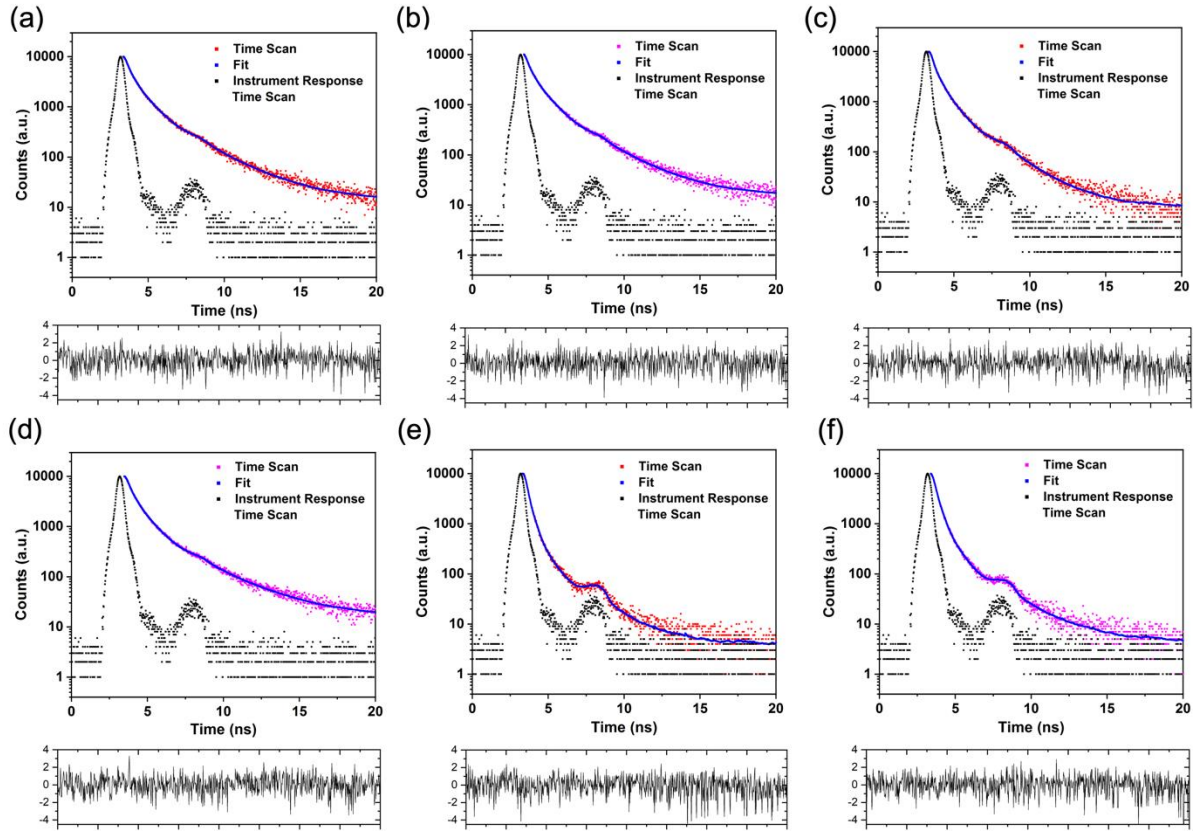

Figure 2.27 Fluorescence lifetime decays of P7 in MeCN purged with N_2 (a) or CO_2 (b) and MeCN/H_2O/TEOA (3/1/1) mixture purged with N_2 (c) or CO_2 (d) (λ_{exc} = 370 nm, λ_{em} = 475 nm) and P1 in MeCN/H_2O/TEOA (3/1/1) mixture purged with N_2 (e) or CO_2 (f) (λ_{exc} = 370 nm, λ_{em} = 450 nm).

Figure 2.27 is the fluorescence life-time decay of P1 and P7 measured in different testing conditions. The red and pink dots are the experimental data. Blue lines represent the fit and the black lines under the figures are weighted residuals of the fit. The instrument responses are shown as black dots. Fluorescence life-times (Table 2.5) in solvent suspension were obtained from fitting time-correlated single photon counting decays (Figure 2.27) to a sum of three exponentials, which yield τ_1, τ_2, and τ_3 according to $\sum_{i=1}^{n}(A + B_i \exp(-\frac{t}{\tau_i}))$. τ_{avg} is the weighted average lifetime calculated as $\sum_{i=1}^{n} B_i \tau_i$. The goodness-of-fit parameter by using chi-squared (χ^2) value is at a minimum by varying B_i and τ_i. Note that the poor χ^2 values are due to ultrafast decays for these materials which were very similar to the instrument response.[37] The average weighted photoluminescence emission lifetime (Table 2.5) of P7 (τ_{avg} = 1.13 ns, λ_{em} = 475 nm) in MeCN purged with N_2 was similar with that (τ_{avg} = 1.05 ns, λ_{em} = 475 nm) in MeCN purged with CO_2. When measured in MeCN / H_2O / TEOA suspension, the average emission lifetime of P7 (τ_{avg} = 0.80 ns, λ_{em} = 475 nm) was longer than that of P1 (τ_{avg} = 0.5 ns, λ_{em} = 453 nm). The different lifetimes for P1 and P7 indicated the various capability for charge stabilization. The longer lifetime of P7 in solvent mixture was also in line with the observed higher activity. However, the exciton lifetime is just one of the influencing factors, and it does not always correlate with the activity.[38] The final performance is affected by different factors. Here, it was demonstrated that extending the excited state lifetime could increase the efficiency of CO_2 reduction by P7. P7 was further explored due to its suitable optical properties, electronic properties, dispersibility, and CO generation performance.

2.8 Optimization of cocatalyst and conditions

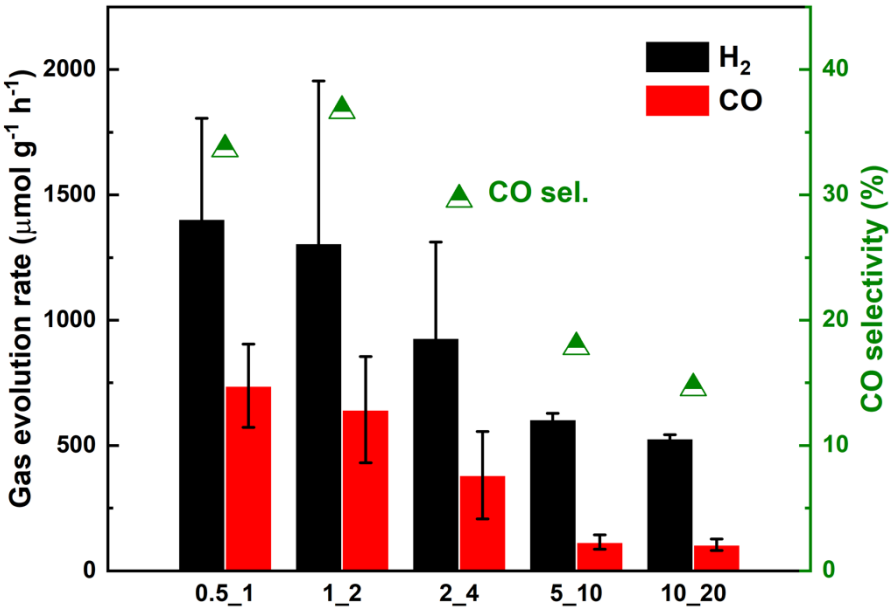

Figure 2.28 CO selectivity and yield of H_2 and CO over P7 with the same ratio of $CoCl_2$ and bpy. Conditions: P7 (5 mg, 0.155 wt. % Pd), solvent (4 mL, MeCN / H_2O=3:1), TEOA (1 mL), solar simulator (5 hours).

Table 2.6 Gas evolution rates of gaseous products of P7 with $CoCl_2$ and bpy at a constant relative ratio.

Entry	$CoCl_2$ (μmol)	bpy (mg)	H_2 Production rate (μmol g^{-1} h^{-1})	CO Production rate (μmol g^{-1} h^{-1})	Selectivity for CO production (%)	$n(H_2)$: $n(CO)$
1[a]	0.5	1	1403.6 ± 284.3	738.3 ± 117.3	34.5	1.9 : 1
2[a]	1	2	1307.3 ± 457.4	642.7 ± 150.1	33.0	2.0 :1
3[a]	2	4	928.9 ± 270.7	381.7 ± 123.4	29.1	2.4 : 1
4[a]	5	10	604.6 ± 16.8	114.7 ± 20.4	15.9	5.3 : 1
5[a]	10	20	528.0 ± 10.9	104.1 ± 15.9	16.5	5.1 : 1

Conditions: P7 (5 mg, 0.155 wt. % Pd), solvent (4 mL, MeCN / H_2O=3:1), TEOA (1 mL), CO_2 atmosphere, solar simulator (5 hours).

Next, P7 (5 mg) with different amounts of $CoCl_2$ and bpy were explored in a high-throughput screening experiment to find the optimized conditions for CO_2 reduction. Various ratios of $CoCl_2$ and Bpy were added into vials. The liquid handling system

transferred degassed jars with acetonitrile/triethanolamine/water mixture into sample vials. After being purged with CO_2 for 3 hours and then capped with a capper tool, vials were taken out and sonicated for several minutes. Finally, vials were irradiated under a 1600 W xenon light source (air mass 1.5 G filter, 350−1000 nm) on a Stuart roller bar SRT9. A Shimadzu 2014 HS-GC was applied to analyze the results. It was observed that an increased amount of $CoCl_2$, while keeping its ratio with bpy constant (Figure 2.28 and Table 2.6), decreases the amounts of both H_2 and CO generated, particularly when 5 µmol or 10 µmol $CoCl_2$ were used. The selectivity for CO was highest with 1 µmol $CoCl_2$ and 2 mg bpy.

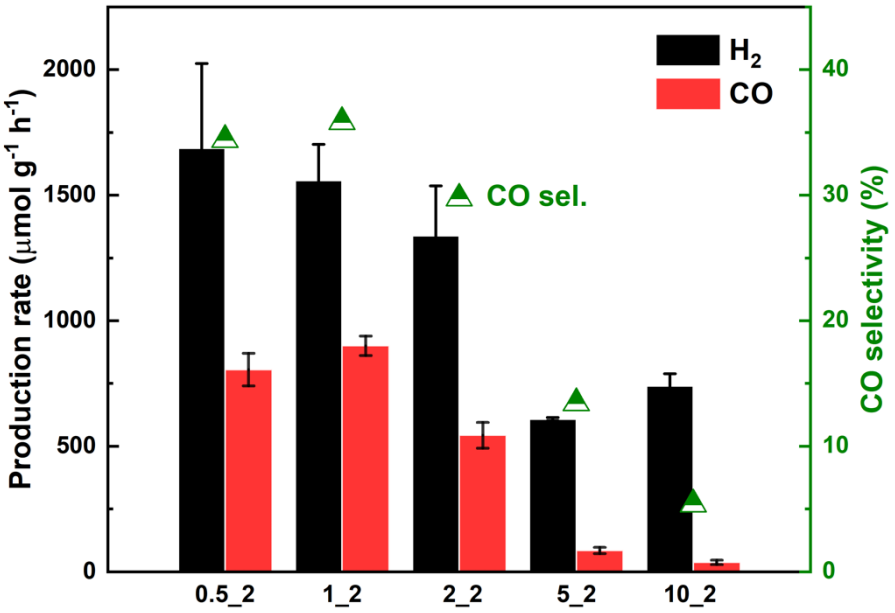

Figure 2.29 CO selectivity and yield of H_2 and CO over P7 with different ratio of $CoCl_2$ and bpy.

Table 2.7 Gas evolution rates of gaseous products of P7 with $CoCl_2$ and bpy at a varied relative ratio.

Entry	$CoCl_2$ (µmol)	bpy (mg)	H_2 Production rate (µmol g^{-1} h^{-1})	CO Production rate (µmol g^{-1} h^{-1})	Selectivity for CO production (%)	$n(H_2)$: n(CO)
1[a]	0.5	2	1686.6 ± 238.9	805.5 ± 45.9	32.3	2.1 : 1
2[a]	1	2	1558.4 ± 102.3	900.3 ± 27.4	36.6	1.7 : 1
3[a]	2	2	1338.7 ± 139.8	543.8 ± 36.3	28.9	2.5 : 1

4[a]	5	2	607.9 ± 4.4	85.1 ± 8.7	12.3	7.1 : 1
5[a]	10	2	739.8 ± 34.8	37.8 ± 6.3	4.9	19.6 : 1

Conditions: P7 (5 mg, 0.155 wt. % Pd), solvent (4 mL, MeCN / H_2O=3:1), TEOA (1 mL), CO_2 atmosphere, solar simulator (5 hours).

Table 2.8 Gas evolution rates of gaseous products of blank experiments with of $CoCl_2$ and bpy.

Entry	**$CoCl_2$ (µmol)**	**bpy (mg)**		**H_2 Production rate (µmol g^{-1} h^{-1})**	**CO Production rate (µmol g^{-1} h^{-1})**
1[a]	0.5	1		-[b]	0.4 ± 0.01
2[a]	1	2		-[b]	0.3 ± 0.01
3[a]	2	4	constant ratio of $CoCl_2$/bpy	-[b]	0.25 ± 0.05
4[a]	5	10		-[b]	0.2 ± 0.01
5[a]	10	20		-[b]	0.3 ± 0.01
6[a]	0.5	2		-[b]	0.25 ± 0.05
7[a]	1	2		-[b]	0.3 ± 0.01
8[a]	2	2	varied ratio $CoCl_2$/bpy	-[b]	0.3 ± 0.01
9[a]	5	2		-[b]	0.25 ± 0.05
10[a]	10	2		-[b]	0.3 ± 0.01

[a] Conditions: solvent (4 mL, MeCN / H_2O=3:1), TEOA (1 mL), CO_2 atmosphere, solar simulator (5 hours); [b] Not detected.

Similar results were observed when increasing the amount of $CoCl_2$ while keeping the amount of bpy constant (Figure 2.29 and Table 2.7). The selectivity for CO was also highest with 1 µmol $CoCl_2$ and 2 mg bpy. Control experiments suggested that $CoCl_2$ and bpy without adding photocatalyst generate only negligible amounts of H_2 and CO, demonstrating that the process is indeed photocatalytic and driven by the polymer photocatalyst (Table 2.8).

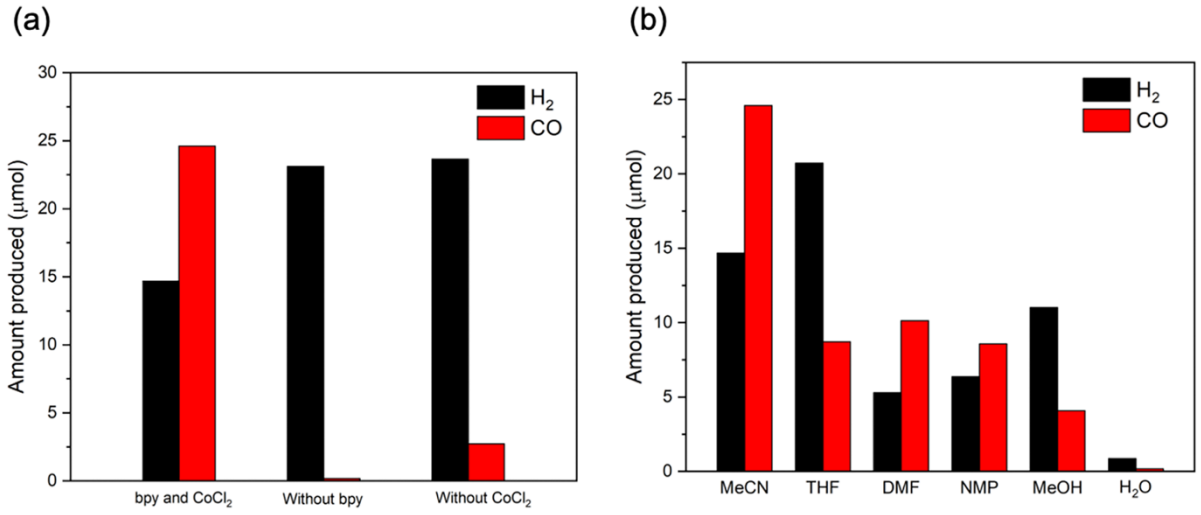

Figure 2.30 (a) CO/H_2 production without 2,2'-bipyridine or $CoCl_2$ using P7-0.5% as catalyst in $MeCN/H_2O$/TEOA mixture (5 mL, 3/1/1) under solar simulator for 5h (AM1.5G, 1600 W xenon light source, air mass 1.5G filter, 350−1000 nm); (b) CO/H_2 production generated using various co-solvents of P7-0.5% as the catalyst and 1 mL TEOA as the sacrificial agent under solar simulator irradiation for 5 hours (AM1.5G, 1600 W xenon light source, air mass 1.5G filter, 350−1000 nm); 3 mL Organic solvent and 1 mL water or 4 mL water only (MeCN: acetonitrile; THF: tetrahydrofuran; DMF: *N*,*N*-dimethylformamide; NMP: *N*-methyl-2-pyrrolidone; MeOH: methanol).

Without bpy or $CoCl_2$, we find that CO production rates are very low (Figure 2.30a), which is consistent with previous reports that prove that both are indispensable to form catalytically active Co centres.[9,20–22,31] When P7 was tested with 1 μmol $CoCl_2$ and 2 mg bpy in different organic solvents such as THF, DMF, NMP and MeOH as alternative co-solvents (Figure 2.30b), P7 had the highest CO production rate in MeCN as the co-solvent. When P7 was tested in pure water with TEOA, P7 had the lowest CO and H_2 generation rates. Hence, we used 1 μmol $CoCl_2$ and 2 mg bpy hereafter as the optimised conditions and 3 mL MeCN, 1 mL H_2O and 1 mL TEOA as the optimised solvent conditions for photocatalytic CO_2 reduction with P7.

2.9 P7 synthesized with different amounts of Pd

Table 2.9 P7 synthesized with various palladium loadings.

Materials	Amount of $[Pd(PPh_3)_4]$ used in polymerisation[a]	Yield / %	Residual Pd[b] / wt %
P7-0.1%	0.1 mol% (2.3 mg)	75	0.043
P7-0.5%	0.5 mol% (11.6 mg)	99	0.073
P7-1%	1 mol% (23 mg)	Quant.	0.237
P7-2%	2 mol% (46.2 mg)	Quant.	0.504
P7-3%	3 mol% (69.3 mg)	Quant.	0.769
P7-5%	5 mol% (115.6 mg)	Quant.	1.444

[a] 3,7-Dibromodibenzo[*b*,*d*]thiophene sulfone (0.748 g, 2.0 mmol), 1,4-benzene diboronic acid (0.331 g, 2.0 mmol), *N*,*N'*-dimethylformamide (40 mL) and K_2CO_3 (aqueous, 2.0 M, 8 mL) were used in this reaction; [b] The amount of residual palladium in the material as measured via ICP-OES.

Residual palladium from the synthesis appears to form active sites for protons and facilitate competing hydrogen evolution. Therefore, controlling the concentration of residual palladium in polymers offers a pathway to producing syngas with different ratios of H_2 and CO.

To do this, the amount of $[Pd(PPh_3)_4]$ used in the synthesis of P7 was varied from 0.1 mol% to 5 mol% (Table 2.9). Inductively coupled plasma optical emission spectrometry (ICP-OES) measurements suggested that residual palladium in polymers ranged from 0.043 wt. % up to 1.444 wt. %. The detected amounts of residual palladium were not same with the amounts used in the polycondensation reaction. It was found that materials that were synthesized by using more palladium also contained more residual palladium, showing an almost linear increase of residual palladium content of the polymer with increased amount of palladium catalyst used in the polymerisation (Figure 2.31a). The obtained samples were named as P7-0.1% to P7-5%, indicating the amount of $[Pd(PPh_3)_4]$ used in the synthesis of each P7 sample.

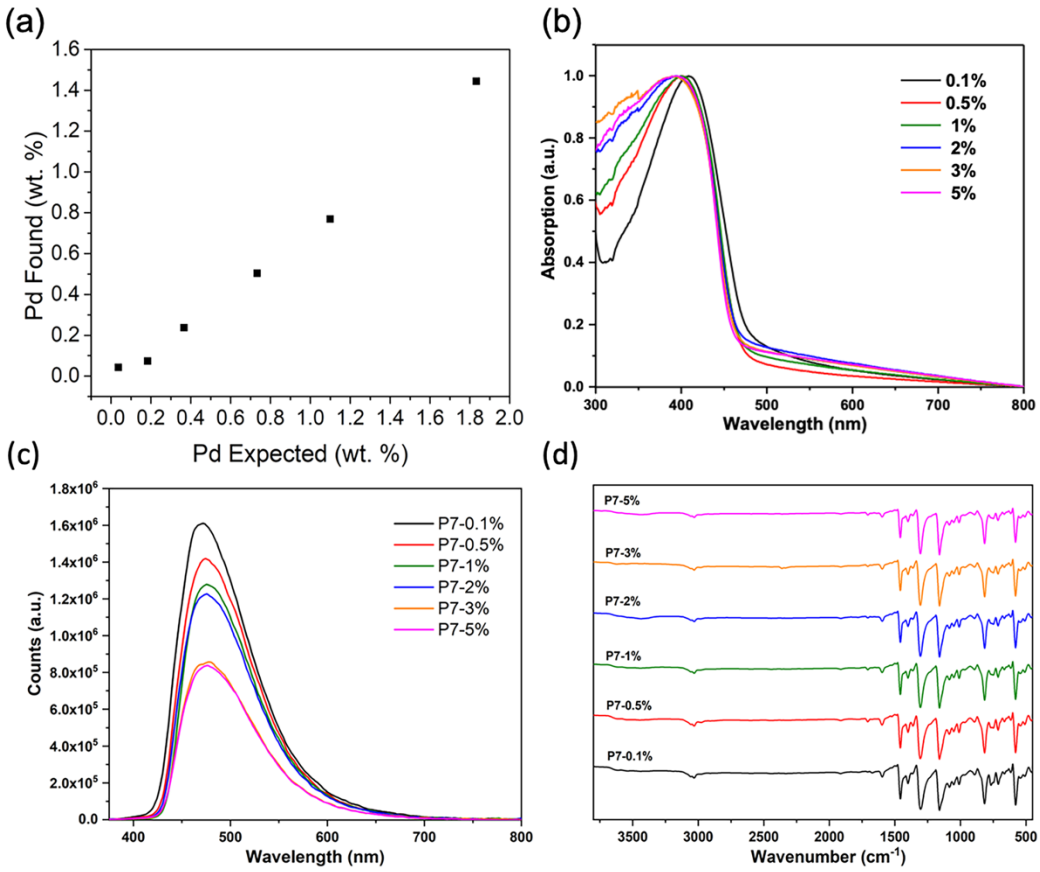

Figure 2.31 (a) Expected and measured palladium content of P7 synthesised with different amounts of $[Pd(PPh_3)_4]$; (b) UV-vis spectra of P7 synthesised with different amounts of $[Pd(PPh_3)_4]$; (c) Photoluminescence spectra (λ_{exc} = 370 nm) of P7 synthesized with different amounts of $[Pd(PPh_3)_4]$; (d) FT-IR spectra of P7 synthesized with different amounts of $[Pd(PPh_3)_4]$.

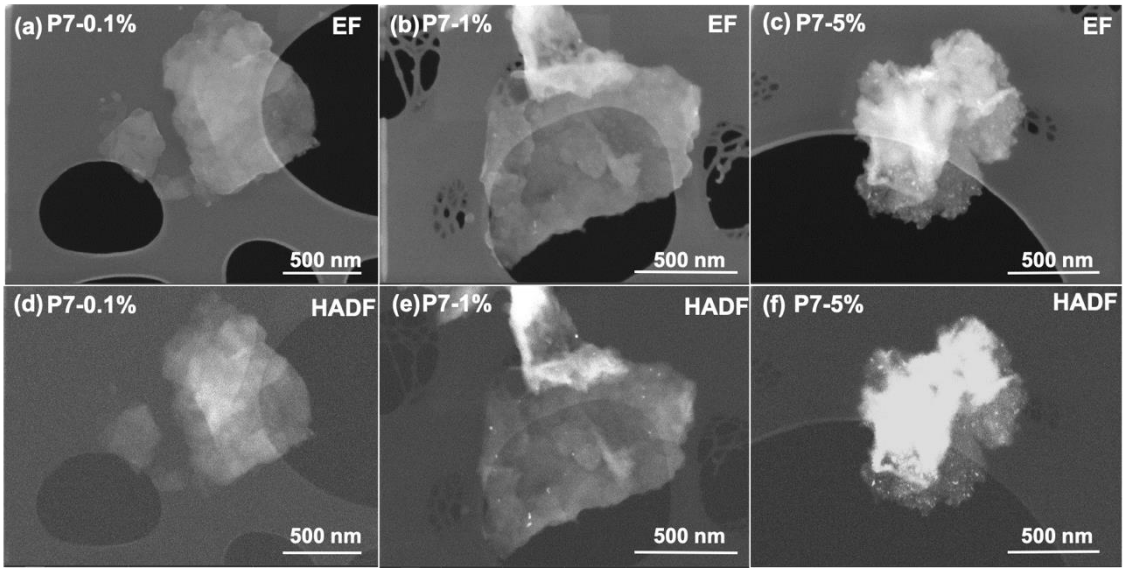

Figure 2.32 TEM images of P7-0.1% (a) (d), P7-1% (b) (e), P7-5% (c) (f) using epifluorescent STEM mode and using HADF STEM mode.

These samples were then characterised to rule out that any other differences in properties beyond the palladium content that could affect the performance of these materials. UV-vis absorption spectra (Figure 2.31b) tested in solid-state showed very little difference in their absorption on-sets, indicating that the optical properties were not affected by the palladium content used in the polycondensation reaction. Similarly, photoluminescence spectra suggested no difference in the maximum emission wavelength position (Figure 2.31c). The photoluminescence intensity reduced with increased palladium content, possibly due to enhanced trapping and quenching of excitons.[39] And FT-IR spectra indicated no noticeable differences between P7 with different amounts of Pd residuals(Figure 2.31d). Transmission electron microscopy (TEM) showed the existence of large Pd clusters in P7-1% and P7-5% with the latter clearly suggesting a larger number of Pd clusters (Figure 2.32). In the previous study, X-ray absorption spectroscopy has proven that only the largest Pd clusters could be resolved and most Pd resides as tiny clusters within the photocatalyst, which might also be the case here.[39] Taken together, all characterisation for P7-0.1% to P7-5% indicates little difference in their physical properties, except for their residual palladium content.

2.10 Controllable syngas generation

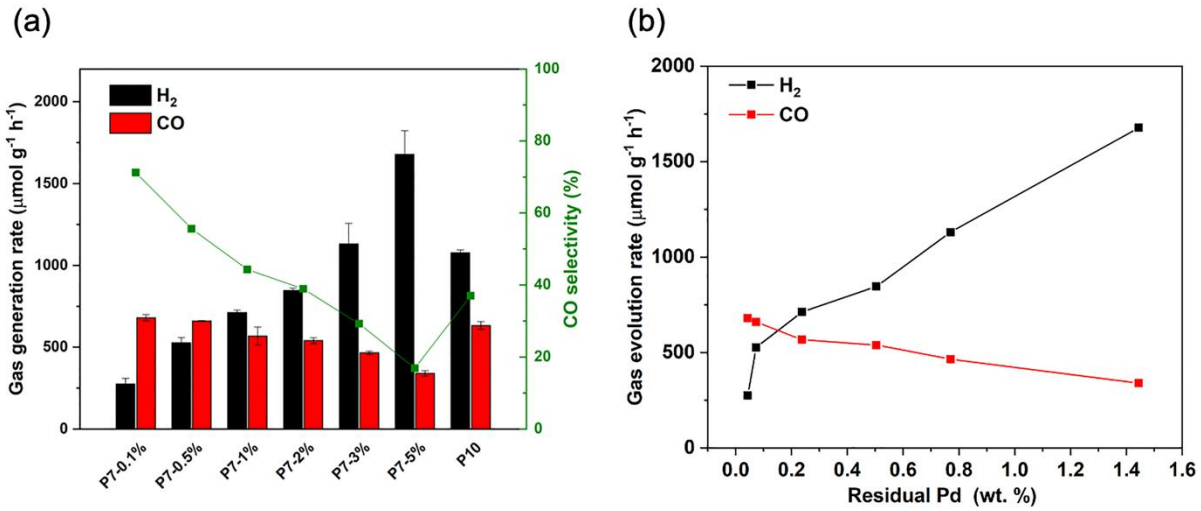

Figure 2.33 (a) Photocatalytic CO and H_2 production of P7-0.1% to P7-5% (5 mg) from MeCN/water/TEOA mixtures (25mL, 3/1/1) under simulated solar irradiation (1 sun, AM 1.5G); (b)

Correlation between the amount of palladium and the CO and hydrogen evolution rates of P7-0.1% to P7-5%.

P7-0.1% to P7-5% were tested as photocatalysts for CO_2 reduction in the optimized condition under solar irradiation (Figure 2.33a). The influence of the amount of residual Pd on the CO production rates for P7-0.1% and P7-0.5% was showed to be insignificant with rates of 680.1 μmol g^{-1} h^{-1} and 660.4 μmol g^{-1} h^{-1}. P7-1% and P7-2% show a slight decrease in CO evolution rates (567.4 μmol g^{-1} h^{-1} and 539.8 μmol g^{-1} h^{-1}), and P7-3% and P7-5% show a significant reduction in their CO evolution rates (465.8 μmol g^{-1} h^{-1} and 340.1 μmol g^{-1} h^{-1}). By contrast, the residual palladium content affects the hydrogen evolution rates significantly. The H_2 evolution rate increases from 275.0 μmol g^{-1} h^{-1} for P7-0.1% to 711.9 μmol g^{-1} h^{-1} for P7-1% and 845.9 μmol g^{-1} h^{-1} for P7-2%. For P7-3% and P7-5%, a significant increase in the rate was again observed (1130.2 μmol g^{-1} h^{-1} and 1677.3 μmol g^{-1} h^{-1}). This strongly demonstrates that hydrogen evolution rates are greatly affected by the residual palladium concentration. The residual Pd also affects the ability to reduce carbon dioxide, especially at higher palladium concentrations.

The observation that the hydrogen evolution rate in the limit of low Pd concentrations (<0.2 wt%, Figure 2.33b) significantly increases with the amount of Pd is a common observation[26,27] and shows that excitons or polarons after dissociation of excitons do not reach Pd to facilitate proton reduction,[39] while abundant Co is present allowing for efficient carbon dioxide reduction. The initial steep increase in activity is followed by a region that is less affected by the increase in Pd, which has also been found for other conjugated materials[26,27] before significantly increased H_2 evolution rate, due to more Pd relative to the amount of cobalt loaded on the materials is available for proton reduction. The ratios of H_2 / CO for P7-0.1% to P7-1% range from 0.4:1 to 1.25:1. H_2 rich syngas ranging from 1.6:1 to 4.9:1 (H_2 / CO) was produced by P7-2% to P7-5%. This makes it possible to produce syngas for the generation of aldehydes via hydroformylation of alkene with a ratio of 1:1 H_2 / CO as well as the methanol synthesis and F-T synthesis of alkanes requiring a ratio of 2:1 H_2 / CO.[13]

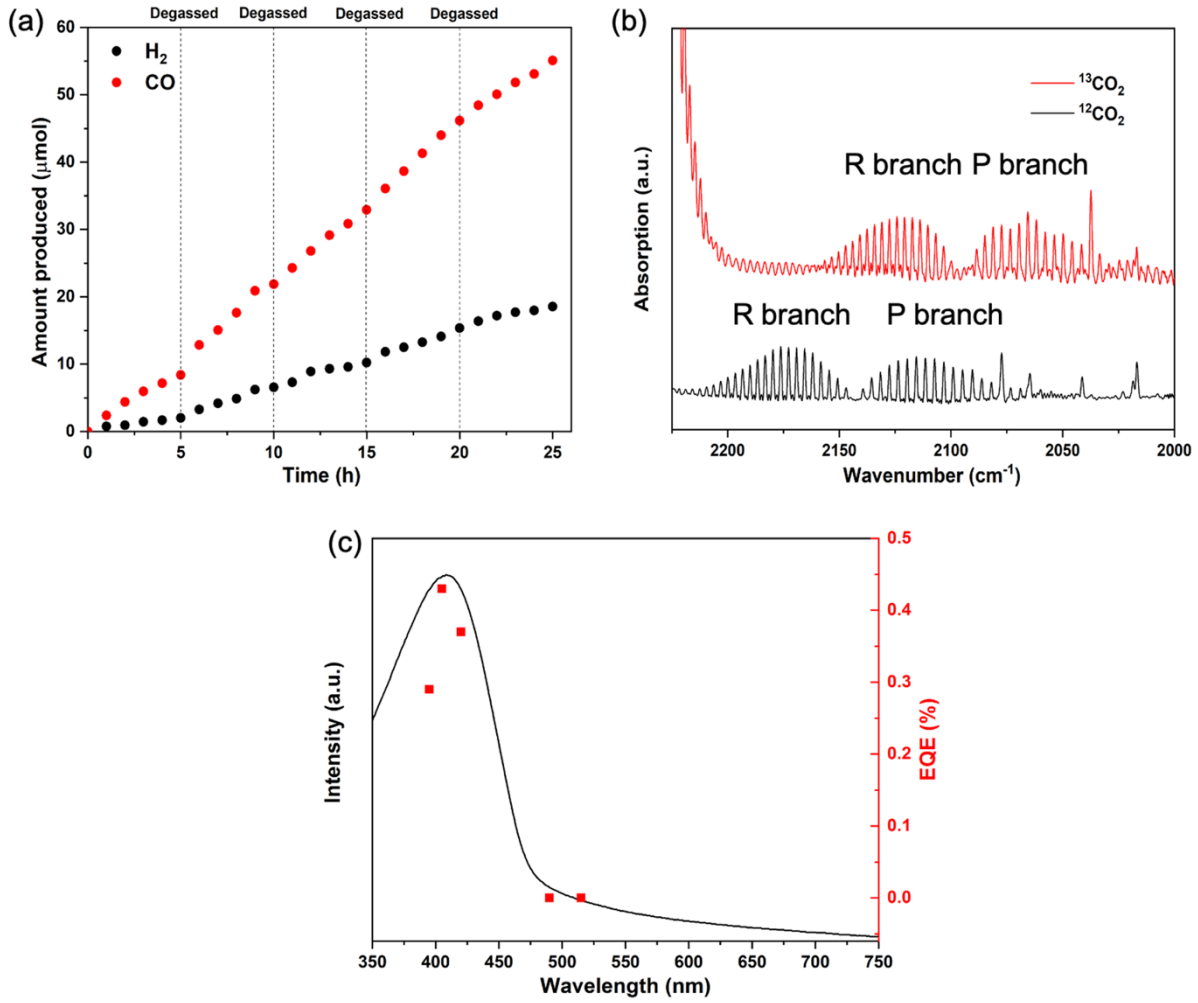

Figure 2.34 (a) Cycling experiments of P7-0.1% (5 mg) under simulated solar irradiation (1 sun, AM 1.5G) over 25 hours irradiation with intermitted degassing every 5 hours; (b) FT-IR spectra of the gaseous products after 1 hour of P7 in MeCN/H_2O/TEOA solution using either $^{12}CO_2$ and $^{13}CO_2$ under solar irradiation (1 sun, AM 1.5G); (c) UV-vis spectrum of P7-0.1% overlaid with the measured external quantum efficiencies (EQE) measured at various wavelengths using LEDs at light sources.

Longer-term stability is a very important factor for photocatalysts. The system used for long-term experiments was the same as that for CO_2 reduction. The flask was re-degassed with fresh CO_2 every 5 hours to reduce the influence of pressure reduction. Longer-term experiments with intermittent degassing every 5 hours demonstrated excellent stability of the sample (P7-0.1%) over 25 hours producing CO rich syngas (Figure 2.34a). Finally, isotopically labelled $^{13}CO_2$ experiments were carried out to prove that the detected CO originated from the reduction of CO_2 rather than

decomposition of the photocatalysts or other components of the photocatalytic system. However, GC-MS was not available at that time. Hence, FTIR spectroscopy was used for $^{13}CO_2$ labelling experiments with an argon-purged custom-made gas IR cell. To do this, a vial containing P7, 2,2'-bipyridine and cobalt (II) chloride in a mixture of acetonitrile/water/triethanolamine (3:1:1) was purged with $^{13}CO_2$ for 3 minutes. Then the resulting suspension was illuminated for 1 hour under a solar simulator with 1 sun output. A sample of the gas headspace (1000 µL) was injected into the gas IR cell, and the IR spectrum was measured. The IR spectrum (Figure 2.34b) shows a series of regularly spaced peaks which corresponds to the vibrational and rotational energy levels of the molecule. The P branch transitions indicated a series of peaks at lower wavenumbers and the R branch series appeared at higher wavenumbers. Using isotopically labelled $^{13}CO_2$ as the carbon source resulted in the formation of ^{13}CO strongly suggesting that CO was produced from CO_2 (Figure 2.34b).[21] As discussed in **Chapter 1**, the external quantum efficiency (EQE) represents the number ratio of electrons transferred toward CO relative to incident photons at a given wavelength. The EQEs of P1-0.1% tested at 395, 405 and 420 nm were 0.29%, 0.43% and 0.37%, respectively (Figure 2.34c). Furthermore, the action spectrum of P7-0.1% follows broadly speaking the light absorption profile also supporting the hypothesis that the CO production is indeed photocatalytic.

2.11 Conclusions

In conclusion, linear conjugated polymers were tested as photocatalysts for CO_2 reduction to CO with a sacrificial hole scavenger. P7 was demonstrated to be the most active photocatalyst for CO_2 reduction, while structurally related P10 performs far worse in terms of CO selectivity, producing a similar amount of CO but much more hydrogen. This difference in selectivity can be rationalized by differences in the predicted thermodynamic driving force for CO_2 and proton reduction between P7 and P10. Residual palladium was proven to result in significant hydrogen production, which was found to compete with CO production at high loadings. Within a certain

concentration range, Pd acts as a co-catalyst for H_2 production without reducing the CO evolution rates significantly, potentially allowing for syngas production, if the production efficiencies can be increased, within a range of H_2/CO ratios that are adjustable by varying the Pd concentration.

2.12 Experimental methods

2.12.1 Fourier-transform infrared spectroscopy

Transmission FT-IR spectra were recorded on a Bruker Tensor 27 at room temperature; samples were prepared as pressed KBr pellets and analysed for 16 scans with a resolution of 4 cm^{-1}.

2.12.2 UV-Vis measurements

UV-Visible absorption spectra of all polymers were collected on an Agilent Cary 5000 UV-Vis-NIR Spectrometer by measuring the reflectance of powders in the solid-state.

2.12.3 Scanning transmission electron microscope

STEM images were obtained on a Tescan S8000G with a TEM detector. Images were recorded at 20 KeV with a current of 125 pA. All images were recorded in both epifluorescent (EF) mode and High Angle Dark Field (HADF) mode.

2.12.4 Inductively coupled plasma - optical emission spectrometry (ICP-OES) analysis

Before measuring, all samples were digested in nitric acid (67–69%, trace metal analysis grade) with a microwave using an in-house procedure. The solutions were diluted with water before the measurement by Spectro Ciros ICP-OES and the instrument was calibrated with standards in an aqueous solution.

2.12.5 TCSPC measurements

TCSPC experiments were obtained on an Edinburgh Instruments LS980-D2S2-STM

spectrometer equipped with picosecond pulsed LED excitation sources and a R928 detector. Suspensions were treated by ultrasonicating the materials in acetonitrile or acetonitrile, water and triethanolamine (3/1/1) solution purged with N_2 or CO_2. The instrument response was collected with colloidal silica (LUDOX® HS-40, Sigma-Aldrich) at the excitation wavelength without any filter. Decay times were fitted in the FAST software employing suggested lifetime estimates.

2.13 References

1 Y. Chen, G. Ji, S. Guo, B. Yu, Y. Zhao, Y. Wu, H. Zhang, Z. Liu, B. Han and Z. Liu, *Green Chem.*, 2017, **19**, 5777–5781.

2 H. P. Liang, A. Acharjya, D. A. Anito, S. Vogl, T. X. Wang, A. Thomas and B. H. Han, *ACS Catal.*, 2019, **10**, 3959–3968.

3 C. Yang, W. Huang, L. C. da Silva, K. A. I. Zhang and X. Wang, *Chem. - A Eur. J.*, 2018, **24**, 17454–17458.

4 S. Zhang, S. Wang, L. Guo, H. Chen, B. Tan and S. Jin, *J. Mater. Chem. C*, 2019, **8**, 192–200.

5 S. Yang, W. Hu, X. Zhang, P. He, B. Pattengale, C. Liu, M. Cendejas, I. Hermans, X. Zhang, J. Zhang and J. Huang, *J. Am. Chem. Soc.*, 2018, **140**, 14614–14618.

6 W. Zhong, R. Sa, L. Li, Y. He, L. Li, J. Bi, Z. Zhuang, Y. Yu and Z. Zou, *J. Am. Chem. Soc.*, 2019, **141**, 7615–7621.

7 Z. Fu, X. Wang, A. M. Gardner, X. Wang, S. Y. Chong, G. Neri, A. J. Cowan, L. Liu, X. Li, A. Vogel, R. Clowes, M. Bilton, L. Chen, R. S. Sprick and A. I. Cooper, *Chem. Sci.*, 2020, **11**, 543–550.

8 X. Wang, Z. Fu, L. Zheng, C. Zhao, X. Wang, S. Y. Chong, F. McBride, R. Raval, M. Bilton, L. Liu, X. Wu, L. Chen, R. S. Sprick and A. I. Cooper, *Chem. Mater.*, 2020, **32**, 9107–9114.

9 S. Wang, X. Hai, X. Ding, S. Jin, Y. Xiang, P. Wang, B. Jiang, F. Ichihara, M. Oshikiri, X. Meng, Y. Li, W. Matsuda, J. Ma, S. Seki, X. Wang, H. Huang, Y. Wada, H. Chen and J. Ye, *Nat. Commun.*, 2020, **11**, 1149.

10 B. Acharya, P. Roy and A. Dutta, *Biofuels*, 2014, **5**, 551–564.

11 S. Hernández, M. A. Farkhondehfal, F. Sastre, M. Makkee, G. Saracco and N. Russo, *Green Chem.*, 2017, **19**, 2326–2346.

12 M. B. Ross, Y. Li, P. De Luna, D. Kim, E. H. Sargent and P. Yang, *Joule*, 2019, **3**, 257–264.

13 S. R. Foit, I. C. Vinke, L. G. J. de Haart and R. A. Eichel, *Angew. Chemie - Int. Ed.*, 2017, 56, 5402–5411.

14 R. S. Sprick, B. Bonillo, R. Clowes, P. Guiglion, N. J. Brownbill, B. J. Slater, F. Blanc, M. A. Zwijnenburg, D. J. Adams and A. I. Cooper, *Angew. Chem. Int. Ed.*, 2016, **55**, 1792–1796.

15 M. Sachs, R. S. Sprick, D. Pearce, S. A. J. Hillman, A. Monti, A. A. Y. Guilbert, N. J. Brownbill, S. Dimitrov, X. Shi, F. Blanc, M. A. Zwijnenburg, J. Nelson, J. R. Durrant and A. I. Cooper, *Nat. Commun.*, 2018, **9**, 4968.

16 R. S. Sprick, L. Wilbraham, Y. Bai, P. Guiglion, A. Monti, R. Clowes, A. I. Cooper and M. A. Zwijnenburg, *Chem. Mater.*, 2018, **30**, 5733–5742.

17 K. Maeda, X. Wang, Y. Nishihara, D. Lu, M. Antonietti and K. Domen, *J. Phys. Chem. C*, 2009, **113**, 4940–4947.

18 M. C. Daniel and D. Astruc, *Chem. Rev.*, 2004, **104**, 293–346.

19 J. Ran, M. Jaroniec and S.-Z. Qiao, *Adv. Mater.*, 2018, **1704649**, 1704649.

20 J. Lin, Z. Pan and X. Wang, *ACS Sustain. Chem. Eng.*, 2014, **2**, 353–358.

21 J. J. Walsh, C. Jiang, J. Tang and A. J. Cowan, *Phys. Chem. Chem. Phys.*, 2016, **18**, 24825–24829.

22 M. Zhou, S. Wang, P. Yang, C. Huang and X. Wang, *ACS Catal.*, 2018, **8**, 4928–4936.

23 S. Wang, B. Y. Guan and X. W. D. Lou, *J. Am. Chem. Soc.*, 2018, **140**, 5037–5040.

24 S. Xie, Y. Wang, Q. Zhang, W. Deng and Y. Wang, *ACS Catal.*, 2014, **4**, 3644–3653.

25 L. Li, Z. Cai, Q. Wu, W. Y. Lo, N. Zhang, L. X. Chen and L. Yu, *J. Am. Chem. Soc.*, 2016, **138**, 7681–7686.

26 J. Kosco, M. Sachs, R. Godin, M. Kirkus, L. Francas, M. Bidwell, M. Qureshi, D. Anjum, J. R. Durrant and I. McCulloch, *Adv. Energy Mater.*, 2018, **8**, 1802181.

27 R. S. Sprick, Y. Bai, A. A. Y. Guilbert, M. Zbiri, C. M. Aitchison, L. Wilbraham, Y. Yan, D. J. Woods, M. A. Zwijnenburg and A. I. Cooper, *Chem. Mater.*, 2019, **31**, 305–313.

28 S. Yanagida and S. Matsuoka, in *Optical Materials Technology for Energy Efficiency and Solar Energy Conversion XI: Photovoltaics, Photochemistry, Photoelectrochemistry*, eds. A. Hugot-Le Goff, C.-G. Granqvist and C. M. Lampert, 1992, vol. 1729, p. 243.

29 Y. Bai, L. Wilbraham, B. J. Slater, M. A. Zwijnenburg, R. S. Sprick and A. I. Cooper, *J. Am. Chem. Soc.*, 2019, **141**, 9063–9071.

30 C. B. Meier, R. Clowes, E. Berardo, K. E. Jelfs, M. A. Zwijnenburg, R. S. Sprick and A. I. Cooper, *Chem. Mater.*, 2019, **31**, 8830–8838.

31 S. Wang, B. Y. Guan, Y. Lu and X. W. Lou, *J. Am. Chem. Soc.*, 2017, **139**, 17305–17308.

32 Y. Wang, A. Vogel, M. Sachs, R. S. Sprick, L. Wilbraham, S. J. A. Moniz, R. Godin, M. A. Zwijnenburg, J. R. Durrant, A. I. Cooper and J. Tang, *Nat. Energy*, 2019, **4**, 746–760.

33 P. Guiglion, C. Butchosa and M. A. Zwijnenburg, *J. Mater. Chem. A*, 2014, **2**, 11996–12004.

34 S. G. Bratsch, *J. Phys. Chem. Ref. Data*, 1989, **18**, 1–21.

35 P. Makuła, M. Pacia and W. Macyk, *J. Phys. Chem. Lett.*, 2018, **9**, 6814–6817.

36 Y. Bai, L. Wilbraham, B. J. Slater, M. A. Zwijnenburg, R. S. Sprick and A. I. Cooper, *J. Am. Chem. Soc.*, 2019, **141**, 9063–9071.

37 X. Wang, L. Chen, S. Y. Chong, M. A. Little, Y. Wu, W. H. Zhu, R. Clowes, Y. Yan, M. A. Zwijnenburg, R. S. Sprick and A. I. Cooper, *Nat. Chem.*, 2018, **10**, 1180–1189.

38 R. S. Sprick, B. Bonillo, M. Sachs, R. Clowes, J. R. Durrant, D. J. Adams and A. I. Cooper, *Chem. Commun.*, 2016, **52**, 10008–10011.

39 M. Sachs, H. Cha, J. Kosco, C. M. Aitchison, L. Francàs, S. Corby, C. L. Chiang, A. A. Wilson, R. Godin, A. Fahey-Williams, A. I. Cooper, R. S. Sprick, I. McCulloch and J. R. Durrant, *J. Am. Chem. Soc.*, 2020, **142**, 14574–14587.

Chapter 3

A stable covalent organic framework for photocatalytic carbon dioxide reduction

3.1 Author contributions

All the materials were synthesized and characterized by the thesis author. The photocatalysis experiments about CO_2 reduction were performed by the thesis author. Dr Linjiang Chen conceived the modelling strategy. Dr Linjiang Chen and Xue Wang performed the calculations. Dr Samantha Y. Chong carried out PXRD analyses. Dr Reiner Sebastian Sprick performed the TCSPC experiments. Dr Gaia Neri and Prof Alexander J. Cowan carried out isotopic labelling experiments. Lunjie Liu performed photoelectrochemical measurements. Dr Adrian M. Gardner carried out TA measurements and analyzed the results with Prof Alexander J. Cowan. Rob Clowes and Dr Xiaobo Li configured the photocatalysis platform, including setup and methods for GC. Rob Clowes, Dr Xiaoyan Wang and Dr Linjiang Chen interpreted the gas sorption isotherms. Dr Matthew Bilton performed STEM imaging. Dr Anastasia Vogel provided expertise and feedback.

Portions of this chapter have been published in:

Z. Fu, X. Wang, A. M. Gardner, X. Wang, S. Y. Chong, G. Neri, A. J. Cowan, L. Liu, X. Li, A. Vogel, R. Clowes, M. Bilton, L. Chen, R. S. Sprick, A. I. Cooper, A Stable Covalent Organic Framework for Photocatalytic Carbon Dioxide Reduction, *Chem. Sci.* **2020**, *11*, 543–550.

3.2 Introduction

From **Chapter 1**, it was found that the residual palladium in conjugated polymers influenced CO_2 and H_2 production. Moreover, the residual Pd is very hard to remove via classical purification methods.[1] Therefore, it is worth trying organic materials without any metal catalysts for CO_2 reduction with high CO selectivity. Covalent organic frameworks (COFs)[2–6] which combine porosity with crystallinity have been investigated as photocatalysts for water splitting,[7,8] and for electrocatalytic CO_2 reduction.[9,10] These materials also have the potential for direct photocatalytic CO_2 reduction: For example, an azine-based COF, N_3-COF, was shown to exhibit gas phase photocatalytic CO_2 reduction.[11] Likewise, a 2D imine triazine-COF loaded with rhenium[12] and a *β*-ketoenamine-linked COF decorated with both nickel and a light-absorbing dye[13] were studied for the same reaction. However, these COFs have limited effective conjugation lengths in the 2D plane of the framework because they are based on imine, azine, or *β*-ketoenamine-linkers. This results in blue-shifted absorption on-sets, which limit the ability of the materials to absorb visible light.[14,15] Moreover, the imine COFs can be decomposed in base experimental conditions. In this chapter, we explored the fully conjugated olefin COFs, which are stable in base and acid conditions, for photocatalytic CO_2 reduction.

3.3 Experimental section

3.3.1 Synthesis of monomers

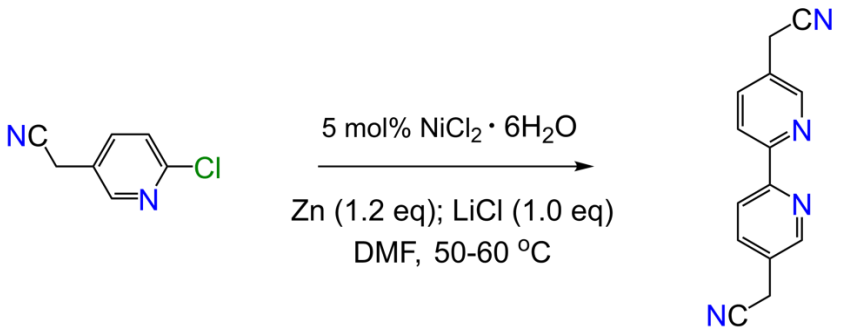

Figure 3.1 Synthesis of 5,5'-bis(cyanomethyl)-2,2'-bipyridine.

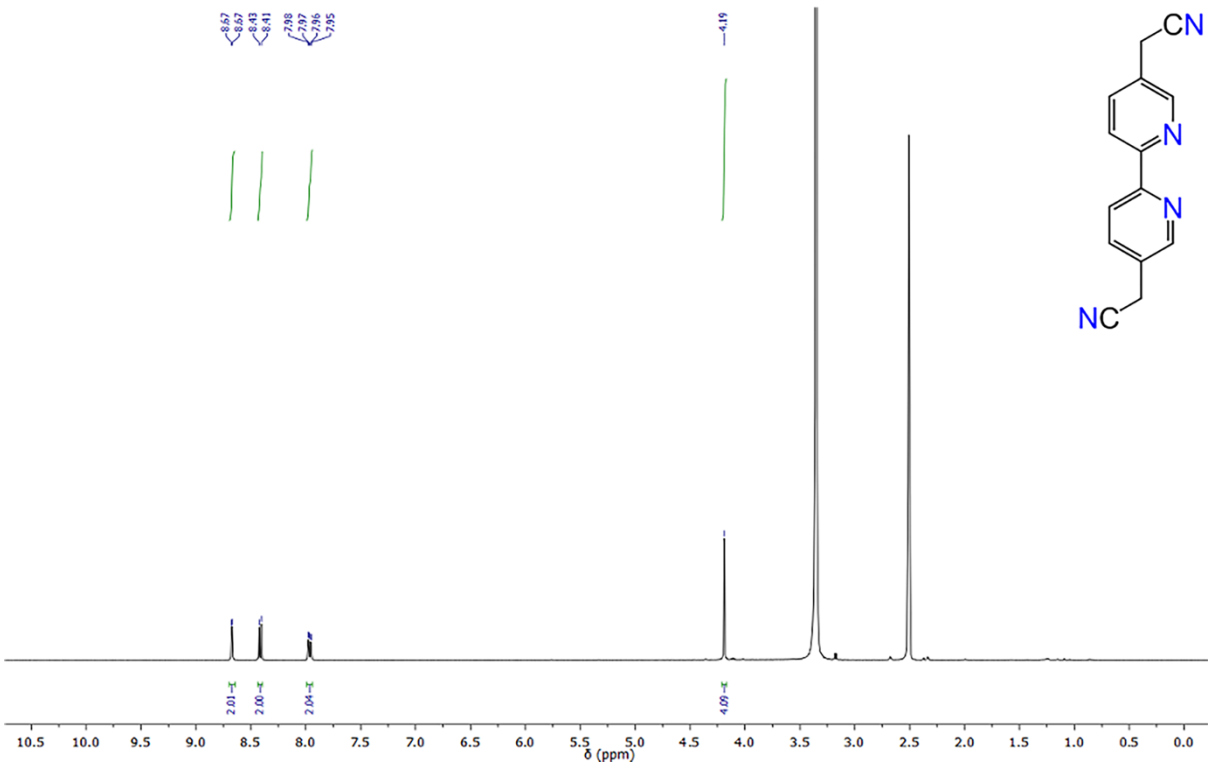

Figure 3.2 ^{1}H NMR spectrum of 5,5'-bis(cyanomethyl)-2,2'-bipyridine in DMSO-d_6.

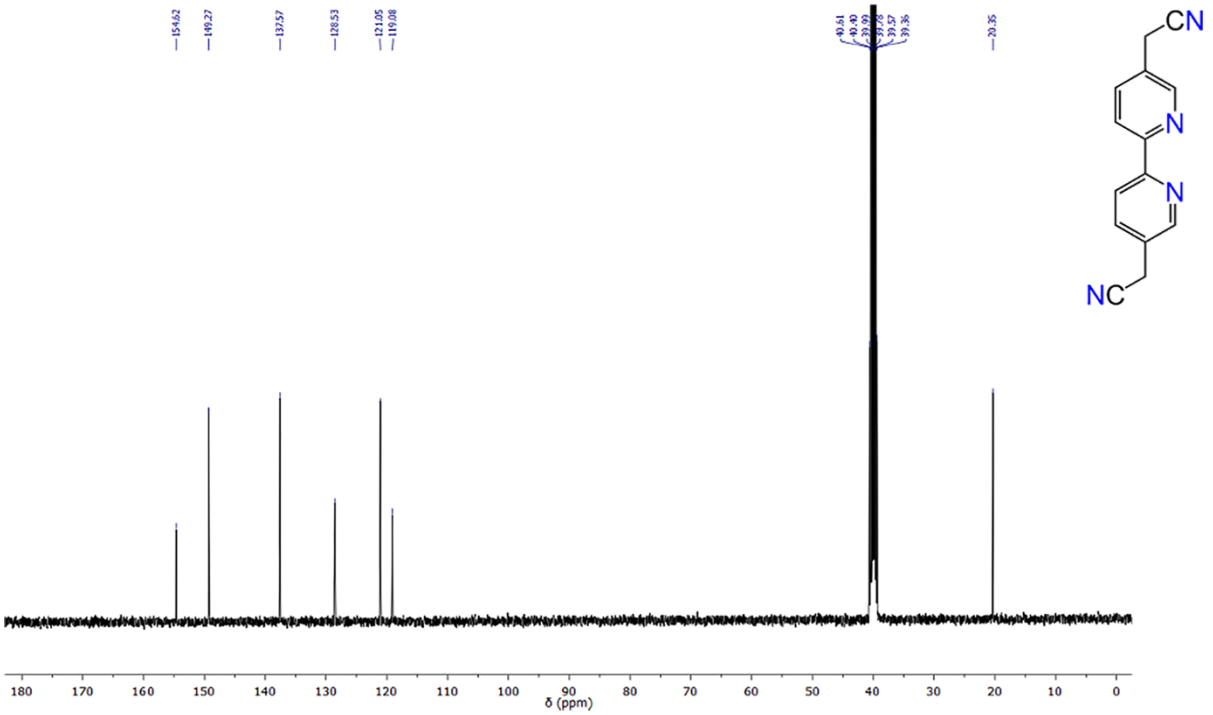

Figure 3.3 ^{13}C{^{1}H} NMR spectrum of 5,5'-bis(cyanomethyl)-2,2'-bipyridine in DMSO-d_6.

Synthesis of 5,5'-bis(cyanomethyl)-2,2'-bipyridine: 5,5'-Bis(cyanomethyl)-2,2'-bipyridine was synthesized based on previous literature procedures.[16] A 100 mL round-bottom flask was charged with $NiCl_2 \cdot 6H_2O$ (0.12 g, 0.5 mmol) and *N*,*N*-dimethylformamide (20 mL). The resulting solution was stirred and heated to 40 °C,

and then 2-chloropyridine-5-acetonitrile (1.53g, 10 mmol), anhydrous LiCl (0.43 g, 10 mmol), and zinc dust (0.78 g, 12 mmol) were added. When the temperature rose to 50 °C, a grain of iodine crystal and two drops of acetic acid were added to the mixture. An immediate rise in temperature and color change to black was caused, indicating the reaction was triggered. The mixture was stirred at 55-60 °C for 2-3 h until the complete conversion of 2-chloropyridine-5-acetonitrile to 5,5'-bis(cyanomethyl)-2,2'-bipyridine (monitored by TLC). To The cooled reaction mixture was added 1 N HCl aqueous solution (15 mL) to consume the remaining zinc dust. The resulting mixture was made alkaline with aqueous ammonia (25%) and extracted with CH_2Cl_2. The organic layers were collected, dried over anhydrous Na_2CO_3, and concentrated. The crude material was purified by flash chromatography to give the desired product. The NMR results were same as those in the literature.[16] ^{1}H NMR (400 MHz, DMSO-d_6) δ 8.67 (d, J = 2.0 Hz, 2H), 8.42 (d, J = 8.2 Hz, 2H), 7.96 (dd, J = 8.2, 2.3 Hz, 2H), 4.19 (s, 4H). ^{13}C NMR (101 MHz, DMSO-d_6) δ 154.62, 149.27, 137.57, 128.53, 121.05, 119.08, 20.35.

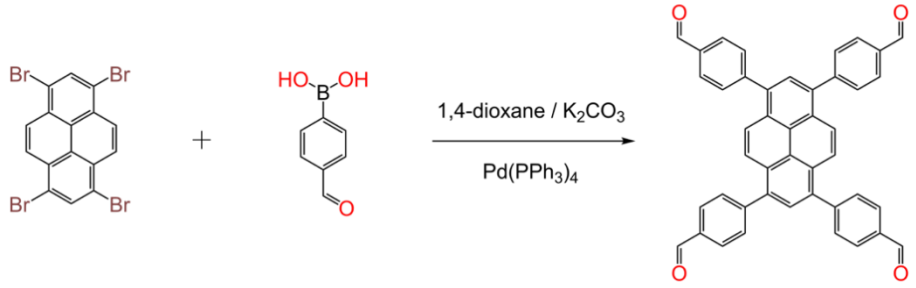

Figure 3.4 Synthesis of 1,3,6,8-tetrakis(4-formylphenyl)pyrene.

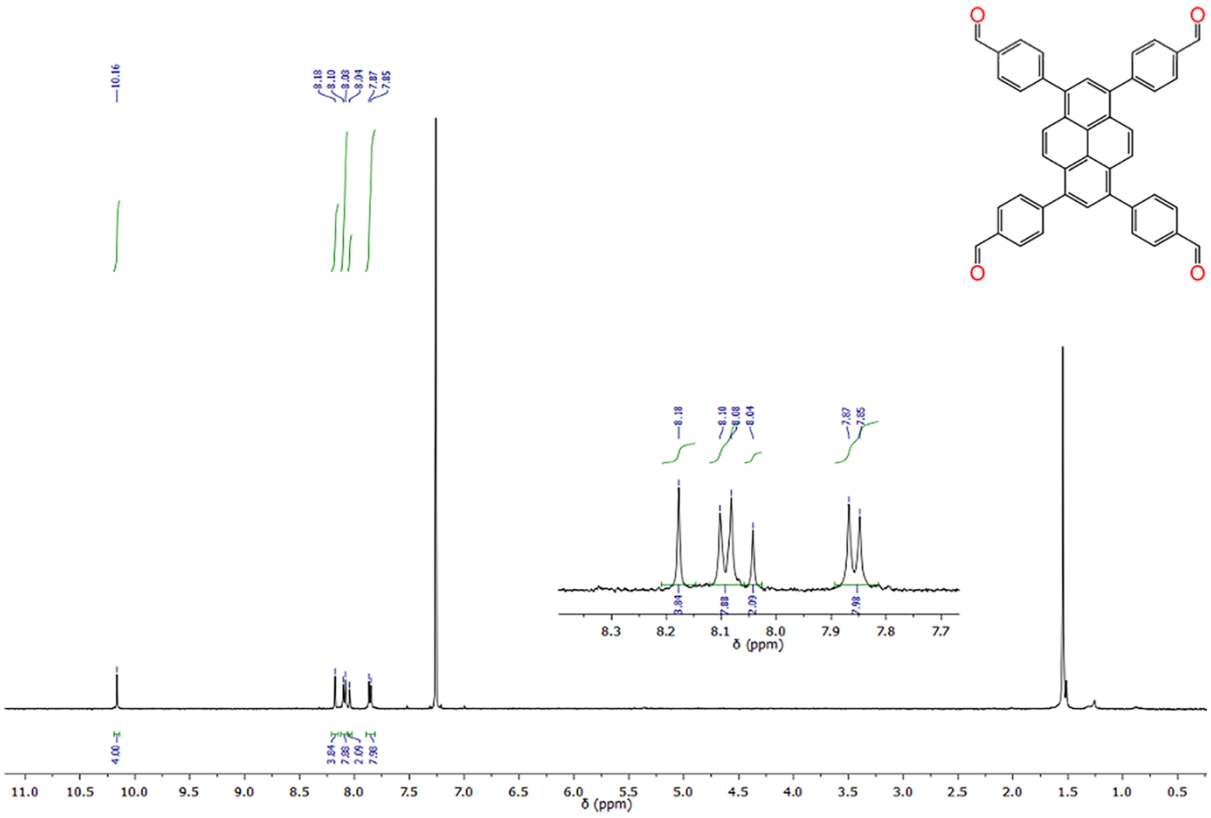

Figure 3.5 ^{1}H NMR spectrum of 1,3,6,8-tetrakis(4-formylphenyl)pyrene $CDCl_3$.

Synthesis of 1,3,6,8-tetrakis(4-formylphenyl)pyrene (TFPPy): TFPPy was synthesized based on previous literature procedures.[17] A mixture of 1,3,6,8-tetrabromopyrene (1.00 g, 1.93 mmol), 4-formylphenylboronic acid (1.74 g, 11.6 mmol), palladium tetrakis(triphenylphosphine) (0.12 g, 0.10 mmol, 5.2 mol %), and potassium carbonate (2.1 g, 15 mmol) in dry dioxane (30 mL) was stirred under nitrogen for 3 days at 85 °C. The yellow suspension reaction mixture was poured into ice-containing concentrated hydrochloric acid. The yellow solid was filtered and washed with 2 M HCl

(20 mL) three times. The product was extracted with $CHCl_3$ (100 mL) three times and dried over $MgSO_4$. After filtration, the solvent was removed under reduced pressure, and the resultant solid residue was recrystallized from hot $CHCl_3$ to afford TFPPy as a bright yellow powder (0.85 g, 72%). ^{1}H NMR (400 MHz, Chloroform-d) δ 10.16 (s, 4H), 8.18 (s, 4H), 8.09 (d, J = 8.0 Hz, 8H), 8.04 (s, 2H), 7.86 (d, J = 8.0 Hz, 8H). Note that a ^{13}C NMR spectrum could not be measured due to the low solubility of TFPPy.[17]

3.3.2 Synthesis of materials

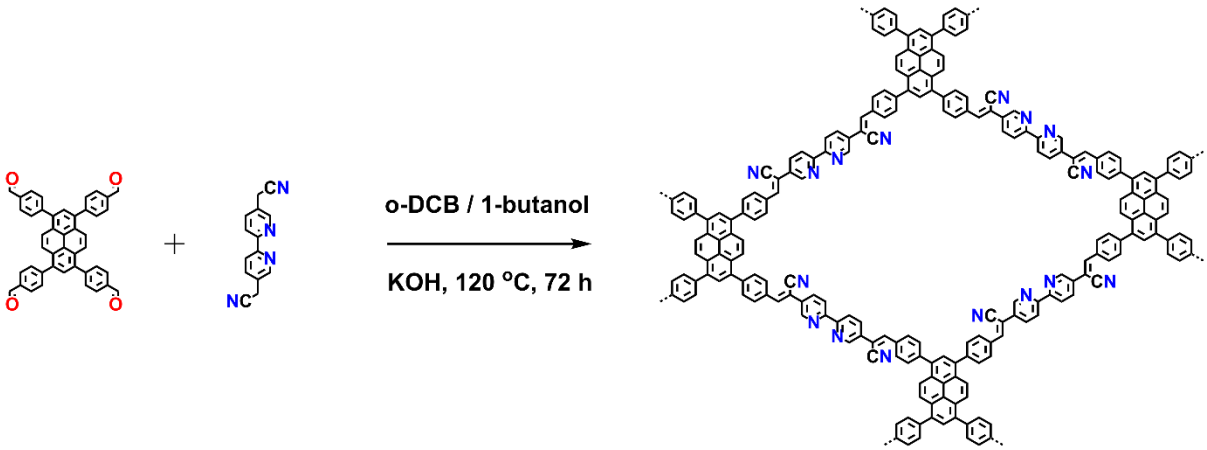

Figure 3.6 Scheme of the synthesis of Bpy-sp^{2}c-COF.

Synthesis of Bpy-sp^{2}c-COF: A Pyrex tube (10 mL) was charged with TFPPy (14.8 mg, 0.024 mmol) and 5,5'-bis(cyanomethyl)-2,2'-bipyridine (11.5 mg, 0.048 mmol), 1,2-dichlorobenze (0.5 mL), 1-butanol (0.5 mL) and aqueous KOH solution (0.1 mL, 4 M). The mixture was ultrasonicated for two minutes and then flash frozen at 77 K (liquid N_2 bath) and degassed through three freeze-pump-thaw cycles and sealed under vacuum using a Schlenk line and oil pump. The tube was heated at 120 °C for 3 days. After cooling to room temperature, the precipitated was washed with HCl (aq. 1 M), water, THF and methanol three times, respectively. The resulting powder was subjected to Soxhlet extraction with THF for two days. The powder was collected and dried at 120 °C under vacuum overnight to afford yellow crystallites in 82% yield. Anal. Calcd for $(C_{72}H_{42}N_8)_n$: C, 84.85; H, 4.15; N, 10.99. Found: C, 70.09; H, 4.09; N, 6.99. Note: The yields and microanalysis data were calculated for an infinite structure and also ignoring the presence of end-groups whose nature is unclear. The predicted theoretical surface areas of Bpy-sp^{2}c-COF is 2041.21 m^2 g^{-1}.

Synthesis of the amorphous analogue Bpy-sp^{2}c-P: A flask (250 mL) was charged with TFPPy (148 mg, 0.24 mmol) and 5,5'-bis(cyanomethyl)-2,2'-bipyridine (115 mg, 0.48 mmol), 1,4-dioxane (100 mL) and aqueous KOH solution (8 mL, 4 M). The mixture was ultrasonicated for two minutes and then heated at 120 °C for 3 days. After cooling to room temperature, the precipitated was washed with HCl (aq. 1 M), water, THF and methanol for three times, respectively. The resulting powder was subjected to Soxhlet extraction with THF for two days. The powder was collected and dried at 120 °C under vacuum overnight to afford yellow crystallites in 81.50% isolated yield. Anal. Calcd for $(C_{72}H_{42}N_8)_n$: C,84.85; H, 4.15; N, 10.99. Found: C, 70.05; H, 3.52; N, 6.34. Note: The yields and microanalysis data were calculated for an infinite structure and also ignoring the presence of end-groups whose nature is unclear.

Synthesis of Re-Bpy-sp^{2}c-COF and Re-Bpy-sp^{2}c-P: Re-Bpy-sp^{2}c-COF and Re-Bpy-sp^{2}c-P were prepared according to a modified literature method.[5] COF or amorphous materials (10 mg) and $[Re(CO)_5Cl]$ (10 mg, 0.028 mmol) were dispersed and refluxed in 10 mL toluene for 40 min. The dark red product was filtered and washed with methanol for three times. The resulting powders were dried under vacuum overnight. ICP-OES analysis shows a Re content in Re-Bpy-sp^{2}c-COF of 18.1 wt. % (0.97 mmol g^{-1}) and Re-Bpy-sp^{2}c-P of 9.4 wt. %. The predicted theoretical surface areas of Re-Bpy-sp^{2}c-COF is 1835.57 m^2 g^{-1}.

Synthesis of Re(bpy)(CO)$_3$Cl: $Re(bpy)(CO)_3Cl$ was prepared according to a modified literature method.[6] In a 50 mL round-bottom flask, $Re(CO)_5Cl$ (0.251g, 0.68 mmol), 2,2′-bipyridine (0.106g, 0.68 mmol), and toluene (20 mL) were added together, and the resultant reaction mixture was refluxed under N_2 for 1 h. Upon cooling, the product was vacuum filtered and rinsed with cold toluene. ^{1}H NMR (δ, 400 MHz, DMSO-d_6): 9.02 (d, 1H), 8.77 (d, 1H), 8.34(t, 1H), 7.76(t, 1H).

3.4 The sp^{2}c-COF

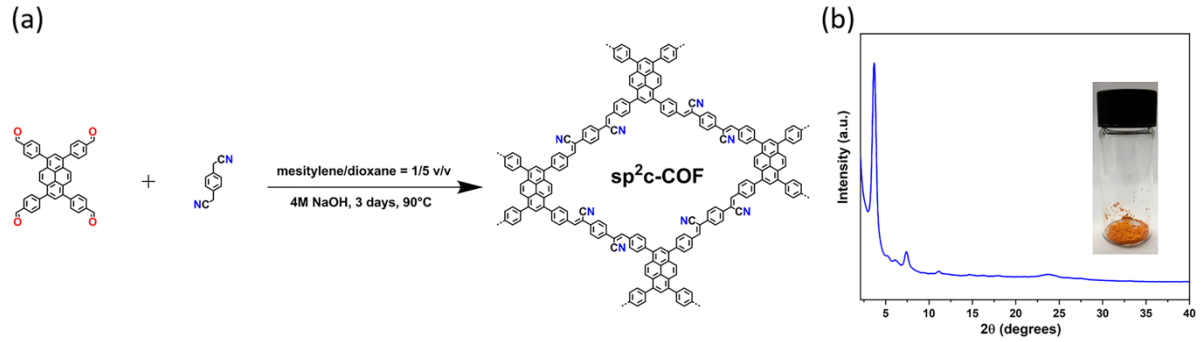

Figure 3.7 (a) Schematic representation of the synthesis of sp^{2}c-COF; (b) PXRD pattern of sp^{2}c-COF. Inset: the image of sp^{2}c-COF).

Table 3.1 Evolution rates of gaseous products of sp^{2}c-COF.

Catalysts	H_2 (μmol g^{-1} h^{-1})	CO (μmol g^{-1} h^{-1})	CO selectivity (%)
sp^{2}c-COF	1609.2	459.1	22.2

COF (1 mg), $CoCl_2$ (1 μmol), 2,2'-biyridine (2 mg, 12.8 μmol), solvent (4 mL, MeCN/H_2O=3:1), TEOA (1 mL), solar simulator (5 h), GC-BID Headspace.

Olefin COFs, which have good light absorbance ability and stability, have shown excellent photocatalytic performance for HER.[18–20] Hence, we try to repeat the sp^{2}c-COF in the literature and test it for photocatalytic CO_2 reduction. The sp^{2}c-COF (Figure 3.7a) was synthesized through Knoevenagel condensation of TFPPy and phenylenediacetonitrile (PDAN) in the presence of NaOH.[31] The powder X-ray diffraction (PXRD) pattern (Figure 3.7b) was the same as that in literature, proving the successful synthesis of sp^{2}c-COF. Next, the orange sp^{2}c-COF was tested for CO_2 reduction under the same system mentioned in **Chapter 1** with $[Co(bpy)_3]^{2+}$ as the cocatalyst and TEOA as the hole scavengers under UV ($\lambda > 295$ nm) light. After 5 hours of irradiation, sp^{2}c-COF generated H_2 with a rate of 1609.2 μmol g^{-1} h^{-1} and CO with a rate of 459.1 μmol g^{-1} h^{-1}, showing 22.2% selectivity over H_2. This demonstrated that such fully π-conjugated COFs had great potential as photocatalysts for CO_2 reduction. This olefin COF inspired us to design and synthesize a new type of sp^{2}c-COF for CO_2 reduction under visible light.

3.5 Bpy-sp^{2}c-COF

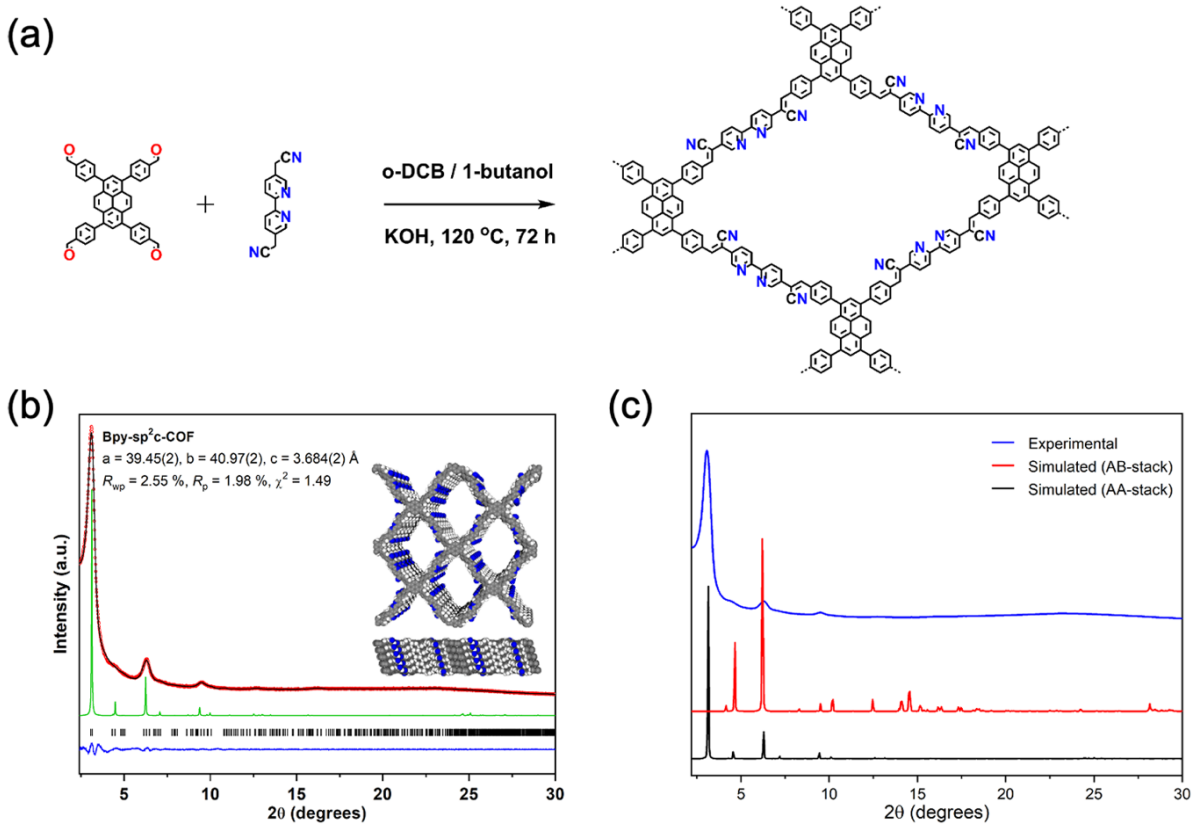

Figure 3.8 (a) Synthesis of **Bpy-sp^{2}c-COF**. Conditions for **Bpy-sp^{2}c-COF**: KOH (4 M) 1,2-dichlorobenzene and 1-butanol (1:1 mixture), 120 °C, 72 hours; (b) PXRD patterns of **Bpy-sp^{2}c-COF** obtained experimentally (red circles), simulated from the eclipsed AA-stacking mode (green), profiles calculated from Le Bail fitting (black) and residual (blue). Reflection positions are shown by tick marks. Inside: Structural models for **Bpy-sp^{2}c-COF** with eclipsed AA stacking patterns, shown parallel to the pore channel along the crystallographic c axis (top) and parallel to the layers (bottom); (c) Experimentally observed powder X-ray diffraction pattern of **Bpy-sp^{2}c-COF** (blue) and simulated profiles for AA and AB stacking modes (red and black).

Here, Knoevenagel condensation (Figure 3.8a) was used such that olefins become the COF linkers.[14,18,21] The aim was to increase the conjugation length in the framework and hence, to improve the performance of these materials for CO_2 reduction. The residual cyanovinyl-groups of the Knoevenagel condensation have been shown to be beneficial for CO_2 uptake,[22] which might also enhance the efficiency of CO_2 reduction. The COF was then loaded with $[Re(CO)_5Cl]$, giving a heterogeneous analogue of the well-studied

homogeneous catalyst [Re(bpy)$(CO)_3$Cl] with enhanced stability.[23] The obtained photocatalyst (Re-Bpy-sp^2c-COF) will be discussed in the next section. A two-dimensional (2D) sp^2c-COF (**Bpy-sp^2c-COF**) was synthesized via the Knoevenagel condensation of TFPPy and 5,5'-bis(cyanomethyl)-2,2'-bipyridine in 1,2-dichlorobenzene and 1-butanol at 120 °C for three days (Figure 3.8a).

The crystallinity of COFs is normally determined by PXRD. By comparing experimental PXRD results with calculated PXRD patterns from predicted COF models, the crystal structure of COFs can be determined. The PXRD pattern of **Bpy-sp^2c-COF** and simulated data are shown in Figure 3.8b. Structural models for **Bpy-sp^2c-COF** with eclipsed AA stacking patterns are show inset in Figure 3.8b. Red circles are the obtained experimentally PXRD pattern. The simulated pattern from the eclipsed AA-stacking mode is represented as a green line. The profiles calculated from Le Bail fitting are the black line and the residual is the blue line. Reflection positions are shown by tick marks. Le Bail refinements confirmed that the diffraction pattern was consistent with a triclinic lattice with unit cell parameters (a = 39.45(2), b = 40.97(2), c = 3.684(2) Å, α = 91.42(4)°, β = 89.5(2)°, γ = 90.5(2)°, V = 5953(5) $Å^3$). Goodness of fit (GoF) or χ relates the weighted profile R factor (R_{wp} = 2.55%) to the statistically expected value (R_p = 1.98%). This suggests that **Bpy-sp^2c-COF** has an eclipsed (AA) stacked structure rather than staggered (AB) stacking (Figure 3.8c), as the experimental PXRD data cannot match the simulated profiles for AB stacking modes. Diffraction peaks are observed at 3.1°, 4.5°, 6.2°, and 9.5°, corresponding to the (110), (200), (220), and (330) reflections, indicating that **Bpy-sp^2c-COF** has uniform 1D diamond-shaped pores.

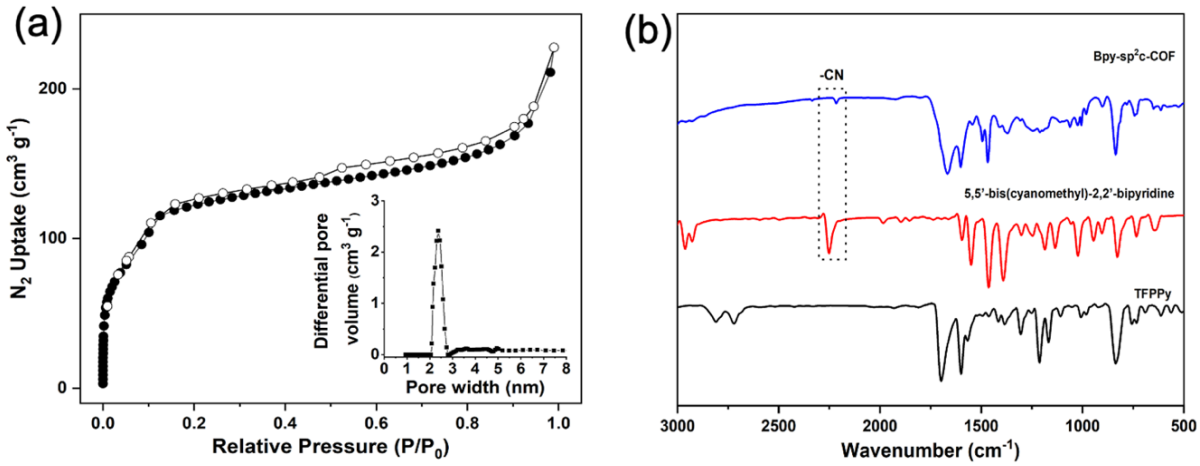

Figure 3.9 (d) N_2 Adsorption (filled dots) and desorption (open dots) isotherm profiles of **Bpy-sp^{2}c-COF** measured at 77 K. Inset: profile of the calculated pore size distribution of **Bpy-sp^{2}c-COF**; (e) FT-IR Spectra of **Bpy-sp^{2}c-COF**, TPFFy and 5,5'-bis(cyanomethyl)-2,2'-bipyridine.

To characterize the porosity of materials, N_2 adsorption experiments were measured at 77K. **Bpy-sp^{2}c-COF** showed reversible type-IV adsorption isotherms since a hysteresis loop was observed, which is associated with capillary condensation taking place in mesopores. Brunauer–Emmett–Teller surface area (SA_{BET}) for **Bpy-sp^{2}c-COF** is 432 m^2 g^{-1} which is measured by nitrogen sorption experiments at 77 K (Figure 3.9). The obtained SA_{BET} is lower than the theoretical SA_{BET} (2041 m^2 g^{-1}) for **Bpy-sp^{2}c-COF** of a perfectly crystalline structure. However, the same phenomenon can be observed for sp^{2}c-COFs which typically have surface areas ranging from 322 m^2 g^{-1} for sp^{2}c-COF-2[24] up to 692 m^2 g^{-1} for sp^{2}c-COF.[14] The pore size distribution profile based on nonlocal density functional theory (NLDFT) gives a narrow pore size distribution with a predominant pore width of 2.4 nm (Figure 3.9, inset curve), further indicating an AA stacking sequence that is predicted to have a pore size of 2.4 nm. Since **Bpy-sp^{2}c-COF** was synthesized via Knoevenagel condensation, fourier-transform infrared (FT-IR) spectroscopy was used to detect the formation of C=C bonds and the presence of the cyano side group. FT-IR spectroscopy reveals the characteristic -C≡N vibration band as a distinct peak at 2217 cm^{-1}, indicating the successful synthesis of **Bpy-sp^{2}c-COF** (Figure 3.9).[24,25] The PXRD, gas sorption and FTIR data demonstrated that the olefin COF (**Bpy-sp^{2}c-COF**)

was successful synthesized, and that this COF has a 2D crystalline and porous structure with a pore size of 2.4 nm.

3.6 Re-Bpy-sp^{2}c-COF

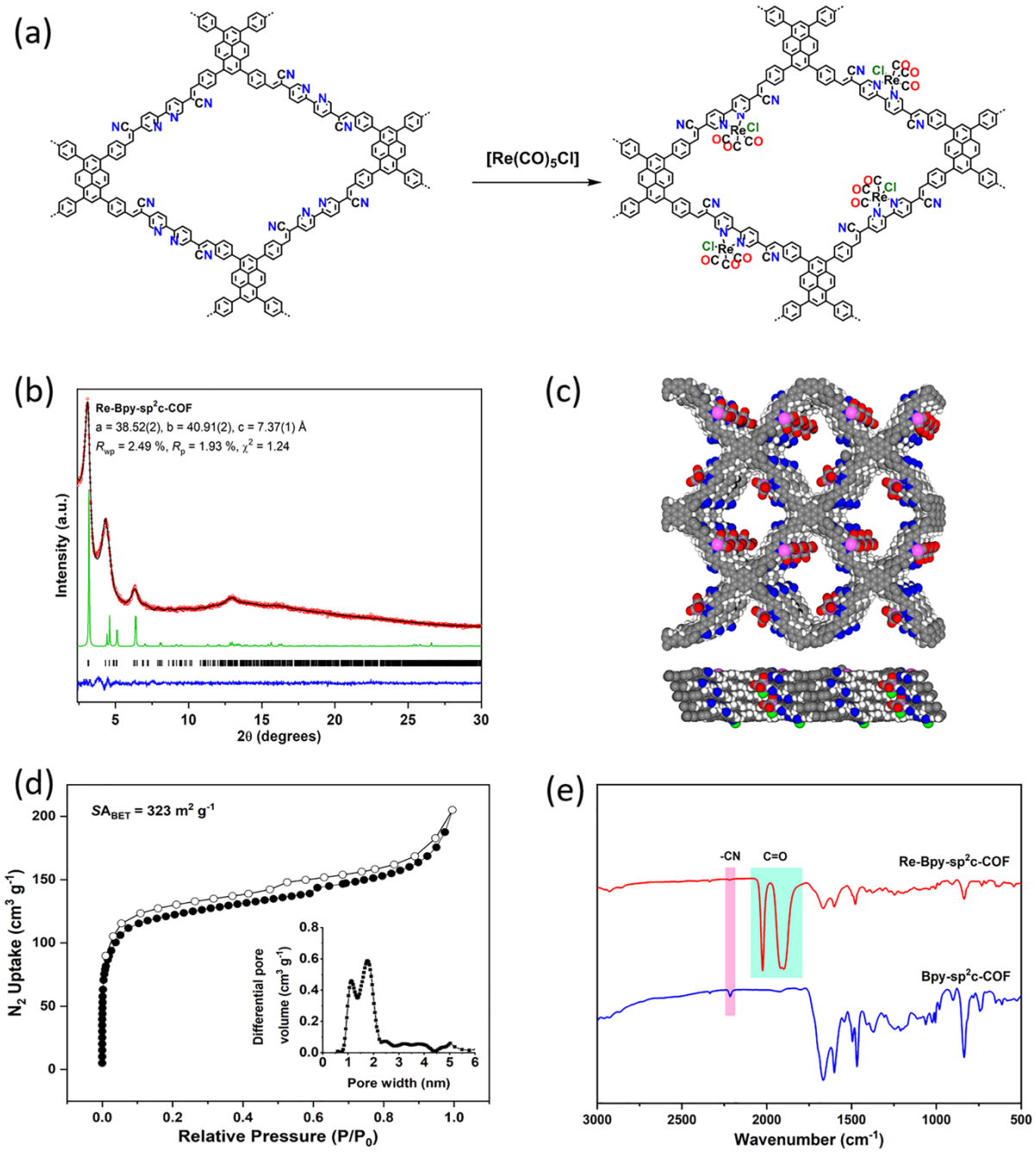

Figure 3.10 (a) Synthesis of **Re-Bpy-sp^{2}c-COF**. Conditions for **Re-Bpy-sp^{2}c-COF**: COF (10 mg), $[Re(CO)_5Cl]$ (10 mg, 0.028 mmol), toluene (10 mL), reflux, 40 mins; (b) PXRD patterns of **Re-Bpy-sp^{2}c-COF** obtained experimentally (red circles), simulated from the eclipsed AA-stacking mode (green), profiles calculated from Le Bail fitting (black) and residual (blue). Reflection positions are shown by tick marks; (c) Structural models for

Re-Bpy-sp^{2}c-COF with eclipsed AA stacking patterns, shown parallel to the pore channel along the crystallographic c axis (top) and parallel to the layers (bottom); (d) N_2 Adsorption (filled dots) and desorption (open dots) isotherm profiles of **Re-Bpy-sp^{2}c-COF** measured at 77 K. Inset: profile of the calculated pore size distribution of Re-Bpy-sp^{2}c-COF; (e) FT-IR Spectra of **Bpy-sp^{2}c-COF** and **Re-Bpy-sp^{2}c-COF**.

Since it was first reported in 1983 for photocatalytic CO_2 reduction,[26] Re complexes have been well studied owing to their high efficiency and selectivity for CO formation.[27,28] Hence, the bipyridine sites in **Bpy-sp^{2}c-COF** were used to ligate [$Re(CO)_5Cl$] to form **Re-Bpy-sp^{2}c-COF** (Figure 3.10a). To do this, 10 mg **Bpy-sp^{2}c-COF** and [$Re(CO)_5Cl$] (10 mg, 0.028 mmol) were dispersed and refluxed in 10 mL toluene for 40 min. The dark red product was filtered and washed with methanol three times.

The PXRD pattern of **Re-Bpy-sp^{2}c-COF** (Figure 3.10b) exhibits peaks at 3.1°, 4.5°, 6.2°, 12.9°, corresponding to (110), (200), (220), (-221) reflections predicted for the Re-loaded, AA-stacked model (Figure 3.10c). Le Bail refinements confirmed that the diffraction pattern was consistent with a triclinic lattice with unit cell parameters (a = 38.52(2), b = 40.91(2), c = 7.37(1) Å, α= 91.3(8)°, β = 91.6(5)°, γ = 89.18(5)°, V = 11608(23) Å^3). The porosity of **Re-Bpy-sp^{2}c-COF** was measured by N_2 sorption experiments. **Re-Bpy-sp^{2}c-COF** also showed reversible type-IV adsorption isotherms. The BET surface area (SA_{BET}) for **Re-Bpy-sp^{2}c-COF** was calculated to be 323 $m^2\ g^{-1}$ (Figure 3.8d). The pore size distribution profile exhibits two overlapping pore size features (Figure 3.8d, inset curve) due to the ligation of Re complex. FT-IR spectrum was used to detect the Re moiety in the COFs. The FT-IR spectrum for the Re-modified COF (Figure 3.10e) is consistent with the CO-stretching bands of the incorporated [$Re(CO)_3Cl$)] complex as new peaks at 1900 cm^{-1}, 1917 cm^{-1}, 2024 cm^{-1}.[12,23] These data demonstrated the successful introduction of Re complexes into a COF backbone and the obtained **Re-Bpy-sp^{2}c-COF** was still crystalline and porous.

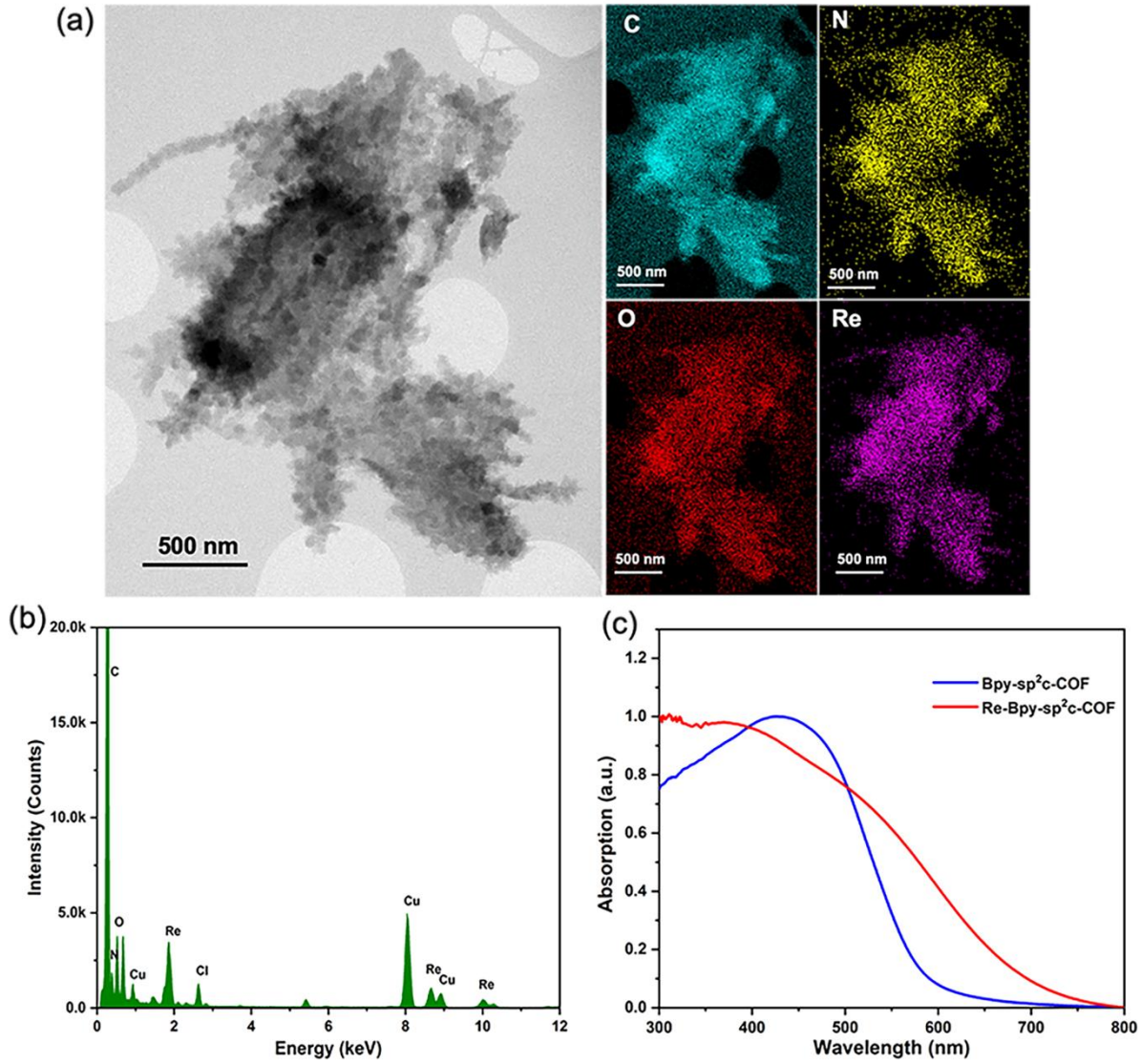

Figure 3.11 (a) STEM images and EDX mapping of **Re-Bpy-sp^{2}c-COF**; (b) EDX spectrum of **Re-Bpy-sp^{2}c-COF**; (c) Solid-state reflectance UV-vis spectra of **Bpy-sp^{2}c-COF** and **Re-Bpy-sp^{2}c-COF**.

A uniform distribution of C, N, O, and Re in **Re-Bpy-sp^{2}c-COF** is demonstrated by scanning transmission electron microscopy (STEM) and energy-dispersive X-ray spectroscopy (EDX) mapping images (Figure 3.11a and b), further suggesting that the Re moiety has been incorporated uniformly throughout the COFs. Inductively coupled plasma - optical emission spectrometry (ICP-OES) measurements suggest that 18 wt. % of Re has been incorporated into **Bpy-sp^{2}c-COF**. It is calculated that half of the bipyridine sites in the COF backbone are coordinated by the Re complex. The ratio is also the same with the calculation in the atomistic model built to represent **Re-Bpy-sp^{2}c-COF** (Figure 3.10c). Compared to **Bpy-sp^{2}c-COF**, a red-shift of the absorption

edge from 589 nm to 694 nm is observed for **Re-Bpy-sp^{2}c-COF** by UV-Visible diffuse reflectance spectra (Figure 3.11c). This means the **Re-Bpy-sp^{2}c-COF** has better visible light absorption ability than the pristine COF. A similar phenomenon was also observed in literature, which was supposed due to the vibronic broadening of materials or the increased delocalization by the chelation of Re complexes.[12]

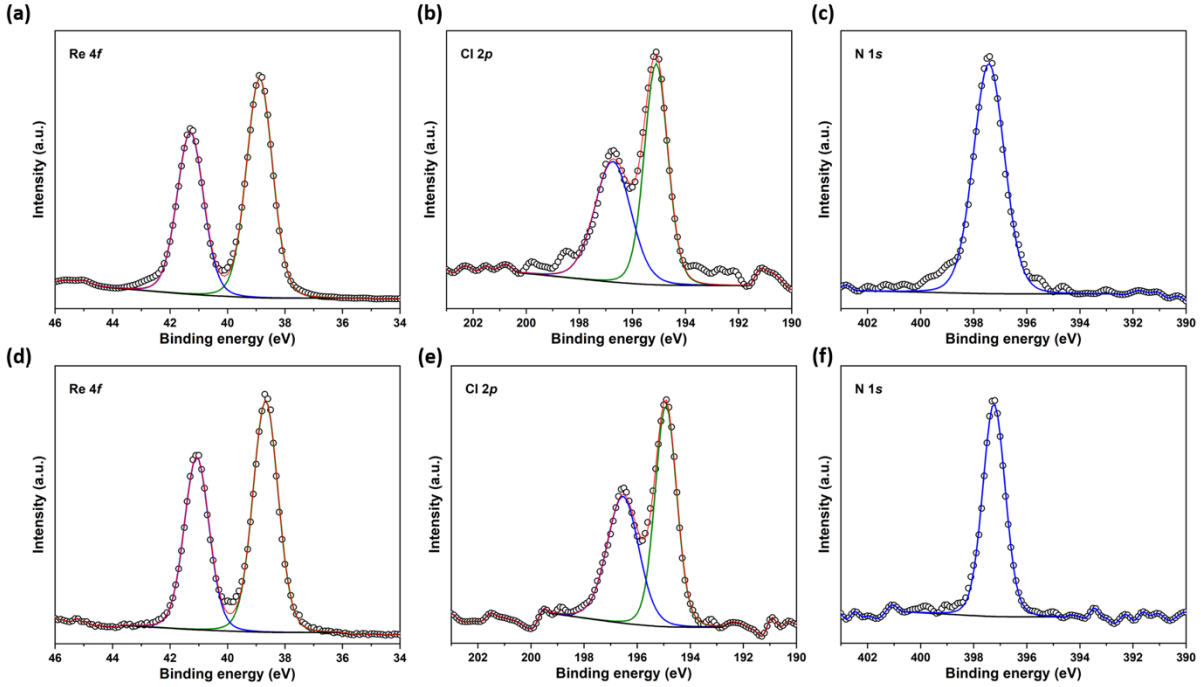

Figure 3.12 HR XPS analysis of Re 4f (a), Cl 2p (b) and N 2s (c) signals of **Re-Bpy-sp^{2}c-COF** and Re 4f (d), Cl 2p (e) and N 2s (f) signals of **Re(bpy)(CO)$_3$Cl**.

Finally, X-ray photoelectron spectra (Figure 3.12) was performed for **Re-Bpy-sp^{2}c-COF** and Re(Bpy)(CO)$_3$Cl to explore the local environment of Re. XPS showed similar features and binding energies for Re 4f $_{5/2}$ at 38.9 eV and 4f $_{7/2}$ at 41.3 eV, indicating that the Re species in both materials had similar coordination environments. The signal for Cl 2p and N 2s was also very similar in both cases. This showed that Re complexation in the COF is very likely to be the same as in the molecular catalyst. Taken together, by refluxing **Bpy-sp^{2}c-COF** with Re complexes in toluene, **Re-Bpy-sp^{2}c-COF** was obtained. Characterizations demonstrated the crystalline and porous structure of **Re-Bpy-sp^{2}c-COF** and the uniform distribution of Re moiety coordinated to the bipyridine moieties. This COF has fully π-conjugated structure and good light absorption ability, which has great potential for photocatalytic CO_2 reduction.

3.7 Re-Bpy-sp^{2}c-P

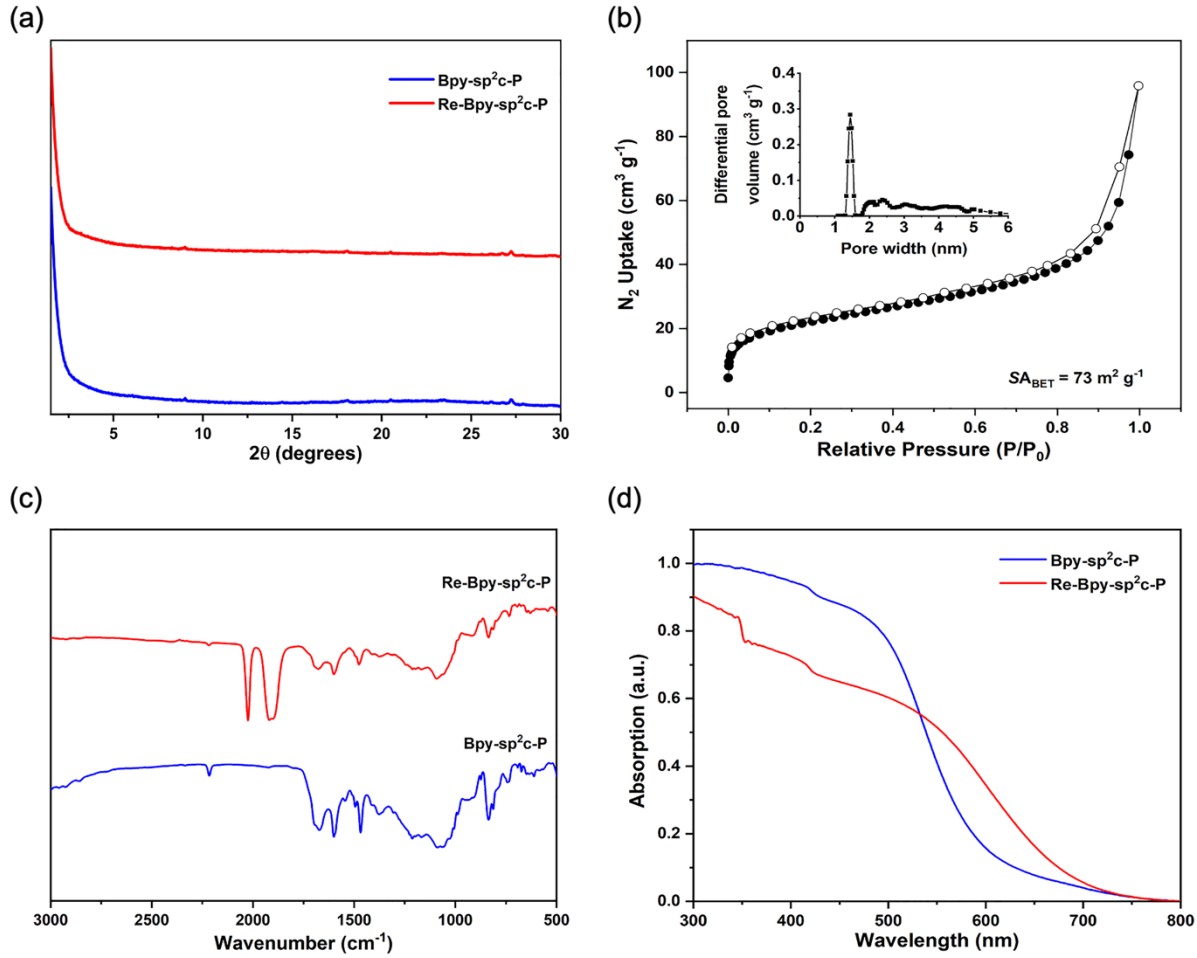

Figure 3.13 (a) PXRD patterns of **Bpy-sp^{2}c-P** and **Re-Bpy-sp^{2}c-P** obtained experimentally; (b) N_2 Adsorption (filled dots) and desorption (open dots) isotherm profiles of **Bpy-sp^{2}c-P** measured at 77 K. Inset: profile of the calculated pore size distribution of **Bpy-sp^{2}c-P**; (c) FT-IR Spectra of **Bpy-sp^{2}c-P** and **Re-Bpy-sp^{2}c-P**; (d) Solid-state reflectance UV-vis spectra of **Bpy-sp^{2}c-P** and **Re-Bpy-sp^{2}c-P**.

In previous literature, crystallinity[8] and accessible surface area[29] have been shown to be crucial factors for the photocatalytic activity of organic photocatalysts. To investigate whether these factors also influence the performance of **Re-Bpy-sp^{2}c-COF** in photocatalytic CO_2 reduction, an amorphous analogue **Bpy-sp^{2}c-P** was synthesized by using 1,4-dioxane instead of a 1,2-dichlorobenze/1-butanol mixture under otherwise exactly the same experimental conditions. **Re-Bpy-sp^{2}c-P** was prepared by using the same method for **Re-Bpy-sp^{2}c-COF**. **Bpy-sp^{2}c-P** (10 mg) and $[Re(CO)_5Cl]$ (10 mg, 0.028 mmol) were dispersed and refluxed in 10 mL toluene for 40 min. ICP-OES

measurements suggested that 9.4 wt. % of Re has been incorporated into **Bpy-sp^{2}c-P**. The BET surface area (SA_{BET}) for **Bpy-sp^{2}c-P** was calculated to be 73 m^2 g^{-1} (Figure 3.13b) which was much lower than those of COFs and caused the lower Re loading amount. The pore size distribution profile exhibits a narrow pore size distribution (Figure 3.13b, inset curve). FT-IR and UV-visible spectra (Figure 3.13c and Figure 3.13d) are comparable to those of **Bpy-sp^{2}c-COF** and **Re-Bpy-sp^{2}c-COF**. The peak at 2217 cm^{-1} belonged to -C≡N vibration band, and peaks at 1900 cm^{-1}, 1917 cm^{-1}, 2024 cm^{-1} was proven as the CO-stretching bands of the incorporated [$Re(CO)_3Cl$)] complex. A red-shift of the absorption edge was also found in the UV-visible spectrum. All of these measurements demonstrated that the successful synthesis of **Bpy-sp^{2}c-P** and **Re-Bpy-sp^{2}c-P** with properties similar to those of **Bpy-sp^{2}c-COF** and **Re-Bpy-sp^{2}c-COF** except smaller surface areas and lower Re loading amounts.

3.8 CO_2 uptake

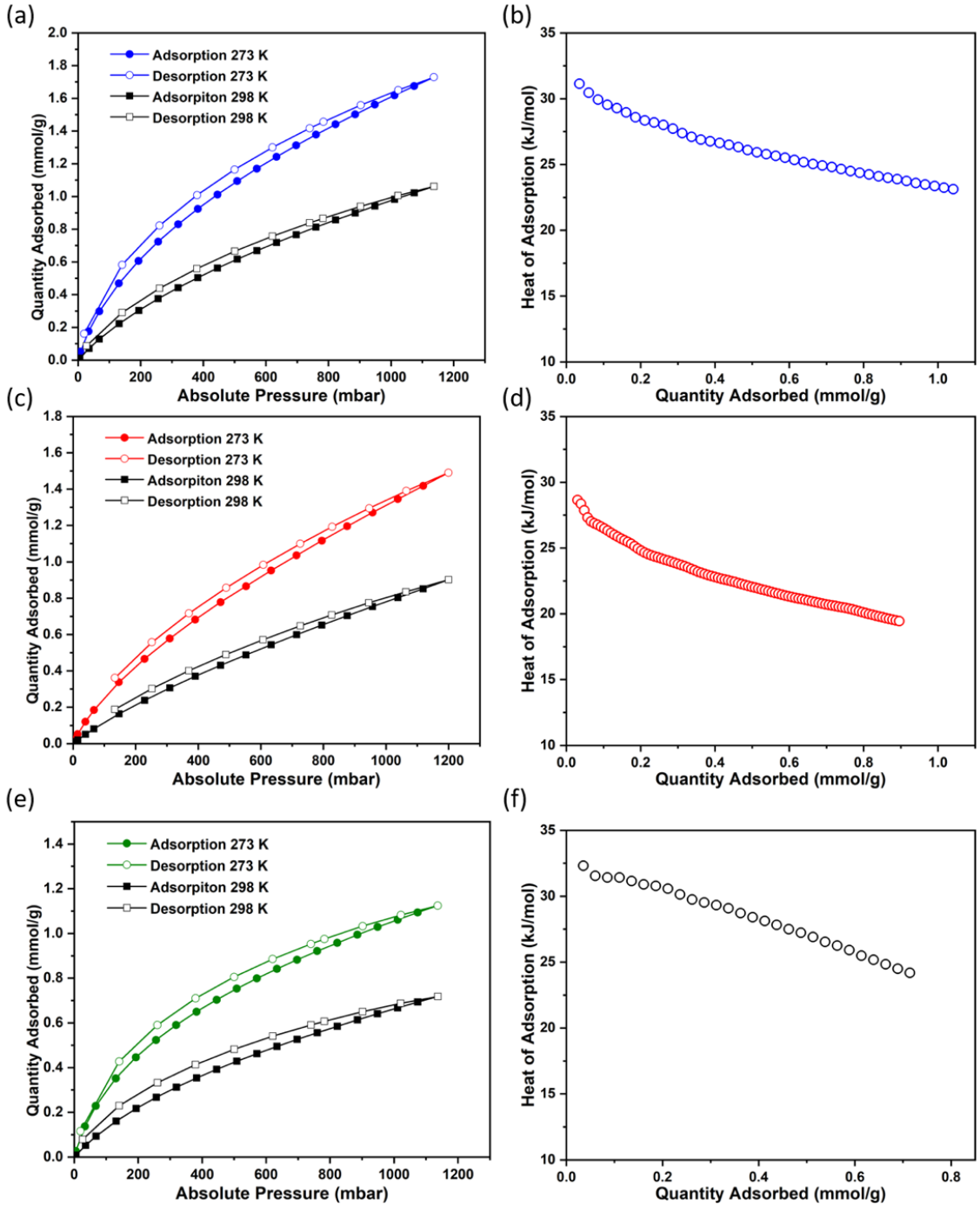

Figure 3.14 CO_2 sorption isotherms and CO_2 isosteric heat of adsorption calculated from 273 K and 298 K of **Re-Bpy-sp^{2}c-COF** (a, b), **Bpy-sp^{2}c-COF** (c, d) and **Bpy-sp^{2}c-P** (e, f).

The efficient interaction between photocatalysts and CO_2 molecules is believed as a factor for CO_2 reduction.[30] Hence, CO_2 uptake was tested for **Bpy-sp^{2}c-COF**, **Re-Bpy-sp^{2}c-COF** and **Bpy-sp^{2}c-P** up to 1200 mbar at both 273 and 298 K. The CO_2 adsorption

of **Re-Bpy-sp^{2}c-COF** was 1.7 mmol g^{-1} at 273 K and 1.1 mmol g^{-1} at 298 K (Figure 3.14a). The CO_2 adsorption of **Bpy-sp^{2}c-COF** was 1.5 mmol g^{-1} at 273 K and 0.9 mmol g^{-1} at 298 K (Figure 3.14c), which were lower than those of **Re-Bpy-sp^{2}c-COF**. **Bpy-sp^{2}c-P** had low CO_2 uptake ability (Figure 3.14e) with 1.1 mmol g^{-1} at 273 K and 0.7 mmol g^{-1} at 298 K. The isosteric heats of adsorption (*Q*st) were calculated to investigate the CO_2 affinity of these materials. The isosteric heat of adsorption of **Re-Bpy-sp^{2}c-COF**, **Bpy-sp^{2}c-COF** and **Bpy-sp^{2}c-P** (Figure 3.14c, d, and f) were 31 kJ mol^{-1}, 28 kJ mol^{-1} and 32 kJ mol^{-1}, respectively. All the materials with residual cyanovinyl-groups of the Knoevenagel condensation demonstrated a good affinity toward CO_2, which might also enhance the efficiency of CO_2 reduction.[22]

3.9 CO_2 reduction characterization

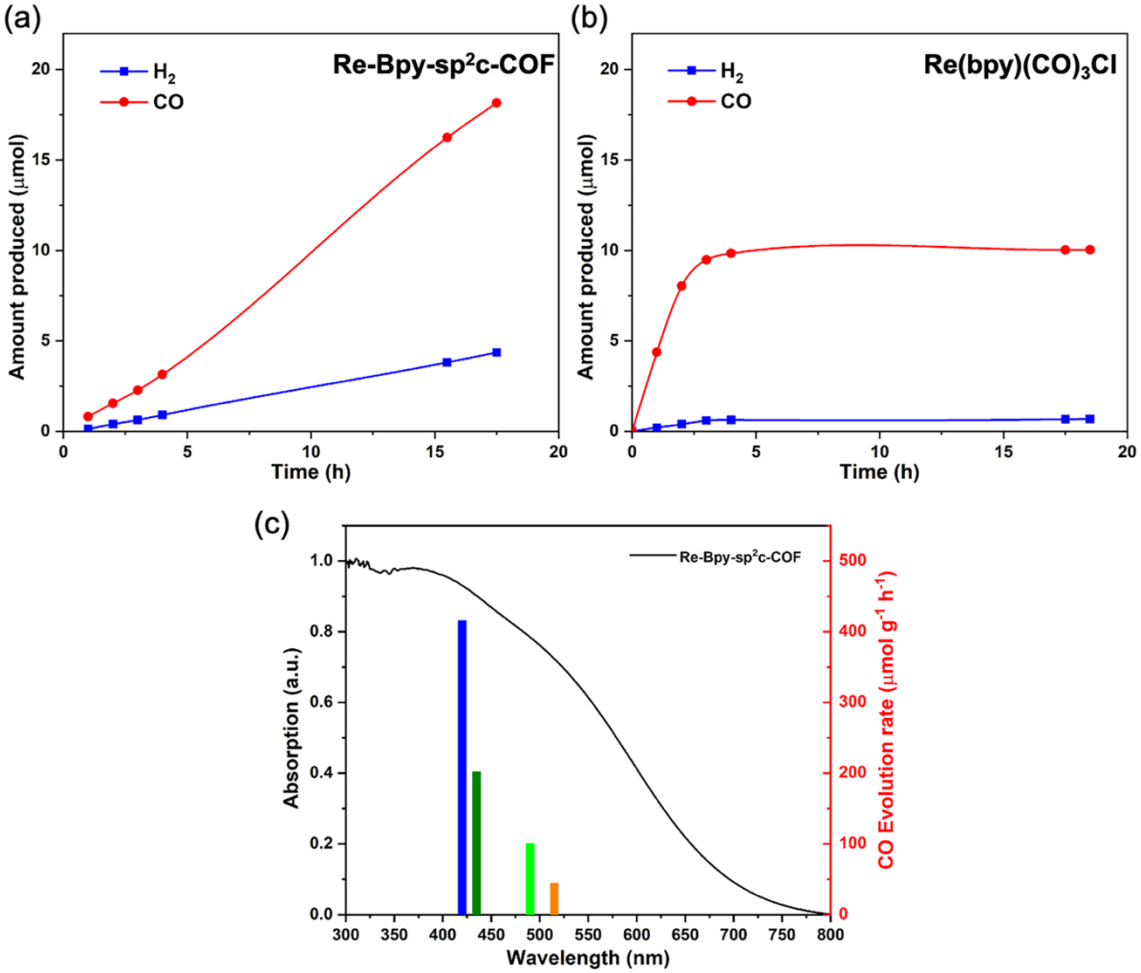

Figure 3.15 CO_2 reduction experiments of **Re-Bpy-sp^{2}c-COF** (1 mg) (a) and **Re(bpy)(CO)$_3$Cl** (0.45 mg, 0.97 μmol) (b) from MeCN and TEOA (5 mL, 30/1) under visible light irradiation (λ > 420 nm, 300 W Xe light source);

(c) Wavelength dependent CO evolution experiments of **Re-Bpy-sp^{2}c-COF** (1 mg) from 5 mL MeCN/TEOA (30/1) solution under monochromatic light (± 10 nm, fwhm) in a photoreactor with path length of 5 cm at 420 nm (blue), 435 nm (deep green), 490 nm (green), and 515 nm (orange).

Photocatalytic CO_2 reduction experiments were performed in a customed quartz cuvette (V = 27 mL) under 1 atmosphere CO_2 and visible light illumination ($\lambda > 420$ nm, 300 W light source). A mixture of acetonitrile and triethanolamine in a 30:1 ratio was used. MeCN acts as a solvent to disperse the catalyst, while TEOA is the sacrificial electron donor and proton source. Gaseous products were taken with a gas-tight syringe and run on a Shimadzu GC-2014 gas chromatograph equipped with a ShinCarbon ST micropacked column (Restek 80-100 mesh, 2 m length, 0.53 mm inner diameter) and a thermal conductivity detector.

As shown in Figure 3.15a, after 17.5 hours of irradiation under visible light ($\lambda > 420$ nm), **Re-Bpy-sp^{2}c-COF** generated CO with a rate of 1040 μmol g^{-1} h^{-1} (TON = 18.7) and 81% selectivity over H_2. Wavelength dependent CO evolution experiments for measuring apparent quantum yield (AQY) were carried out at 420, 435, 490 and 515 nm, respectively. An AQY of 0.5% was measured at 420 nm for CO production (Figure 3.15c). In contrast, the homogeneous counterpart deactivated after 3 hours with a TON of 10.3 under the same conditions (Figure 3.15b). In such an experimental condition, competing proton reduction of water traces in the TEOA or oxidative dehydrogenation of TEOA might cause a small amount of H_2 to be produced by **Re-Bpy-sp^{2}c-COF**.[31] The critical role of the Re-complex was proved by **Bpy-sp^{2}c-COF** (Table 3.2) which only generated trace amounts of CO and a non-detectable amount of H_2 in the absence of the Re complex. Integrating the Re complex into the COF backbone can significantly improve its performance.

Table 3.2 Photocatalytic CO_2 reduction using different experimental conditions.

Entry	Photocatalyst	CO (μmol)	H_2 (μmol)	Re content (μmol)	TON (CO)	CO selectivity (%)

1[a]	Re-Bpy-sp^{2}c-COF	12.48	2.99	0.97	12.9	80.7
2[a]	Bpy-sp^{2}c-COF	0.21	n.d.	0	/	/
3[b]	Re-Bpy-sp^{2}c-COF	0.18	3.42	0.97	0.2	5.0
4[c]	Re-Bpy-sp^{2}c-COF	n.d.	n.d.	0.97	/	/
5[d]	Re-Bpy-sp^{2}c-COF	n.d.	n.d.	0.97	/	/
6[e]	Re-Bpy-sp^{2}c-COF	2.32	0.76	0.97	2.4	75.2
7[a]	Re-Bpy-sp^{2}c-P	1.15	0.07	0.50	2.3	94.5
8[a]	Bpy-sp^{2}c-P	-	0.18	0	/	-
9[e]	Re(bpy)(CO)$_3$Cl	10.03	0.67	0.97	10.3	93.8

[a] Reaction conditions: Photocatalyst (1 mg), solvent (5 mL, acetonitrile/TEOA = 30 : 1), CO_2 (1 atm.), 300 W Xe light source equipped with $\lambda > 420$ nm cut-off filter, 12 hours; [b]Ar atmosphere instead of CO_2; [c]In the dark; [d]Without TEOA; [e] Acetonitrile was replaced with dimethylformamide; [f]Photocatalyst (0.45 mg, 0.97 μmol), Solvent (5 mL, acetonitrile/TEOA = 30 : 1), CO_2 (1 atm.), 300 W Xe light source equipped with $\lambda > 420$ nm cutoff filter, 12 hours; n.d.: none detected.

The crucial factors of crystallinity and porosity are demonstrated by the amorphous polymer **Re-Bpy-sp^{2}c-P**, showing significantly lower activity for CO_2 reduction (Table 3.2) with a TON of 2.3 after 12 hours compared to 12.9 for **Re-Bpy-sp^{2}c-COF**. This is the first study that compares crystalline COFs directly with amorphous analogs for photocatalytic CO_2 reduction. The crystalline COFs are much more active for the CO production from CO_2.

A series of control experiments were conducted as easy, cheap, and fast ways to confirm that the source of the CO generated is indeed a photocatalytic process (Table 3.2). Under an argon atmosphere in the absence of CO_2, **Re-Bpy-sp^{2}c-COF** produced H_2 and CO at a rate of 285.3 μmol g^{-1} h^{-1} and 14.9 μmol g^{-1} h^{-1}, respectively. Decomposition of organic residues during photocatalysis[32] or ineffective side-reaction of decomposition of TEOA might be the source of the small amount of CO generated.[31] Without light or scavengers,

no gas production was determined. Liquid phase products, *i.e.*, HCOOH and methanol, were tested for by NMR and could not be observed for **Re-Bpy-sp^{2}c-COF**, indicating the CO is the only product from CO_2. Results from control experiments show the CO was the product from photocatalytic CO_2 reduction in the system, and the process is indeed photocatalytic and driven by the COFs.

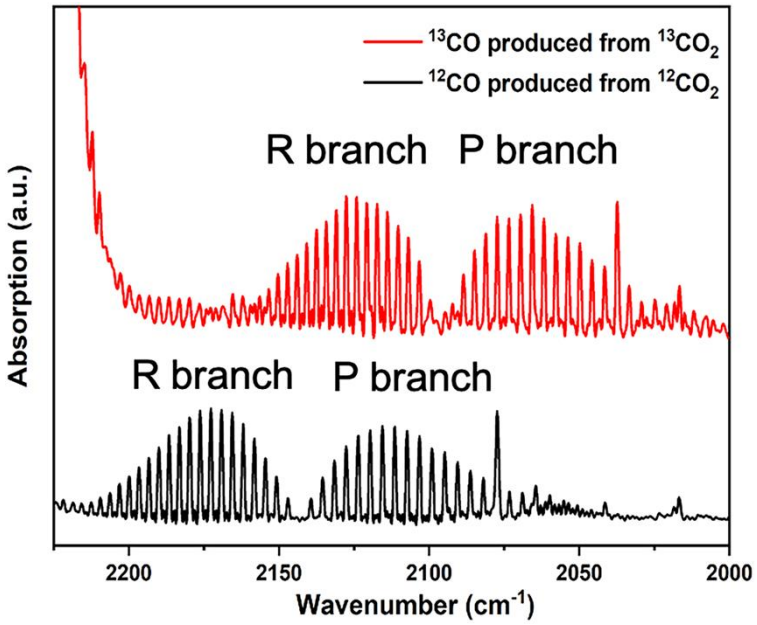

Figure 3.16 FT-IR Spectra of ^{13}CO produced in the photoreduction of $^{13}CO_2$.

Finally, an experiment by using $^{13}CO_2$ was carried out to further prove CO_2 was the carbon source for the CO. To do this, a 12 mL vial was used to ensure the concentration of generated CO was sufficient for measurement. The vial was charged with 1 mg Re-Bpy-sp^{2}c-COF and 5 mL solvent (acetonitrile/TEOA = 30 : 1). The mixture was purged with $^{13}CO_2$ for 3 minutes, then the vial was illuminated for 4 hours using a 300 W Xe light source equipped with a $\lambda > 420$ nm filter. FT-IR spectra showed a series of regularly spaced peaks centered at 2140 cm^{-1} and 2098 cm^{-1}, respectively, belonging to the P and R branch transitions of ^{12}CO and ^{13}CO.[33] FT-IR spectra with isotope labelling under $^{12}CO_2$ and $^{13}CO_2$ atmospheres confirmed the formation of ^{13}CO, strongly supporting that CO_2 was the source of the produced CO (Figure 3.16).[33]

Table 3.3 Previously reported photocatalytic CO_2 reduction using COFs.

Photocatalyst	Main products and highest yield	TON	Selectivity	Reaction solvent	Irradiation condition	Reference

	(μmol h^{-1} g^{-1})					
Re-bpy-sp^2c-COF	1040 (CO)	18.7 (17.5 h)	80.7% (CO)	MeCN / TEOA (30/1)	λ > 420 nm (300 W Xe light source)	This work
Re-COF	750 (CO)	48	98% (CO)	MeCN / TEOA (3:0.2)	λ > 420 nm (225 W Xe light source)	12
Ni-TpBpy-COF $[Ru(bpy)_3]Cl_2$	966 (CO)	13.6	96% (CO)	MeCN / H_2O / TEOA (3/1/1)	λ ≥ 420 nm (300 W Xe light source)	13
Re-TpBpy-COF	270 (CO)	-	-	MeCN / H_2O (10/1.8 mL), 0.1 M TEOA	λ > 390 nm (200 W Xe light source)	34
DQTP-COF-Co $[Ru(bpy)_3]Cl_2$	1020 (CO)	2.18	59.4% (CO)	MeCN / TEOA (4/1)	λ ≥ 420 nm (300 W Xe light source)	35
ACOF-1	0.36 (CH_3OH)	-	-	CO_2 and H_2O (0.4 MPa, 80 °C)	800 nm ≥ λ ≥ 420 nm (500 W Xe light source)	11
N_3-COF	0.57 (CH_3OH)	-	-	CO_2 and H_2O (0.4 MPa, 80 °C)	800 nm ≥ λ ≥ 420 nm (500 W Xe light source)	11

The photocatalytic performance of **Re-Bpy-sp^2c-COF** is comparable with other reported COFs in terms of CO generation rate and CO/H_2 selectivity (Table 3.3). For instance, a rhenium modified 2D imine-triazine COF produced around 750 μmol g^{-1} h^{-1} CO with 98% selectivity,[12] and a *β*-ketoenamine-linked COF modified with nickel gave a CO production rate of 811 μmol g^{-1} h^{-1} CO with 96% selectivity with an additional dye.[13] However, these COFs cannot maintain their crystalline structures after photocatalysis. Some of them need additional photosensitizers due to their limited light harvesting and/or subsequent energy transfer abilities. Considering different experimental set-up affect photocatalytic rates, comparisons between materials in literature should make with caution.[36]

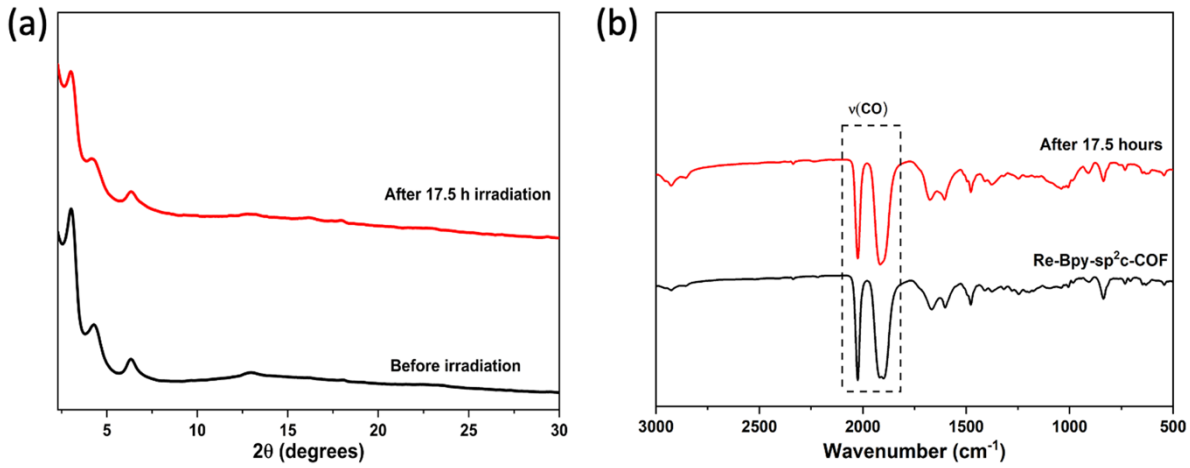

Figure 3.17 (a) Experimentally observed powder X-ray diffraction pattern of **Re-Bpy-sp^{2}c-COF** before and after 17.5 hours irradiation; (b) FT-IR spectra of **Re-Bpy-sp^{2}c-COF** before and after 17.5 hours of visible light irradiation (300 W Xe light source, $\lambda > 420$ nm).

Stability is a very important factor for photocatalysts. PXRD and FTIR were tested for **Re-Bpy-sp^{2}c-COF** before and after photocatalysis to determine the crystalline structure and Re complexes inside the COFs. **Re-Bpy-sp^{2}c-COF** can also keep its crystallinity, evident from the post-illumination PXRD patterns (Figure 3.17a) of the sample after photolysis of 17.5 hours. This shows that the material has very good stability compared to other previous reports of Re-COF and Ni-TpBpy-COF.[12,13] From the post-illumination FT-IR spectra (Figure 3.17b), **Re-Bpy-sp^{2}c-COF** appears to be stable under the photocatalysis conditions after 17.5 hours of continuous visible light illumination ($\lambda > 420$ nm, 300 W Xe light source). The peaks at 1900 cm^{-1}, 1917 cm^{-1}, 2024 cm^{-1} corresponding to the CO-stretching bands of the incorporated [$Re(CO)_3Cl$)] complex were same for **Re-Bpy-sp^{2}c-COF** before and after photocatalysis, further proving the excellent stability of **Re-Bpy-sp^{2}c-COF**.

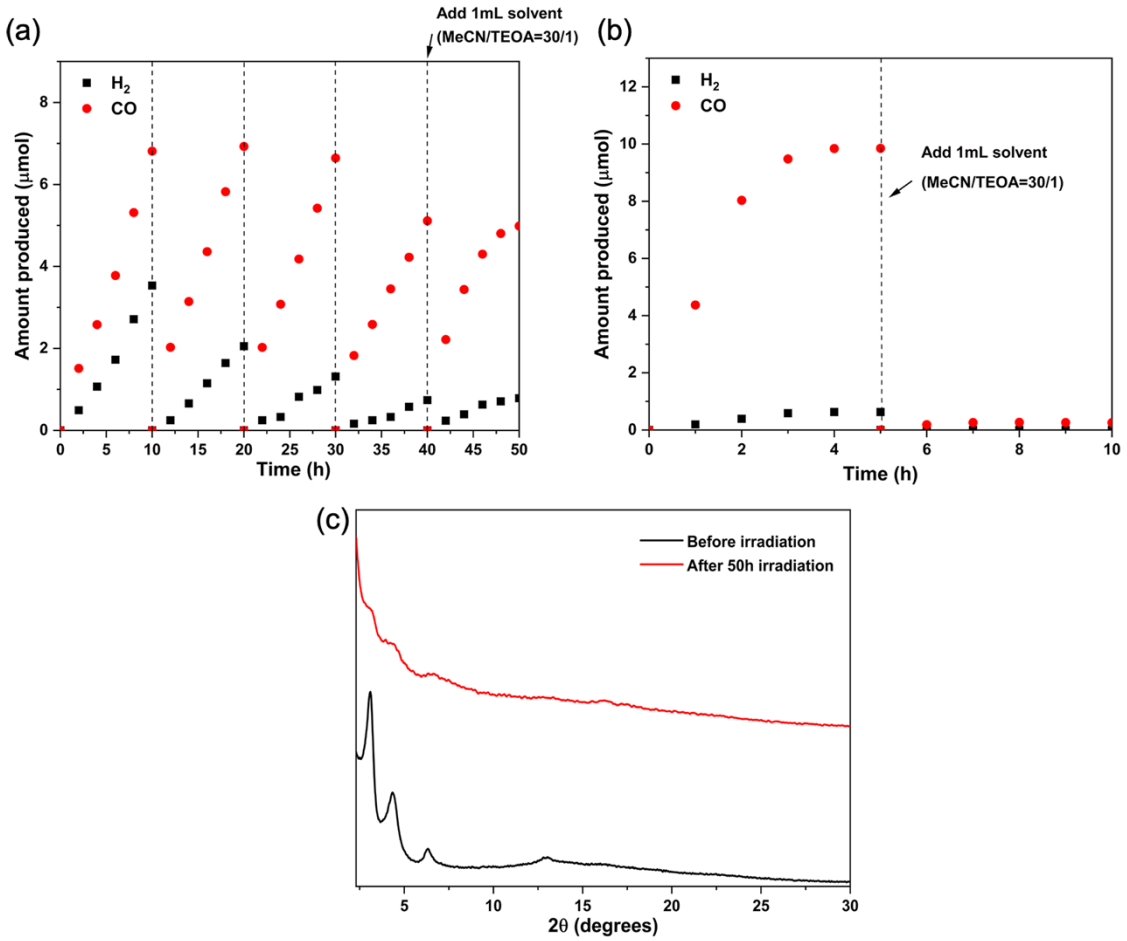

Figure 3.18 (a) Stability and reusability test using **Re-Bpy-sp^{2}c-COF** (1mg) (a) and **Re(Bpy)(CO)$_3$Cl** (0.97 μmol) (b) as a photocatalyst under visible light irradiation (λ > 420 nm) in 5 mL MeCN/TEOA (30/1) solvent for 50 h and 10 h.; (c) Experimentally observed powder X-ray diffraction pattern of **Re-Bpy-sp^{2}c-COF** before and after 50 hours irradiation.

To further study the stability of **Re-Bpy-sp^{2}c-COF**, a 50 hour experiment was performed. The quartz flask was degassed with CO_2 every 10 hours. Results in Figure 3.18a indicated **Re-Bpy-sp^{2}c-COF** could produce CO constantly while the molecular catalyst stopped after 5 hours. However, the molecular catalyst lost its activity after 4 hours irradiation (Figure 3.18b). After adding 1 mL fresh MeCN/TEOA mixture and re-degassing with CO_2, the molecular catalyst still has no activity. PXRD patterns of **Re-Bpy-sp^{2}c-COF** after photocatalysis (Figure 3.18c) showed a loss of crystallinity. This along with a loss of activity highlighted that structural stability is still one of the important challenges in the field. Nevertheless, it seems that in making a heterogeneous

analogue of [Re(bpy)(CO)$_3$Cl] an increase in stability is observed (Figure 3.18a and b), possibly by preventing the formation of the dimer of the Re-complex[23] which occurs in Re(bpy)CO$_3$Cl followed by catalyst degradation, and shielding of the Re-centre in the photocatalyst from light.[37]

3.10 Photoelectrochemical characterization

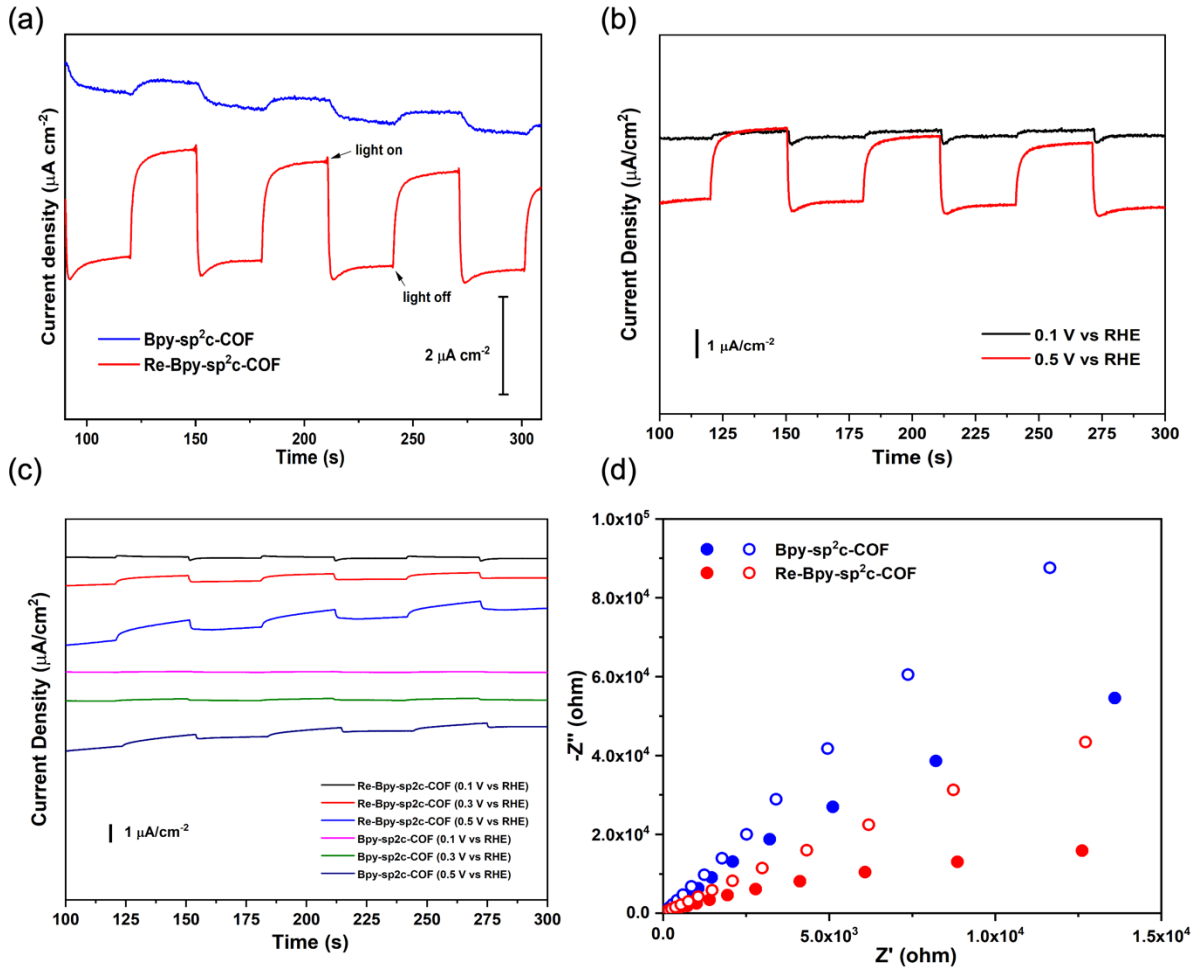

Figure 3.19 (a) Transient photocurrent response at 0.5 V vs RHE in 0.1 M Na_2SO_4 solution under intermittent light irradiation for **Bpy-sp^{2}c-COF** and **Re-Bpy-sp^{2}c-COF**; (b) Transient photocurrent response at different potentials in aqueous solution vs RHE under intermittent light irradiation for **Re-Bpy-sp^{2}c-COF**; (c) Transient photocurrent response at different potentials in acetonitrile vs RHE under intermittent light irradiation for B**py-sp^{2}c-COF** and **Re-Bpy-sp^{2}c-COF**; (d) Nyquist plots of **Bpy-sp^{2}c-COF** (blue) and **Re-Bpy-sp^{2}c-COF** (red) at a voltage of 0.5 V vs. RHE in 0.1 M Na_2SO_4 solution under dark (open dots) and light irradiation (closed dots).

The origins of excellent photocatalytic CO_2 reduction performance of **Re-Bpy-sp^{2}c-COF** were further studied. To investigate its charge separation and transformation properties, photoelectrochemical experiments were employed using FTO glass as a photocathode in 0.1 M Na_2SO_4 solution (Figure 3.19a). All samples were tested at a constant voltage of 0.5 V vs reversible hydrogen electrode (RHE). The photocurrent of **Re-Bpy-sp^{2}c-COF** photocathode was about 2 μA cm^{-1}, which was more than four times higher than a Re-free **Bpy-sp^{2}c-COF** photoanode. A potential of +0.5 V vs. RHE was selected because at this potential the observed photocurrents were highest (Figure 3.19b). The photocurrents could be further optimized, but these are just supporting experiments to show that the Re complex COF generates higher photocurrents than the metal-free COF. The experiments were also performed by using acetonitrile with **Bpy-sp^{2}c-COF** and **Re-Bpy-sp^{2}c-COF** as the support electrolyte at a range of different potentials. The results are similar to those obtained in aqueous solutions (Figure 3.19c), with the COF bearing the Re complex generating higher photocurrents. However, the observed photocurrents are all lower than when using aqueous solutions.

Moreover, when under irradiation, the arc radii for **Bpy-sp^{2}c-COF** and **Re-Bpy-sp^{2}c-COF** in Nyquist plots (Figure 3.19d) were smaller than those in the dark. This indicated that charge carriers were generated in **Bpy-sp^{2}c-COF** and **Re-Bpy-sp^{2}c-COF** under irradiation. The Nyquist plots of **Re-Bpy-sp^{2}c-COF** under irradiation have smaller semicircles than those of **Bpy-sp^{2}c-COF**. Taken together, these measurements demonstrated that **Re-Bpy-sp^{2}c-COF** acts as a better photo-electrocatalyst suggesting that this COF is better at separating and transferring charges, which is also in line with computational predictions (*vide infra*).

3.11 TCSPC measurements

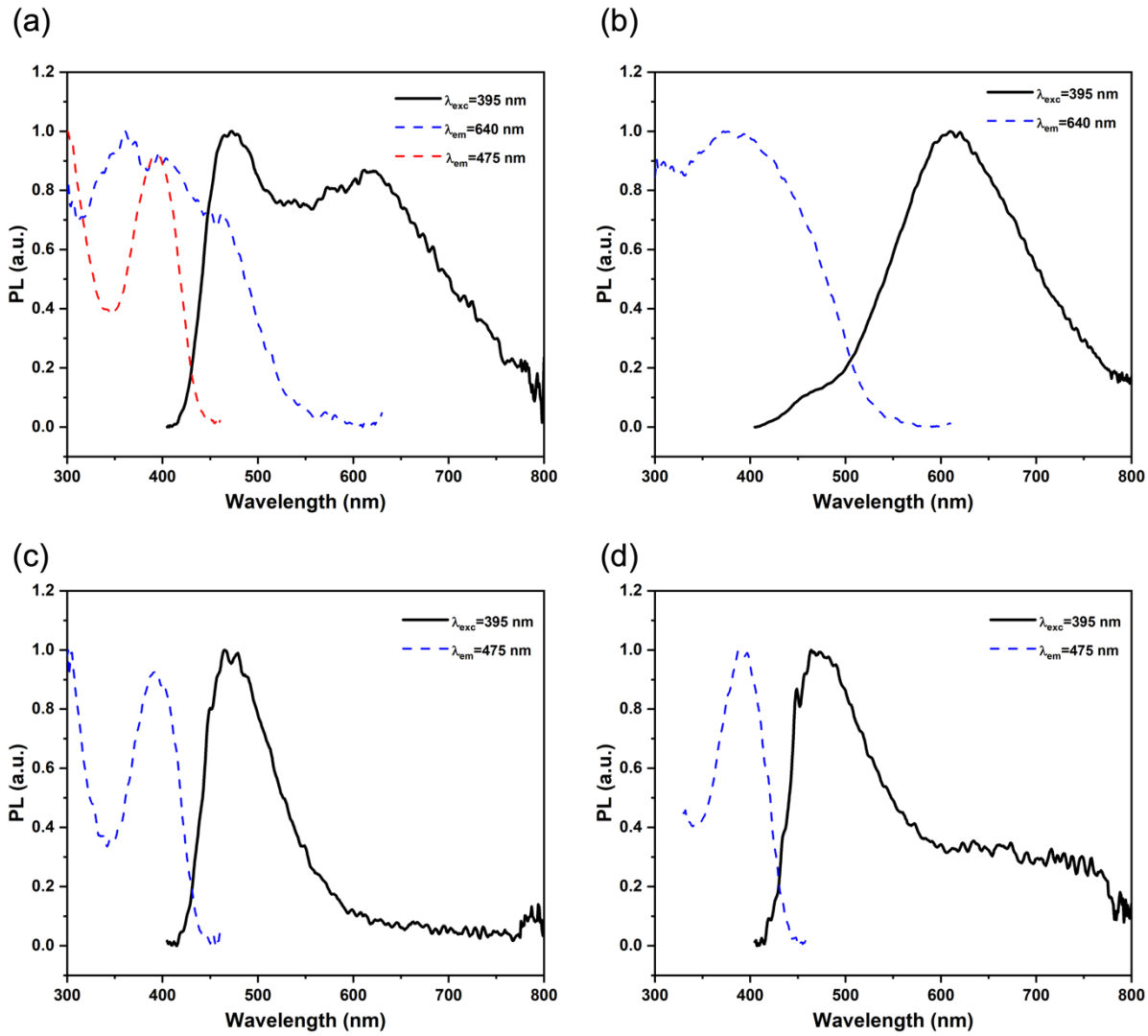

Figure 3.20 (a) Fluorescence emission and excitation spectra of **Bpy-sp^{2}c-COF** in acetonitrile; (b) Fluorescence emission and excitation spectra of **Bpy-sp^{2}c-COF** in acetonitrile and triethanolamine (30/1) mixture; (c) Fluorescence emission and excitation spectra of **Re-Bpy-sp^{2}c-COF** in acetonitrile; (d) Fluorescence emission and excitation spectra of **Re-Bpy-sp^{2}c-COF** in acetonitrile and triethanolamine (30/1) mixture.

Emission spectroscopy and TCSPC measurements was then applied to study the mechanism of photocatalysis for **Re-Bpy-sp^{2}c-COF**. Two emissive states with λ_{max} at 475 and 640 nm were observed for the photocatalyst **Bpy-sp^{2}c-COF** in acetonitrile suspension (Figure 3.20a). From the excitation spectrum in Figure 3.20a, the 640 nm emission results from a broad range of absorption bands in the UV/Vis spectrum (from 300 to 500 nm). By comparison, excitation into a single band at 390 nm causes the sharp

emission band centred at 475 nm. PL spectra of **Bpy-sp^{2}c-P** and **Re-Bpy-sp^{2}c-P** (Figure 3.21a) are comparable to those of **Bpy-sp^{2}c-COF** and **Re-Bpy-sp^{2}c-COF**. Two emissive states with λ_{max} at 475 and 620 nm were observed for **Bpy-sp^{2}c-P** in acetonitrile suspension, and one emissive state with λ_{max} at 475 nm (Figure 3.21b, c and d) was detected for **Bpy-sp^{2}c-P** and **Re-Bpy-sp^{2}c-P** in acetonitrile/TEOA suspension.

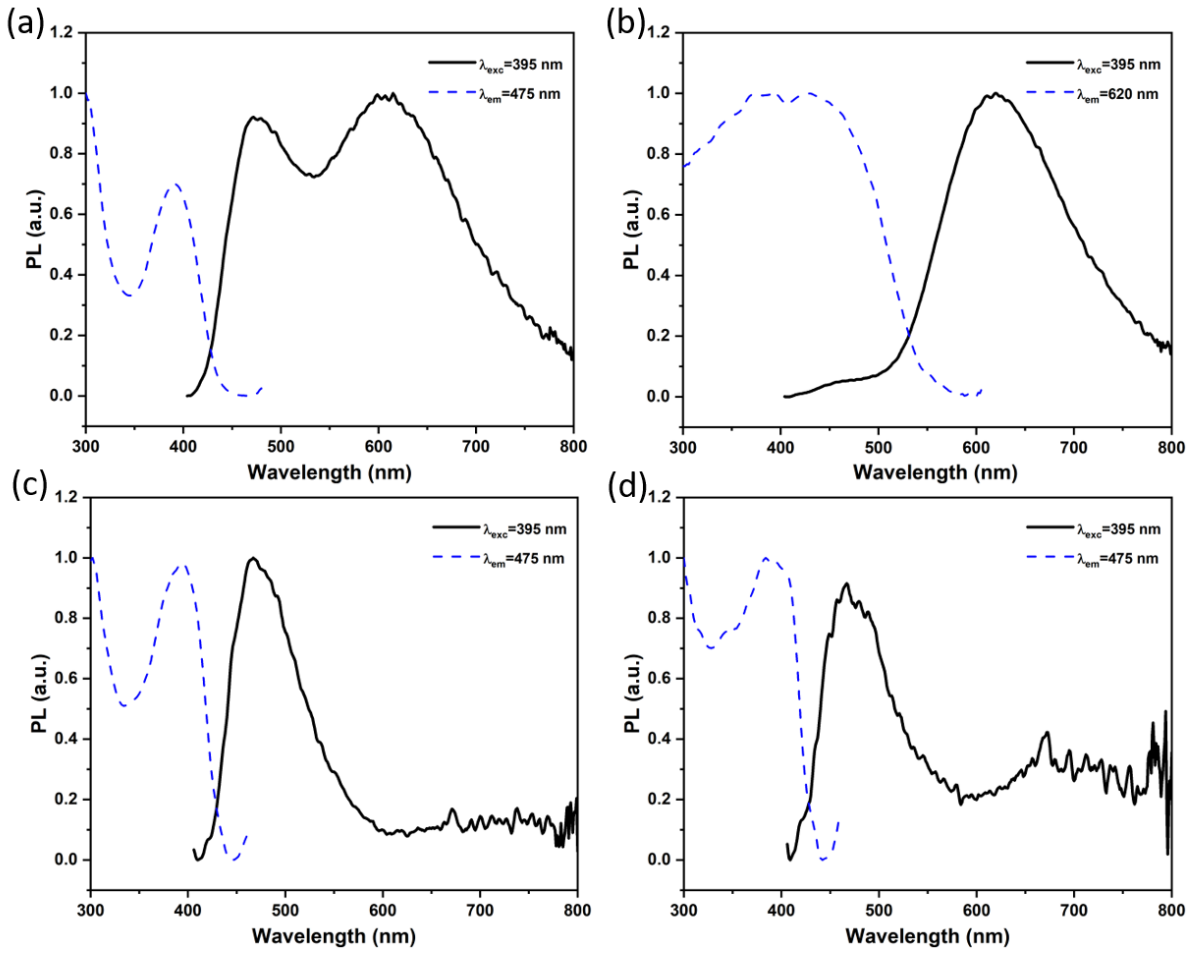

Figure 3.21 Fluorescence emission and excitation spectra of **Bpy-sp^{2}c-P** in MeCN (a) and MeCN/TEOA (30/1) (b) and **Re-Bpy-sp^{2}c-P** in MeCN (c) and MeCN/TEOA (30/1) (d).

Table 3.4 Fluorescence life-time measurements.

Materials	λ_{em} / nm	τ_1 / ns	B_1 / %	τ_2 / ns	B_2 / %	τ_3 / ns	B_3 / %	χ^2	τ_{AVG}
Bpy-sp^{2}c-COF[a]	475	0.56	5.11	2.55	84.22	4.16	10.66	1.18	2.62
Bpy-sp^{2}c-COF[b]	475	0.06	9.16	1.95	31.27	3.13	59.57	1.25	2.48
Bpy-sp^{2}c-COF[a]	640	0.64	34.16	2.56	46.82	7.5	19.02	1.19	2.84
Bpy-sp^{2}c-COF[b]	640	0.66	38.23	2.48	42.59	7.34	19.18	1.19	2.72
Bpy-sp^{2}c-COF[c]	475	0.15	16.42	0.55	60.10	1.19	18.48	1.20	0.60
Bpy-sp^{2}c-COF[d]	475	0.08	6.14	0.66	87.52	2.20	6.34	1.02	0.72
Bpy-sp^{2}c-COF[c]	620	0.79	35.05	2.74	46.03	7.94	18.93	1.19	3.04
Bpy-sp^{2}c-COF[d]	620	0.72	33.59	2.57	46.47	7.54	19.94	1.16	2.94
Re-Bpy-sp^{2}c-COF[a]	475	0.14	5.90	1.98	44.30	3.09	49.80	1.39	2.42
Re-Bpy-sp^{2}c-COF[b]	475	0.25	4.89	2.57	78.73	4.26	16.38	1.25	2.73
Re-Bpy-sp^{2}c-COF[c]	475	0.22	28.82	0.75	67.21	3.96	3.97	1.29	0.72
Re-Bpy-sp^{2}c-COF[d]	475	0.23	26.95	0.77	68.78	3.83	4.27	1.33	0.76
Bpy-sp^{2}c-P[a]	475	0.33	7.65	2.24	55.04	3.23	37.31	1.31	2.47
Bpy-sp^{2}c-P[b]	475	0.41	4.94	2.57	65.68	3.67	29.37	1.11	2.79
Bpy-sp^{2}c-P[a]	620	0.36	41.04	1.42	43.42	4.39	15.55	1.37	1.44
Bpy-sp^{2}c-P[b]	620	0.37	40.39	1.45	42.51	4.52	17.11	1.41	1.54
Bpy-sp^{2}c-P[c]	620	0.52	30.22	1.94	50.57	6.24	19.22	1.31	2.34
Bpy-sp^{2}c-P[d]	620	0.52	30.50	1.92	50.19	6.18	19.31	1.24	2.32
Re-Bpy-sp^{2}c-P[a]	475	0.37	27.92	1.91	30.20	3.14	41.88	1.13	1.99
Re-Bpy-sp^{2}c-P[b]	475	0.39	23.77	2.43	50.10	3.60	26.12	1.19	2.25
Re-Bpy-sp^{2}c-P[c]	475	0.38	66.06	0.99	31.10	5.25	2.85	1.01	0.71
Re-Bpy-sp^{2}c-P[d]	475	0.38	57.86	0.98	38.00	6.13	4.15	1.13	0.85

[a] Acetonitrile purged with N_2; [b] Acetonitrile purged with CO_2; [c] Acetonitrile and triethanolamine (30/1) purged with N_2; [d] Acetonitrile and triethanolamine (30/1) purged with CO_2; [e] Fluorescence lifetimes were obtained upon excitation at λ_{exc} = 405 nm with a laser and observed at λ_{em} = 475, 640 nm. Fluorescence lifetimes in solvent suspension obtained from fitting time-correlated single photon counting decays to a sum of three exponentials, which yield τ_1, τ_2, and τ_3 according to $\sum_{i=1}^{n}(A + B_i \exp(-\frac{t}{\tau_i}))$. τ_{AVG} is the weighted average lifetime calculated as $\sum_{i=1}^{n} B_i \tau_i$. Note that the poor χ^2 values are due to ultrafast decays for these materials which were very similar to the instrument response.

TCSPC measurements are used to estimate the excited-state lifetimes of the COFs under

different conditions. The lifetimes of the 640 nm emissive state of **Bpy-sp^{2}c-COF** and the 620 nm emissive state of **Bpy-sp^{2}c-P** seem insensitive to the presence of the TEOA scavenger (Table 3.4). The average weighted photoluminescence emission lifetimes of **Bpy-sp^{2}c-COF** (τ_{avg} = 2.62 ns, λ_{em} = 475 nm; τ_{avg} = 2.84 ns, λ_{em} = 640 nm) in MeCN purged with N_2 were similar with that (τ_{avg} = 2.48 ns, λ_{em} = 475 nm; τ_{avg} = 2.72 ns, λ_{em} = 640 nm) in MeCN purged with CO_2. **Bpy-sp^{2}c-P** also has a similar lifetime in MeCN purged with N_2 and CO_2. The emission yields at 640 nm are also unchanged (Figure 3.20a and Figure 3.21a). The lifetime of the 475 nm emissive state of **Bpy-sp^{2}c-COF**, in contrast, decreases from 2.48 ns to 0.72 ns when tested in the presence of the TEOA electron donor (Table 3.4, Figure 3.20b). The lifetime of the 475 nm emissive state of **Bpy-sp^{2}c-P** also decreases from 2.79 ns to 1.54 ns when tested in the presence of the TEOA electron donor (Table 3.4, Figure 3.21b). The emission yields are also very sensitive to TEOA. This indicates that that reductive quenching of this excited state can occur when the system contains TEOA.

In previous studies, sp^{2}c-COF-2 synthesized with TFPPy and 2,2'-(biphenyl-4,4'-diyl)diacetonitrile shows a similar structure to **Bpy-sp^{2}c-COF**. Two emissive states are also presented for sp^{2}c-COF-2 bulk and exfoliated thin film samples.[24] Therein, emission at 640 nm was attributed to the presence of a delocalised excited state across both pyrene and the sp^2-carbon backbone on the basis of the significantly redshifting of the emission when compared to that typically measured for excimer state of pyrene systems alone (*ca.* 480 nm). It is quite interesting to observe a second emission at *ca.* 468 nm for exfoliated sp^{2}c-COF-2 thin film samples in literature. The exfoliation of COF can remove the π-π stacking force between COF layers, allowing twisting of the structure and a loss of conjugation across the backbone.

Here, the samples (**Bpy-sp^{2}c-COF** and **Re-Bpy-sp^{2}c-COF**) are sonicated in solvent before testing and a similar assignment is also proposed. Additionally, the introduction of a Re complex into **Bpy-sp^{2}c-COF** results in a significant change in the measured photophysical behaviour. With **Re-Bpy-sp^{2}c-COF** a single emissive state (λ_{max} = 475

nm), proposed to be due exfoliated COF material remains. Exfoliation of COFs might cause the loss of conjugation, leading to limited electron or energy transfer from the COF framework to the Re centre. That is why emission at this wavelength is insensitive to the presence of the Re centre. Besides, the emissive state with λ_{max} at 640 nm of **Bpy-sp^{2}c-COF** is totally absent in the **Re-Bpy-sp^{2}c-COF** (Figure 3.20c and d). This strongly demonstrates that the delocalized COF excited state is quenched by the Re complex. The assignment of the sensitization of the Re centre by the delocalized COF in the bulk material framework excited state is supported by the good agreement between the wavelength dependent CO measurement (Figure 3.15) and the excitation spectrum of the 640 nm emission of the **Bpy-sp^{2}c-COF** sample (Figure 3.20a).

3.12 Transient absorption (TA) spectroscopy

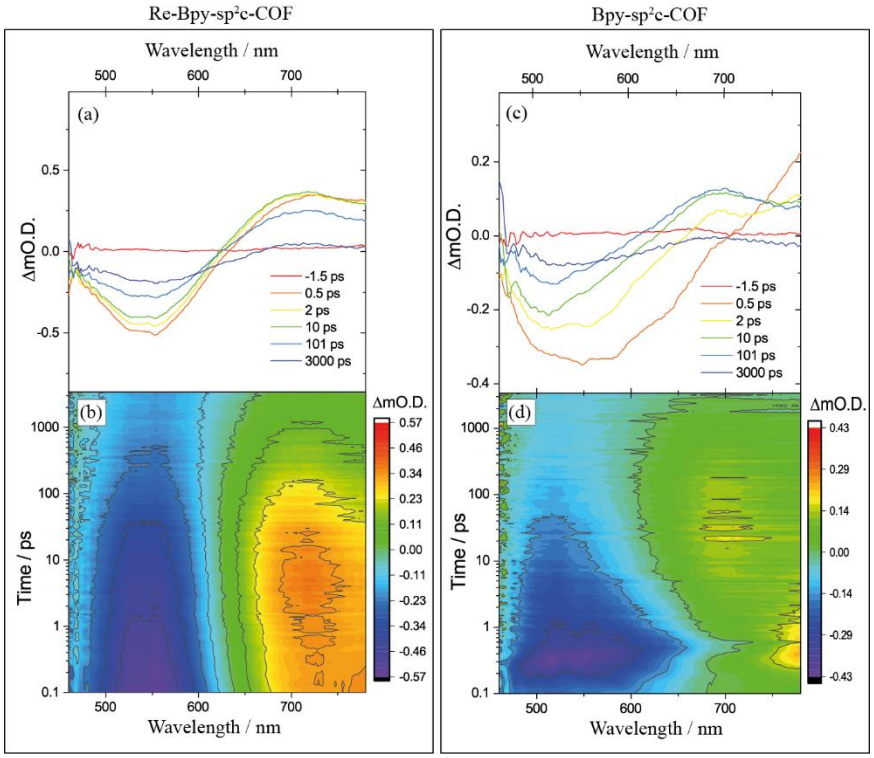

Figure 3.22 Transient absorption spectra of (a) **Re-Bpy-sp²c-COF** and (c) **Bpy-sp²c-COF** in pure acetonitrile at pump-probe time delays chosen to highlight the changing nature of the excited electronic states probed. Complete transient absorption surface probed (b) **Re-Bpy-sp²c-COF** and (d) **Bpy-sp²c-COF** in pure acetonitrile.

To further explore the photophysics of the system, transient absorption (TA) spectroscopy was involved to study both **Re-Bpy-sp²c-COF** and **Bpy-sp²c-COF** (Figure 3.22). Following excitation at 400 nm, 80 μW (5 kHz) of **Bpy-sp²c-COF**, complex TA spectra (Figure 3.22 c and d) were shown with broad negative bands between 450 to *ca*. 700 nm that formed within 0.5 ps. The minimal absorption by the ground state of **Bpy-sp²c-COF** is observed at wavelengths longer than 600 nm (Figure 3.11b). Therefore, the negative signal is proposed to be the overlap of stimulated emission from both the conjugated **Bpy-sp²c-COF** structure (λ_{max} = 640 nm) and the exfoliated **Bpy-sp²c-COF** (λ_{max} = 475 nm), overlapped with the ground state bleach, giving rise to the complex shape.

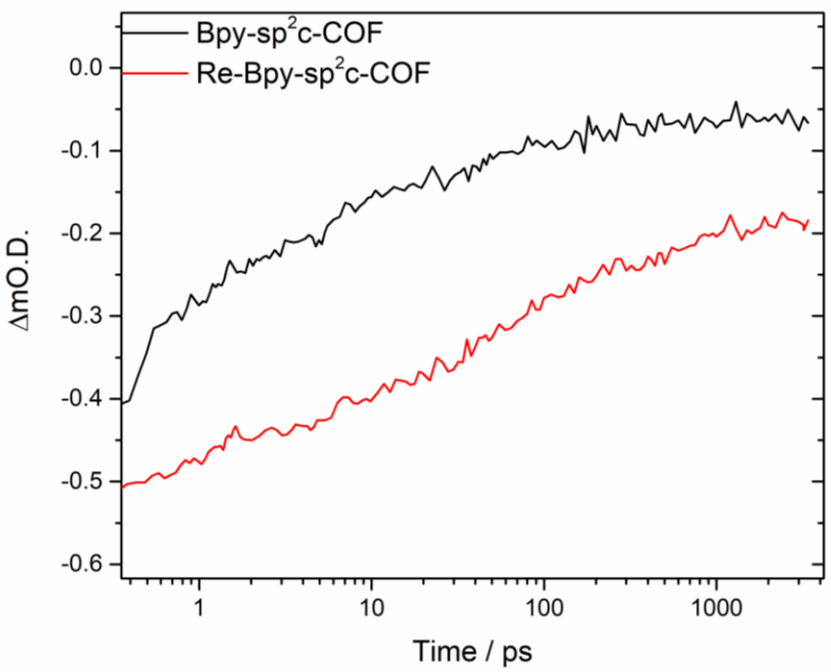

Figure 3.23 Transient absorption kinetics recorded at 550 nm following 400 nm excitation of the samples indicated in CH_3CN.

It is difficult to determine accurate kinetics due to the complex nature of the bleach. Hence, the time taken for the bleach to decrease by 50% (named $t_{50\%}$) was used as a rough measure of the lifetime of the photogenerated excited state. For **Bpy-sp^{2}c-COF** at 550 nm, $t_{50\%}$ = *ca.* 5 ps (Figure 3.23). Within 0.5 ps a photoinduced absorption (PIA) is observed at 770 nm. This PIA decays within 10 ps to form a new PIA centred at 700 nm which decays over the course of the experiment to leave only a small PIA by 3 ns.

Re-Bpy-sp^{2}c-COF, on the contrary, gives a simpler TA spectrum following 400 nm excitation (Figure 3.22 a and b). The negative signal centred at 540 nm is contributed to a combination of ground state bleaching and stimulated emission from the exfoliated COF framework (λ_{max} =475 nm). Notably, the negative band of **Re-Bpy-sp^{2}c-COF** is narrower than that of **Bpy-sp^{2}c-COF**. For **Re-Bpy-sp^{2}c-COF** at 550 nm, $t_{50\%}$ = *ca.* 200 ps (Figure 3.23), significantly longer than that observed for **Bpy-sp^{2}c-COF**. Within 0.5 ps a PIA is also observed for **Re-Bpy-sp^{2}c-COF** at 770 nm. Within the first 5 ps, a blue shift of this initially formed PIA is occurred and a band centred at *ca.* 720 nm is formed.

This state decays over the course of the time-delays, demonstrating the negative band is contributed to ground state bleaching and stimulated emission recovers.

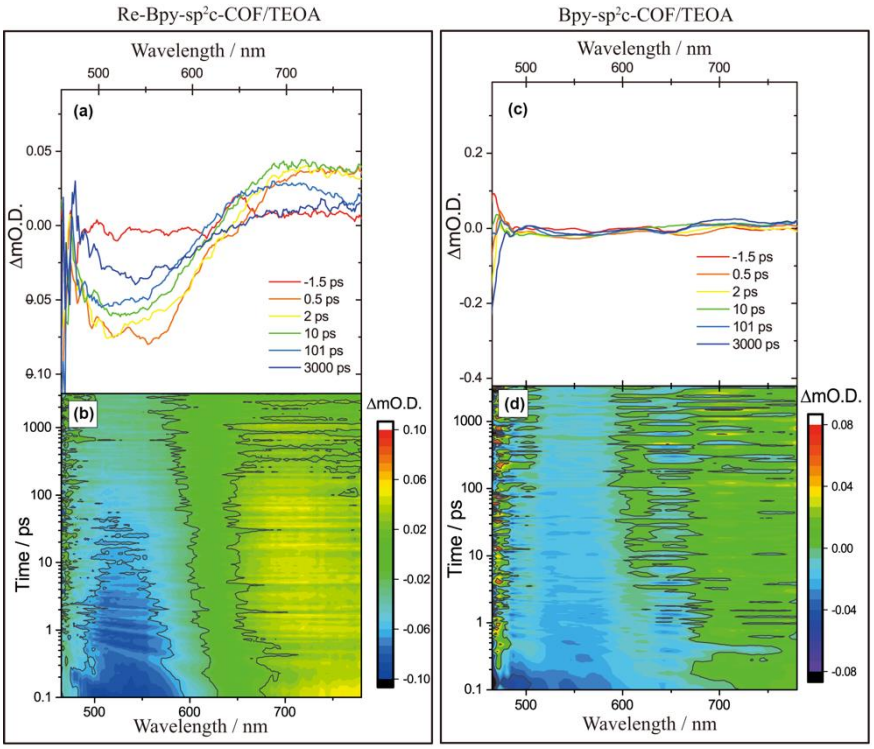

Figure 3.24 Transient absorption spectra of (a) **Re-Bpy-sp^{2}c-COF** and (c) **Bpy-sp^{2}c-COF** in a 30:1 mixture of acetonitrile and TEOA at pump-probe time delays chosen to highlight the changing nature of the excited electronic states probed. Complete transient absorption surface probed (b) **Re-Bpy-sp^{2}c-COF** and (d) **Bpy-sp^{2}c-COF** in a 30:1 mixture of acetonitrile and TEOA.

In the presence of TEOA, we again find that the TA signals are significantly weaker with **Re-Bpy-sp^{2}c-COF** (Figure 3.24a and c). The ground state bleach of **Re-Bpy-sp^{2}c-COF** centred at ca. 540 nm is significantly (ca. 85%, 1 ps) diminished in the presence of TEOA even at the earliest timescales studied indicating that the TEOA can act as an electron donor. Interestingly the addition of TEOA to **Bpy-sp^{2}c-COF** leads to only weak signals being recorded in the TA spectrum indicating that TEOA can reductively quench the excited states probed by wavelengths employed in the TA experiment – in contrast to results of the TCSPC experiments.

Although no direct spectral fingerprint is observed for the formation of the reduced Re centre by TA spectroscopy in the UV/Vis spectral region, it is clear from the simplified TA spectra, combined with the significantly increased lifetime of the ground state bleach

for **Re-Bpy-sp^{2}c-COF**, that the rhenium can promote charge separation within the structure, reinforcing the TCSPC study.

3.13 Calculations

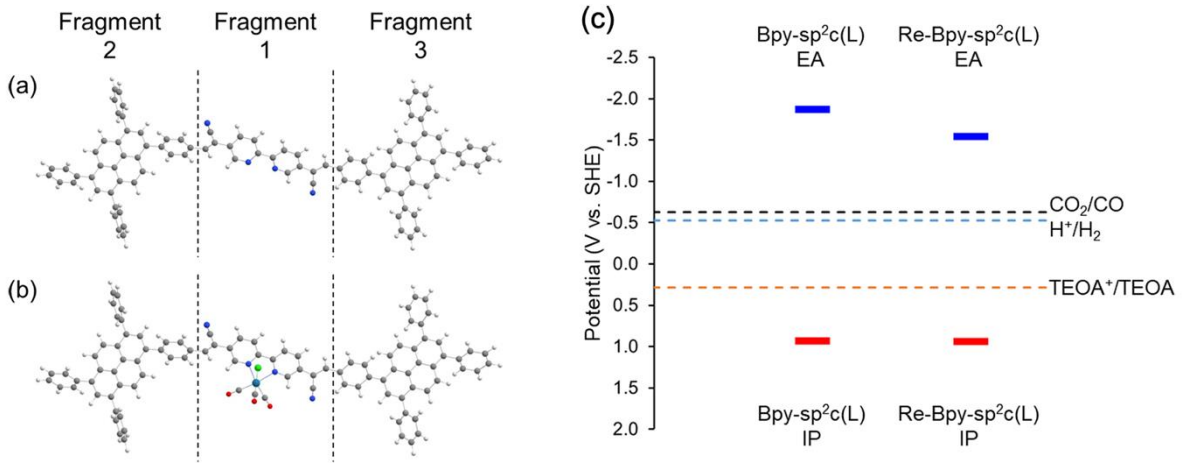

Figure 3.25 Representative molecular models (a) Bpy-sp^{2}c(L) and (b) Re-Bpy-sp^{2}c(L) of **Bpy-sp^{2}c-COF** and **Re-Bpy-sp^{2}c-COF**, respectively, together with fragment definition for inter-fragment charge transfer calculations; (c) (TD-)CAM-B3LYP calculated IP, EA, and IP* potentials of Bpy-sp^{2}c(L) and Re-Bpy-sp^{2}c(L). Dashed coloured lines indicate the potentials for CO_2 reduction to CO, proton reduction, and TEOA oxidation, respectively.

Density functional theory (DFT) calculations were carried out for representative molecular fragments of the COFs to further investigate the excellent CO_2 reduction performance of the COFs. Molecular models Bpy-sp^{2}c(L) and Re-Bpy-sp^{2}c(L) in Figure 3.25a and Figure 3.25b represent **Bpy-sp^{2}c-COF** and **Re-Bpy-sp^{2}c-COF**, respectively. These fragments were also used for inter-fragment charge transfer calculations, which will be discussed later. By comparing the electron affinity (EA) and the ionization potential (IP) values of COF models with potentials of CO_2 reduction and oxidation of TEOA, the driving forces were estimated for CO_2 reduction systems. Using these models, DFT and time-dependent (TD) DFT calculations were performed (Figure 3.25c) and indicated that the EA and the IP values of both COFs straddle the reduction potential of CO_2 to CO, as well as the proton reduction potential, and the oxidation potential of

TEOA. The DFT calculations show that **Re-Bpy-sp^{2}c-COF** has thermodynamic driving force for CO_2 reduction to CO in the system with TEOA as the sacrificial agent.

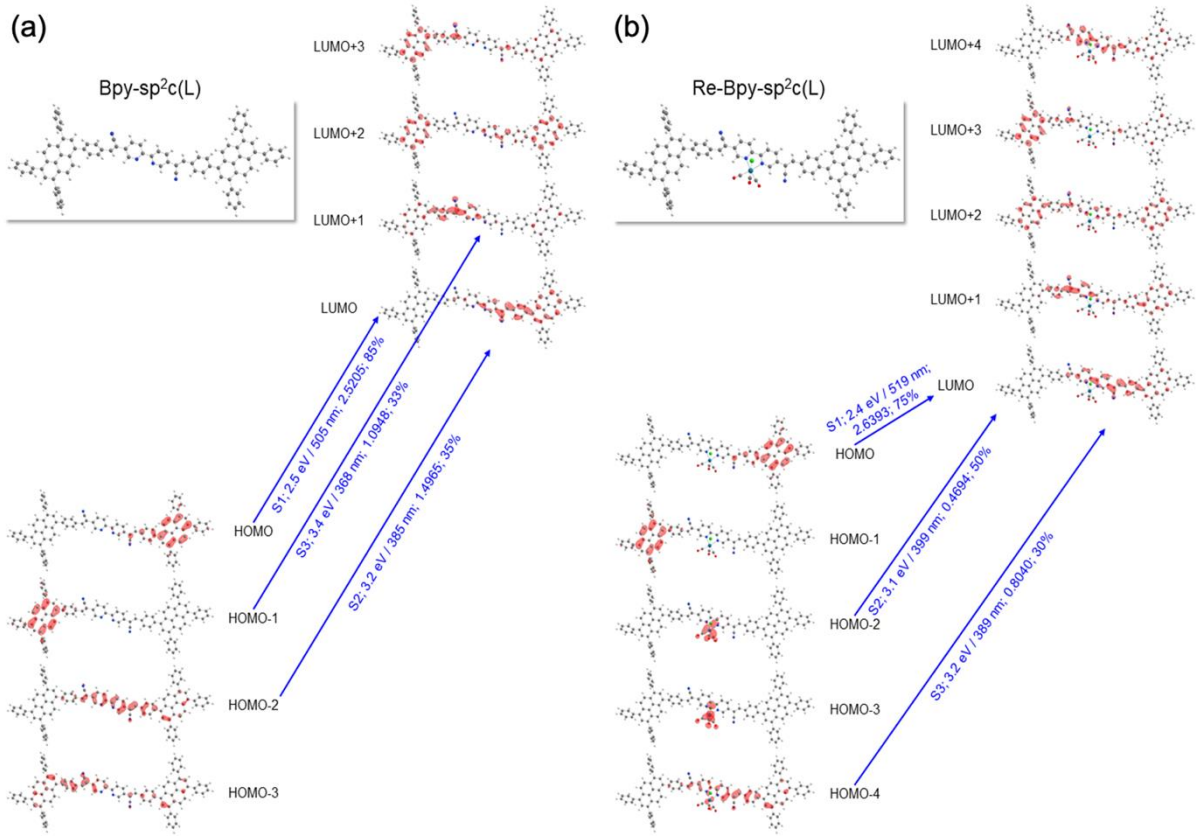

Figure 3.26 The frontier orbitals of Bpy-sp^{2}c(L) (a) and Re-Bpy-sp^{2}c(L) (b) in the excited state (TD-CAM-B3LYP/Def2SVP); isodensity = 0.03 a.u.

Table 3.5 Calculated TD-DFT (TD-CAM-B3LYP) excitation energies for the lowest transition (*E*), oscillator strengths (*f*), and composition in terms of molecular orbital contributions.

	State	Composition [a]	*E* (eV, nm)	*f*	Δ*r* (Å) [16]
Bpy-sp^{2}c(L)	S1	84.8% H → L	2.4537 (505.29)	2.52	5.49
	S2	35.1% H-2 → L; 13.9% H-1 → L+1; 12.0% H → L+2	3.2197 (385.08)	1.50	8.72
	S3	32.8% H-1 → L+1; 17.7% H-1 → L+2; 11.0% H-2 → L	3.3683 (368.09)	1.09	10.45
Re-Bpy-sp^{2}c(L)	S1	76.0% H → L; 10.2% H → L+1	2.3880 (519.19)	2.64	7.61
	S2	49.8% H-2 → L	3.1047 (399.34)	0.47	6.80
	S3	30.0% H-4 → L; 16.7% H-2 → L	3.1889 (388.80)	0.80	6.29

a H = HOMO, L = LUMO, Δr is state-specific charge-transfer length.

Figure 3.26 shows the frontier orbitals of Bpy-sp^{2}c(L) and Re-Bpy-sp^{2}c(L) in the excited state. The major contribution to each of the first three electronic excitations is indicated by the arrow, together with the state, excitation energy (eV, nm), oscillator strength and percentage of the transition. In Table 3.5, TD-CAM-B3LYP calculations predict that the lowest-energy, excited electronic state (S1) for both Bpy-sp^{2}c(L) and Re-Bpy-sp^{2}c(L) corresponds to the LUMO ← HOMO transition, with a strong oscillator strength. Electron distributions of the excited-state frontier orbitals suggest that for both Bpy-sp^{2}c(L) and Re-Bpy-sp^{2}c(L) the HOMO orbital is predominantly located on the pyrene unit of the COF. And the LUMO orbital is mainly located on the bipyridine unit (with or without ligated Re complex; Figure 3.26).

Table 3.6 Calculated inter-fragment charge transfer (in number of electrons) in the excited state (TD-CAM-B3LYP), with fragment definitions shown in Figure 3.24.

Bpy-sp^{2}c(L)					
1st Excited state					
1 → 2:	0.00	1 ← 2:	0.00	Net 1 → 2:	0.00
1 → 3:	0.12	1 ← 3:	0.25	Net 1 → 3:	-0.14
2 → 3:	0.00	2 ← 3:	0.00	Net 2 → 3:	0.00
2nd Excited state					
1 → 2:	0.08	1 ← 2:	0.11	Net 1 → 2:	-0.03
1 → 3:	0.13	1 ← 3:	0.16	Net 1 → 3:	-0.02
2 → 3:	0.10	2 ← 3:	0.08	Net 2 → 3:	0.01
3rd Excited state					
1 → 2:	0.07	1 ← 2:	0.13	Net 1 → 2:	-0.06
1 → 3:	0.03	1 ← 3:	0.05	Net 1 → 3:	-0.02
2 → 3:	0.13	2 ← 3:	0.13	Net 2 → 3:	0.00
Re-Bpy-sp^{2}c(L)					
1st Excited state					
1 → 2:	0.00	1 ← 2:	0.00	Net 1 → 2:	0.00
1 → 3:	0.11	1 ← 3:	0.31	Net 1 → 3:	-0.20
2 → 3:	0.00	2 ← 3:	0.00	Net 2 → 3:	0.00
2nd Excited state					
1 → 2:	0.05	1 ← 2:	0.07	Net 1 → 2:	-0.01
1 → 3:	0.15	1 ← 3:	0.13	Net 1 → 3:	0.02
2 → 3:	0.02	2 ← 3:	0.01	Net 2 → 3:	0.01

3rd Excited state					
1 → 2:	0.09	1 ← 2:	0.13	Net 1 → 2:	-0.03
1 → 3:	0.12	1 ← 3:	0.12	Net 1 → 3:	0.01
2 → 3:	0.04	2 ← 3:	0.03	Net 2 → 3:	0.01

Table 3.6 shows the results of the calculated inter-fragment charge transfer in the excited states of Bpy-sp^{2}c(L) and Re-Bpy-sp^{2}c(L). Arrows in Table 3.6 indicate the electron transfer direction between the fragments defined in Figure 3.25. A negative value for the net transfer means that the electrons are transferred in the opposite direction to the one indicated by the arrow. Analyses of excited-state, inter-fragment charge transfer between the building units of the COFs demonstrate that considerable amounts of electrons are transferred from the pyrene fragment to the bipyridine fragment (Table 3.6), with a sizable electron–hole distance as measured by the charge centroids of the orbitals involved (Δr in Table 3.5).

From the computational results, it is clear that there is electron transfer from the COF backbone to the catalytically active Re complex. Compared to the homogeneous catalyst, the CO_2 reduction mechanism of the **Re-Bpy-sp^{2}c-COF** are different. Here we propose pyrene excitation to a bipyridine based LUMO. In contrast, in solution excitation upon irradiation forms a metal to bipyridine excited state (^{3}MLCT) which is then quenched by an electron donor (Figure 1.6 in **Chapter 1**).[38] The same results about the photogenerated electron transfer from COF to Re complexes were also demonstrated for 2D Re-COF.[12] The proposed mechanism includes three steps. Initially, an intramolecular charge transfer state occurs under irradiation, which is reduced by TEOA to form a $TEOA^+$-$(COF\text{-}Re)^-$ charge separation state. Then, the chloride ion is eliminated from the Re complex. CO_2 is bound at the empty coordination site to form an intermediate species such as $TEOA^+$-$(COF\text{-}Re[CO_2])^-$ or/and $TEOA^+$-$(COF\text{-}Re[CO_2H])^-$. Finally, carbon monoxide is released.

3.14 Dye sensitization

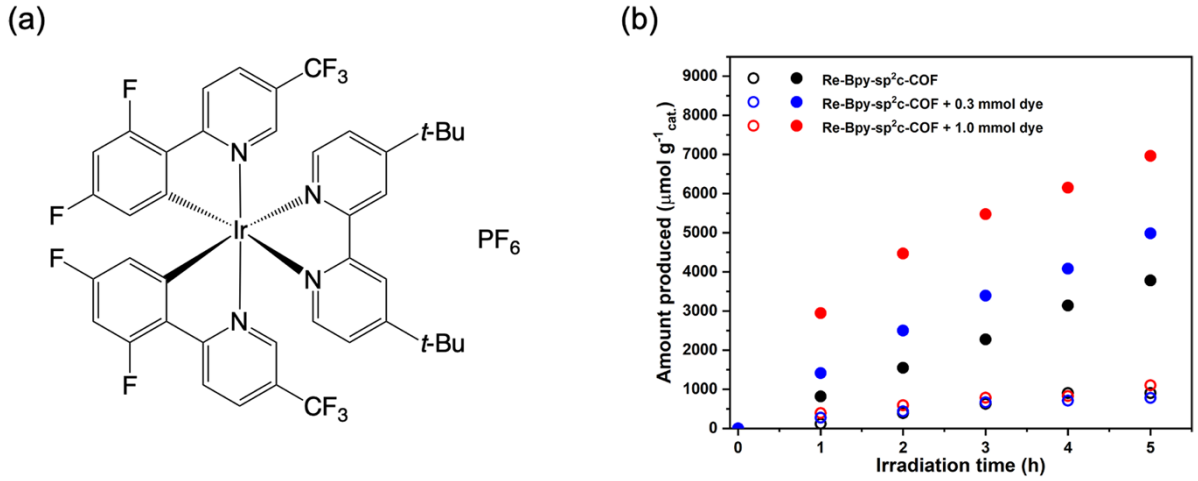

Figure 3.27 (a) structure of (Ir[dF(CF_3)ppy]$_2$(dtbpy))PF_6; (b) CO (closed dots) and H_2 (open dots) production using visible light (λ > 420 nm, 300 W Xe light source) for **Re-Bpy-sp^{2}c-COF** (1 mg) and **Re-Bpy-sp^{2}c-COF** with dye (1 mg catalyst with 0.3 mmol or 1.0 mmol dye in 5 mL solvent with ratio of MeCN/TEOA = 30/1).

In previous literature, FS-COF was indicated to have accessible pores which can potentially act as a host for dyes to further enhance photocatalytic activity for hydrogen evolution.[8] Here, (Ir[dF(CF_3)ppy]$_2$(dtbpy))PF_6 (ppy = 2-phenylpyridine, tbpy = 4,4′-di-*tert*-butyl-2,2′-dipyridyl) was used in conjunction with **Re-Bpy-sp^{2}c-COF** to increase the photocatalytic CO_2 reduction performance (Figure 3.27a).

Different amounts of the dye were used, and the CO production rates were enhanced by 32% and 84% compared to the unsensitized COF when using 0.3 mmol and 1.0 mmol of the dye, respectively, with 1 mg COF over 5 hours (Figure 3.27b). The H_2 production rates were unchanged. When **Re-Bpy-sp^{2}c-COF** was loaded with 1.0 mmol dye, the highest CO production rates were 1400 μmol h^{-1} g^{-1}, with a selectivity of 86% for CO, over 5 hours.

A series of control experiments was conducted for the systems with dye to investigate the crucial factors influencing the photocatalytic CO_2 reduction performance. Under an argon atmosphere in the absence of CO_2, **Re-Bpy-sp^{2}c-COF** with dye produced H_2 and CO at a rate of 511.7 μmol g^{-1} h^{-1} and 18.3 μmol g^{-1} h^{-1}, respectively. **Bpy-sp^{2}c-COF**

with or without dye only generated a negligible amount of H_2, proving the crucial role of the Re complexes in the COFs. Without COFs, no gas production was measured by systems with dye, demonstrating the dye alone cannot be a photocatalyst for CO_2 reduction and the crucial role of COFs.

Table 3.7 Photocatalytic CO_2 reduction using different experimental conditions.

Entry	**Photocatalyst**	**CO (μmol)**	**H_2 (μmol)**	**Re content (μmol)**	**TON (CO)**	**CO selectivity (%)**
1[a]	Re-Bpy-sp^2c-COF	12.48	2.99	0.97	12.9	80.7
2[a]	Re-Bpy-sp^2c-COF + dye	16.80	2.64	0.97	17.3	86.4
3[a]	Bpy-sp^2c-COF	0.21	n.d.	0	/	/
4[b]	Re-Bpy-sp^2c-COF + dye	0.22	6.14	0.97	0.2	3.4
5[a]	Bpy-sp^2c-COF + dye	0.19	n.d.	0	/	/
6[a]	dye	n.d.	n.d.	0	/	/
7[c]	$Re(bpy)(CO)_3Cl$	10.03	0.67	0.97	10.3	93.8

[a] Reaction conditions: Photocatalyst (1 mg), solvent (5 mL, acetonitrile/TEOA = 30 : 1), CO_2 (1 atm.), 300 W Xe light source equipped with λ > 420 nm cut-off filter, 12 hours; [b]Ar atmosphere instead of CO_2; [c]Photocatalyst (0.45 mg, 0.97 μmol), Solvent (5 mL, acetonitrile/TEOA = 30 : 1), CO_2 (1 atm.), 300 W Xe light source equipped with λ > 420 nm cutoff filter, 12 hours. n.d.: none detected; Dye: $(Ir[dF(CF_3)ppy]_2(dtbpy))PF_6$.

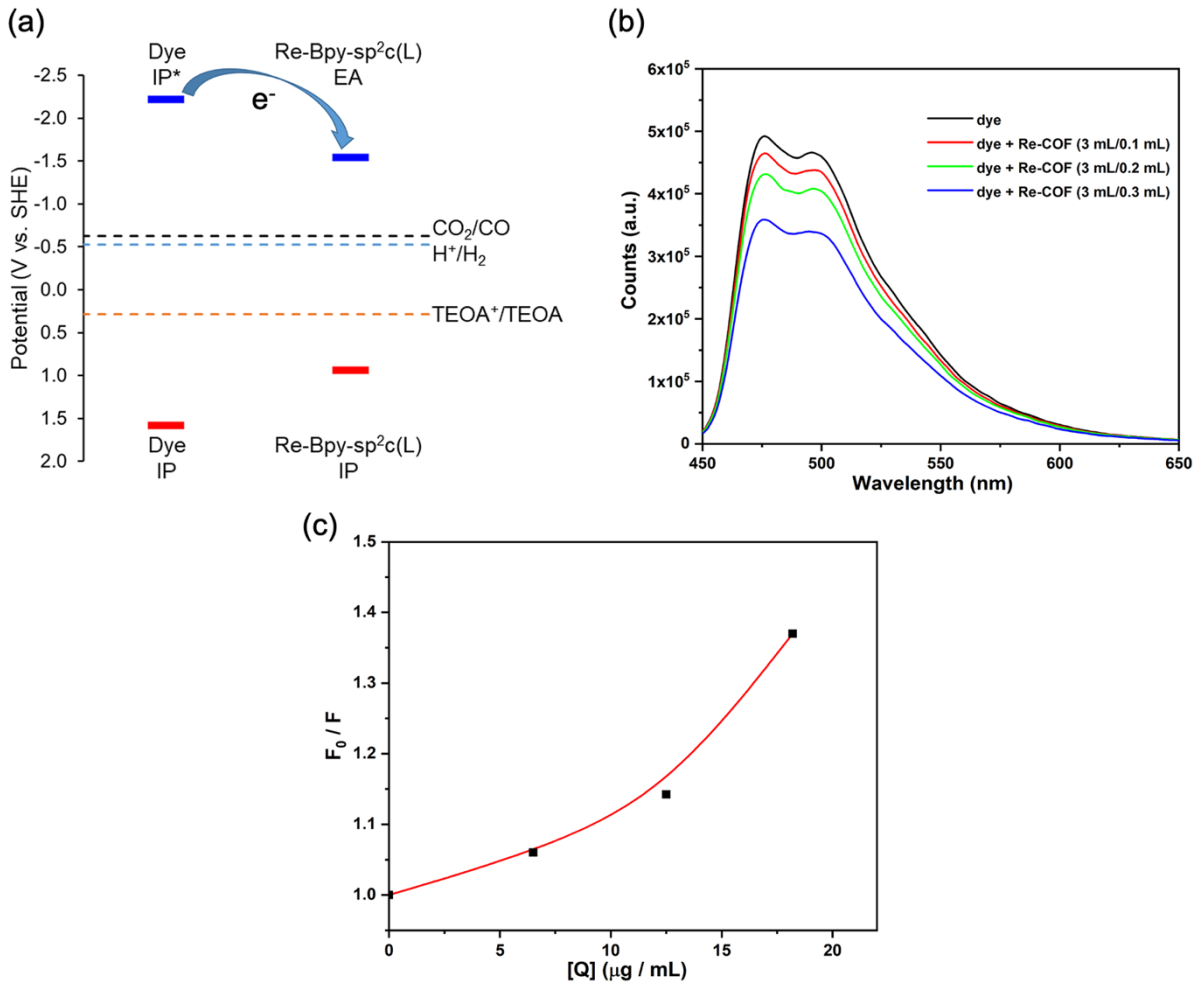

Figure 3.28 (a) (TD-)CAM-B3LYP calculated IP, EA, and IP* potentials of $(Ir[dF(CF_3)ppy]_2(dtbpy))^-$ (dye) and Re-Bpy-sp^{2}c(L). Dashed coloured lines indicate the potentials for CO_2 reduction to CO, proton reduction, and TEOA oxidation, respectively; (b) Fluorescence emission spectra (λ_{exc} = 440 nm) of $(Ir[dF(CF_3)ppy]_2(dtbpy))PF_6$ in acetonitrile (3 mL) and $(Ir[dF(CF_3)ppy]_2(dtbpy))PF_6$ with different amounts of **Re-Bpy-sp^{2}c-COF** and acetonitrile (1 mg in 5 mL) mixture; (c) Stern-Volmer plot of F_0/F versus **Re-Bpy-sp^{2}c-COFs** concentration, [Q], in acetonitrile.

To investigate the interaction between COF and dye, calculations and fluorescence emission measurements were carried out. DFT calculation was also performed to estimate the EA and IP values of the dye and **Re-Bpy-sp^{2}c-COF**. Relative energy levels of the dye and the molecular COF models (Figure 3.28a) suggest that the dye provides the thermodynamic driving force for excited electrons to be transferred to **Re-Bpy-sp^{2}c-COF**. To further study the photogenerated electron transfer from dye to the **Re-Bpy-sp^{2}c-COF**, PL quenching experiments were carried out. $(Ir[dF(CF_3)ppy]_2(dtbpy))PF_6$ shows two broad

emission peaks around 475 and 500 nm under 440 nm excitation. With the addition of different amounts of **Re-Bpy-sp^{2}c-COF**, the PL peaks of excited $(Ir[dF(CF_3)ppy]_2(dtbpy))PF_6$ were quenched. Emission quenching experiments suggest an electron transfer mechanism between the dye and the COF via oxidative quenching (Figure 3.28b). Stern-Volmer plots were used to investigate the quenching behaviors. Stern-Volmer plots based on fluorescence quenching intensity ratios F_0/F of dye and **Re-Bpy-sp^{2}c-COF** solutions are plotted in Figure 3.28c to quantify the quenching behavior. F_0 is the fluorescence intensity of the dye without quencher (**Re-Bpy-sp^{2}c-COF**) and fluorescence intensity F is for the dye with **Re-Bpy-sp^{2}c-COF** added in various concentrations. As shown in Figure 3.28c, the Stern-Volmer plots show an upward deviation (positive deviation) from a linear trend for F_0/F ratios with increasing quencher concentration, which suggesting the simultaneous presence of dynamic and static quenching.

3.15 Syngas generation

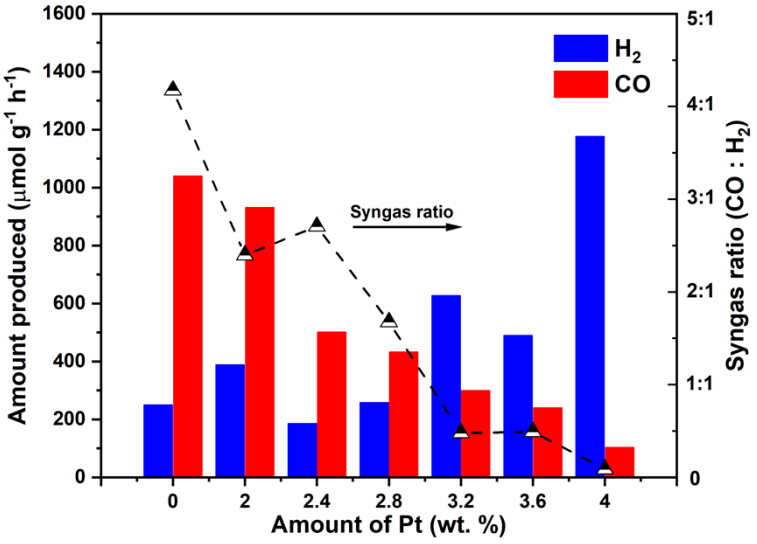

Figure 3.29 Photocatalytic syngas generation of Pt modified **Re-Bpy-sp^{2}c-COF** under visible light irradiation ($\lambda > 420$ nm, 300 W Xe light source).

Syngas plays an important role in chemical industry on large scale for processes. Control of the ratio is crucial as Fischer–Tropsch process requiring a ratio of 2:1 H_2 / CO. Electrocatalysts[39,40] and inorganic photocatalysts[41,42] have been explored for the production of syngas with tunable ratios of CO and H_2. In **Chapter 1**, it has been proven

that residual metal could act as cocatalyst and influence the ratio of obtained syngas. Here, **Re-Bpy-sp^{2}c-COF** loaded with additional *in situ* photodeposited colloidal Pt, which is a well-studied cocatalyst for HER, was used as a photocatalyst for syngas production. By adding different amounts of Pt, **Re-Bpy-sp^{2}c-COF** could generate CO-rich or H_2-rich mixtures ranging from approximately 4:1 to 1:10 for CO:H_2 (Figure 3.29). This demonstrated the versatility of **Re-Bpy-sp^{2}c-COF** as a photocatalyst for CO_2 reduction to meet the different needs in industrial areas of generating CO with high selectivity or specific ratios of syngas.

3.16 Conclusions

In conclusion, a new porous, crystalline bipyridine-containing sp^{2}c-COF was synthesized via a Knoevenagel condensation reaction, which was then post-synthetically modified with a rhenium complex to enhance the photocatalytic CO_2 reduction performance. **Re-Bpy-sp^{2}c-COF** is very stable and can constantly generate CO at a rate of 1040 μmol g^{-1} h^{-1} with 81% selectivity over H_2 over 17.5 h illumination. **Re-Bpy-sp^{2}c-COF** is porous and its CO_2 reduction performance can be further improved over 5 hours by up to 84% by dye-sensitization, giving a CO production rate of 1400 μmol h^{-1} g^{-1} and a CO/H_2 selectivity of 86%. A series of experimental and computational studies suggest that the COF is excited followed by charge-transfer to the Re-centre, which is a different mechanism compared to the homogeneous catalyst [Re(bpy)(CO)$_3$Cl]. **Re-Bpy-sp^{2}c-COF** outperforms the homogeneous catalyst in terms of stability. Crystallinity and porosity are proven to be important in these materials since an amorphous, low-porosity analogue showed almost no photocatalytic activity. The catalytic selectivity of the COF can be tuned from favouring CO to favouring H_2 by varying the level of platinum cocatalyst, and this can be used to produce syngas directly.

3.17 Experimental Methods

3.17.1 Materials and methods

All reagents were obtained from Sigma-Aldrich, TCI Europe or Fluorochem Ltd. Anhydrous solvents were purchased from Acros Organics or Fisher Scientific. All chemicals were used as received and without further purification.

3.17.1.1 Solution nuclear magnetic resonance

^{1}H and $^{13}C\{^{1}H\}$ NMR spectra were recorded on a Bruker Avance 400 NMR spectrometer, operating at frequencies of 400 MHz and 100 MHz, respectively.

3.17.1.2 Powder X-ray diffraction

Powder X-ray diffraction (PXRD) measurements were carried out on a Panalytical Empyrean diffractometer, equipped with a Cu X-ray source (λ = 1.5418 Å, Cu Kα), PIXcel3D detector and X-ray focusing mirror. The loose powdered sample was held on Mylar film in aluminium well plates and screened in high throughput transmission mode. Powder diffraction analysis was performed using TOPAS-Academic.[3]

3.17.1.3 Thermogravimetric analysis

Thermogravimetric analysis (TGA) was measured on an EXSTAR6000 with an automated vertical overhead thermobalance under nitrogen flow, ramping heating at 10 °C min^{-1} from 25 °C to 600 °C.

3.17.1.4 Gas sorption analysis

Nitrogen adsorption and desorption were measured at 77.3 K using a Micromeritics ASAP 2020 volumetric adsorption analyzer. Powder samples were degassed offline at 393 K for 12 hours under dynamic vacuum (10^{-5} bar) before analysis. BET surface areas were fitted over relative pressure (p/p°) from 0.1 to 0.2. Pore size distributions of COFs were obtained from the adsorption data by fitting a nonlocal density functional theory (NL-DFT) model with method of N_2-cylindrical pores-oxide surface. CO_2 isotherms were collected up to a pressure of 1200

mbar on a Micromeritics ASAP 2020 at 273 K and 298 K.

3.17.1.5 Fourier-transform infrared spectroscopy

FT-IR spectra were collected on a Bruker Tensor 27 FT-IR spectrometer. Samples were prepared as KBr disks before analyzing for 16 scans with a resolution of 4 cm^{-1}.

3.17.1.6 UV-Visible absorption spectra

UV-Visible absorption spectra were measured on an Agilent Cary 5000 UV-Vis-NIR Spectrometer by measuring the reflectance of powders in the solid-state.

3.17.1.7 Scanning electron microscopy

The morphology of the materials was studied using a Hitachi S-4800 cold field emission scanning electron microscope (FE-SEM). Samples were prepared by depositing the powders with an adhesive high-purity carbon tab on Hitachi M4 aluminium stubs.

3.17.1.8 Scanning transmission electron microscopy

STEM and EDX images were obtained on a JEOL 2100F Cs-corrected analytical FEG S/TEM operating at 200 kV, and fitted with an EDAX Octane T Optima windowless 60 mm^2 SDD EDX detector. The samples were prepared by drop-casting sonicated ethanol suspensions of the materials onto a copper grid.

3.17.1.9 Isotopic labelling experiments

$^{13}CO_2$ Labelling experiments were carried on a Bruker Vertex 70V Fourier-transform infrared spectrometer with an argon-purged custom-made gas IR cell. A vial containing COF powders, acetonitrile and triethanolamine was purged with $^{13}CO_2$ (Sigma-Aldrich, 99 atom % ^{13}C, <3 atom % ^{18}O) for 3 minutes, then it was illuminated for 4 hours using a 300 W Xe light source equipped with $\lambda > 420$ nm filter. Gas from the headspace of the vial (500 μL) was injected into the gas IR cell and a spectrum was measured (32 scans with a resolution of 0.5 cm^{-1}).

3.17.1.10 Photoelectrochemical measurements

1 mg of the photocatalyst was dispersed in 0.1 mL acetonitrile and ultrasonicated for ten minutes giving a homogenous suspension. Fluoride-tin oxide (FTO) glass slides were covered with a copper mask giving an area of 0.28 cm^2. 10 μL of the suspension was drop-casted on the FTO glass and dried overnight at room temperature. The photocurrent response was measured using a three-electrode setup with a working electrode (COF on FTO glass), counter electrode (Pt wire), and reference electrode (Ag/AgCl). An Oriel Instruments LSH-7320 Solar Simulator (IEC ABA certified) with 1 Sun output was used to illuminate the sample. A 0.1 M Na_2SO_4 (pH = 7) solution with a bias voltage of -0.1 V was used for the measurement. The EIS spectra were recorded by applying a 10 mV AC signal in the frequency range from 100 kHz to 0.01 Hz. The potential was converted to reversible hydrogen electrode (RHE) using the following equation[4]:

$$E_{\mathrm{RHE}} = E_{\mathrm{Ag/AgCl}} + 0.059\mathrm{pH} + E^{0}_{\mathrm{Ag/AgCl}} \left(E^{0}_{\mathrm{Ag/AgCl}} = 0.199\mathrm{V}\right)$$

3.17.1.11 ICP-OES analysis

Samples were digested in nitric acid (67–69%, trace metal analysis grade) with a microwave using an in-house procedure. The obtained solutions were diluted with water before the measurement by Spectro Ciros ICP-OES and the instrument was calibrated with standards in an aqueous solution.

3.17.1.12 Transmission and backscattering experiments

Samples were tested on a Formulaction S.A.S. Turbiscan AGS with an 880 nm NIR diode and a detector at 180° or 45° (relative to the light source) in a cylindrical glass cell. Before the measurements, samples were dispersed in 20 mL acetonitrile and sonicated for 15 minutes. Then, the transmission and backscattering of the suspensions were measured in cylindrical glass cells from 5000 to 30,000 μm every 40 μm.

3.17.1.13 TCSPC measurements

TCSPC experiments were performed on an Edinburgh Instruments LS980-D2S2-STM spectrometer equipped with picosecond pulsed LED excitation sources and a R928 detector, with a stop count rate below 3%. An EPL-375 diode (λ = 370.5 nm, instrument response 100 ps, fwhm) with a 450 nm high pass filter for emission detection was used. Suspensions were prepared by ultrasonicating the materials in acetonitrile or acetonitrile with triethanolamine (30/1) purged with N_2 and CO_2. The instrument response was measured with colloidal silica (LUDOX® HS-40, Sigma-Aldrich) at the excitation wavelength without filter. Decay times were fitted in the FAST software using suggested lifetime estimates.

3.17.1.14 Determination of apparent quantum yield (AQY) for CO production

The apparent quantum yield of CO production was determined using monochromatic LED light (λ = 420 nm). The reactions were conducted on the same photochemical experimental setup under the optimized reaction conditions. For the experiments, COFs (1 mg) was suspended in acetonitrile and triethanolamine (30:1 vol. mixture, 5 mL). The illuminated area was 8 cm^2 and the light intensity was measured by a ThorLabs PM100D Power and Energy Meter Console with a ThorLabs S120VC photodiode power sensor. The AQY was calculated as follow:

$$AQY\% = 2 \times [(n\ CO) \times N_A \times \hbar \times c)] \times 100\% / (I \times S \times t \times \lambda)$$

Where N_A is Avogadro constant (6.022×10^{23} mol^{-1}), ħ is the Planck constant (6.626×10^{-34} J s), c is the speed of light (3×10^8 m s^{-1}), S is the irradiation area (cm^2), I is the intensity of irradiation light (W cm^{-2}), t is the photoreaction time (s), λ is the wavelength of the monochromatic light (m).

3.17.1.15 Photocatalytic CO_2 reduction experiments

A quartz flask was charged with the COF powder (1 mg), acetonitrile (MeCN) and triethanolamine (TEOA) (30:1 vol. mixture, 5 mL) and sealed with a septum. The resulting suspension was ultrasonicated for 5 minutes and then purged with CO_2 for 15 minutes. The reaction mixture was illuminated with a 300 W Newport Xe light source (model: 6258, Ozone

free) equipped with a λ > 420 nm cut-off filter. Gaseous products were taken with a gas-tight syringe and run on a Shimadzu GC-2014 gas chromatograph equipped with a ShinCarbon ST micropacked column (Restek 80-100 mesh, 2 m length, 0.53 mm inner diameter) and a thermal conductivity detector.

3.17.1.16 X-ray photoelectron spectroscopy (XPS) measurements

X-ray photoelectron spectroscopy (XPS) measurements were performed using a Kratos AXIS Ultra DLD instrument. The chamber pressure during the measurements was 5×10^{-9} Torr. Wide energy range survey scans were collected at pass energy of 80 eV in hybrid slot lens mode and a step size of 0.5 eV. Wide scan and high-resolution data on the C 1s, O 1s, Cl 2p, Re 4f and Co 2p photoelectron peaks was collected at pass energy 20 eV over energy ranges suitable for each peak, and collection times of 5 min, step sizes of 0.1 eV. The charge neutralizer filament was used to prevent the sample charging over the irradiated area. The X-ray source was a monochromated Al Kα emission, run at 10 mA and 12 kV (120 W). The energy range for each 'pass energy' (resolution) was calibrated using the Kratos Cu 2p3/2, Ag $3d_{5/2}$ and Au $4f_{7/2}$ three-point calibration method. The transmission function was calibrated using a clean gold sample method for all lens modes and the Kratos transmission generator software within Vision II.

3.17.1.17 TA spectroscopy

The apparatus employed to obtain transient absorption, TA, spectra of the COFs of interest consists of an Ytterbium laser system (PHAROS Short-Pulse 10 W, PH1-SP-10W, Light Conversion) with an output power of 10 W, wavelength of 1028 nm, repetition rate of 10 kHz and pulse duration of ~180 fs. Of this, ~1 W is used to drive an Optical Parametric Amplifier, OPA (ORPHEUS, Light Conversion) in tandem with a second harmonic generation module (LYRA, Light Conversion) in order to generate radiation centred at 400 nm with a bandwidth (FWHM) of 3 nm.

This 400 nm output was used as the pump source for subsequent TA measurements which employed a commercial TA spectrometer (HARPIA, Light Conversion). The probe light was

visible white light super continuum generated by focusing < 0.1 W of 1028 nm radiation onto a sapphire window. Variable delay times between the pump and probe beams were obtained by passing the pump beam through a multi-pass mechanical delay stage allowing pump-probe delays up to 3.6 ns to be achieved. The pump and probe beams were focused to 600 and 400 μm spots at the sample. The pump laser beam was chopped, allowing, or blocking several pump pulses, resulting in an effective pumping repetition rate of 5 kHz to be obtained; the state of pumping of the sample (i.e. pumped/unpumped), along with stability of the pump laser power, is monitored using a photodiode. The power of the chopped beam incident on the sample was 0.8 mW. The samples were suspensions of the COF of interest, in either pure acetonitrile, or a 30:1 mixture of acetonitrile and TEOA, held within a quartz cuvette with a 2 mm path length.

The white light supercontinuum was collimated and routed to the detector. Here the white light was spectrally dispersed by a spectrograph (Kymera 193i, Andor), employing a grating of 150 lines/mm, blazed at 800 nm, and detected using an NMOS detector (S3901, Hamamatsu).

3.17.1.18 Density functional theory (DFT) and time-dependent DFT (TD-DFT) calculations

Representative molecular fragments of the COFs studied here were calculated for their standard reduction potentials of half-reactions for free electrons/holes and excitons, using density functional theory (DFT) and time-dependent DFT (TD-DFT). The CAM-B3LYP density functional was used for all the DFT and TD-DFT calculations, together with the Def2-SVP basis set, using the Gaussian 16 software. Vertical reduction potentials (*i.e.*, IP and EA) and vertical exciton potentials (*i.e.*, IP* and EA*) were calculated using the geometry optimized in the ground state, which had been confirmed to be a true minimum by a frequency calculation. For calculations of excited-state properties, S1 optimizations were first carried out using the Tamm–Dancoff approximation as this is more robust than full TD-DFT away from the ground-state geometry. Single-point, full TD-DFT calculations were then performed to obtain all necessary information for the electron excitation analyses using Multiwfn.[15] The effect of solvation by acetonitrile was accounted for by using the PCM/SMD solvation model.

3.18 References

1 J. Kosco, M. Sachs, R. Godin, M. Kirkus, L. Francas, M. Bidwell, M. Qureshi, D. Anjum, J. R. Durrant and I. McCulloch, *Adv. Energy Mater.*, 2018, **8**, 1802181.

2 S. Matsuoka, T. Kohzuki, C. Pac, A. Ishida, S. Takamuku, M. Kusaba, N. Nakashima and S. Yanagida, *J. Phys. Chem.*, 1992, **96**, 4437–4442.

3 N. Huang, P. Wang and D. Jiang, *Nat. Rev. Mater.*, 2016, 1, 16068.

4 S. J. Lyle, P. J. Waller and O. M. Yaghi, *Trends Chem.*, 2019, 1, 172–184.

5 C. S. Diercks and O. M. Yaghi, *Science*, 2017, 355, eaal1585.

6 M. S. Lohse and T. Bein, *Adv. Funct. Mater.*, 2018, **28**, 1705553.

7 V. S. Vyas, F. Haase, L. Stegbauer, G. Savasci, F. Podjaski, C. Ochsenfeld and B. V. Lotsch, *Nat. Commun.*, 2015, **6**, 1–9.

8 X. Wang, L. Chen, S. Y. Chong, M. A. Little, Y. Wu, W. H. Zhu, R. Clowes, Y. Yan, M. A. Zwijnenburg, R. S. Sprick and A. I. Cooper, *Nat. Chem.*, 2018, **10**, 1180–1189.

9 S. Lin, C. S. Diercks, Y. B. Zhang, N. Kornienko, E. M. Nichols, Y. Zhao, A. R. Paris, D. Kim, P. Yang, O. M. Yaghi and C. J. Chang, *Science*, 2015, **349**, 1208–1213.

10 H. Liu, J. Chu, Z. Yin, X. Cai, L. Zhuang and H. Deng, *Chem*, 2018, **4**, 1696–1709.

11 Y. Fu, X. Zhu, L. Huang, X. Zhang, F. Zhang and W. Zhu, *Appl. Catal. B Environ.*, 2018, **239**, 46–51.

12 S. Yang, W. Hu, X. Zhang, P. He, B. Pattengale, C. Liu, M. Cendejas, I. Hermans, X. Zhang, J. Zhang and J. Huang, *J. Am. Chem. Soc.*, 2018, **140**, 14614–14618.

13 W. Zhong, R. Sa, L. Li, Y. He, L. Li, J. Bi, Z. Zhuang, Y. Yu and Z. Zou, *J. Am. Chem. Soc.*, 2019, **141**, 7615–7621.

14 E. Jin, M. Asada, Q. Xu, S. Dalapati, M. A. Addicoat, M. A. Brady, H. Xu, T. Nakamura, T. Heine, Q. Chen and D. Jiang, *Science (80-.).*, 2017, **357**, 673–676.

15 R. Chen, J. L. Shi, Y. Ma, G. Lin, X. Lang and C. Wang, *Angew. Chem. Int. Ed.*, 2019, **58**, 6430–6434.

16 L. Y. Liao, X. R. Kong and X. F. Duan, *J. Org. Chem.*, 2014, **79**, 777–782.

17 M. G. Rabbani, A. K. Sekizkardes, O. M. El-Kadri, B. R. Kaafarani and H. M. El-Kaderi, *J. Mater. Chem.*, 2012, **22**, 25409–25417.

18 E. Jin, Z. Lan, Q. Jiang, K. Geng, G. Li, X. Wang and D. Jiang, *Chem*, 2019, **5**, 1632–1647.

19 S. Wei, F. Zhang, W. Zhang, P. Qiang, K. Yu, X. Fu, D. Wu, S. Bi and F. Zhang, *J. Am. Chem. Soc.*, 2019, **141**, 14272–14279.

20 S. Bi, C. Yang, W. Zhang, J. Xu, L. Liu, D. Wu, X. Wang, Y. Han, Q. Liang and F. Zhang, *Nat. Commun.*, 2019, **10**, 2467.

21 X. Zhuang, W. Zhao, F. Zhang, Y. Cao, F. Liu, S. Bi and X. Feng, *Polym. Chem.*, 2016, **7**, 4176–4181.

22 A. Yassin, M. Trunk, F. Czerny, P. Fayon, A. Trewin, J. Schmidt and A. Thomas, *Adv. Funct. Mater.*, 2017, **27**, 1700233.

23 K. M. Choi, D. Kim, B. Rungtaweevoranit, C. A. Trickett, J. T. D. Barmanbek, A. S. Alshammari, P. Yang and O. M. Yaghi, *J. Am. Chem. Soc.*, 2017, **139**, 356–362.

24 E. Jin, J. Li, K. Geng, Q. Jiang, H. Xu, Q. Xu and D. Jiang, *Nat. Commun.*, 2018, **8**, 4143.

25 E. Jin, M. Asada, Q. Xu, S. Dalapati, M. A. Addicoat, M. A. Brady, H. Xu, T. Nakamura, T. Heine, Q. Chen and D. Jiang, *Science*, 2017, **357**, 673–676.

26 J. Hawecker, J.-M. Lehn and R. Ziessel, *Chem. Commun.*, 1983, 536–538.

27 G. Sahara and O. Ishitani, *Inorg. Chem.*, 2015, **54**, 5096–5104.

28 T. Nakajima, Y. Tamaki, K. Ueno, E. Kato, T. Nishikawa, K. Ohkubo, Y. Yamazaki, T. Morimoto and O. Ishitani, *J. Am. Chem. Soc.*, 2016, **138**, 13818–13821.

29 R. S. Sprick, Y. Bai, A. A. Y. Guilbert, M. Zbiri, C. M. Aitchison, L. Wilbraham, Y. Yan, D. J. Woods, M. A. Zwijnenburg and A. I. Cooper, *Chem. Mater.*, 2019, **31**, 305–313.

30 K. Li, B. Peng and T. Peng, *ACS Catal.*, 2016, **6**, 7485–7527.

31 J. Lin, Z. Pan and X. Wang, *ACS Sustain. Chem. Eng.*, 2014, **2**, 353–358.

32 K. Li, B. Peng and T. Peng, *ACS Catal.*, 2016, **6**, 7485–7527.

33 R. S. Sprick, B. Bonillo, M. Sachs, R. Clowes, J. R. Durrant, D. J. Adams and A. I. Cooper, *Chem. Commun.*, 2016, **52**, 10008–10011.

34 S. Y. Li, S. Meng, X. Zou, M. El-Roz, I. Telegeev, O. Thili, T. X. Liu and G. Zhu, *Microporous Mesoporous Mater.*, 2019, **285**, 195–201.

35 M. Lu, Q. Li, J. Liu, F. M. Zhang, L. Zhang, J. L. Wang, Z. H. Kang and Y. Q. Lan, *Appl. Catal. B Environ.*, 2019, **254**, 624–633.

36 M. Schwarze, D. Stellmach, M. Schröder, K. Kailasam, R. Reske, A. Thomas and R. Schomäcker, *Phys. Chem. Chem. Phys.*, 2013, **15**, 3466–3472.

37 E. E. Benson and C. P. Kubiak, *Chem. Commun.*, 2012, **48**, 7374–7376.

38 T. W. Schneider, M. Z. Ertem, J. T. Muckerman and A. M. Angeles-Boza, *ACS Catal.*, 2016, **6**, 5473–5481.

39 M. B. Ross, Y. Li, P. De Luna, D. Kim, E. H. Sargent and P. Yang, *Joule*, 2019, **3**, 257–264.

40 M. B. Ross, C. T. Dinh, Y. Li, D. Kim, P. De Luna, E. H. Sargent and P. Yang, *J. Am. Chem. Soc.*, 2017, **139**, 9359–9363.

41 J. S. Lee, D. Il Won, W. J. Jung, H. J. Son, C. Pac and S. O. Kang, *Angew. Chem. Int. Ed.*, 2017, **56**, 976–980.

42 J. C. Hu, M. X. Gui, W. Xia, J. Wu, Y. N. Zhou, N. Feng, J. Xiao, H. Liu, C. H. Tung, L. Z. Wu and F. Wang, *J. Mater. Chem. A*, 2019, **7**, 10475–10482.

Chapter 4

Highly selective photocatalytic CO_2 reduction from fluorinated covalent organic frameworks with molecular Co co-catalysts

4.1 Contribution

All the materials were synthesized and characterized by the thesis author. The photocatalysis experiments about CO_2 reduction were performed by the thesis author. Dr Linjiang Chen conceived the modelling strategy. Dr Linjiang Chen and Xue Wang performed the calculations. Dr Xiaoyan Wang carried out PXRD analyses. Lunjie Liu performed photoelectrochemical measurements. Dr Kewei Wang is thanked for the help with the monomers. Rob Clowes helped to interpret the gas sorption isotherms.

4.2 Introduction

In previous reports, COFs have been designed as the scaffold to anchor non-noble metal molecular catalysts (*e.g.* bipyridine Co, Ni complex) for photocatalytic CO_2 reduction which additional noble metal photosensitizers, such as bipyridine Ru complex, were indispensable for such systems.[1–3] Photoactive tricarbonylchloro(bipyridyl) Re complex molecular catalyst was also integrated into COFs for efficient CO_2 reduction.[4,5] Recently, a Zn-based porphyrintetrathiafulvalene COF was used for photocatalytic CO_2 reduction with almost 100% selectivity using H_2O as the electron donor, while the CO production rate is still low.[6] Thus, to our best knowledge, it is still challenging to achieve both high CO_2 reduction efficiency and selectivity for non-noble metal organic CO_2 reduction photocatalysts. Fluorination is a strategy to improve the affinity of materials to CO_2 molecules.[3,7–9] Besides, fluorinated 2D-COFs shows better crystallinity and larger surface areas than non-fluorinated analogues because fluorination results in the polarization of the aromatic rings leading to stronger interlayer interactions.[10]

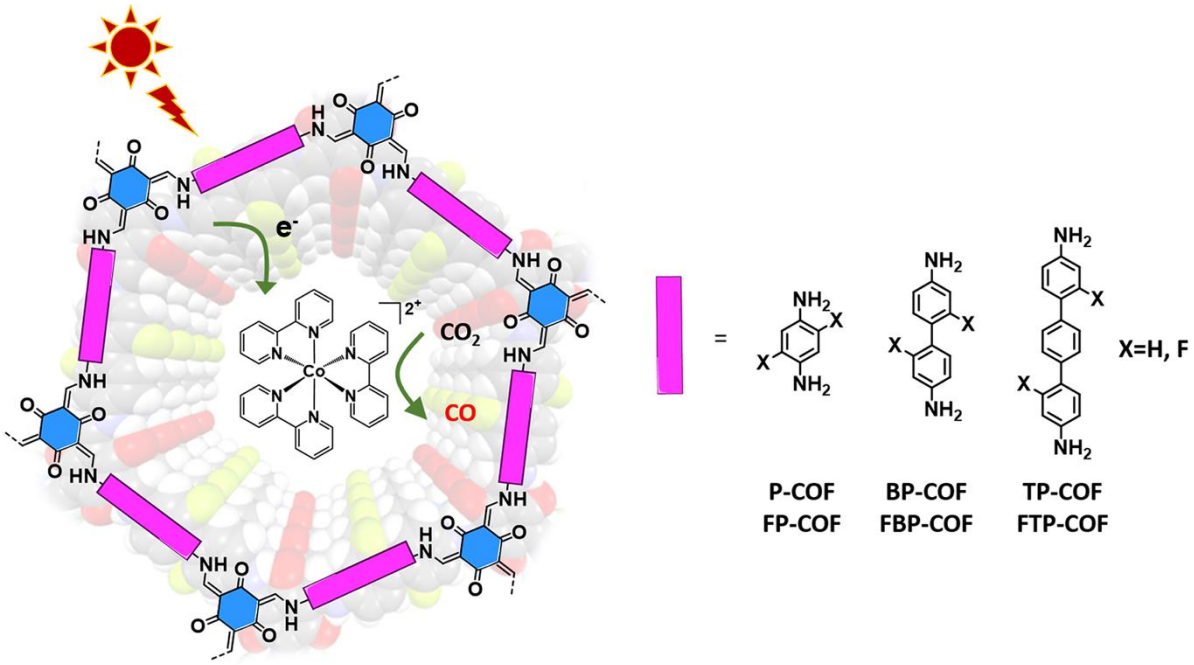

Figure 4.1 Schematic representation of structures of non-fluorinated COFs and fluorinated COFs.

In this chapter, taking full advantage of COFs and fluorination, we reported a series of *β*-ketoenamine-linkers COFs synthesized with aromatic linkers of different lengths and their isostructural fluorinated forms (Figure 4.1). The obtained fluorinated COFs with various pore

sizes and band gaps were applied as photosensitizers, coupled with a low-cost, molecular cobalt (II) bipyridine complex ($[Co(bpy)_3]^{2+}$) as a cocatalyst for photocatalytic CO_2 reduction under visible light. Their structure−property−activity relationships were explored by screening CO_2 reduction photoactivity for isostructural COFs under the same conditions. CO_2 affinity, pore size and light absorption of photosensitizer had significant influences on photocatalytic CO_2 reduction activity.

4.3 NMR Spectra

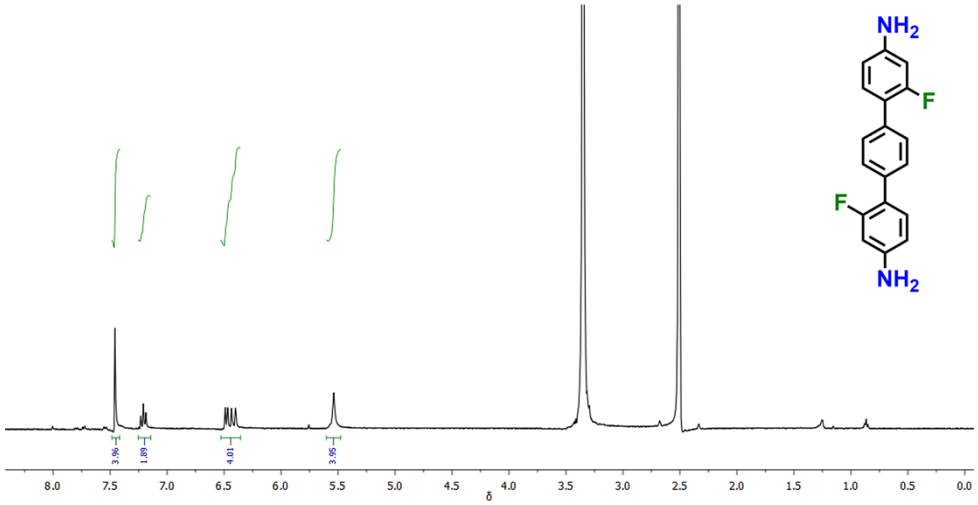

Figure 4.2 ^{1}H NMR spectrum of 2,2"-difluoro-[1,1':4',1"-terphenyl]-4,4"-diamine in DMSO-d_6.

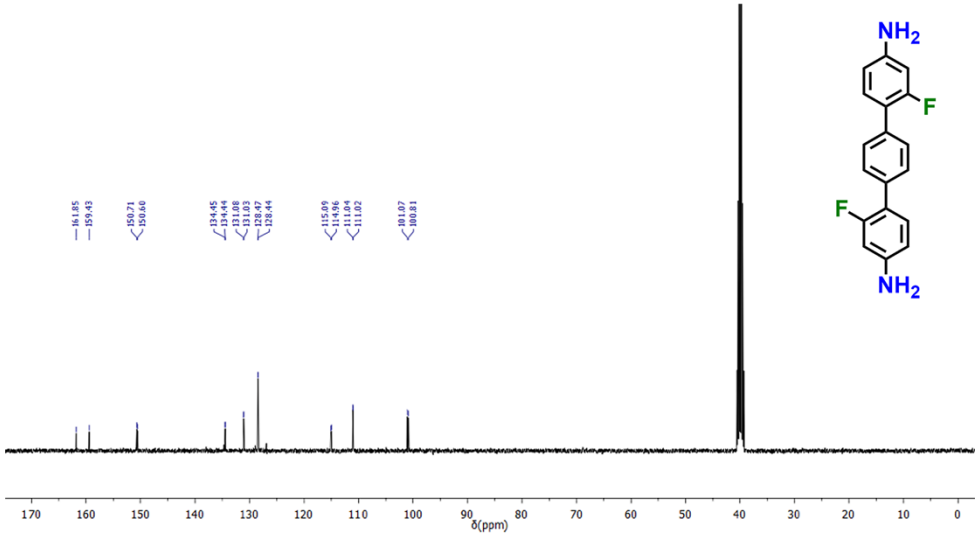

Figure 4.3 $^{13}C\{1H\}$ NMR spectrum of 2,2"-difluoro-[1,1':4',1"-terphenyl]-4,4"-diamine in DMSO-d_6.

2,2"-difluoro-[1,1':4',1"-terphenyl]-4,4"-diamine was first used for synthesizing COFs and obtained from Shanghai Kaiyulin Pharmaceutical Technology Co. Ltd. $(M+H)^+$ = 297.1. ^{1}H NMR (400 MHz, DMSO-d_6) d 7.46 (s, 4H), 7.21 (t, J = 8.8 Hz, 2H), 6.45 (dd,

J = 24.5, 11.0 Hz, 4H), 5.54 (s, 4H). ^{13}C NMR (101 MHz, DMSO-d_6) d 161.85, 159.43, 150.71, 150.60, 134.45, 134.44, 131.08, 131.03, 128.47, 128.44, 115.09, 114.96, 111.04, 111.02, 101.07, 100.81.

4.4 Synthetic procedures

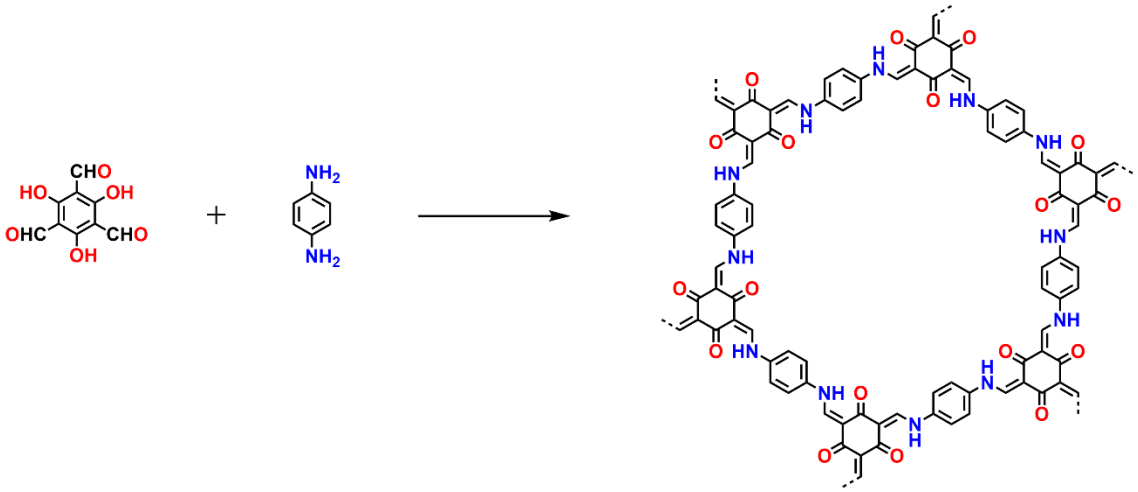

Figure 4.4 Scheme of the synthesis of P-COF.

Synthesis of P-COF: A Pyrex tube (25 mL) was charged with 1,3,5-triformylphloroglucinol (63 mg, 0.3 mmol), p-phenylenediamine (48.66 mg, 0.45 mmol), mesitylene (1.5 mL), 1,4-dioxane (1.5 mL) and aqueous acetic acid (0.3 mL, 6 M). The mixture was ultrasonicated for two minutes and then flash frozen at 77 K (liquid N_2 bath) and degassed through three freeze-pump-thaw cycles and sealed under vacuum using a Schlenk line and oil pump. The tube was heated at 120 °C for three days. After cooling to room temperature, the precipitate was washed with acetone and THF three times. The resulting powder was then solvent exchanged with acetone six times. The powder was collected and dried at 120 °C under a vacuum overnight. Anal. Calcd for $(C_{36}H_{24}N_6O_6)_n$: C, 67.92; H, 3.80; N, 13.2. Found: C, 49.59; H, 4.21; N, 8.08.

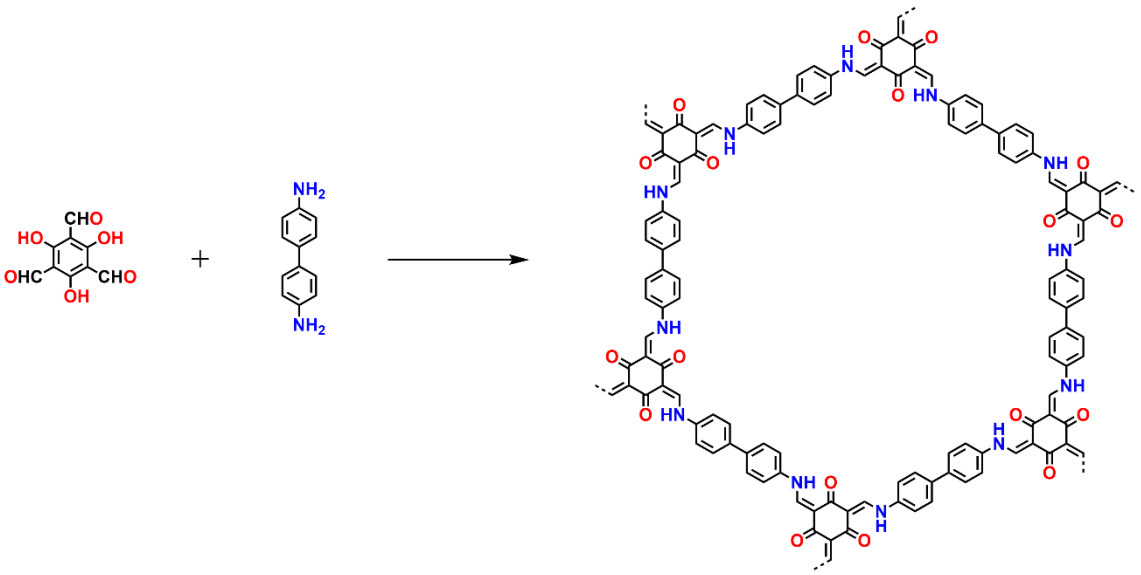

Figure 4.5 Scheme of the synthesis of BP-COF.

Synthesis of BP-COF: A Pyrex tube (25 mL) was charged with 1,3,5-triformylphloroglucinol (63 mg, 0.3 mmol) and benzidine (82.9 mg, 0.45 mmol), mesitylene (1.5 mL), 1,4-dioxane (1.5 mL) and aqueous acetic acid (0.3 mL, 6 M). The mixture was ultrasonicated for two minutes and then flash frozen at 77 K (liquid N_2 bath) and degassed through three freeze-pump-thaw cycles and sealed under vacuum using a Schlenk line and oil pump. The tube was heated at 120 °C for three days. After cooling to room temperature, the precipitate was washed with acetone and THF three times. The resulting powder was then solvent exchanged with acetone six times. The powder was collected and dried at 120 °C under a vacuum overnight. Anal. Calcd for $(C_{54}H_{36}N_6O_6)_n$: C, 74.99; H, 4.20; N, 9.72. Found: C, 64.89; H, 4.21; N, 8.08.

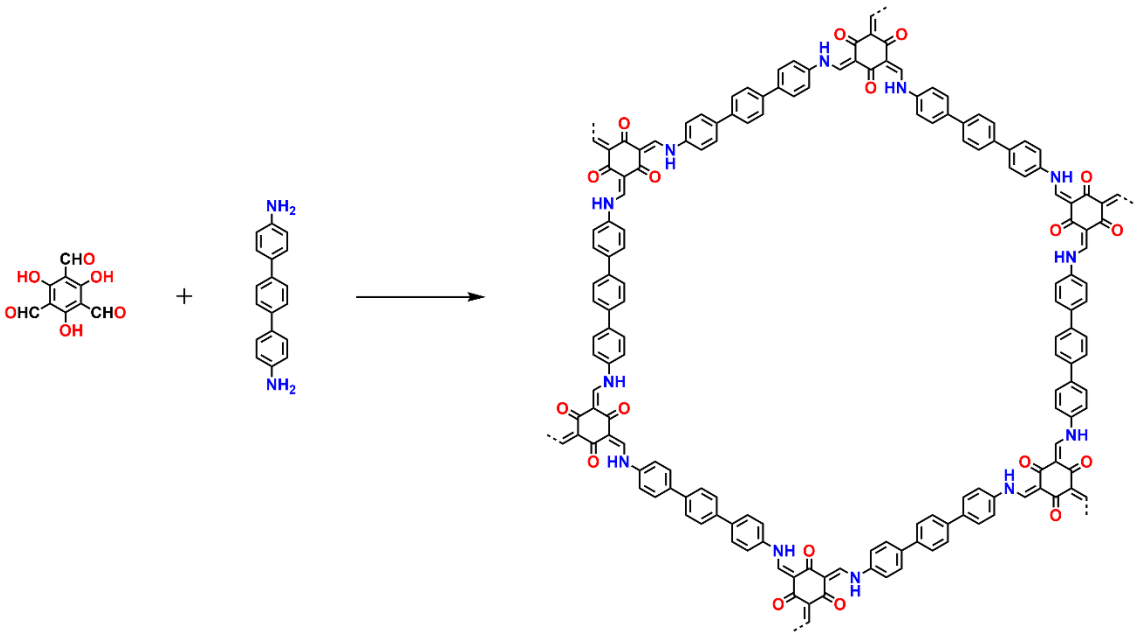

Figure 4.6 Scheme of the synthesis of TP-COF.

Synthesis of TP-COF: A Pyrex tube (25 mL) was charged with 1,3,5-triformylphloroglucinol (63 mg, 0.3 mmol) and 4,4"-diamino-p-terphenyl (117.2 mg, 0.45 mmol), 1,2-dichlorobenzene (1.5 mL), 1-butanol (1.5 mL) and aqueous acetic acid (0.3 mL, 6 M). The mixture was ultrasonicated for two minutes and then flash frozen at 77 K (liquid N_2 bath) and degassed through three freeze-pump-thaw cycles and sealed under vacuum using a Schlenk line and oil pump. The tube was heated at 150 °C for three days. After cooling to room temperature, the precipitate was washed with acetone and THF three times. The resulting powder was then solvent exchanged with acetone six times. The powder was collected and dried at 120 °C under a vacuum overnight. Anal. Calcd for $(C_{72}H_{48}N_6O_6)_n$: C, 79.11; H, 4.43; N, 7.69. Found: C, 74.90; H, 4.39; N, 7.14.

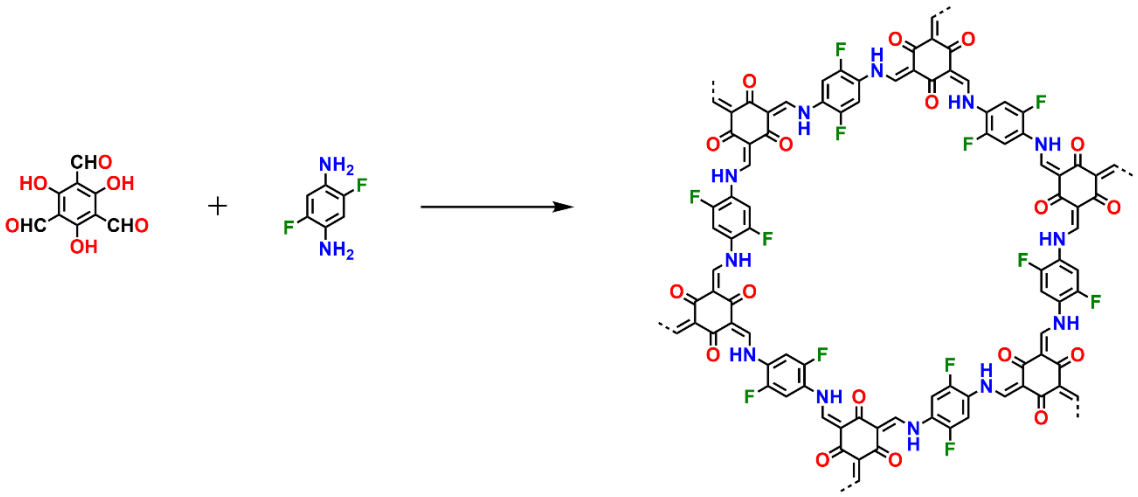

Figure 4.7 Scheme of the synthesis of FP-COF.

Synthesis of FP-COF: A Pyrex tube (25 mL) was charged with 1,3,5-triformylphloroglucinol (63 mg, 0.3 mmol) and 1,4-diamino-2,5-diflurobenzene (64.8 mg, 0.45 mmol), mesitylene (1.5 mL), 1,4-dioxane (1.5 mL) and aqueous acetic acid (0.3 mL, 6 M). The mixture was ultrasonicated for two minutes and then flash frozen at 77 K (liquid N_2 bath) and degassed through three freeze-pump-thaw cycles and sealed under vacuum using a Schlenk line and oil pump. The tube was heated at 120 °C for three days. After cooling to room temperature, the precipitate was washed with acetone and THF three times. The resulting powder was then solvent exchanged with acetone six times. The powder was collected and dried at 120 °C under a vacuum overnight. Anal. Calcd for $(C_{36}H_{18}N_6O_6F_6)_n$: C, 58.07; H, 2.44; N, 11.29. Found: C, 49.07; H, 2.80; N, 7.63.

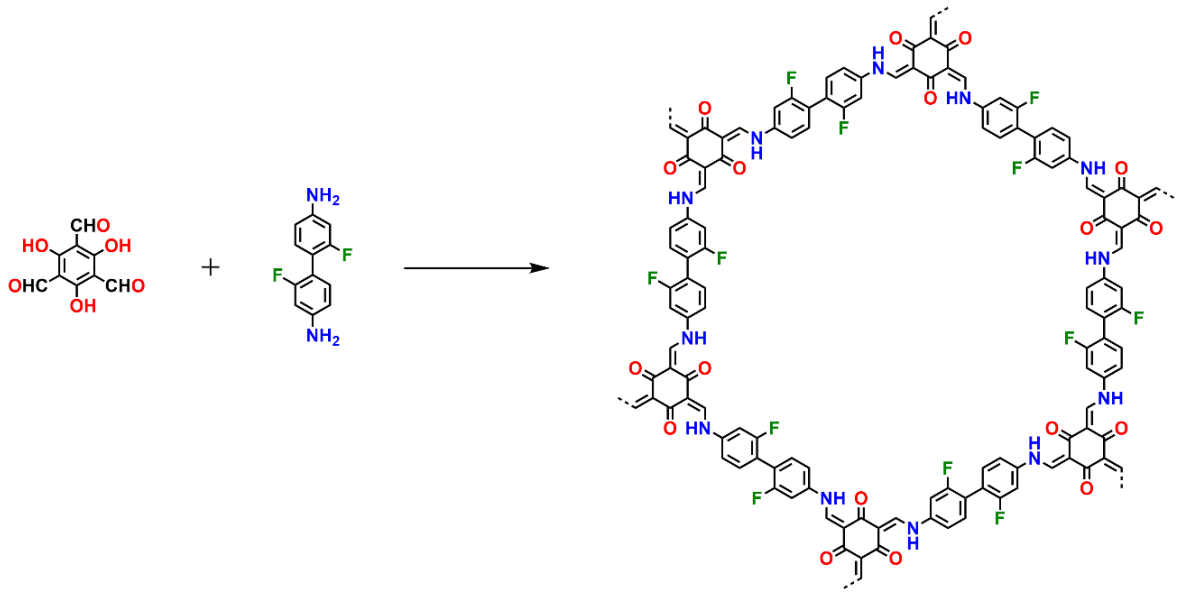

Figure 4.8 Scheme of the synthesis of FBP-COF.

Synthesis of FBP-COF: A Pyrex tube (25 mL) was charged with 1,3,5-triformylphloroglucinol (63 mg, 0.3 mmol) and 4,4'-diamino-2,2'-difluorobiphenyl (99.1 mg, 0.45 mmol), mesitylene (1.5 mL), 1,4-dioxane (1.5 mL) and aqueous acetic acid (0.3 mL, 6 M). The mixture was ultrasonicated for two minutes and then flashed frozen at 77 K (liquid N_2 bath) and degassed through three freeze-pump-thaw cycles and sealed under vacuum using a Schlenk line and oil pump. The tube was heated at 120 °C for three days. After cooling to room temperature, the precipitate was washed with acetone and THF three times. The resulting powder was then solvent exchanged with acetone six times. The powder was collected and dried at 120 °C under a vacuum overnight. Anal. Calcd for $(C_{54}H_{30}N_6O_6F_6)_n$: C, 66.67; H, 3.11; N, 8.64. Found: C, 57.05; H, 2.88; N, 4.45.

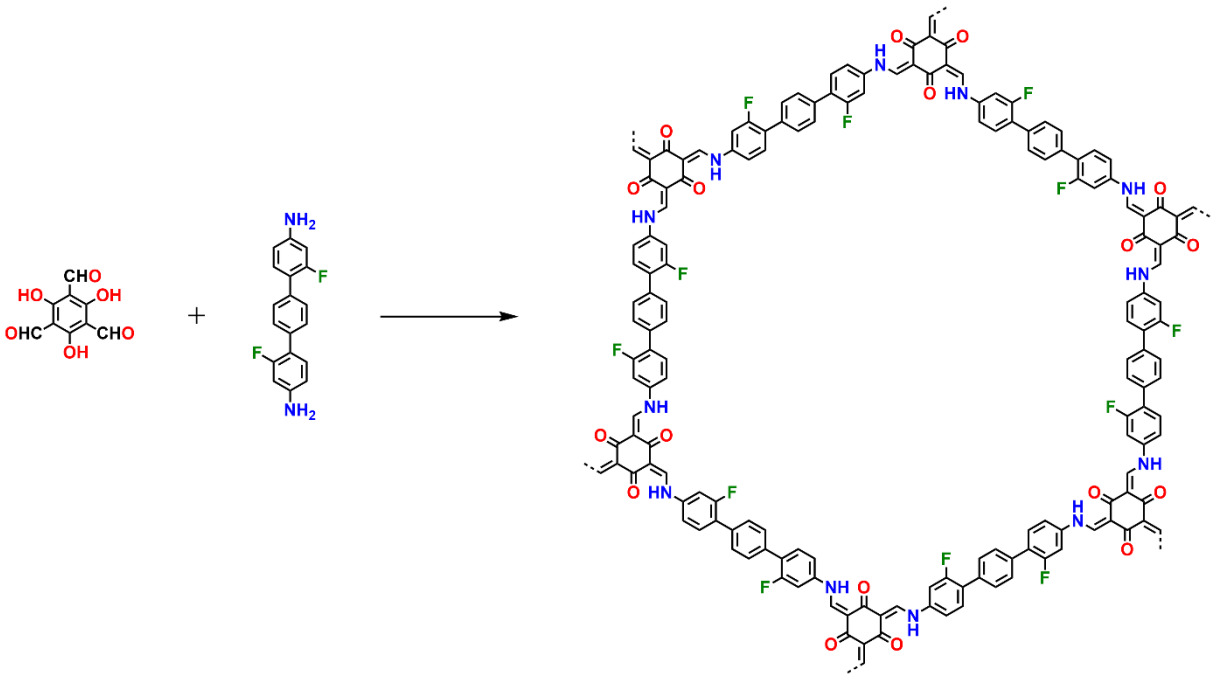

Figure 4.9 Scheme of the synthesis of FTP-COF.

Synthesis of FTP-COF: A Pyrex tube (25 mL) was charged with 1,3,5-triformylphloroglucinol (63 mg, 0.3 mmol) and 2,2"-difluoro-[1,1':4',1"-terphenyl]-4,4"-diamine (133.3 mg, 0.45 mmol), 1,2-dichlorobenze (1.5 mL), 1-butanol (1.5 mL) and aqueous acetic acid (0.3 mL, 6 M). The mixture was ultrasonicated for two minutes and then flashed frozen at 77 K (liquid N_2 bath) and degassed through three freeze-pump-thaw cycles and sealed under vacuum using a Schlenk line and oil pump. The tube was heated at 150 °C for three days. After cooling to room temperature, the precipitate was washed with acetone and THF three times. The resulting powder was then solvent exchanged with acetone six times. The powder was collected and dried at 120 °C under a vacuum overnight. Anal. Calcd for $(C_{72}H_{42}N_6O_6F_6)_n$: C, 72.00; H, 3.52; N, 7.00. Found: C, 68.51; H, 3.49; N, 6.29.

4.5 Powder X-ray diffraction analysis

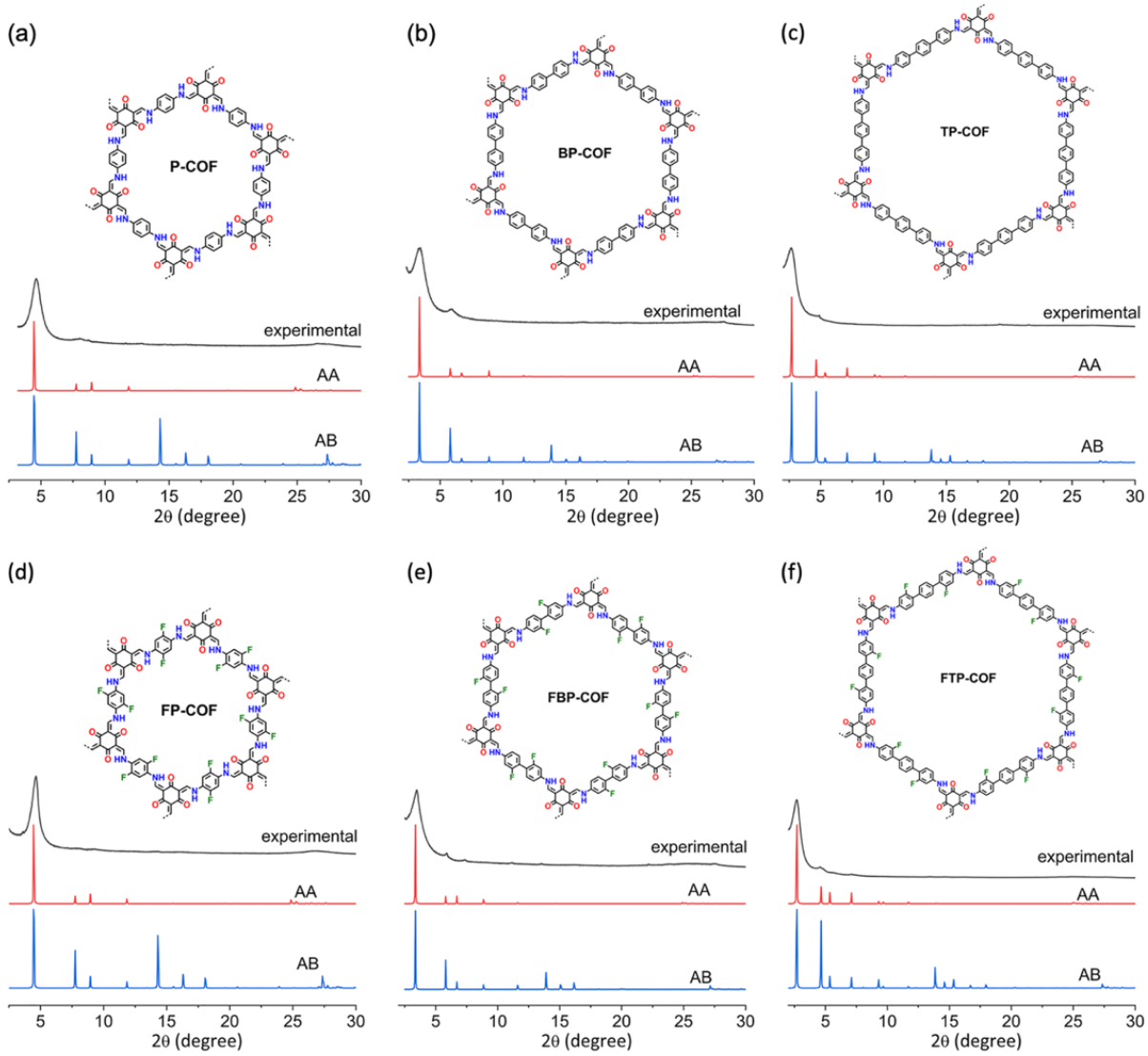

Figure 4.10 PXRD patterns of P-COF (a), BP-COF (b), TP-COF (c), FP-COF (d), FBP-COF (e) and FTP-COF (f): experimental (black), calculated with the eclipsed (AA) stacking (red) and staggered (AB) stacking models (blue).

A series of six COFs were designed and synthesized as illustrated in Figure 4.1. Three *β*-ketoenamine COFs (P-COF, BP-COF and TP-COF) were synthesized according to the methods in literature via Schiff base condensation of 1, 3, 5-triformylphloroglucinol (TFG) with p-phenylenediamine (P), 4,4'-diaminobiphenyl (BP) and 4, 4"-diamino-p-terphenyl (TP).[11–13] The fluorinated isostructural COFs (FP-COF, FBP-COF and FTP-COF) were yielded via condensation of TFG with 1,4-Diamino-2,5-difluorobenzene (FP), 4,4′-diamino-2,2′-difluorobiphenyl (FBP) and 2,2"-difluoro-[1,1':4',1"-terphenyl]-4,4"-diamine (FTP).

Powder X-ray diffraction (PXRD) measurements were used to characterize the crystallinity of all the COFs (Figure 4.10). The PXRD pattern of P-COF exhibited an intense peak at 4.7°, corresponding to the reflection from the (100) plane.[11] Minor peaks also appeared at 8.3° and 25.2° for P-COF, which were assigned to the (200) and (001) planes, respectively. The PXRD pattern of BP-COF showed diffraction peaks at 3.4°, 5.9° and 25.3°, corresponding to the (100), (2-10) and (001) planes, respectively.[12] The PXRD pattern of TP-COF gave diffraction peaks at 2.7, 4.9 and 25.2°, which were assigned to the (100), (2-10) and (001) planes, respectively.[13] PXRD results of non-fluorinated COFs demonstrated that the COFs were successfully synthesized by the methods in the literature.

Figure 4.10d, e and f exhibited the experimental and simulated PXRD patterns of fluorinated COFs. The PXRD pattern of FP-COF showed diffraction peaks at 4.5°, 7.8°, 9.3 and 26.9°, which were assigned to the (100), (110), (200) and (001) planes, respectively. FBP-COF gave strong PXRD peaks at 3.5°, 5.9°, 6.8° and 9.1°, corresponding to (100), (110), (200) and (210) planes, respectively. FTP-COF exhibited diffraction peaks at 2.7°, 4.6° and 7.2°, which were assigned to the (100), (110) and (120) planes, respectively.

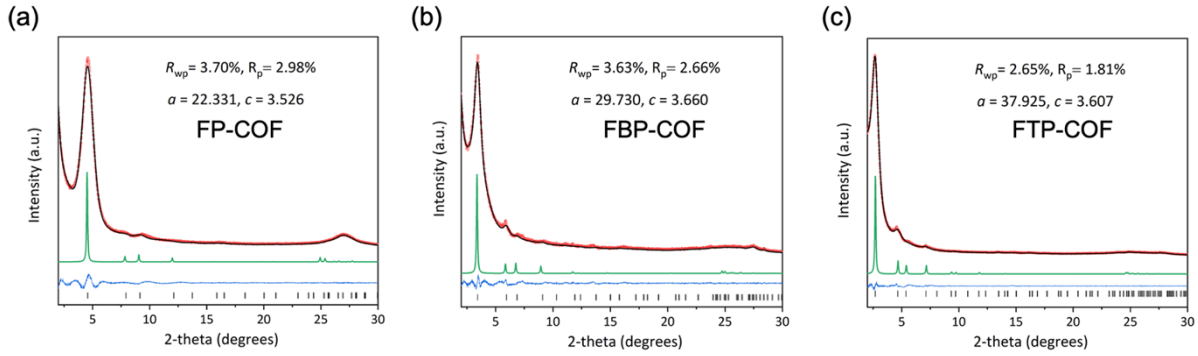

Figure 4.11 Experimental PXRD pattern (red), profile calculated from Pawley fitting (black) showing the residual (blue), compared with the pattern simulated from the eclipsed AA-stacking mode (green) for as synthesized FP-COF (a), FBP-COF and FTP-COF (c). Reflection positions are shown by tick marks.

Since all the fluorinated COFs were new reported COFs, Pawley refinements were involved in confirming the crystalline structures of fluorinated COFs. Experimental PXRD pattern, profile calculated from Pawley fitting, the residual and the pattern simulated from the structural model were shown as red, black, blue, and green lines, respectively, for each fluorinated COF.

Reflection positions were shown by tick marks. Unit cell parameters of these fluorinated COFs extracted by Pawley refinements with a *P*6/*m* space group (a = b = 22.331 Å and c = 3.526 Å for FP-COF; a = b = 29.730 Å and c = 3.660 Å for FBP-COF; a = b = 37.925 Å and c = 3.607 Å for FTP-COF), which are consistent with the AA-stacked models of FP-COF, FBP-COF and FTP-COF (Figure 4.11).

4.6 Gas sorption analysis

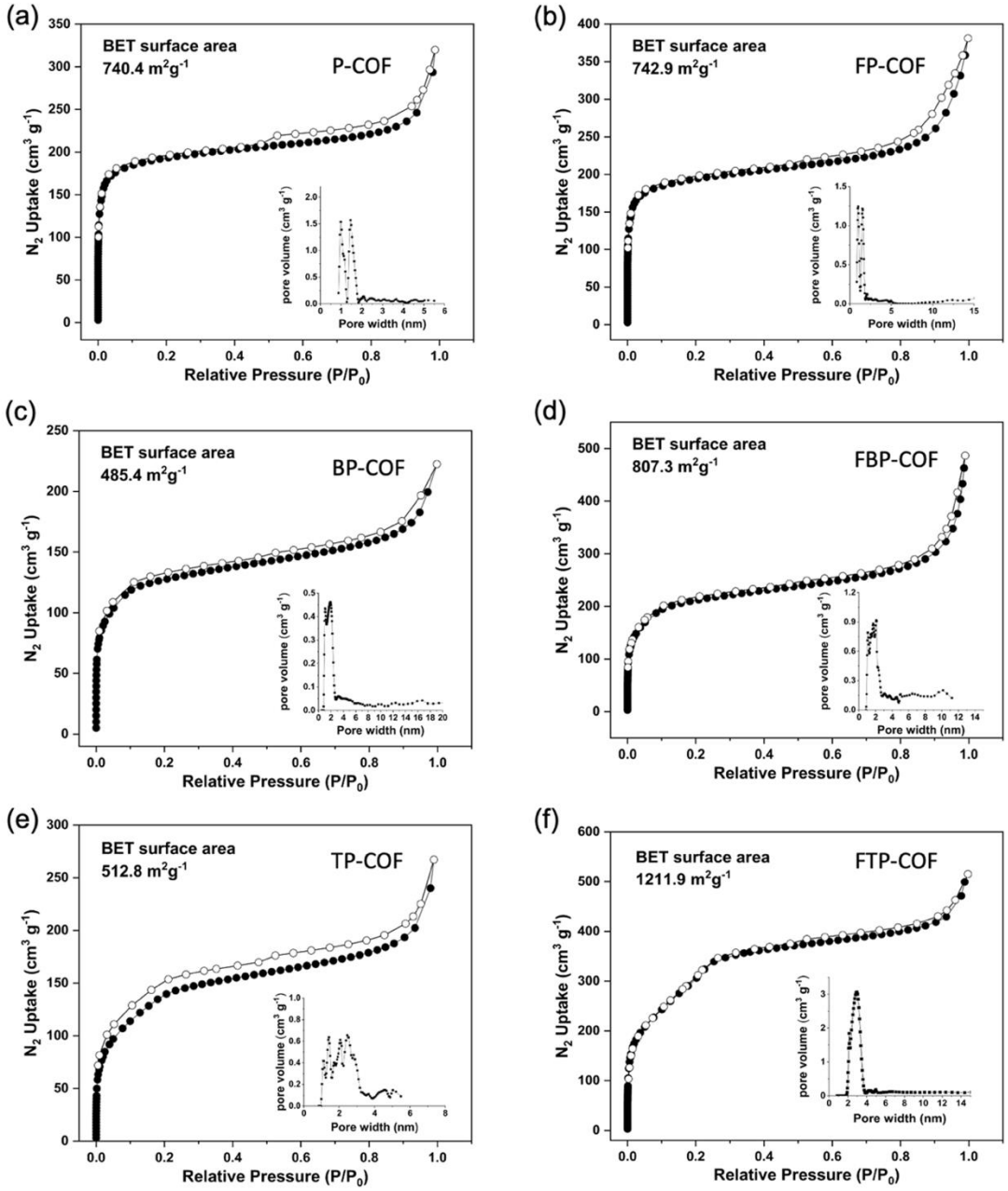

Figure 4.12 Nitrogen adsorption/desorption isotherms for P-COF (a), FP-COF (b), BP-COF (c), FBP-COF (d), TP-COF (e) and FTP-COF (f) recorded at 77.3 K (filled symbols = adsorption; open symbols = desorption). The inset shows the calculated pore size distribution.

The permanent porosity of the obtained COFs was confirmed by nitrogen sorption experiments at 77 K (Figure 4.12). All the COFs exhibited reversible type-I adsorption isotherms. The Brunauer–Emmett–Teller (BET) surface areas were 740.4, 485.4 and 512.8 m^2 g^{-1} for P-COF, BP-COF and TP-COF, respectively. The theoretical pore diameters of P-COF, BP-COF and

TP-COF were calculated to be 16.7, 24.2 and 31.8 Å, respectively. BET surface areas were calculated as 742.9, 807.3 and 1211.9 m^2 g^{-1} for FP-COF, FBP-COF, and FTP-COF, respectively. The theoretical pore diameters of FP-COF, FBP-COF and FTP-COF were calculated to be 15.5, 23.1 and 31.3 Å, respectively. The pore size distribution profiles based on nonlocal density functional theory (NLDFT) in Figure 4.12 were close to the theoretical results. However, the pore size distribution profiles based on NLDFT did not show ideal narrow pore size distributions for all the COFs, which might be due to the fitting methods not being matched with COFs, or the COFs materials not being uniform inside due to the changing of morphology in the process of preparation.

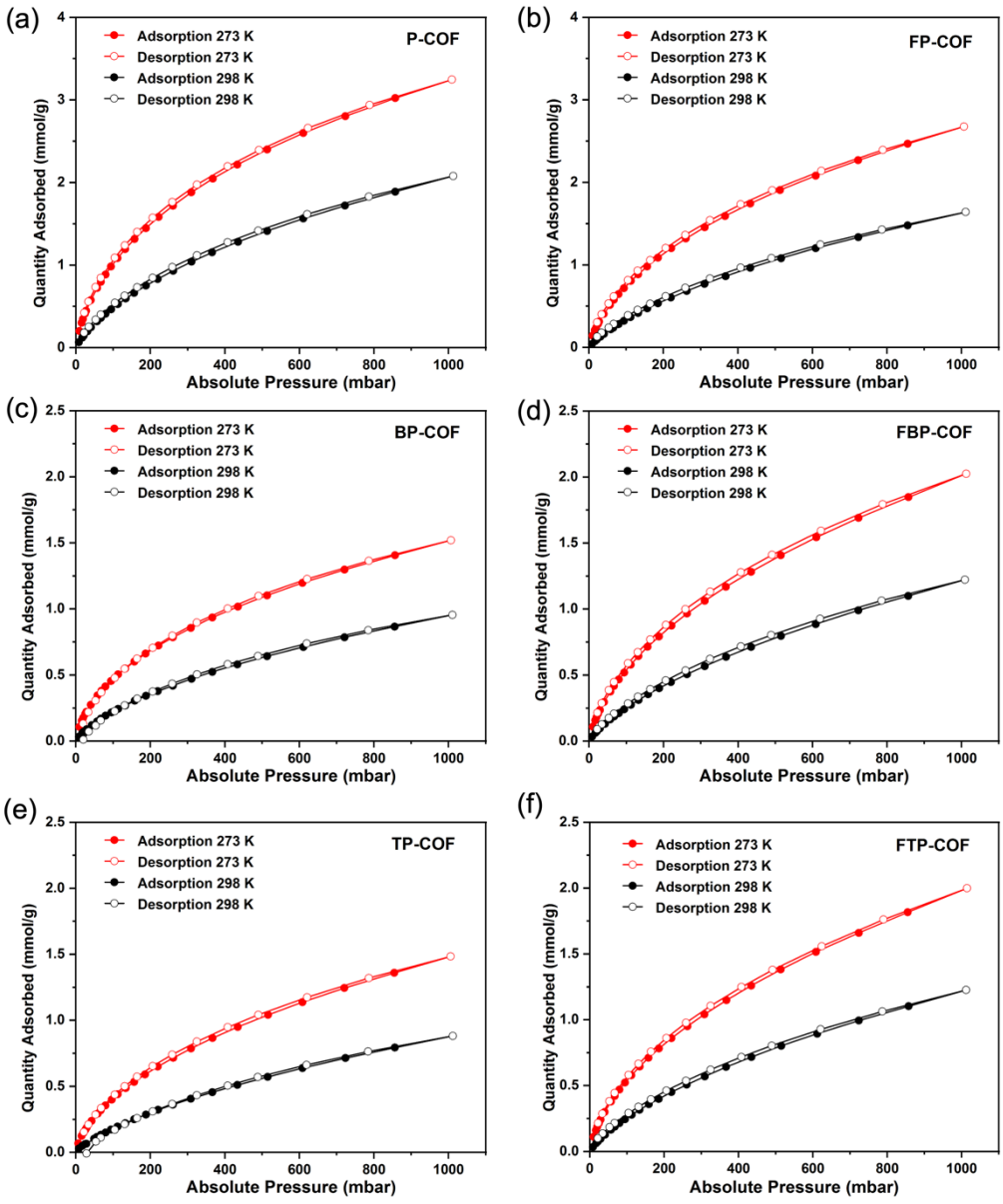

Figure 4.13 CO_2 adsorption isotherms of COFs collected at 273 K and 298 K.

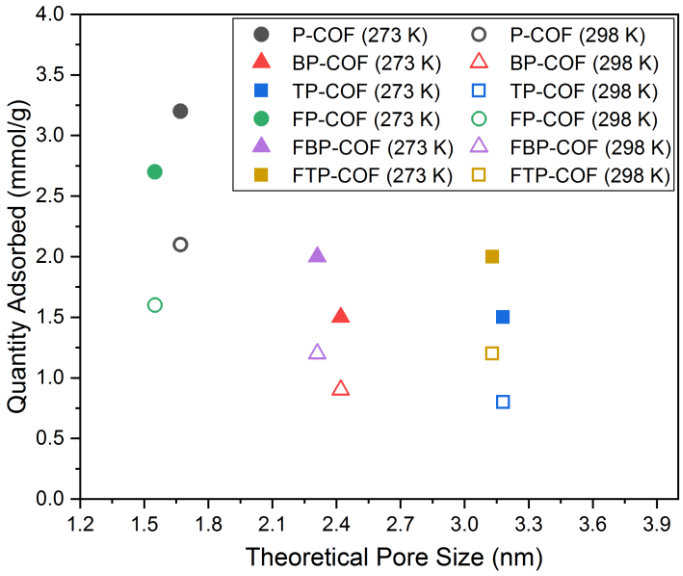

Figure 4.14 Comparison of theoretical pore sizes and CO_2 adsorptions of COFs.

CO_2 adsorption (Figure 4.13) and CO_2 isosteric heat of adsorption (Figure 4.15) were measured at both 273 and 298K to investigate the CO_2 uptake capacity and affinity of all the COFs. Figure 4.14 showed the comparison of theoretical pore sizes and CO_2 adsorptions of COFs. The CO_2 adsorptions of P-COF were 3.2 mmol g^{-1} at 273 K and 2.1 mmol g^{-1} at 298 K (Figure 4.13a), which were higher than those of FP-COF, showing 2.7 mmol g^{-1} at 273 K and 1.6 mmol g^{-1} at 298 K (Figure 4.13b). For other COFs, fluorinated COFs had higher CO_2 adsorption amounts than non-fluorinated COFs. For instance, the CO_2 adsorptions of BP-COF (Figure 4.13c) were 1.5 mmol g^{-1} at 273 K and 0.9 mmol g^{-1} at 298 K and the CO_2 adsorptions of FBP-COF (Figure 4.13d) were 2.0 mmol g^{-1} at 273 K and 1.2 mmol g^{-1} at 298 K. Gas sorption data demonstrated that the P-COF and FP-COF were microporous materials with pore sizes of 1.70 and 1.6 nm, and the other COFs were mesoporous polymers with pore sizes between 2.3 and 3.2 nm. All of them had good CO_2 capture and adsorption abilities.

The isosteric heat of adsorption (Q_{st}) was calculated to investigate the CO_2 affinity of materials. The isosteric heat of adsorption of P-COF, BP-COF and TP-COF (Figure 4.15a) were 33.6 kJ mol^{-1}, 36.2 kJ mol^{-1} and 32.9 kJ mol^{-1}, respectively. Moreover, the Q_{st} of fluorinated COFs (Figure 4.15b) were 34.1 kJ mol^{-1}, 36.5 kJ mol^{-1} and 33.2 kJ mol^{-1}, respectively. The Q_{st} results (Figure 4.15c) demonstrated that fluorinated COFs had stronger interactions between fluorinated COFs with CO_2 than non-fluorinated COFs. FBP-COF and FTP-COF showed

higher CO_2 capture amounts and CO_2 isosteric heat of adsorption than their analogues (Figure 4.15c), indicating their good CO_2 capture and adsorption abilities. FP-COF had comparable CO_2 capture amounts to P-COF.

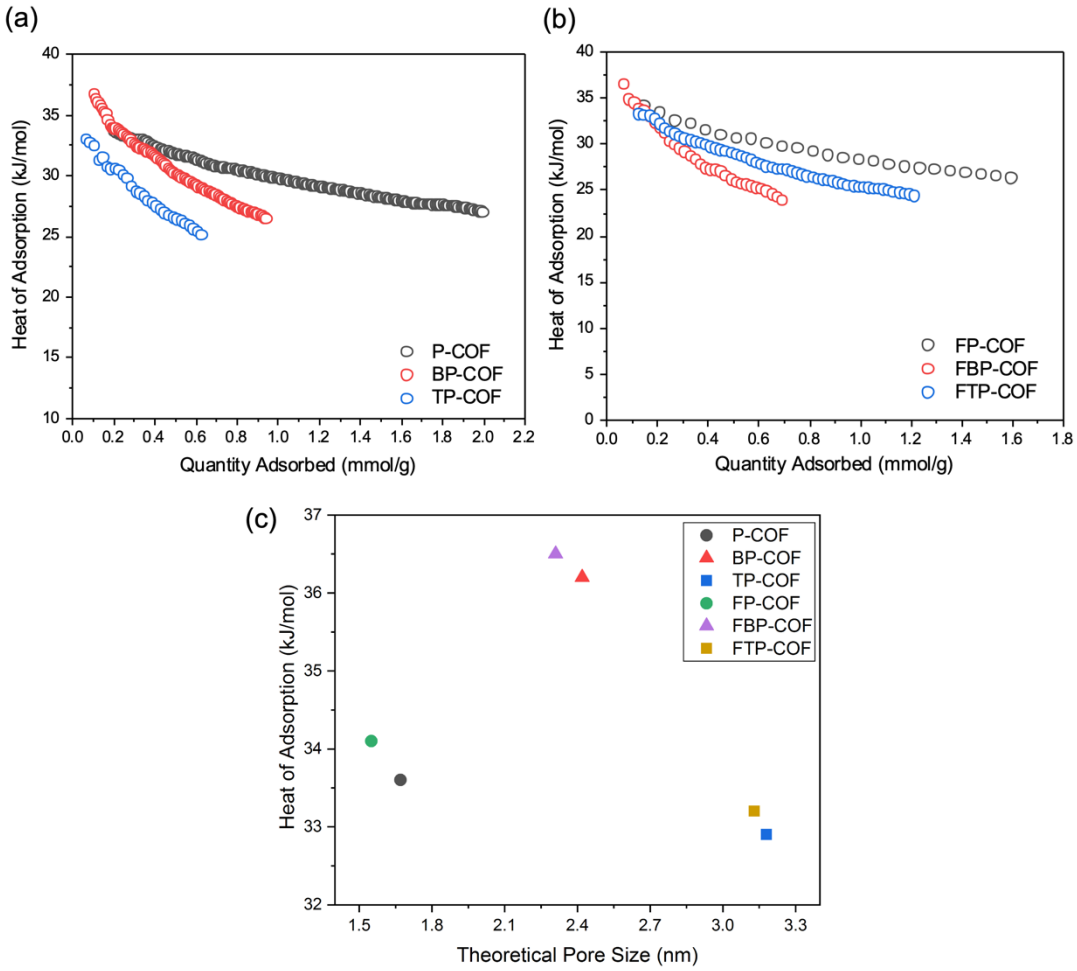

Figure 4.15 CO_2 isosteric heats of adsorption calculated from 273 K and 298 K of (a) P-COF, BP-COF and TP-COF and (b) Fluorinated COFs; (c) Comparison of theoretical pore size and CO_2 isosteric heats of adsorption.

4.7 UV-visible spectra and band gaps

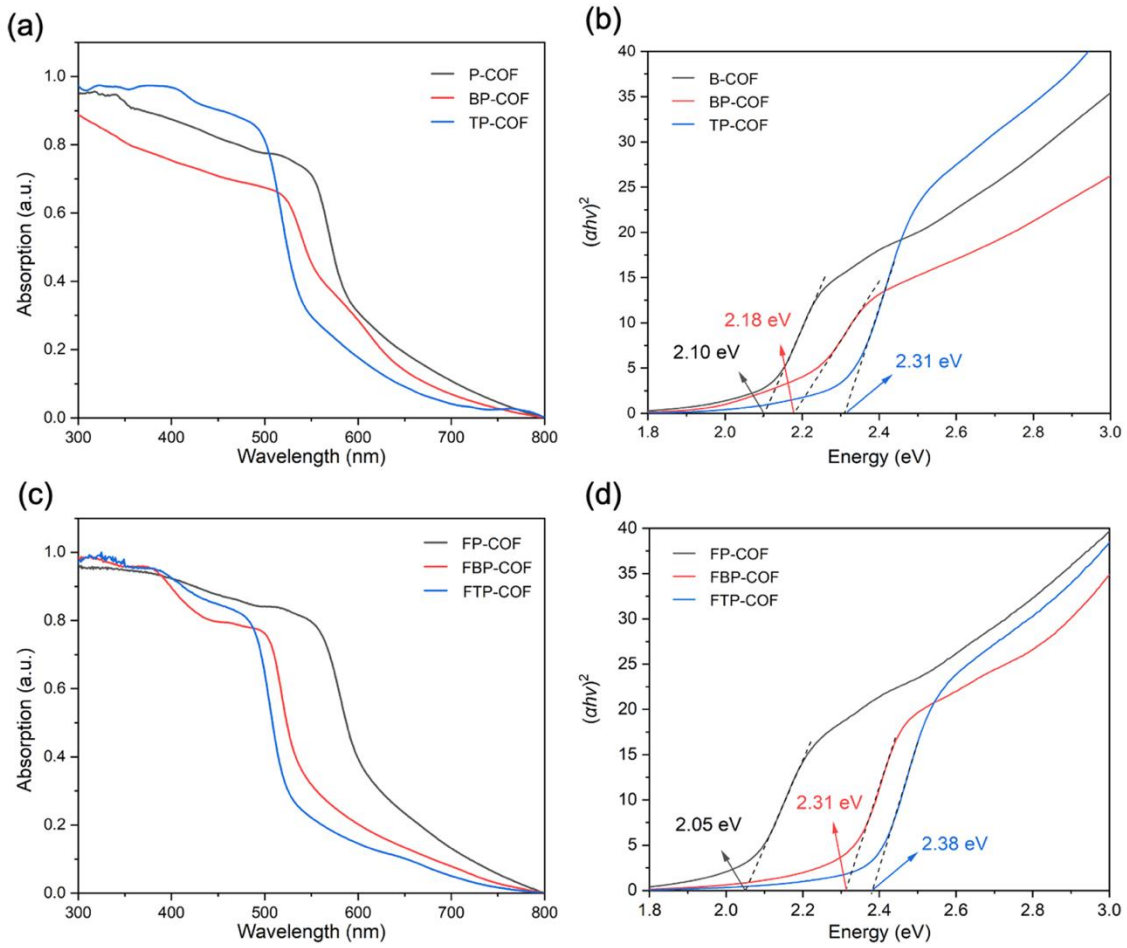

Figure 4.16 (a) UV-Vis absorption spectra of P-COF, BP-COF and TP-COF in the solid state; (b) Band gaps of non-fluorinated COFs determined from the Kubelka-Munk function; (c) UV-Vis absorption spectra of FP-COF, FBP-COF and FTP-COF in the solid state; (d) Band gaps of fluorinated COFs determined from the Kubelka-Munk function.

UV-vis reflectance spectra of the COFs were measured in the solid state for comparing light absorption ability. As shown in Figure 4.16a, the absorption onsets were found at 615, 598 and 558 nm for P-COF, BP-COF and TP-COF. The absorption onsets had a significant blue shift as the pore size increases of linker length. FP-COF, FBP-COF and FTP-COF showed a similar phenomenon. The absorption onsets of FP-COF, FBP-COF and FTP-COF were 631, 560 and 538 nm, respectively (Figure 4.16c). Taking BP-COF and FBP-COF as examples, when compared to UV-vis spectra of COFs and their isostructural COFs, the introduction of fluorine atoms into the COF backbone caused a blue shift of 38 nm. The optical band gaps of P-COF, BP-COF and TP-COF were estimated according to the Kubelka-Munk equation (Figure 4.16b),

corresponding to bandgaps of 2.10, 2.18 and 2.31 eV, respectively. In comparison, the bandgaps of FP-COF, FBP-COF and FTP-COF (Figure 4.16d) were estimated to be 2.05, 2.31 and 2.38 eV, respectively. The COFs synthesized with longer linkers have bigger pore sizes and larger band gaps, restricting their visible light absorption. FP-COF has comparable band gap to P-COF; however, for FBP-COF and FTP-COF, the introduction of fluorine atoms also results in a blue shift.

4.8 CO_2 reduction characterization

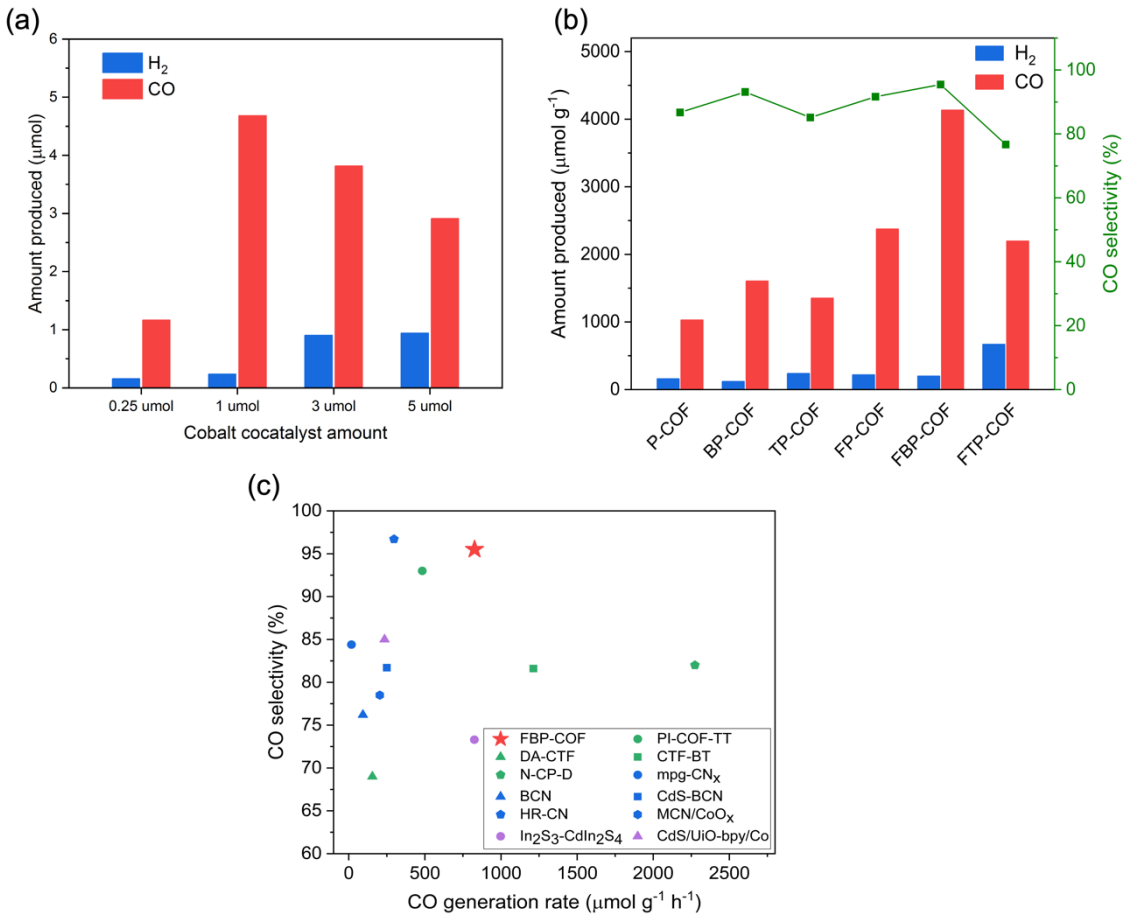

Figure 4.17 (a) CO/H_2 production generated by FBP-COF using various amounts of Co cocatalyst in $MeCN/H_2O$/TEOA (3:1:1) under visible light irradiation (300 W Xe light source, $\lambda > 420$ nm) for 5h; (b) CO and H_2 production and CO selectivity by P-COF, BP-COF, TP-COF, FP-COF, FBP-COF and FTP-COF, over 5 hours under visible-light irradiation (λ > 420 nm, 300 W Xe light source); (c) Comparison of CO_2 reduction performances for FBP-COF and other representative photocatalysts in Table with molecular cocatalysts such as $Co(bpy)_3^{2+}$, $Ni(bpy)_3^{2+}$ and polymeric cobalt phthalocyanine catalyst[14,15,24,16–23].

Photocatalytic CO_2 reduction experiments were carried out under visible light irradiation ($\lambda >$ 420 nm) with the appropriate amount of cobalt (II) bipyridine complexes (Figure 4.17a) as cocatalyst without adding other noble metal complexes as photosensitizer or cocatalyst. When adding 0.25 μmol $[Co(bpy)_3]^{2+}$, CO generation was low due to the lack of active reduction sites. When adding more than 1 μmol $[Co(bpy)_3]^{2+}$, the CO generation amount decreased because excess cocatalyst will impact the light absorption efficiencies of materials in the system.[25] Hence, we used 1 μmol $[Co(bpy)_3]^{2+}$ as the cocatalyst for CO_2 reduction. A 4 mL mixture of acetonitrile (MeCN) / water (3:1 in volume) with 1 mL triethanolamine (TEOA) as the sacrificial agent was applied for the system. UV-vis spectra (Figure 4.16) of P-COF and FP-COF indicated excellent light absorption ability. After 5 hours irradiation (Figure 4.17b), fluorinated FP-COF had a better performance than P-COF, showing a CO production of 2374.1 μmol g^{-1} with a CO selectivity of 91.7%. Similarly, FTP-COF showed higher performance than TP-COF, exhibiting a CO production of 2196.1 μmol g^{-1} with a CO selectivity of 76.7%. BP-COF with medium pore size showed the best performance among non-fluorinated COFs, producing 1603.4 μmol g^{-1} of CO with a selectivity of 93.2% over 5 hours. Among all the COFs, FBP-COF achieved the best performance for CO_2 reduction. After 5 hours irradiation under visible light, FBP-COF achieved a CO production of 4132.1 μmol g^{-1} with a very high CO selectivity of 95.5%. The influence of fluorination, porosity and light absorption on photocatalytic activity will be discussed later. FBP-COF showed an external quantum efficiency (EQE) of 0.24% at 420 nm. Compared with other photocatalysts tested with molecular cocatalyst (Figure 4.17c), FBP-COF showed a high CO generation rate with an excellent CO/H_2 selectivity. For instance, N-CP-D only has a CO selectivity of 82%, even though the CO generation rate is good.[15] HR-CN could achieve a CO selectivity of 96.7% but only produced CO at a rate of 297 μmol g^{-1} h^{-1}.[23] However, these comparisons should be made with caution since CO_2 reduction performance also depends strongly on the precise experimental setup that is used.[15]

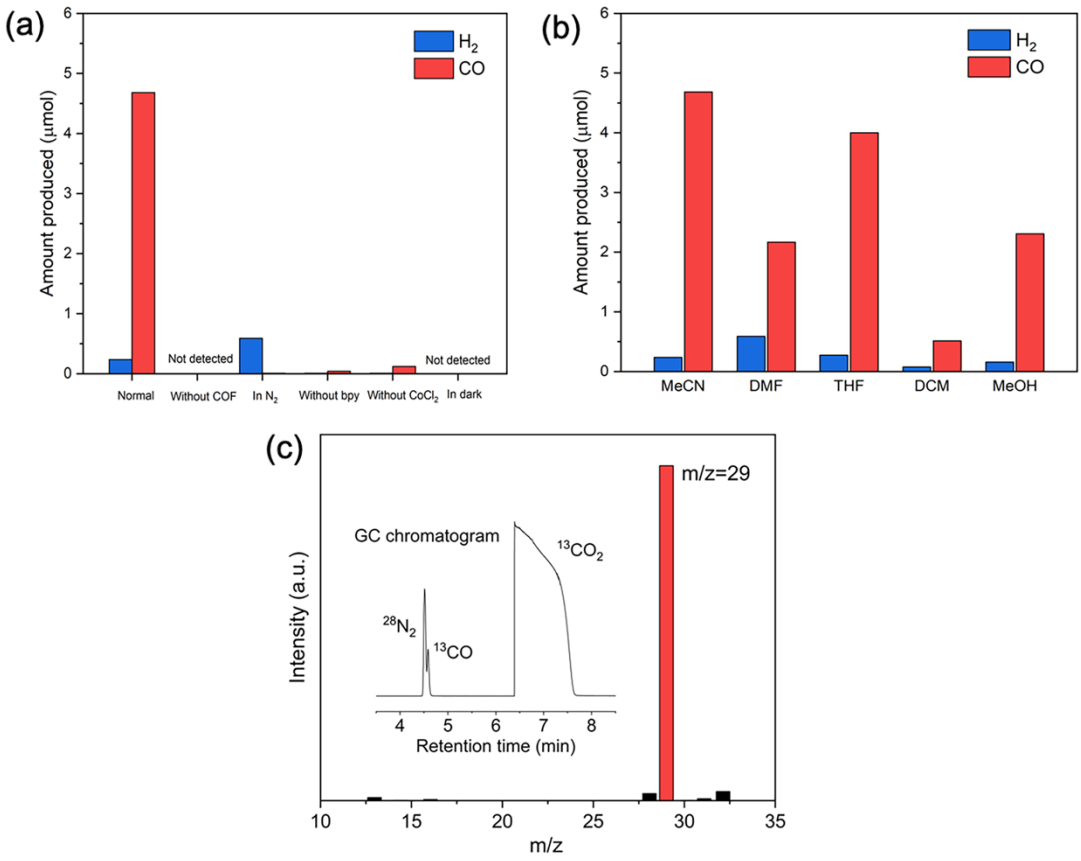

Figure 4.18 (a) Control experiments using FBP-COF for CO_2 photoreduction in 5h under different conditions; (b) CO/H_2 production generated using various co-solvents of FBP-COF as the photosensitizer, $[Co(bpy)_3]^{2+}$ as the cocatalyst and 1 mL TEOA as the sacrificial agent under visible light irradiation (300 W Xe light source, $\lambda > 420$ nm) for 5h; 3 mL Organic solvent and 1 mL water (MeCN: acetonitrile; DMF: *N*, *N*-dimethylformamide; THF: tetrahydrofuran; DCM: dichloromethane; MeOH: methanol); (c) Results of GC-MS spectrum of ^{13}CO produced by FBP-COF in the photocatalytic reduction of $^{13}CO_2$; inset: the corresponding gas spectrum.

Control experiments were performed under the same conditions using FBP-COF to identify the key factors for CO_2 reduction (Figure 4.18a). Without COF there was no CO_2 to CO conversion, indicating the crucial role of COFs as the photosensitizer. The cocatalyst of cobalt bipyridine was indispensable for photocatalytic CO_2 reduction. Without 2,2'-bipyridine or $CoCl_2$ added, the system generated a negligible amount of CO. Moreover, no CO or H_2 was detected when the system was in the dark, demonstrating the process is indeed photocatalytic and driven by the COFs and cobalt complexes. The absence of TEOA as the sacrificial agent results in no product generation. When CO_2 was switched with N_2, only H_2 formation was observed, proving the CO_2 was the source of CO. In such reaction conditions, no liquid products were detected.

When CO_2 reduction was performed in solutions containing various organic solvents (Figure 4.18b), FBP-COF exhibited a higher CO production rate in MeCN than *N*,*N*-dimethylformamide (DMF), tetrahydrofuran (THF), dichloromethane (DCM) and methanol (MeOH). Finally, GC-MS was involved in further demonstrating the source of CO. As shown in Figure 4.18c, the peak at 4.6 min in the GC spectrum with an m/z value of 29 in the MS spectrum was assigned to ^{13}CO. The isotope labelling study for $^{13}CO_2$ reduction proved that the CO was generated from CO_2, ruling out the degradation of the COFs or scavenger as the source of the produced CO.

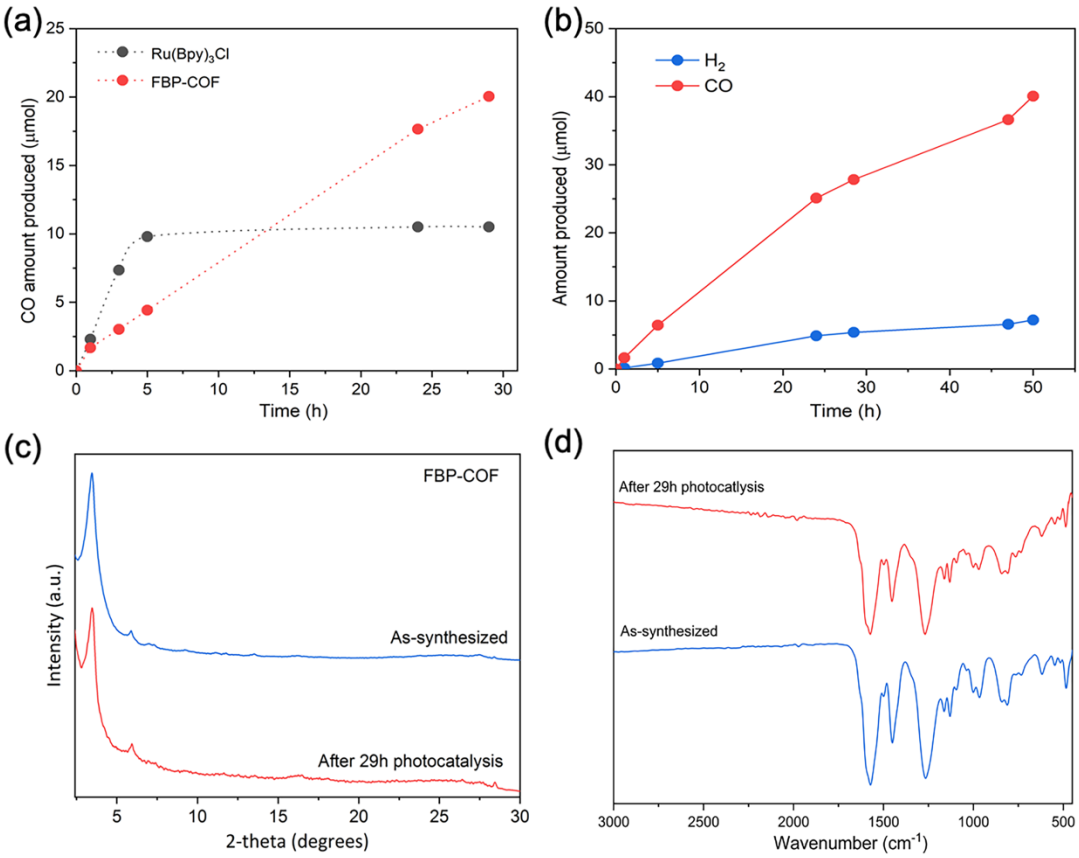

Figure 4.19 (a) CO production comparison using visible light (λ > 420 nm, 300 W Xe light source) for 1 mg FBP-COF (red dots) or 1mg $[Ru(bpy)_3]^{2+}$ with 1 μmol $[Co(bpy)_3]^{2+}$ (black dots); (b) CO (red dots) and H_2 (blue dots) production using visible light (λ > 420 nm, 300 W Xe light source) for 1 mg FBP-COF in 5 mL solvent with ratio of MeCN/H_2O/TEOA = 3/1/1) for 50 hours; (c) PXRD patterns of FBP-COF before and after 29 hours photocatalysis; (d) FT-IR spectra of FBP-COF before and after 29 hours of visible light irradiation (300 W Xe light source, λ > 420 nm).

To demonstrate the excellent photoactivity of FBP-COF, $[Ru(bpy)]^{2+}$ was applied as the molecular photosensitizer in the same system for comparison. When applied $[Ru(bpy)]^{2+}$ as the photosensitizer and $[Co(bpy)_3]^{2+}$ as the cocatalyst (Figure 4.19a), CO generation almost stopped after 5 hours irradiation under visible light. On the contrary, FBP-COF could continuously produce CO with a high rate of up to 29 hours, proving the excellent stability of FBP-COF under such experimental conditions. The amount of CO produced by the FBP-COF system in 29 hours was almost two times higher than the amount generated by the bipyridine Ru complex system. When the experimental time was further extended to 50 hours (Figure 4.19b), FBP-COF could still generate CO constantly at a high rate, showing a TON of 40, which is four times higher than that of bipyridine Ru complex containing system. The PXRD pattern and FTIR spectrum of FBP-COF after photocatalysis in Figure 4.19c and Figure 4.19d showed negligible difference with those of pristine COF, demonstrating FBP-COF still had its crystalline structure. All the data proved that FBP-COF could act as an excellent photosensitizer for CO_2 reduction.

4.9 Analysis of fluorinated COFs

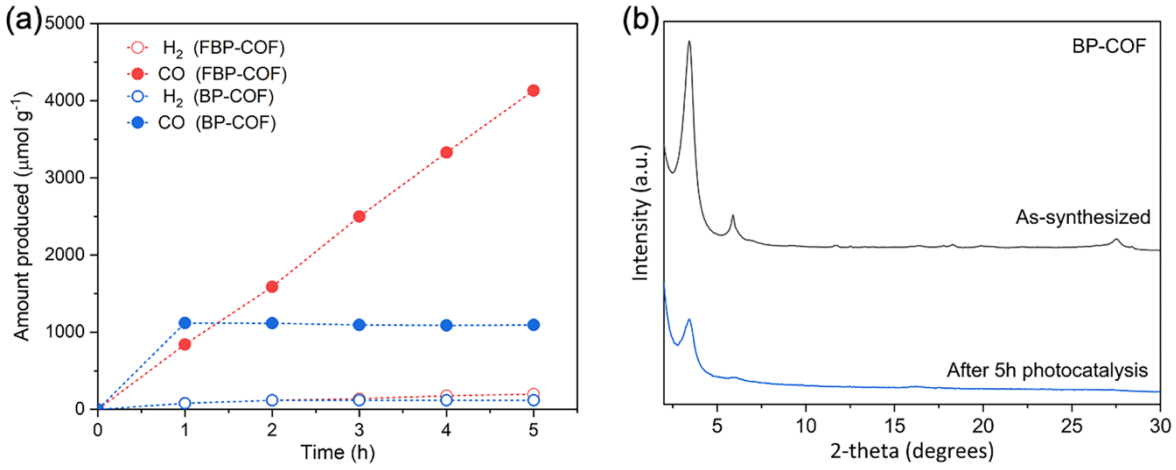

Figure 4.20 (a) CO (red dots) and H_2 (blue dots) production using visible light (λ > 420 nm, 300 W Xe light source) for 1 mg FBP-COF (red) and BP-COF (black) in 5 mL solvent with a ratio of MeCN/H_2O/TEOA = 3/1/1); (b) PXRD patterns of BP-COF before and after 5 hours photocatalysis.

As shown in Figure 4.17a, all fluorinated COFs showed better performance than their non-fluorinated counterparts. We attribute this to the enhanced interaction between layers after

fluorination, resulting in more excellent stability. As shown in Figure 4.20a, the CO generation of BP-COF stopped after 1 hour of irradiation. On the contrary, FBP-COF could generate CO constantly. The PXRD pattern of BP-COF after photocatalysis (Figure 4.20b) indicated that BP-COF lost its crystallinity after 5 hours irradiation under visible light. The stability of COF seems to have a significant influence on the performance.

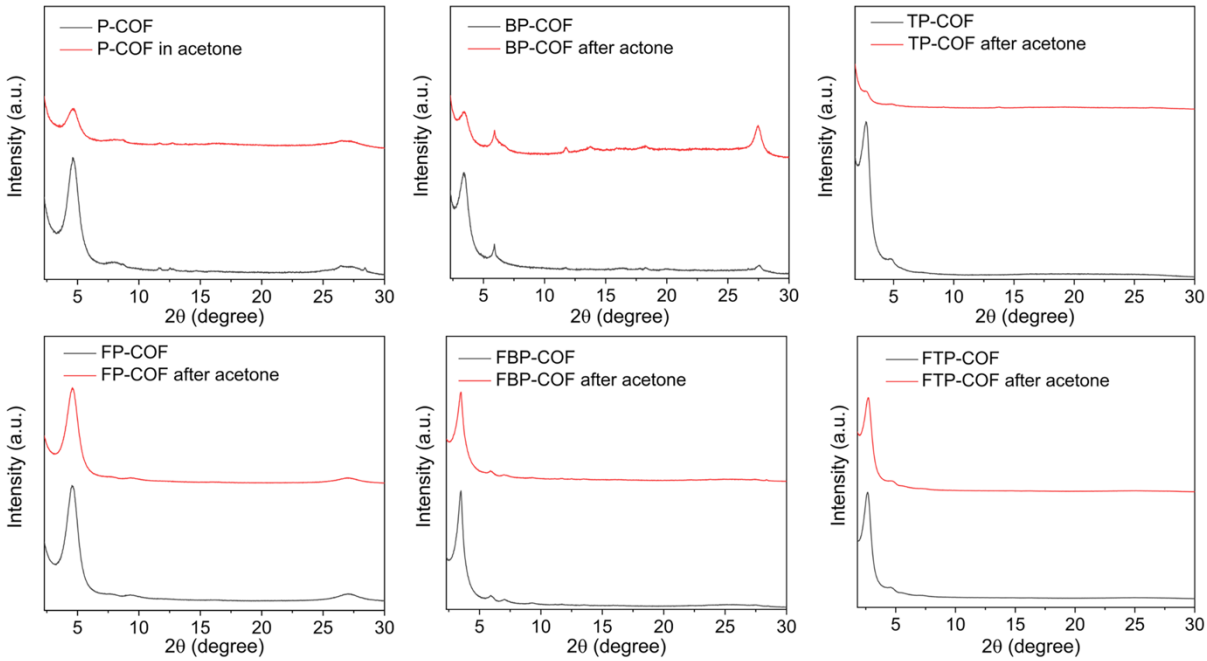

Figure 4.21 PXRD patterns of COFs before and after soaked in acetone overnight.

The stability of all COFs was checked by soaking the COFs in acetone overnight. PXRD patterns of all non-fluorinated COFs after soaking in acetone exhibited weak peaks at small angles, while fluorinated COFs still had intense peaks at small angles. Results of all the COFs after soaking in acetone indicated that the non-fluorinated COFs lost crystallinity, while the fluorinated COFs retained their crystallinity (Figure 4.21). The introduction of fluorine atoms into COFs backbones could increase the interaction between layers.[12] Non-fluorinated COFs might decompose in acetone which contains a small amount of water inside. This indicates the better stability of fluorinated COFs than their non-fluorinated analogues resulting in higher CO_2 reduction performance.

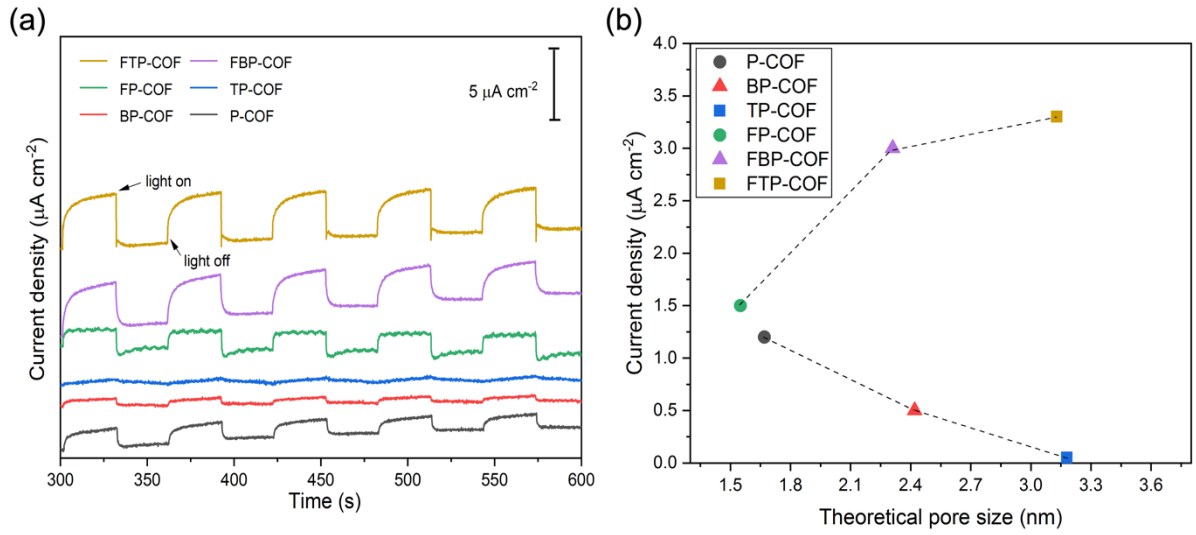

Figure 4.22 (a) Transient photocurrent response at -0.2 V vs. Ag/AgCl under intermittent light irradiation for the COFs; (b) Comparison of theoretical pore size and current density.

To investigate the charge separation and transformation properties of non-fluorinated COFs and fluorinated COFs, photoelectrochemical experiments were employed using FTO glass as a photocathode in 0.5 M Na_2SO_4 solution. To do this, 2 mg of the COFs and 10 µL Nafion were dispersed in 0.2 mL ethanol and then ultrasonicated for 10 minutes giving a slurry. the slurry was then coated onto FTO glass electrodes with an active area of 0.28 cm^2 and dried overnight at room temperature. A three-electrode system with a working electrode (COFs on FTO glass), counter electrode (Pt wire), and reference electrode (Ag/AgCl) was used for testing. Transient photocurrent measurements (Figure 4.22) showed that the photocurrents of fluorinated COF photocathodes are higher than those of non-fluorinated COFs. Among them, FBP-COF and FTP-COF showed the fastest photoresponse with a photocurrent of about 3.2 µA cm^{-2}. It was found that photocurrents of fluorinated COFs increased with pore size (Figure 4.22b). By contrast, photocurrents of non-fluorinated COFs decreased with increased pore size. This might be due to the introduction of fluorine atoms enhancing the conjugation of COFs.

4.10 Time-correlated single photon counting experiments

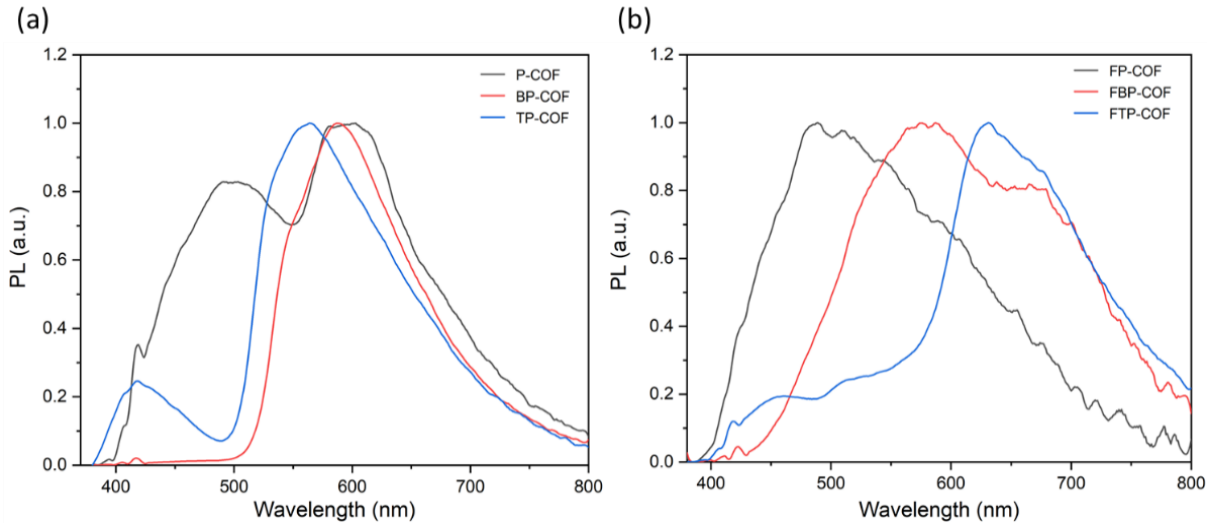

Figure 4.23 Photoluminescence spectra of P-COF, BP-COF and TP-COF (a) and FP-COF, FBP-COF and FTP-COF (b) suspended in acetonitrile (λ_{exc} = 375 nm).

Table 4.1 Fluorescence lifetime measurements.

Material	λ_{exc} / nm	τ_1 / ns	B_1 / %	τ_2 / ns	B_2 / %	τ_3 / ns	B_3 / %	χ^2	τ_{avg}[a] / ns
P-COF	375	0.74	65.87	1.64	32.96	8.12	1.17	1.16	1.12
BP-COF	375	0.14	74.91	0.73	19.12	2.84	5.97	1.41	0.41
TP-COF	375	0.14	81.64	0.65	13.57	2.68	4.79	1.47	0.33
FP-COF	375	0.50	37.21	1.18	57.22	3.48	5.57	1.10	1.05
FBP-COF	375	0.44	38.36	1.01	44.99	3.03	16.65	1.31	1.13
FTP-COF	375	0.16	67.04	0.59	22.60	2.73	10.36	1.30	0.52

[a] Fluorescence lifetimes obtained upon excitation at λ_{exc} = 375 nm with a laser and observed at λ_{em} = 500, 580 or 630 nm. Fluorescence lifetimes in solvent suspension obtained from fitting time-correlated single photon counting decays to a sum of three exponentials, which yield τ_1, τ_2, and τ_3 according to $\sum_{i=1}^{n}(A + B_i \exp(-\frac{t}{\tau_i}))$. τ_{AVG} is the weighted average lifetime calculated as $\sum_{i=1}^{n} B_i \tau_i$. Note that the poor χ^2 values are due to ultrafast decays for these materials which were very similar to the instrument response.

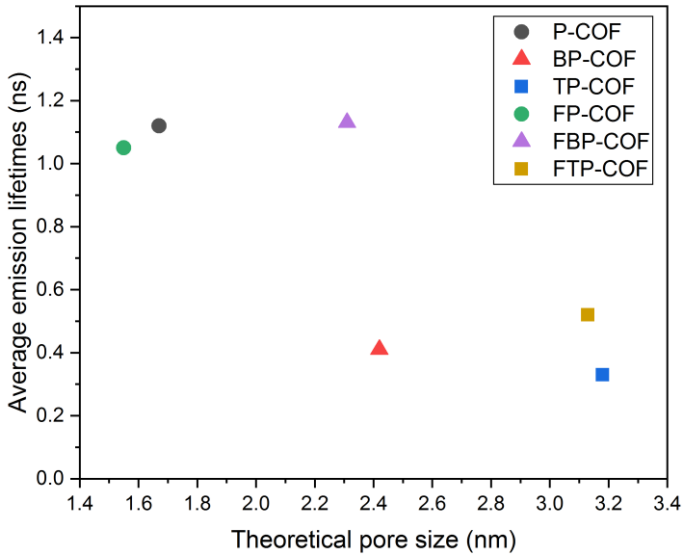

Figure 4.24 Comparison of theoretical pore size and average emission lifetimes of COFs.

The lifetimes of the excited states of all the COFs were investigated by time-correlated single photon counting (TCSPC) experiments. In acetonitrile suspension, two emissive states with λ_{max} at 490 and 590 nm were observed for P-COF (Figure 4.23). BP-COF had one emissive state with λ_{max} at 585 nm. TP-COF also showed two emissive states with λ_{max} at 420 and 565 nm. FP-COF, FBP-COF and FTP-COF had one emissive state with λ_{max} at 489, 580, and 632 nm in acetone suspension. Fluorescence lifetimes were obtained upon excitation at λ_{exc} = 375 nm with a laser and observed at λ_{em} = 500, 580 or 630 nm. The average weighted photoluminescence emission lifetime (Table 4.1) of FP-COF (τ_{avg} = 1.05 ns) was similar with that of P-COF (τ_{avg} = 1.12 ns), while the average emission lifetimes of FBP-COF (τ_{avg} = 1.13 ns) and FTP-COF (τ_{avg} = 0.52 ns) were longer than those of their isostructural COFs, BP-COF (τ_{avg} = 0.41 ns) and TP-COF (τ_{avg} = 0.33 ns), which correlates with the observed photocatalytic performance. Lifetimes of non-fluorinated COFs decreased with the large pore sizes (Figure 4.24) due to the longer linkers could influence the conjugation of COFs. The introduction of fluorine atoms into COFs backbones could increase the lifetimes which could facilitate the CO_2 reduction.

4.11 Influence of pore size with cobalt complexes

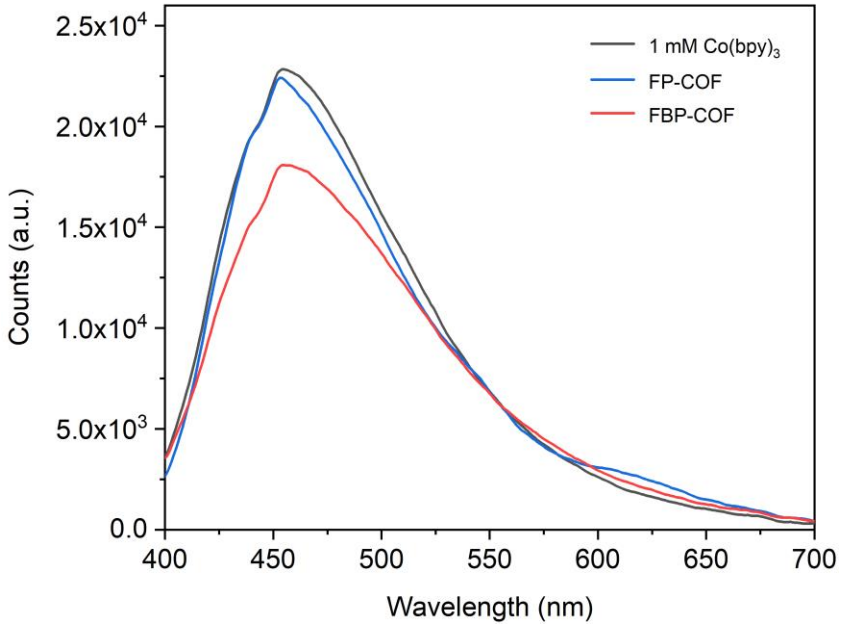

Figure 4.25 Photoluminescence spectra of 1 mM $[Co(bpy)_3]^{2+}$ acetonitrile solution upon the addition 5 mg of FP-COF, FBP-COF (excitation at 350 nm).

FP-COF with a pore size of 1.6 nm has better light absorption than FBP-COF with a pore size of 2.3 nm; however, the CO generation rate of FP-COF was lower than that of FBP-COF. We supposed the activity difference was due to pore size, which could let molecular cocatalyst into the COFs and increase the efficiency of interaction between COFs and cocatalyst. It was proven that the $[Co(bpy)_3]^{2+}$ molecules were mainly dispersed at the external surface of DA-CTF with a pore size of 1.2 nm.[17] We supposed that COFs with different pore sizes could influence the interaction between COFs and molecular cocatalysts which restrict the CO_2 reduction performance. Hence, the influence of porosity on activity was investigated by measuring the adsorption capability of the cocatalyst for FP-COF and FBP-COF. To do this, 10 mL of 1 mM $[Co(bpy)_3]^{2+}$ acetonitrile solution and 5 mg FP-COF and FBP-COF were added into vials. After 4 hours, the solution was then separated by centrifugation, and the concentration of the $[Co(bpy)_3]^{2+}$ in the liquid supernatant was determined using a PL spectrophotometer. As shown in Figure 4.25d, the PL intensity showed little difference between pristine $[Co(bpy)_3]^{2+}$ solution and that soaked with FP-COF, indicating that the cobalt complexes are located at the external surface of FP-COF with only a small portion inside the pores.[17] However, PL intensity of $[Co(bpy)_3]^{2+}$ solution after soaking with FBP-COF shows a decrease compared to the pristine

solution, indicating the accessibility of $[Co(bpy)_3]^{2+}$ in the pores of FBP-COF.[3] Therefore, we suppose the larger pores can improve the interaction between the cocatalyst and the COFs, but at the same time it will limit their visible light absorption and conjugation. Hence, FBP-COF has medium-sized pores and a suitable band gap, giving the best photocatalytic performance.

4.12 Conclusion

In summary, we have synthesized a series of fluorinated COFs and achieved photocatalytic CO_2 reduction with TEOA as a scavenger and Co (II) bipyridine complexes as a low-cost cocatalyst. Fluorinated COFs exhibited better performance than non-fluorinated COFs. Among them, FBP-COF with appropriate band gap and medium pore size achieved the best performance, demonstrating a CO generation rate of 4132.1 μmol g^{-1} with 95.5% selectivity over H_2 over 5 h visible light illumination. FBP-COF can generate CO for up to 50 hours with a TON of 40. This result was higher than that of the system that applied Ru complex as a dye. Fluorination improves the stability of COFs dramatically. Our findings demonstrated CO_2 affinity and pore size of the COFs and the light absorption of the photosensitizer have a significant influence on photocatalytic CO_2 reduction activity.

4.13 Materials and methods

All reagents were purchased from Sigma-Aldrich, TCI Europe, ABCR, Carbosynth, Shanghai Kaiyulin Pharmaceutical Technology or Fluorochem. Anhydrous solvents used for synthesis and experiment were obtained from Acros Organics or Fisher Scientific. All chemicals were used as received and without further purification. 1,3,5-triformylphloroglucinol was purchased from Carbosynth. P-phenylenediamine was obtained from Sigma-Aldrich. Benzidine was purchased from Fluorochem. 4,4"-diamino-p-terphenyl was obtained from TCI. 1,4-diamino-2,5-diflurobenzene and 4,4’-diamino-2,2’-difluorobiphenyl were purchased from ABCR.

4.13.1 Solution nuclear magnetic resonance

A Bruker Avance 400 NMR spectrometer operating at frequencies of 400 MHz and 100 MHz

was used to record ^{1}H and $^{13}C\{^{1}H\}$ NMR spectra.

4.13.2 Powder X-ray diffraction

Powder X-ray diffraction (PXRD) measurements were collected on a Panalytical Empyrean diffractometer, applying with a Cu X-ray source (λ = 1.5418 Å, Cu Kα), PIXcel3D detector and X-ray focusing mirror. After loading loose powdered samples on Mylar film in aluminium well plates, samples were screened in high throughput transmission mode.

4.13.3 Thermogravimetric analysis

Thermogravimetric analysis (TGA) was measured on an EXSTAR6000 under nitrogen flow, heating at 10 °C min^{-1} from room temperature to 1000 °C.

4.13.4 Gas sorption analysis

Nitrogen adsorption and desorption were obtained at 77.3 K using a Micromeritics ASAP 2020 volumetric adsorption analyzer. Before analysis, all the COF powder samples were degassed offline at 120 ℃ for 12 hours under a dynamic vacuum (10^{-5} bar). Pore size distributions of COFs were calculated from the adsorption data by fitting a nonlocal density functional theory (NL-DFT) model. CO_2 isotherms were measured on a Micromeritics ASAP 2020 at 273 K and 298 K.

4.13.5 Fourier-transform infrared spectroscopy

FT-IR spectra were obtained on a Bruker Tensor 27 FT-IR spectrometer. Data of samples prepared as KBr disks were collected for 16 scans with a resolution of 4 cm^{-1}.

4.13.6 UV-Visible absorption spectra

UV-Visible absorption spectra of all the materials were performed on an Agilent Cary 5000 UV-Vis-NIR Spectrometer by testing the reflectance of powders in the solid state.

4.13.7 Scanning electron microscopy

Scanning electron microscopy (SEM) observations were performed on a Hitachi S-4800 cold field emission scanning electron microscope. Samples were first deposited on Hitachi M4 aluminium stubs with an adhesive high-purity carbon tab and then coated with a 2 nm layer of gold using an Emitech K550X automated sputter coater.

4.13.8 Isotopic labelling experiments

$^{13}CO_2$ labelling experiments were performed using COF powder (1 mg), 2,2'-bipyridyl (2 mg), $CoCl_2$ (1 μmol), acetonitrile, water and triethanolamine (3:1:1 vol. mixture, 5 mL) and sealed with a septum. The resulting suspension was ultrasonicated for 5 minutes and then purged with $^{13}CO_2$ for 5 minutes. The reaction mixture was illuminated with a 300 W Newport Xe light source (model: 6258, Ozone free) equipped with a $\lambda > 420$ nm cut-off filter. The gas phase was run on Agilent GC-MS 7890B gas chromatograph with a mass spectrometer (Agilent GC-MS 5977B) equipped with a GC-CARBONPLOT column (60 m length, 0.32 mm inner diameter).

4.13.9 Photoelectrochemical measurements

2 mg of the photocatalyst and 10 μL Nafion were dispersed in 0.2 mL ethanol and ultrasonicated for 10 minutes giving a slurry. The slurry was then coated onto FTO glass electrodes with an active area of 0.28 cm^2 and dried overnight at room temperature. The photocurrent response was tested using a three-electrode system with a working electrode (COF on FTO glass), counter electrode (Pt wire), and reference electrode (Ag/AgCl) in 0.5 M Na_2SO_4 (pH = 7) aqueous solution. An Oriel Instruments LSH-7320 Solar Simulator (IEC ABA certified) with 1 Sun output was applied to illuminate the sample. The applied bias for the intermittent photocurrent intensity measurement was -0.2 V vs. Ag/AgCl.

4.13.10 TCSPC measurements

An Edinburgh Instruments LS980-D2S2-STM spectrometer equipped with picosecond pulsed LED excitation sources, and a R928 detector was applied for TCSPC experiments. An EPL-

375 diode (λ = 375 nm, instrument response 100 ps, fwhm) was used for emission detection. Suspensions of COFs were prepared by ultrasonicating the materials in acetonitrile. The instrument response was tested with colloidal silica (LUDOX® HS-40, Sigma-Aldrich) at the excitation wavelength without any filter. Decay times were fitted in the FAST software using suggested lifetime estimates.

4.13.11 External quantum efficiency (EQE) for CO production

A monochromatic LED light (λ = 420 nm) was applied for measuring the external quantum efficiency of CO production. For the experiments, COF (1 mg), 2,2'-bipyridine (2 mg), and $CoCl_2$ (1 μmol) were suspended in acetonitrile, water and triethanolamine (3:1:1 vol. mixture, 5 mL). The illuminated area was 5 cm^2 and the light intensity was measured by a ThorLabs PM100D Power and Energy Meter Console with a ThorLabs S120VC photodiode power sensor. The EQE was calculated as follow:

$$EQE\% = 2 \times [(n\ CO) \times N_A \times h \times c)] \times 100\% / (I \times S \times t \times \lambda)$$

Where N_A is Avogadro constant (6.022×10^{23} mol^{-1}), h is the Planck constant (6.626×10^{-34} J s), c is the speed of light (3×10^8 m s^{-1}), S is the irradiation area (cm^2), I is the intensity of irradiation light (W cm^{-2}), t is the photoreaction time (s), and λ is the wavelength of the monochromatic light (m).

4.13.12 Photocatalytic CO_2 reduction experiments

A quartz flask was charged with the COFs (1 mg), 2,2'-bipyridine (2 mg) and $CoCl_2$ (1 μmol) in acetonitrile, water and triethanolamine (3:1:1 vol. mixture, 5 mL) and sealed with a septum. The resulting suspension was ultrasonicated for 5 minutes and then purged with CO_2 for 15 minutes. The reaction mixture was illuminated with a 300 W Newport Xe light source (model: 6258, Ozone free) equipped with a λ > 420 nm cut-off filter. Gaseous products were taken with a gas-tight syringe and run on a Shimadzu GC-2014 gas chromatograph equipped with a ShinCarbon ST micropacked column (Restek 80-100 mesh, 2 m length, 0.53 mm inner diameter) and a thermal conductivity detector.

4.14 References

1 W. Zhong, R. Sa, L. Li, Y. He, L. Li, J. Bi, Z. Zhuang, Y. Yu and Z. Zou, *J. Am. Chem. Soc.*, 2019, **141**, 7615–7621.

2 M. Lu, Q. Li, J. Liu, F. M. Zhang, L. Zhang, J. L. Wang, Z. H. Kang and Y. Q. Lan, *Appl. Catal. B Environ.*, 2019, **254**, 624–633.

3 X. Wang, Z. Fu, L. Zheng, C. Zhao, X. Wang, S. Y. Chong, F. McBride, R. Raval, M. Bilton, L. Liu, X. Wu, L. Chen, R. S. Sprick and A. I. Cooper, *Chem. Mater.*, 2020, **32**, 9107–9114.

4 S. Yang, W. Hu, X. Zhang, P. He, B. Pattengale, C. Liu, M. Cendejas, I. Hermans, X. Zhang, J. Zhang and J. Huang, *J. Am. Chem. Soc.*, 2018, **140**, 14614–14618.

5 Z. Fu, X. Wang, A. M. Gardner, X. Wang, S. Y. Chong, G. Neri, A. J. Cowan, L. Liu, X. Li, A. Vogel, R. Clowes, M. Bilton, L. Chen, R. S. Sprick and A. I. Cooper, *Chem. Sci.*, 2020, **11**, 543–550.

6 M. Lu, J. Liu, Q. Li, M. Zhang, M. Liu, J. L. Wang, D. Q. Yuan and Y. Q. Lan, *Angew. Chem. Int. Ed.*, 2019, **58**, 12392–12397.

7 G. Li, B. Zhang and Z. Wang, *Macromolecules*, 2016, **49**, 2575–2581.

8 A. H. Alahmed, M. E. Briggs, A. I. Cooper and D. J. Adams, *J. Mater. Chem. A*, 2019, **7**, 549–557.

9 Z. Yang, S. Wang, Z. Zhang, W. Guo, K. Jie, M. I. Hashim, O. Miljanić, D. E. Jiang, I. Popovs and S. Dai, *J. Mater. Chem. A*, 2019, **7**, 17277–17282.

10 S. B. Alahakoon, G. T. McCandless, A. A. K. Karunathilake, C. M. Thompson and R. A. Smaldone, *Chem. - A Eur. J.*, 2017, **23**, 4255–4259.

11 S. Kandambeth, A. Mallick, B. Lukose, M. V. Mane, T. Heine and R. Banerjee, *J. Am. Chem. Soc.*, 2012, **134**, 19524–19527.

12 B. P. Biswal, S. Kandambeth, S. Chandra, D. B. Shinde, S. Bera, S. Karak, B. Garai, U. K. Kharul and R. Banerjee, *J. Mater. Chem. A*, 2015, **3**, 23664–23669.

13 Y. Zhu and W. Zhang, *Chem. Sci.*, 2014, **5**, 4957–4961.

14 X. Chen, Q. Dang, R. Sa, L. Li, L. Li, J. Bi, Z. Zhang, J. Long, Y. Yu and Z. Zou, *Chem. Sci.*, 2020, **11**, 6915–6922.

15 S. Wang, X. Hai, X. Ding, S. Jin, Y. Xiang, P. Wang, B. Jiang, F. Ichihara, M. Oshikiri, X. Meng, Y. Li, W. Matsuda, J. Ma, S. Seki, X. Wang, H. Huang, Y. Wada, H. Chen and J. Ye, *Nat. Commun.*, 2020, **11**, 1149.

16 S. Roy and E. Reisner, *Angew. Chem. Int. Ed.*, 2019, **58**, 12180–12184.

17 H. Zhong, Z. Hong, C. Yang, L. Li, Y. Xu, X. Wang and R. Wang, *ChemSusChem*, 2019, **12**, 4493–4499.

18 C. Yang, W. Huang, L. C. da Silva, K. A. I. Zhang and X. Wang, *Chem. - A Eur. J.*, 2018, **24**, 17454–17458.

19 C. Chen, T. Wu, H. Wu, H. Liu, Q. Qian, Z. Liu, G. Yang and B. Han, *Chem. Sci.*, 2018, **9**, 8890–8894.

20 M. Zhou, S. Wang, P. Yang, C. Huang and X. Wang, *ACS Catal.*, 2018, **8**, 4928–4936.

21 S. Wang, B. Y. Guan, Y. Lu and X. W. Lou, *J. Am. Chem. Soc.*, 2017, **139**, 17305–17308.

22 C. Huang, C. Chen, M. Zhang, L. Lin, X. Ye, S. Lin, M. Antonietti and X. Wang, *Nat. Commun.*, 2015, **6**, 7698.

23 Y. Zheng, L. Lin, X. Ye, F. Guo and X. Wang, *Angew. Chem. Int. Ed.*, 2014, **53**, 11926–11930.

24 J. Lin, Z. Pan and X. Wang, *ACS Sustain. Chem. Eng.*, 2014, **2**, 353–358.

25 J. Lin, Y. Hou, Y. Zheng and X. Wang, *Chem. - An Asian J.*, 2014, **9**, 2468–2474.

26 L. Shi, T. Wang, H. Zhang, K. Chang and J. Ye, *Adv. Funct. Mater.*, 2015, **25**, 5360–5367.

Chapter 5

Summary and outlook

The development of new materials for the conversion of carbon dioxide to value-added chemical fuels is a major goal in materials chemistry.[1] Inorganic semiconductors, such as metal oxides, have been studied widely for this application, but they often lack a suitable electronic band structure, and this can be hard to tune.[2,3] On the other hand, homogeneous molecular catalysts, such as organometallic complexes, are synthetically versatile but have poor long-term stability.[4–6]

Porous organic materials, such as carbon nitrides, conjugated microporous polymers (CMPs),[7,8] covalent triazine-based frameworks (CTFs),[7,8] and covalent organic frameworks (COFs),[9–12] have attracted growing interest for photocatalytic CO_2 reduction. These organic materials are synthesized under mild conditions and their properties are easily tuned through the modular incorporation of different building blocks. In this thesis, we synthesized organic semiconductors such as linear conjugated polymers and COFs and explored their application to photocatalytic CO_2 reduction.

In Chapter 2, linear conjugated polymers achieved photocatalytic CO_2 reduction for syngas production. The 'one-pot' generation of syngas (H_2/CO) mixtures by the simultaneous reduction of water and CO_2 is of significant interest because syngas is used in large-scale industrial processes. Direct photocatalytic syngas production has the potential to be technologically simple and scalable, necessary for large-scale applications. We firstly tested different linear conjugated polymers for CO_2 reduction with cobalt bipyridine complexes as cocatalysts and TEOA as scavengers. Dibenzo[*b*,*d*]thiophene sulfone containing polymer photocatalysts (P7 and P10) were found to be highly active. A dibenzo[*b*,*d*]thiophene sulfone-phenylene co-polymer, P7, showed a CO production rate of 959.1 μmol g^{-1} h^{-1}, but it also produced H_2 at a rate of 1523.7 μmol g^{-1} h^{-1}, while a dibenzo[*b*,*d*]thiophene sulfone homopolymer P10 produced very little CO with a rate of 156.5 μmol g^{-1} h^{-1} and significantly more H_2 (2575.6 μmol g^{-1} h^{-1}). The selectivity over CO production for P10 can be explained by differences in thermodynamic driving force with the LUMO of P10 being less negative than for P7, resulting in the lower reduction potential of P10 relative to P7.

We next studied in detail the influence of residual palladium on the catalytic activity and found

that the selectivity for CO increased when poly(*p*-phenylene) and P10 were made using a nickel-based coupling reaction. This shows that residual palladium acts as a co-catalyst for proton reduction, which competes with carbon dioxide reduction. We were able to control the composition of the H_2/CO mixtures for P7 by varying the amount of palladium used in the synthesis, which allowed us to vary the H_2:CO ratio between 1.9:1 to 5.3:1. Unlike imine linked COFs, these materials are conjugated polymers with irreversible covalent bonds; as such, they exhibit very good physicochemical stability and we observed little change in their activities over a period of 25 hours.

COFs combine porosity with crystallinity and have shown strong potential as solar fuels photocatalysts; for example, we recently reported a highly active COF photocatalyst for photochemical hydrogen evolution from water.[13] The synthetic reactions of COFs do not use metal-based catalysts, which reduces the competitive hydrogen production reactions compared to CO_2 reduction and improves the selectivity of products. However, one challenge here is the reversible bond-formation chemistry needed to make most COFs, which leads to varying degrees of long-term instability under photocatalytic conditions. For example, for a COF synthesized via a Schiff-base condensation, the CO production rate stayed linear over a time span of less than two hours.[10] In another recent study, more stable CO production was observed up to 10 hours, but the rate plateaued after that.[14] This marked instability is perhaps the central challenge for such materials, even more than catalytic rate and selectivity.

In Chapter 3, we designed and synthesized a new COF, Bpy-sp^{2}c-COF, via Knoevenagel condensation of 1,3,6,8-tetrakis(4-formylphenyl)pyrene and 5,5'-bis(cyanomethyl)-2,2'-bipyridine. Bpy-sp^{2}c-COF incorporates bipyridine sites to allow ligation of a rhenium complex. Re-Bpy-sp^{2}c-COF was made by refluxing Bpy-sp^{2}c-COF with $[Re(CO)_5Cl]$ in toluene. The Re-Bpy-sp^{2}c-COF is significantly more stable than previous examples, discussed above, and shows steady photochemical reduction of CO_2 to CO under visible light irradiation ($\lambda > 420$ nm) over 17.5 hours. Re-Bpy-sp^{2}c-COF generated CO at a rate of 1040 μmol g^{-1} h^{-1} (TON = 18.7) with 81% selectivity over H_2. An apparent quantum yield (AQY) of 0.5% was measured at 420 nm for CO production. In contrast, the homogeneous counterpart deactivated after 3

hours with a TON of 10.3 under the same conditions. The chemical robustness of the COF stems from its fully π-conjugated backbone, which is also beneficial for efficient light-harvesting and charge transport, and hence photocatalytic activity.

The Bpy-sp^{2}c-COF is porous and can also be dye-sensitized, giving CO production rates of up to 1,400 μmol g^{-1} h^{-1} with a selectivity of 86%, which is the highest rate reported for a COF so far. We also show that the crystalline COF shows a much higher and more stable catalytic activity than an amorphous analogue, illustrating that isoreticular design principles provide a strong practical advantage in this application. The catalytic selectivity of the COF can be tuned from favouring CO to favouring H_2 by varying the level of platinum cocatalyst, and this can be used to produce syngas directly.

In previous reports, most COFs were designed as a scaffold to integrate a molecular catalyst for photocatalytic CO_2 reduction.[12,14,15] Inevitably, additional noble metal photosensitizers such as ruthenium(II) complexes were necessary for such systems and the stability of the reported COFs are relatively poor as they are based on Schiff-base chemistry.[10] On the other hand, photoactive COF photosensitizers still need noble metal complexes; for example, our rhenium complex acts as a cocatalyst to achieve CO_2 reduction with good selectivity.[14] The Re-Bpy-sp^{2}c-COF in Chapter 3 used rhenium complexes as cocatalysts. Until now, COFs photosensitizers have rarely been reported for highly selective CO_2 reduction to CO without noble metal complexes as cocatalysts.[16] Introducing fluorine heteroatoms into organic semiconductors has been well studied to improve the photovoltaic performance for organic solar cell.[17] COF photosensitizers incorporating fluorine and chlorine were applied and investigated for photocatalytic H_2 evolution.[18] Obtaining low-cost and high performance photoactive COFs through minor changes of reported COFs with heteroatom fluorine is very attractive. Therefore, it is worthwhile to explore COFs as photosensitizers with this strategy and develop systems with earth-abundant catalysts.[19]

In Chapter 4, we reported a series of *β*-ketoenamine-linkers COFs with various pore sizes and band gaps made by reacting 1,3,5-triformylphloroglucinol (TFG) with aromatic linkers of different lengths or their isostructural fluorinated analogues. The obtained fluorinated and non-

fluorinated COFs were tested as photosensitizers, coupled with the low-cost molecular cobalt (II) bipyridine complex ($[Co(bpy)_3]^{2+}$) as a cocatalyst for photocatalytic CO_2 reduction under visible light. Compared with those of other obtained COFs, results indicated that FBP-COF with $[Co(bpy)_3]^{2+}$ as co-catalyst had the best CO evolution rate of 826.4 μmol h^{-1} g^{-1} with a selectivity of 95.5%. This system showed steady CO evolution for 50 hours, showing a TON of 40, which is four times higher than the equivalent bipyridine Ru complex containing system.

Taken together, the results of this thesis show that both linear conjugated polymers and COFs were demonstrated to be promising photocatalysts for CO_2 reduction under different experimental conditions. Precious metal complexes (rhenium complexes) and non-noble metal complexes (cobalt bipyridine complexes) were applied as cocatalysts for generating CO.

However, it is believed that this is just the beginning of photocatalytic CO_2 reduction using organic semiconductors. Products such as CH_4 and methanol are more challenging to make but more rewarding. However, additional sacrificial electron donors are still needed. Without any other scavengers, systems that can effectively achieve overall CO_2 reduction with low-cost organic semiconductors, non-noble metal complexes as cocatalysts and water as electron donor are the ideal choice. The work in this thesis suggests that, overall, COFs might be the better choice for CO_2 reduction photocatalysts, largely because of their high crystallinity and our ability to control atomistically the placement of functionality in predictable way. This will only be true, however, if the materials are sufficiently stable. There are various strategies here, such as fluorination and the introduction of more stable sp^2 carbon-carbon bonding, both of which are explored in this thesis.

It is hoped that the results in this thesis will encourage work on photocatalytic CO_2 reduction using organic semiconductors toward the long-term goal of materials that yield useful products without the use of any additional sacrificial agents.

References

1 S. R. Foit, I. C. Vinke, L. G. J. de Haart and R. A. Eichel, *Angew. Chem. Int. Ed.*, 2017, 56, 5402–5411.

2 J. L. White, M. F. Baruch, J. E. Pander, Y. Hu, I. C. Fortmeyer, J. E. Park, T. Zhang, K. Liao, J. Gu, Y. Yan, T. W. Shaw, E. Abelev and A. B. Bocarsly, *Chem. Rev.*, 2015, **115**, 12888–12935.

3 Y. Kohno, T. Tanaka, T. Funabiki and S. Yoshida, *Chem. Commun.*, 1997, **0**, 841–842.

4 Y. Tamaki and O. Ishitani, *ACS Catal.*, 2017, **7**, 3394–3409.

5 H. Takeda, C. Cometto, O. Ishitani and M. Robert, *ACS Catal.*, 2017, **7**, 70–88.

6 A. Call, M. Cibian, K. Yamamoto, T. Nakazono, K. Yamauchi and K. Sakai, *ACS Catal.*, 2019, **9**, 4867–4874.

7 Y. Chen, G. Ji, S. Guo, B. Yu, Y. Zhao, Y. Wu, H. Zhang, Z. Liu, B. Han and Z. Liu, *Green Chem.*, 2017, **19**, 5777–5781.

8 H. P. Liang, A. Acharjya, D. A. Anito, S. Vogl, T. X. Wang, A. Thomas and B. H. Han, *ACS Catal.*, 2019, **10**, 3959–3968.

9 S. Yang, W. Hu, X. Zhang, P. He, B. Pattengale, C. Liu, M. Cendejas, I. Hermans, X. Zhang, J. Zhang and J. Huang, *J. Am. Chem. Soc.*, 2018, **140**, 14614–14618.

10 W. Zhong, R. Sa, L. Li, Y. He, L. Li, J. Bi, Z. Zhuang, Y. Yu and Z. Zou, *J. Am. Chem. Soc.*, 2019, **141**, 7615–7621.

11 Z. Fu, X. Wang, A. M. Gardner, X. Wang, S. Y. Chong, G. Neri, A. J. Cowan, L. Liu, X. Li, A. Vogel, R. Clowes, M. Bilton, L. Chen, R. S. Sprick and A. I. Cooper, *Chem. Sci.*, 2020, **11**, 543–550.

12 X. Wang, Z. Fu, L. Zheng, C. Zhao, X. Wang, S. Y. Chong, F. McBride, R. Raval, M. Bilton, L. Liu, X. Wu, L. Chen, R. S. Sprick and A. I. Cooper, *Chem. Mater.*, 2020, **32**, 9107–9114.

13 X. Wang, L. Chen, S. Y. Chong, M. A. Little, Y. Wu, W. H. Zhu, R. Clowes, Y. Yan, M. A. Zwijnenburg, R. S. Sprick and A. I. Cooper, *Nat. Chem.*, 2018, **10**, 1180–1189.

14 S. Yang, W. Hu, X. Zhang, P. He, B. Pattengale, C. Liu, M. Cendejas, I. Hermans, X. Zhang, J. Zhang and J. Huang, *J. Am. Chem. Soc.*, 2018, **140**, 14614–14618.

15 Z. Fu, X. Wang, A. M. Gardner, X. Wang, S. Y. Chong, G. Neri, A. J. Cowan, L. Liu, X. Li, A. Vogel, R. Clowes, M. Bilton, L. Chen, R. S. Sprick and A. I. Cooper, *Chem. Sci.*, 2020, **11**, 543–550.

16 X. Chen, Q. Dang, R. Sa, L. Li, L. Li, J. Bi, Z. Zhang, J. Long, Y. Yu and Z. Zou, *Chem. Sci.*, 2020, **11**, 6915–6922.

17 Q. Fan, U. A. Méndez-Romero, X. Guo, E. Wang, M. Zhang and Y. Li, *Chem. - An Asian J.*, 2019, **14**,

3085–3095.

18 W. Chen, L. Wang, D. Mo, F. He, Z. Wen, X. Wu, H. Xu and L. Chen, *Angew. Chem. Int. Ed.*, 2020, **59**, 16902–16909.

19 J. Kou, C. Lu, J. Wang, Y. Chen, Z. Xu and R. S. Varma, *Chem. Rev.*, 2017, **117**, 1445–1514.

Appendix

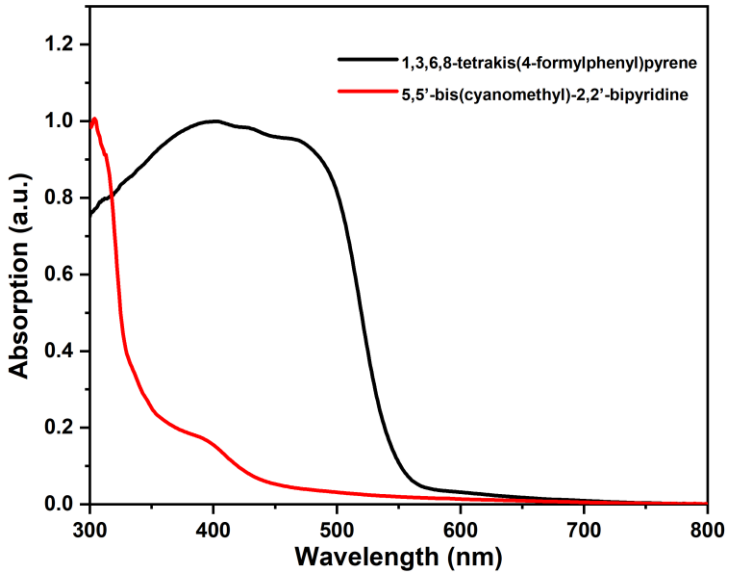

Figure A-1 UV-Vis absorption spectra of 5,5'-bis(cyanomethyl)-2,2'-bipyridine and 1,3,6,8-tetrakis(4-formylphenyl)pyrene in the solid-state.

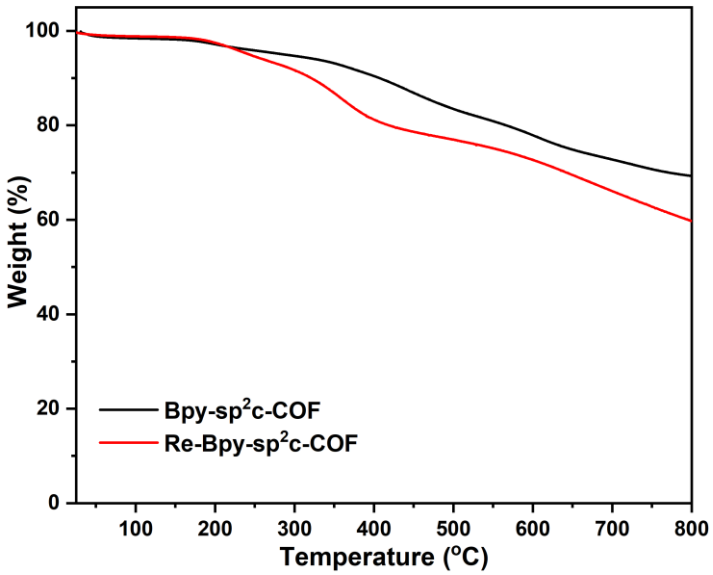

Figure A-2 TGA traces of **Bpy-sp²c-COF** and after loading with $[Re(CO)_5Cl]$ (**Re-Bpy-sp²c-COF**) measured under nitrogen.

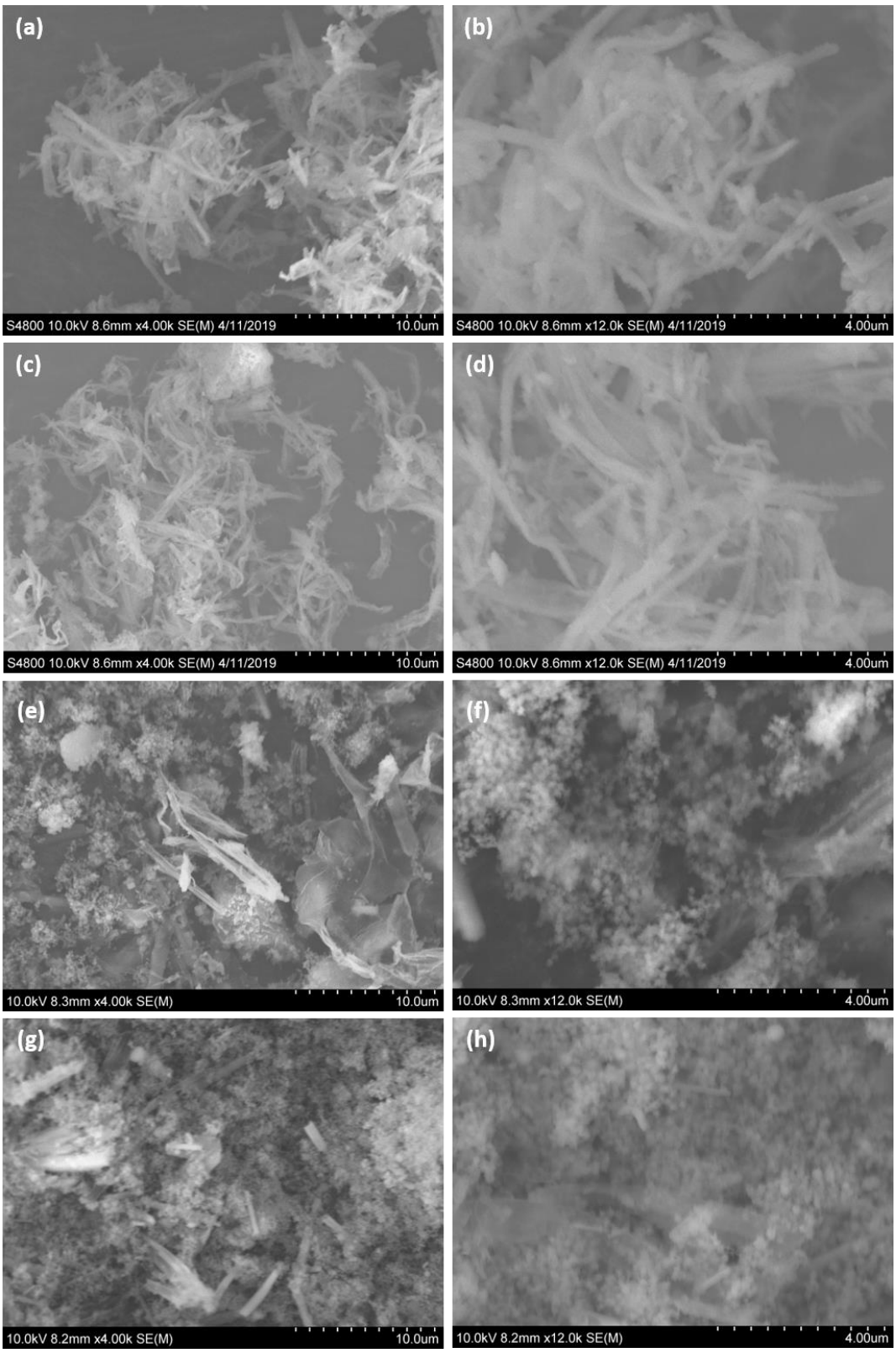

Figure A-3 SEM images of **Bpy-sp^{2}c-COF** (a, b), **Re-Bpy-sp^{2}c-COF** (c, d), **Bpy-sp^{2}c-P** (e, f) and **Re-Bpy-sp^{2}c-P** (g, h).

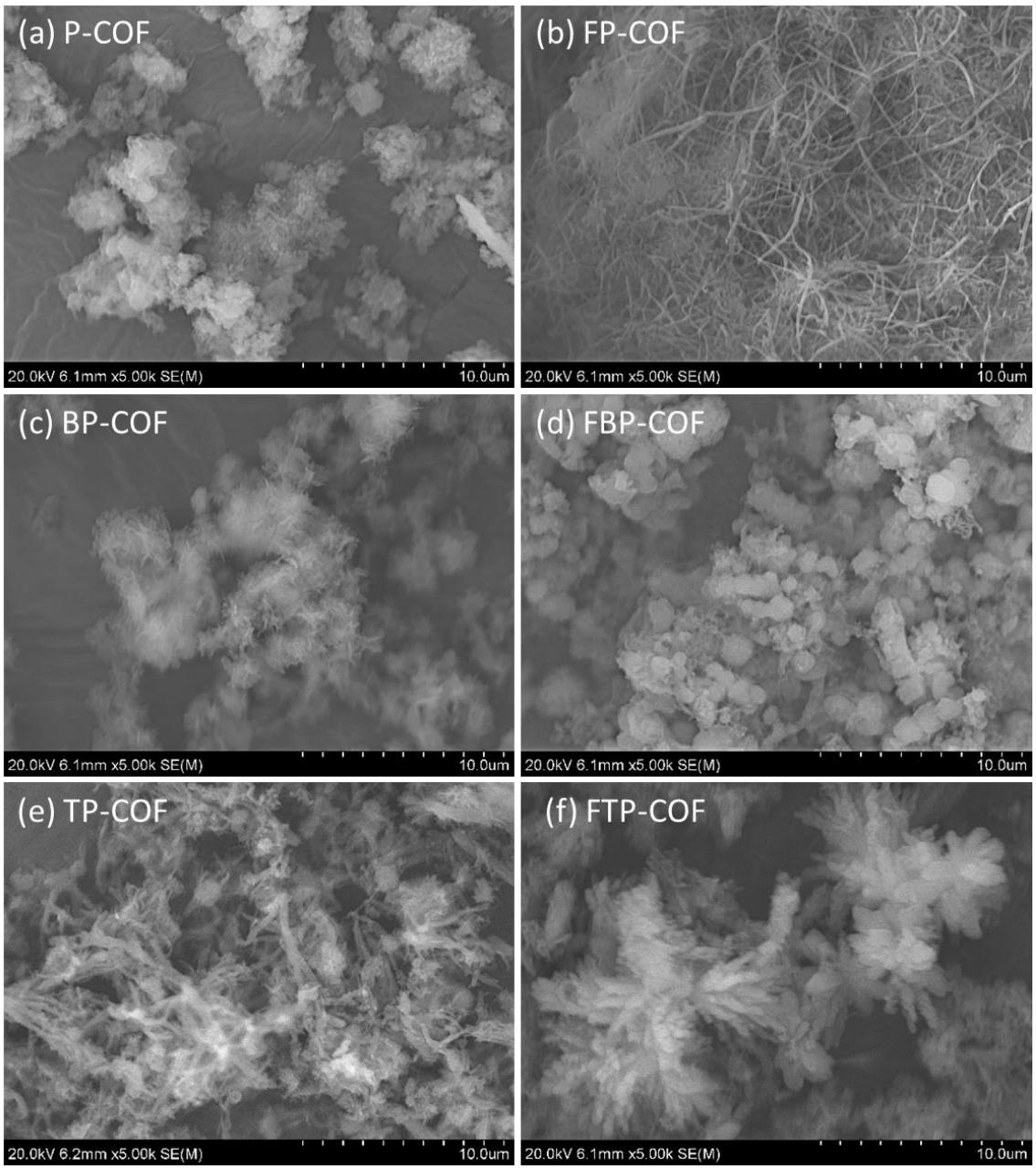

Figure A-4 SEM images of P-COF (a), FP-COF (b), BP-COF (c), FBP-COF (d), TP-COF (e), and FTP-COF (f).

Table A-1 Previously reported photocatalytic CO_2 reduction using different photocatalysts with molecular cocatalysts in Figure 4.17c.

Photocatalyst	Cocatalyst	Main products and highest yield (μmol h^{-1} g^{-1})	Selectivity	Reaction solvent	Irradiation condition
FBP-COF	$[Co(bpy)_3]^{2+}$	826.4 (CO)	95.5% (CO)	MeCN / H_2O / TEOA (3/1/1)	1 atm, λ > 420 nm (300 W Xe light source)
PI-COF-TT	$[Ni(bpy)_3]^{2+}$	483 (CO)	93% (CO)	MeCN / H_2O / TEOA (3/1/1)	UV-vis light (300 W Xe light source)
N-CP-D	$[Co(bpy)_3]^{2+}$	2274	82% (CO)	MeCN / H_2O / TEOA (7/3/1)	80 kPa, λ > 400 nm (300 W Xe light source)
mpg-CN_x	CoPPc	17.9	84.4% (CO)	MeCN / TEOA (4/1)	1 atm, UV-Vis light (AM 1.5G, 100 $mWcm^{-2}$, λ > 300 nm)
DA-CTF	$[Co(bpy)_3]^{2+}$	155 (CO)	69% (CO)	MeCN / TEOA (2/1)	1 atm, λ ≥ 420 nm (225 W Xe light source)
CTF-BT	$[Co(bpy)_3]^{2+}$	1213 (CO)	81.6% (CO)	MeCN / H_2O / TEOA (4/1/1)	1 atm, λ > 420 nm (300 W Xe light source)
CdS/UiO-bpy/Co	-	235 (CO)	85% （CO）	MeCN / TEOA (4/1)	1 atm, λ > 420 nm (300 W Xe light source)
CdS-BCN	$[Co(bpy)_3]^{2+}$	250 (CO)	81.7% (CO)	MeCN / H_2O / TEOA (4/2/1)	1 atm, λ > 420 nm (300 W Xe light source)
In_2S_3-$CdIn_2S_4$	$[Co(bpy)_3]^{2+}$	825	73.3% (CO)	MeCN / H_2O / TEOA (3/2/1)	1 atm, λ > 400 nm (300 W Xe light source)
CNNS-UiO-66(Zr)	-	9.9	-	MeCN / TEOA (4/1)	1 atm, 400 nm < λ < 800 nm (300 W Xe light source)
BCN	$[Co(bpy)_3]^{2+}$	93 (CO)	76.2% (CO)	MeCN / H_2O / TEOA (4/2/1)	1 atm, λ > 420 nm (300 W Xe light source)
HR-CN	$[Co(bpy)_3]^{2+}$	297 (CO)	96.7% (CO)	MeCN / H_2O / TEOA (3/1/1)	1 atm, λ > 420 nm (300 W Xe light source)
MCN/CoO_x	$[Co(bpy)_3]^{2+}$	204 (CO)	78.5% (CO)	MeCN / TEOA (2/1)	1 atm, λ > 420 nm (300 W Xe light source)